CHALMERS

Proceedings of the 25th European VLBI Group for Geodesy and Astrometry Working Meeting

14–18 March 2021
Cyberspace

edited by R. Haas

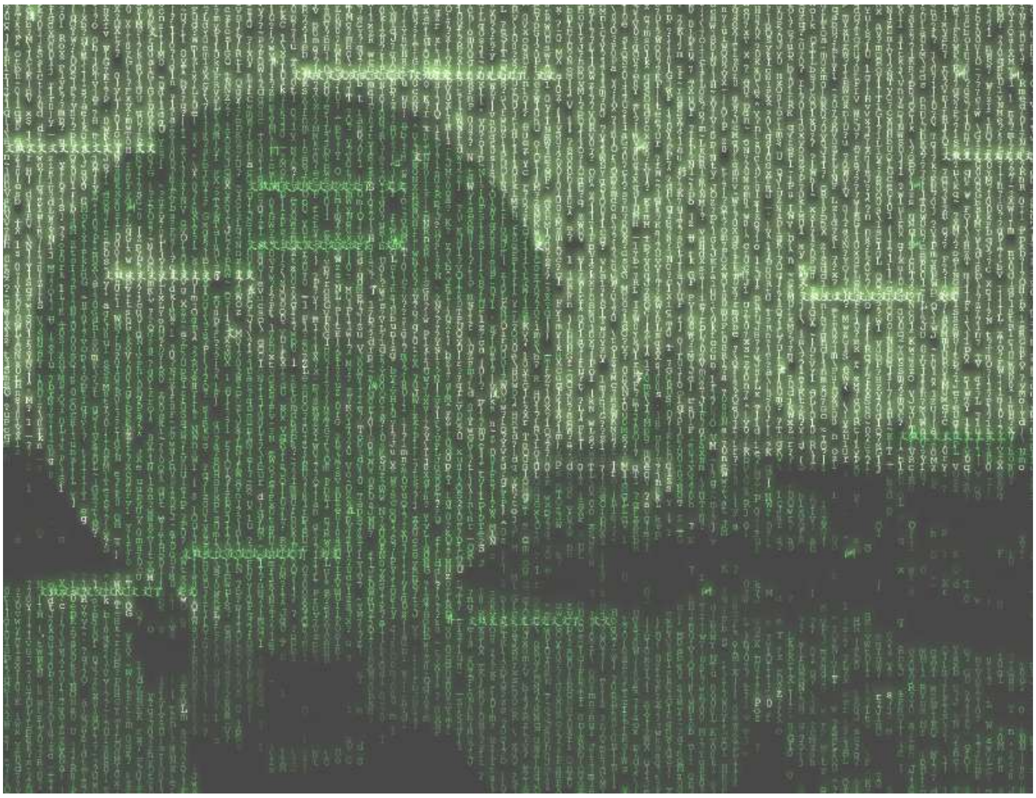

Proceedings of the 25th European VLBI Group for Geodesy and Astrometry Working Meeting

edited by
Rüdiger Haas

Cover: A Cyberspace representation of the Onsala twin telescopes.

December 2021, Gothenburg, Sweden

ISBN: 978-91-88041-41-8
(2021 | ed. Rüdiger Haas | Proceedings of the 25th European VLBI Group for Geodesy and Astrometry Working Meeting | E-bok)

Preface

The 25th Working Meeting of the European VLBI Group for Geodesy and Astrometry (EVGA) was held 14-18 March 2021 during the ongoing Covid-19 Pandemic. For this reason it was organized by Chalmers University of Technology as a virtual meeting in Cyberspace, see `https://www.chalmers.se/en/conference/EVGA2021/Pages/default.aspx`.

The meeting started with a virtual ice breaker party on Sunday, 14 March. This party used the `wonder.me` software for virtual events, that allowed to meet the colleagues in larger and smaller groups to chat and discuss online. The same software was also used later during the meeting for the poster/movie sessions.

On Monday, 15 March, the real scientific program started with oral presentations and poster/movie sessions. The oral presentations were given using the `zoom` software, while posters were made available as pdf-files on the meeting webpage. Also a number of prerecorded movies were made available. This allowed to read and watch this material offline and then to discuss with the responsible authors during the poster/movie sessions. All material, both the oral presentations, the poster presentations and the movies, are still available at the meeting webpage.

To allow as many people from different continents to participate in EVGA 2021, the events started at 11 UT every day, and lasted until 17 UT. The last day was extending a bit more in the evening to hold the IVS Analysis Workshop.

In total there were 170 registered participants (Fig. 1) which is a new record for EVGA working meetings. Another new record is that 25 % of the registered participants were women.

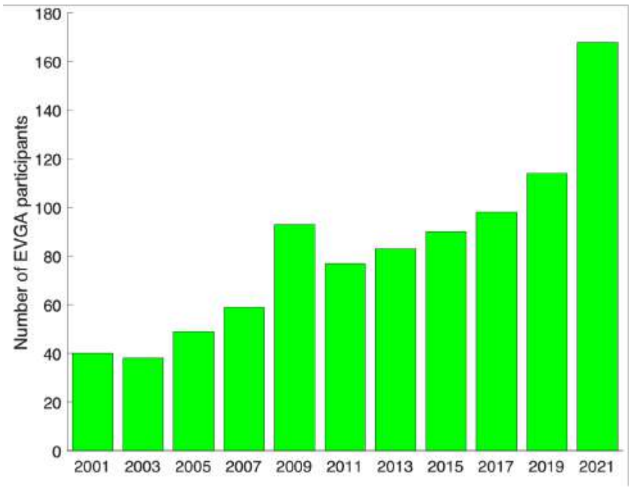

Figure 1: Number of registered participants at EVGA meetings during the last two decades.

Of course it was not possible to have coffee breaks and a conference dinner together with the colleagues. Neither it was possible to take a conference picture. Instead we put together a collage of selfies that some of the participants kindly provided, see Figure 2.

Figure 2: A collage of pictures of EVGA 2021 participants.

The large number of participants at the EVGA 2021 Working Meeting, and the high quality of the presented contributions are very strong indicators for an active and prospering European VLBI community. This is very encouraging for the future!

We want to thank all participants for sharing their interesting findings with the audience during interesting oral and poster presentations. We want to thank the scientific organising committee (SOC) for putting together a very interesting meeting program and the virtual organising committee for organising (VOC) the sessions.

We are grateful to all authors for preparing their proceedings contributions. The proceedings are available in electronic form at the EVGA webpage `evga.org`.

December 2021
Rüdiger Haas (EVGA chair)

EVGA 2021 organising committees

Scientific Organising Committee (SOC)

- Simone Bernhart (Reichert GmbH/BKG/MPIfR Bonn)
- Sigrid Böhm (Technische Universität Wien)
- Susana Garcia-Espada (Kartverket)
- Anastasiia Girdiuk (BKG Frankfurt)
- Rüdiger Haas (Chalmers University of Technology)
- Karine Le Bail (Chalmers University of Technology)
- Nataliya Zubko (Finnish Geospatial Research Institute)

Virtual Organising Committee (VOC)

- Periklis-Konstantinos Diamantidis (Chalmers University of Technology)
- Susana Garcia-Espada (Kartverket)
- Rüdiger Haas (Chalmers University of Technology)
- Karine Le Bail (Chalmers University of Technology)

Series of events during the EVGA 2021

Date	Time	Event
14 March	UT 16:00-18:00	Icebreaker party
15 March	UT 10:50-17:00	EVGA 2021 day-1
16 March	UT 11:00-17:00	EVGA 2021 day-2
17 March	UT 11:00-17:00	EVGA 2021 day-3
18 March	UT 11:00-14:45	EVGA 2021 day-4
18 March	UT 14:45-18:30	IVS Analysis Workshop

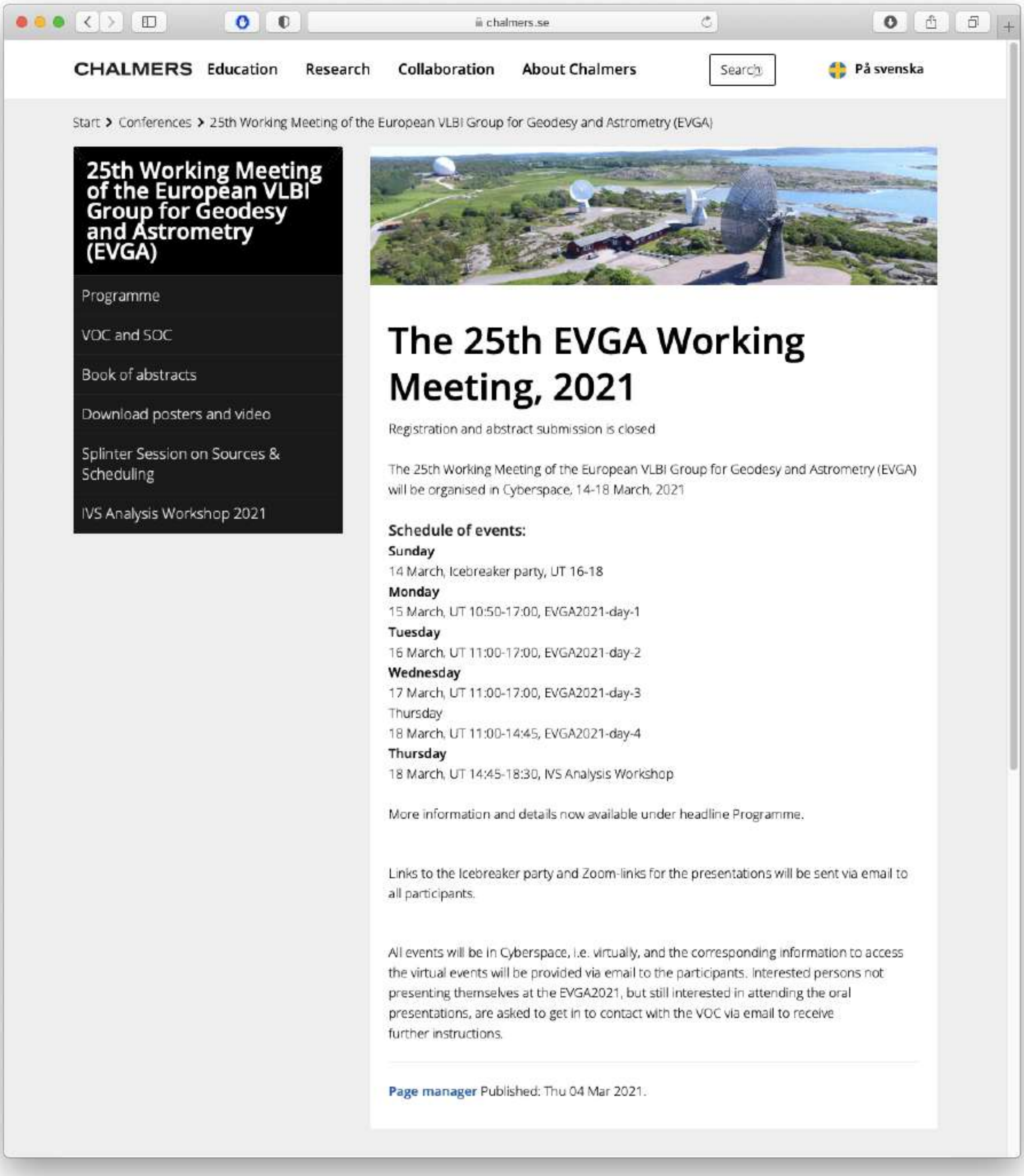

The 25th EVGA Working Meeting, 2021

Registration and abstract submission is closed

The 25th Working Meeting of the European VLBI Group for Geodesy and Astrometry (EVGA) will be organised in Cyberspace, 14-18 March, 2021

Schedule of events:
Sunday
14 March, Icebreaker party, UT 16-18
Monday
15 March, UT 10:50-17:00, EVGA2021-day-1
Tuesday
16 March, UT 11:00-17:00, EVGA2021-day-2
Wednesday
17 March, UT 11:00-17:00, EVGA2021-day-3
Thursday
18 March, UT 11:00-14:45, EVGA2021-day-4
Thursday
18 March, UT 14:45-18:30, IVS Analysis Workshop

More information and details now available under headline Programme.

Links to the Icebreaker party and Zoom-links for the presentations will be sent via email to all participants.

All events will be in Cyberspace, i.e. virtually, and the corresponding information to access the virtual events will be provided via email to the participants. Interested persons not presenting themselves at the EVGA2021, but still interested in attending the oral presentations, are asked to get in to contact with the VOC via email to receive further instructions.

Page manager Published: Thu 04 Mar 2021.

Figure 3: The webpage for the EVGA 2021 Working Meeting. For the time being, all provided oral presentations, poster presentatios and movies are still available for download.

Program

EVGA working meeting 2021

2021-03-14	**Icebreaker party - online**	UT 16:00-18:00

2021-03-15

Haas	**Welcome and Introduction**	UT 10:50-11:00
Session-01	**Chairperson: Rüdiger Haas**	
McCallum J	A wideband observing mode for the AuScope array	UT 11:00-11:15
Tangen	Current status at Ny-Ålesund Geodetic Earth Observatory	UT 11:15-11:30
Lopez-Perez	The current status of RAEGE	UT 11:30-11:45
Lopez-Perez	Preamplifier module for VGOS and legacy S/X observations compatibility in the presence of RFI signals	UT 11:45-12:00
	break - shake your legs	UT 12:00-12:15
Session-02	**Chairperson: Nataliya Zubko**	
Gomez-Molina	New Designs in VGOS Frontends in Yebes Observatory	UT 12:15-12:30
Tuccari	The BRAND EVN receiver and the new DBBC4 backend	UT 12:30-12:45
Plötz	Advances in automatized schedule generation at the VLBI operation center DACH and introduction of the VLBI correlation center at Wettzell	UT 12:45-13:00
Schartner	Automated VLBI scheduling utilizing Artificial Intelligence based parameter optimization	UT 13:00-13:15
	break - shake your legs	UT 13:15-13:30
Session-03	**Chairperson: Karine Le Bail**	
Ricci	A geodetic VLBI experiment with the dissemination of a clock via coherent optical fibre link	UT 13:30-13:45
Jaron	EU-VGOS activities in Vienna	UT 13:45-14:00
Barrett	A first look at mixed VGOS-S/X correlation and post-processing	UT 14:00-14:15
Ruszczyk	Experience from S/X–VGOS mixed-mode observations	UT 14:15-14:30
	break - shake your legs	UT 14:30-14:45
Poster and movie session and discussions		UT 14:45-17:00

2021-03-16

Session-04	**Chairperson: Sigrid Böhm**	
McCallum L	Australian mixed-mode sessions	UT 11:00-11:15
Takagi	A superconductor filter installed in the broadband feed of Ishioka VLBI station	UT 11:15-11:30
Gruber	Simulation of VGOS observations at the raw data level with VieRDS	UT 11:30-11:45
Varenius	ONTIE: Short-baseline interferometry at Onsala Space Observatory	UT 11:45-12:00
	break - shake your legs	UT 12:00-12:15
Session-05	**Chairperson: Nataliya Zubko**	
Kern	VLBI Intensive sessions: the selection of baselines for UT1 estimation	UT 12:15-12:30
Kurdubov	Approaches of optimal scheduling of UT1 geodetic VLBI sessions	UT 12:30-12:45
Malkin	On the selection of prospective sources for ICRF extension	UT 12:45-13:00
de Witt	Improving the S/X Celestial Reference Frame in the South: A Status Update	UT 13:00-13:15
	break - shake your legs	UT 13:15-13:30
Session-06	**Chairperson: Anastasiia Girdiuk**	
Gomez	Determination of the geodetic position of non-geodetic EVN antennas	UT 13:30-13:45
Hase	Spectrum Management for the VGOS	UT 13:45-14:00
Behrend	New Ingest Software at IVS Data Centers	UT 14:00-14:15
Jacobs	X/Ka Network Enhanced by Misasa, Japan’s 54-meter antenna	UT 14:15-14:30
	break - shake your legs	UT 14:30-14:45
Poster and movie session and discussions		UT 14:45-17:00

2021-03-17

Session-07	**Chairperson: Karine Le Bail**	
Salarpour	An empirical review of structure index characteristics for geodetic VLBI observations	UT 11:00-11:15
Kurdubov	The source structure as main error source in Russian intensive sessions	UT 11:15-11:30
Kareinen	Mitigating the effect of extended source structure in geodetic VLBI by re-weighting observations using baseline-to-jet orientation	UT 11:30-11:45
Lösler	On the impact of the coordinate representation onto the estimates in least-squares adjustment	UT 11:45-12:00
	break - shake your legs	UT 12:00-12:15
Session-08	**Chairperson: Susana Garcia-Espada**	
Wang	VLBI Processing in the PANDA Software	UT 12:15-12:30
Flohrer	VLBI enhancement of the Bernese GNSS Software for multi-technique analysis at BKG	UT 12:30-12:45
Hellmers	Combined IVS contribution to the ITRF2020	UT 12:45-13:00
Girdiuk	Intensives and 24-hour session data reprocessing for BKG AC 2020a solutions	UT 13:00-13:15
	break - shake your legs	UT 13:15-13:30
Session-09	**Chairperson: Anastasiia Girdiuk**	
Balidakis	On the Origin of Clock Breaks Detected in Geodetic VLBI Data	UT 13:30-13:45
Krasna	Baseline-dependent clock offsets in VLBI analysis	UT 13:45-14:00
Nilsson	Evaluation of the results from the VGOS sessions	UT 14:00-14:15
Gipson	Review of Operational VGOS Sessions in 2020	UT 14:15-14:30
	break - shake your legs	UT 14:30-14:45
Poster and movie session and discussions		UT 14:45-17:00

Gipson	**Splinter Session on Source & Scheduling**	UT 18:00-19:30

2021-03-18

Session-10	**Chairperson: Susana Garcia-Espada**	
Xu S	The K Band Geodesy with the East Asian VLBI Network	UT 11:00-11:15
Zubko	Ionosphere comparison study of VGOS and Total Electron Content global maps	UT 11:15-11:30
Negusini	A Broadband VLBI experiment with transportable stations between Japan and Italy with a new observation scheme using closure delay relation	UT 11:30-11:45
Teke	Ocean tide loading displacements from VLBI and the long term ocean tide variability	UT 11:45-12:00
	break - shake your legs	UT 12:00-12:15
Session-11	**Chairperson: Anastasiia Girdiuk**	
Puente	Consistency of VLBI estimates in the CONT17 campaign	UT 12:15-12:30
Diamantidis	Inter- and intra-technique combination on the observation level between VLBI and GPS - a study case for CONT17	UT 12:30-12:45
Lengert	Combination of GNSS and VLBI data for consistent estimation of Earth Rotation Parameters	UT 12:45-13:00
Haas	VGOS Intensives Ishioka-Onsala	UT 13:00-13:15
	break - shake your legs	UT 13:15-13:30
Session-12	**Chairperson: Rüdiger Haas**	
de Witt	K-band Imaging of 732 ICRF3 sources	UT 13:30-13:45
Xu M	Imaging VGOS observations and the effects of source structure	UT 13:45-14:00
Hunt	Update on VLBA Imaging of ICRF3 Sources	UT 14:00-14:15
Le Bail	Source flux-density monitoring in the VGOS era	UT 14:15-14:30

Haas	**Closing remarks - good bye**	UT 14:30-14:45

Gipson	**IVS Analysis Workshop 2021**	UT 14:45-18:30

POSTERS		
Zubko	Status of the VGOS project at the Metsähovi Geodetic Research Station	P-01
Chuan	AuScope VLBI Dynamic Observing	P-02
Nickola	HartRAO weather data	P-03
Nurul Huda	Measuring the impact of Indonesian antennae to Earth Orientation Parameter estimation	P-04
Anderson	Effects of Source Weighting in Geodetic VLBI Analysis	P-05
Anderson	The Potsdam Open Source Radio Interferometry Tool (PORT)	P-06
Basu	Source structure and position stability of celestial reference frame sources in the Deep South	P-07
Elgered	Small scale atmospheric variations sensed with very short baseline interferometry (VSBI) and microwave radiometry	P-08
Kirkvik	First results from the new station NYALE13S	P-09
Liu	Comparison of tropospheric zenith wet delay from VLBI and GNSS Time Series	P-10
Mammadaliyev	Precise orbit determination with VLBI to satellites: a simulation study	P-11
Mironova	Combination of IVS Intensive sessions using SINCOM software	P-12
Mironova	Improving of the covariance functions of the clock and troposphere parameters	P-13
Nothnagel	Reference epochs in VLBI estimations of clock parameters	P-14
Raut	Assessment of sub-daily Earth Rotation Parameters from VLBI with GNSS during the CONT17 campaign	P-15
Seitz	First VLBI-only TRF/CRF solution based on DGFI-TUM data for ITRF2020	P-16
Soja	The New IVS Associate Analysis Center at ETH Zurich	P-17
Xu M	Impacts of source structure as seen from the Gaia and VLBI comparison	P-18

MOVIES		
Neidhardt	Data Unlimited – The IVS Seamless Auxiliary Data Archive at the Wettzell observatory	M-01
Neidhardt	Autonomous Observations at the Wettzell observatory	M-02
Jaradat	10 years of AuScope VLBI	M-03
Titov	A jump in the VLBI position of the radio galaxy J1147+3501	M-04

This page is intentionally left blank.

Contents

The current status of RAEGE

José A. López-Pérez, João S. Ferreira, Javier González-García, Francisco J. Beltrán-Martínez,
Carlos Albo-Castaño, Abel García-Castellano, J. López-Ramasco, P. de Vicente-Abad,
José A. López-Fernández, Francisco W. Macedo, Luís R. Santos, Sara Pavão

Abstract When complete, the *Red Atlántica de Estaciones Geodinámicas y Espaciales* (RAEGE) will be composed of four VGOS radio-telescopes, two in Spain (Yebes and Gran Canaria) and two in Portugal (Santa María and Flores islands). The Yebes VGOS radio-telescope is fully operational and integrated in the VGOS core network. The Santa María VGOS radio-telescope is undergoing major maintenance operations. However, in November 2020 it performed joint observations of Bepi-Colombo at 8.4 and 32 GHz simultaneously, together with JPL/NASA Deep Space Network (DSN) antennas. More details on this experiment will be provided. The current status of all the four RAEGE radio-telescopes will be presented.

Keywords RAEGE, VLBI, VGOS, radiotelescope, receiver

1 Introduction

RAEGE stands for Atlantic network of geodynamic and space stations. It is a joint project between the Spanish Instituto Geográfico Nacional (IGN) and the Portuguese Gobierno Regional de Açores (GRA).

It plans to install 4 stations as shown in figure 1: Yebes, Santa María, Flores and Gran Canaria, each one equipped with a VGOS radiotelescope, GNSS receivers, a gravimeter and a local-tie network. In addition, Yebes will be equipped with an SLR station. The contract for this SLR station started last year, and it will be ready by January 2023.

So far, Yebes and Santa María are established only. Yebes is operating with a VGOS receiver while Santa María is working with a tri-band (S/X/Ka) receiver, but it will become a VGOS station along the second half of 2022.

Some changes were done in the organization of RAEGE project: a new director and deputy director were appointed in early 2020, the deputy director is now the station manager in Santa María, and new staff from Portugal and Spain has been engaged for Santa María.

2 RAEGE Yebes station

At the time of this meeting, Yebes station has participated in the VGOS and Euro-VGOS observations shown in table 1.

The radiotelescope has gone under some maintenance works, as servo UPS batteries update, grease pumps replacement, air-conditioning reparations and some electronic servo module replacements.

José A. López-Pérez[1], João S. Ferreira[2], Javier González-García[1], Francisco J. Beltrán-Martínez[1], Carlos Albo-Castaño[1], Abel García-Castellano[1], J. López-Ramasco[1], P. de Vicente-Abad[1], José A. López-Fernández[1], Francisco W. Macedo[3], Luís R. Santos[3], Sara Pavão[3]

(1) Yebes Observatory, Instituto Geográfico Nacional, Cerro de la Palera s/n, Yebes, E-19141 Guadalajara, España

(2) Associação RAEGE Açores, Estação RAEGE de Santa María, Estrada dos Piquinhos s/n, 9580-324 Vila do Porto (Santa María - Açores, Portugal)

(3) Estrutura de Missão dos Açores para o Espaço, Rua do Mercado n. 21, 9500-326 Ponta Delgada (São Miguel - Açores, Portugal)

Corresponding author: ja.lopezperez@oan.es

Fig. 1 Map of RAEGE stations and approximate baseline lengths.

Table 1 RAEGE Yebes observations

Year	VGOS	EU-VGOS
2018	19	-
2019	23	13
2020	25	15
2021	5	-

Currently it is equipped with the VGOS receiver for Santa María station, because the Yebes VGOS receiver is under upgrade in the laboratory, and the Santa María VGOS backends are not available yet to be installed there.

The improvements on the RAEGE Yebes VGOS receiver will include the following:

- A revisited and improved Quad Ridge Feed Horn with better input matching. A new design has been developed (see (2)) with improvements over the previous QRFH generation (see (3)).
- 30 dB directional couplers for calibration signal inyection to reduce the total receiver noise by 3 Kelvin .
- Balanced LNAs, which provide a much better input matching than single-ended LNAs, so they reduce very much the band-pass ripple due to mismatch between feed and LNAs (see (4)).
- The PhaseCal AU is going to be improved too, with better flatness of the pulse train envelope.
- A new PhaseCal GU for a suitable cable delay measurement.
- A new post-dewar pre-amplification and filtering stage.

Figure 2 shows the Santa Maria VGOS receiver noise temperature, as measured in the laboratory of Yebes Observatory (5), (6). This receiver is equipped with a couple of balanced low-noise amplifiers. This configuration largely reduced the ripple in the receiver band-pass, in particular above 6 GHz. Below this frequency, there are still some effects due to the QRFH. These will be solved with the new QRFH design.

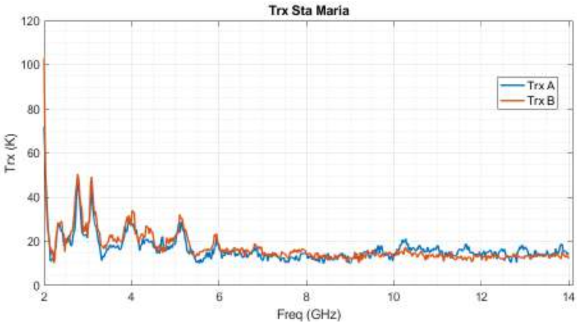

Fig. 2 RAEGE Santa Maria VGOS receiver noise temperature measurement.

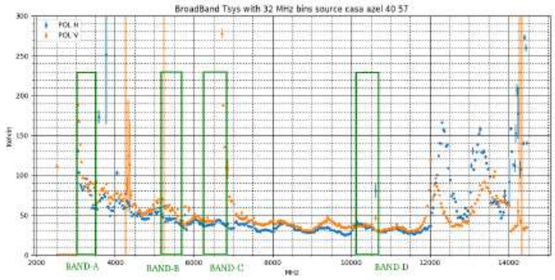

Fig. 3 RAEGE Yebes VGOS receiver system noise temperature measurement.

Figure 3 shows the system noise temperature across the full VGOS band. The green rectangles represent the current observing sub-bands: A, B, C and D. The high noise level in A and B seems to be due feed effects that are explained in (1). RFI is a problem too, in particular in S and C bands. The high levels in the range 12 - 14GHz are due to the current 3 GHz high-pass filter required for RFI rejection to avoid saturation. Its band-pass is up to 12 GHz. This will be solved during the receiver upgrade with a new high-pass filter.

3 RAEGE Santa Maria station

No observations have been performed due to heavy maintenance and reparation works, like the following:

Fig. 4 Rust in RAEGE Santa Maria radiotelescope pinions.

Fig. 5 Replacement of RAEGE Santa Maria radiotelescope servo container.

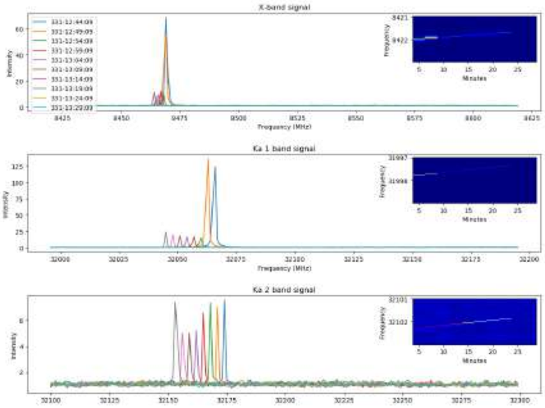

Fig. 6 Bepi-Colombo X and Ka band signals detected with RAEGE Santa Maria radiotelescope during tests with JPL.

- Heating system to avoid moisture on azimuth encoder tape
- Reparation of the tri-band receiver, which was re-installed in March 2020 (7)
- Retuning of the hydrogen maser (8)
- Substitution of hatch door in azimuth cabin

However, the biggest problems along 2020 and part of 2021 were:

- Corrosion in the Az and El gear rims and pinions
- Weather station problems
- Problems with the UPS
- Corrosion in the servo container floor
- Azimuth encoder tape damaged with scratches

All this problems have been solved in 2020, except for the Azimuth encoder tape, which is being substituted during this meeting.

Figure 4 that shows the corrosion on the gear rims and pinions and figure 5 shows the removal of the old servo container, which has been substituted by a new one.

Currently, we plan to perform fringe tests after Eastern, so we can resume operations in S/X by early May at latest.

Despite all these difficulties, in November 2020 we were able to perform a join observation between JPL Deep Space Network and Santa María in both X and Ka bands. The radio-source was Bepi-Colombo, which is a space probe heading to planet Mercury. The observation was a proof-of-concept observation, as JPL wanted to check if the accuracy of Doppler shift measurements can be improved by the use of corrections provided from smaller and stiffer antennas like VGOS ones. Figure 6 shows some plots of the detected signals.

This station will join legacy S/X VLBI observations until mid-2022, when the VGOS receiver will be installed, together with the required backeds.

4 RAEGE Flores station

The land for this station was bought and a topographic survey was performed. In addition, a GNSS receiver and a weather station were installed last year.

Currently, the contract for antenna design is in preparation. It has to be a special reinforced design due to the constant and sometimes strong winds in the island.

Fig. 7 Artistic view of RAEGE VGOS Gran Canaria station.

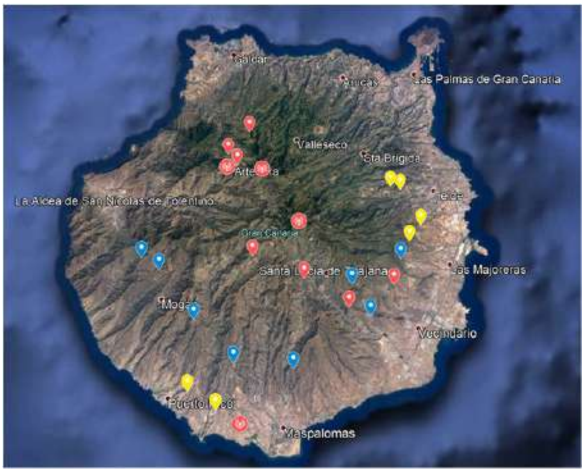

Fig. 8 Explored locations (blue points) in Gran Canaria island for RAEGE.

5 RAEGE Gran Canaria station

A site called Artenara was selected for the station some years ago. Figure 7 shows an artist impression of what the station was supposed to look. However, the surrounding area was declared World Heritage by UNESCO in July 2020, so IGN decided to look for another site, in order to avoid the loss of such declaration, which is very important for the island.

Several alternative sites were explored from July-November 2020. The map shown in figure 8 shows the locations that were explored. A new site has been identified. IGN and island authorities are evaluating how to buy the land and get all the permissions for the station. After this, the site will be granted to IGN.

6 Conclusions and outlook

Concerning RAEGE Yebes station, VGOS and EU-VGOS observations will continue with Santa Maria VGOS receiver, while the upgrade of Yebes VGOS receiver is finished.

With regard to Santa María, the reparation works will finish this month and S/X legacy observations will be resumed until mid-2022, when the VGOS receiver will be installed together with the corresponding backends.

The contract for Flores station radiotelescope is in preparation to be published in 2022.

Finally, for Gran Canaria, the projects of civil works have to be updated for the new site, if finally granted.

7 Acknowledgments

Special thanks are given to all the Spanish and Portuguese staff that supports RAEGE activities and goals.

References

1. G. Gomez-Molina, O. García-Pérez, J. M. Serna-Puente, F. Tercero. New Designs in VGOS frontends in Yebes Observatory. 25th EVGA meeting. March 15-18, 2021.
2. A. García, O. García-Pérez, F. Tercero. QRFH antenna for VGOS receiver (YQR-03-001). CDT Technical Report 2020-25
3. A. García, O. García-Pérez, F. Tercero. QRFH antenna for NMA VGOS receiver (YQR-02-002). CDT Technical Report 2020-1.
4. J.D. Gallego, I. López-Fernández, I. Malo, A. García, C. Diez, R. Amils. Ultra-wide Band LNAs for BRAND Front-ends: Single-ended and Balanced Approaches. BRAND/Yeb-TR-2018-001, CDT Tech. Rep. 2018-4.
5. J.M. Serna-Puente, J. A. López-Pérez, P. García-Carreño, M. Patino-Esteban, F. Valle, A. Alonso. Santa María VGOS receiver upgrade. CDT Technical Report 2020-21.
6. J.M. Serna-Puente, J. A. López-Pérez, P. García-Carreño, M. Patino-Esteban. Santa María VGOS receiver FAT. CDT Technical Report 2020-22
7. J.M. Serna-Puente, J. Fernández-Paniagua. Santa María Triband receiver setup. CDT Technical Report 2020-12
8. J. González. Frequency stability of the H-maser in Santa María. CDT Technical Report 2020-9.

New Designs in VGOS Front-ends in Yebes Observatory

G. Gómez-Molina, O. García-Pérez, F. Tercero

Abstract The Yebes Observatory has designed and built five VGOS compliant receivers (2-14 GHz bandwidth) for their own radio telescopes and for other European IVS partners under contract or agreement since 2015. Although such receivers are successfully working in their respective sites, we consider that there is still room for some improvements in the receiver design. A second generation of this receiver is going to be built at Yebes Observatory with a new design of the feed and the cryostat. Four of these new receivers are scheduled for 2022. This paper summarizes the first-generation receivers built until now and shows the improvements of the second generation.

Keywords VGOS, Radio telescope, Front-end

1 Introduction

In 2015 a first VGOS front-end was successfully installed in the 13.2 meters RAEGE radio telescope. This front-end had been designed and built at Yebes Observatory laboratories. Preliminary observations and tests proved that goals were achieved and four more front-ends have been built, one for Santa Maria Island in the Azores archipelago, one for the Metsähovi Radio Observatory (Finland), and two for the Ny-Ålesund Geodetic Observatory (Norway).

These five front-ends belong to the first generation. Currently a second generation is being designed, and at least four of this second-generation front-ends are planned to be built in 2022. Figure 1 shows the full receiver; including the front-end, phase cal units, cryogenic control unit, etc. This paper is centered in the front-end and the electrical components inside it, as well as the improvements foreseen from first to second generation.

2 First-generation VGOS front-ends

The main features of the VGOS front-end are listed in Table 1. There are three key technological aspects in the design of the front-end: the feed horn geometry, the LNA configuration (single-ended or balanced) and the cryostat which encloses these components as well as the cryogenic RF components.

Table 1: VGOS Front-end main features

Frequency band	2.3-14 GHz
Physical temperature	<35 K intermediate stage <10 K cold stage
Pressure	$<10^{-5}$mbar
Pressure leaks	$<10^{-5}$mbar·l/sec
Gain	>25 dB
Noise temperature	<35 K (from 4.5 to 14GHz)
Input	• 0.5mm Mylar Vacuum window to QRFH feed • Phase calibration through directional couplers: SMA (2 ports)
Output	2 linear polarizations: SMA 50 Ohm (2 ports)
Cold head	Sumitomo RDK-408S2

Gabriel Gómez-Molina[1], Oscar García-Pérez[1], Félix Tercero[1]
(1) Observatorio de Yebes, Instituto Geográfico Nacional (IGN), 19141 Yebes (Spain)
Corresponding author: `ggomez@oan.es`

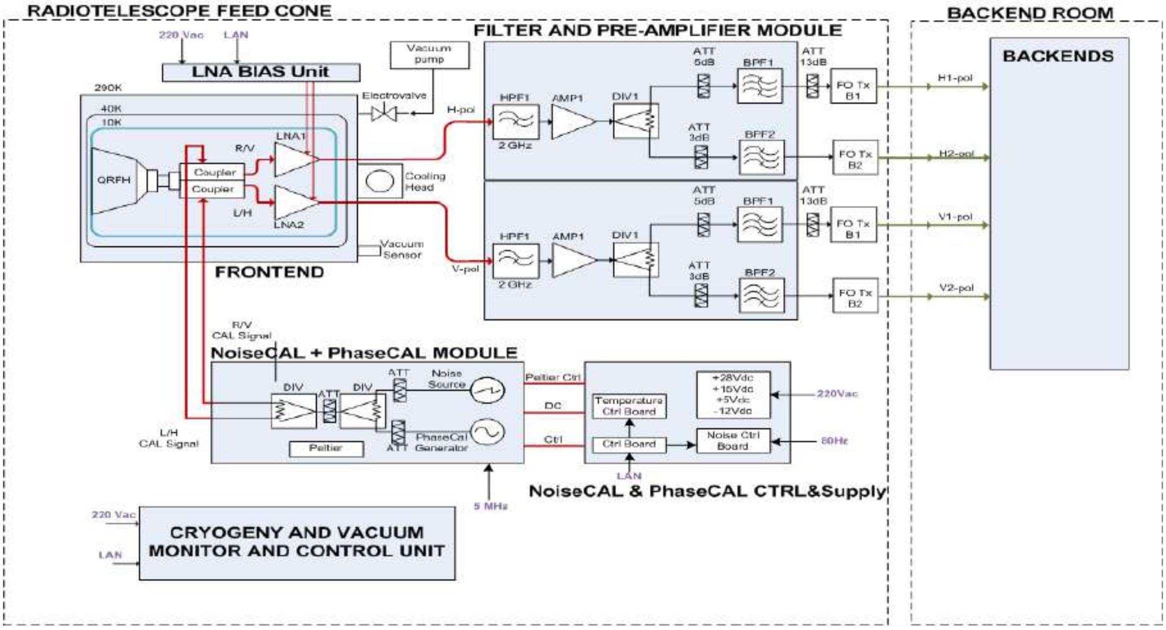

Fig. 1: VGOS front-end schematic

Feed and LNAs determine the behaviour of the front-end. Main characteristics of these two components are briefly shown in the next paragraphs.

The feed horn used in this front-end is a Quad-Ridge Flared Horn (QRFH) designed at Yebes Observatory, the YQR-02-xxx A. Baldominos et al. (2019). The main features of this feed horn are shown in Table 2.

Table 2: Main features of QRFH YQR-02-xxx

QRFH version	YQR-02-xxx
Frequency range	2.3-14 GHz
Return losses	-10 dB (typ.) -6 dB (max.)
Port isolation	30 dB (min.)
Aperture efficiency (In the radio telescope)	60% (min.)

The QRFH is shown in Figure 2 and its return losses in Figure 3. The last one shows the maximum value of the return losses (-6dB) and the slight difference between both polarizations.

Fig. 2: Feed horn model YQR-02-004

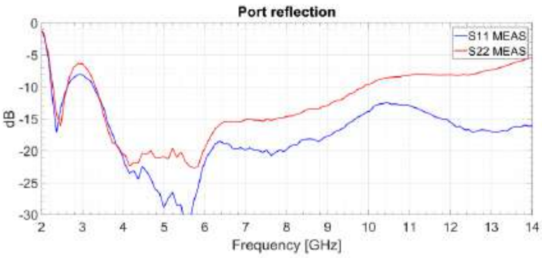

Fig. 3: YQR-02-004 return losses

The LNA is fully described in C. Diez et al. (2020) with an average noise temperature of 7.1K and return losses shown in Figure 4.

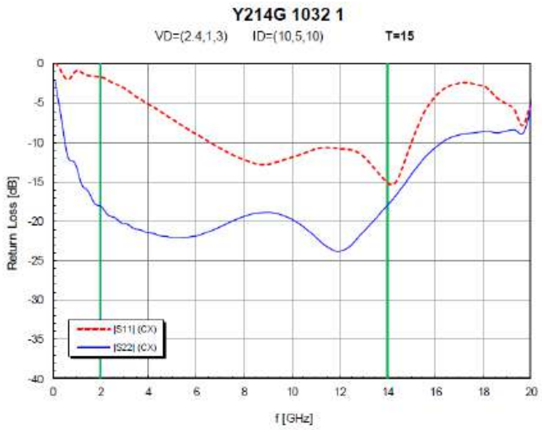

Fig. 4: Single-ended LNA return losses

During the development of the five first-generation front-ends, feed and LNAs have been assembled in single-ended configuration in the beginning, moving to a balanced configuration in the last front-end units.

The single-ended configuration consists of an LNA connected directly to the output of the directional coupler for each port of the QRFH (V and H polarizations). In this case, the input return losses of the LNA generate a stationary wave between the QRFH and the LNA itself.

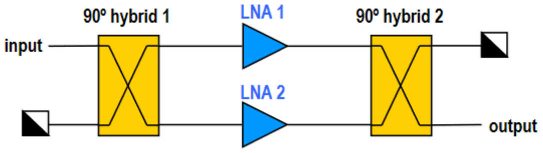

Fig. 5: Balanced LNA configuration

The balanced configuration uses a pair of LNA per polarization combined with two 90-degree hybrids (Figure 5). This doubles the number active elements compared to the single-ended configuration. The return losses of this configuration are below -18dB across the whole band (Figure 6), which is much lower than in single-ended configuration. This configuration significantly improves the gain ripple and the reflections between the LNA and the feed.

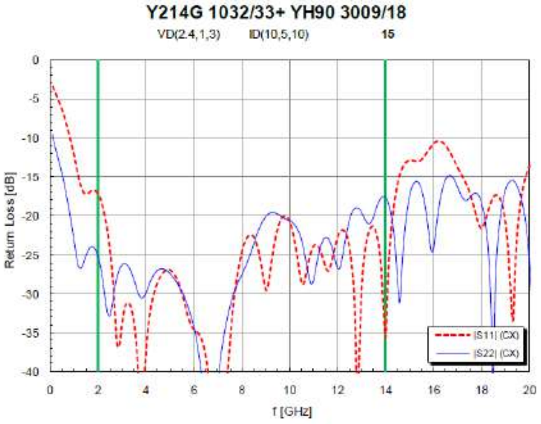

Fig. 6: Balanced LNA configuration return losses

The cryostat is the third key component for the frontend performance. The first implementation is based on the one used in a previous tri-band receiver J.A. López-Pérez et al. (2021). It features a cold stage at 9 K and an intermediate stage at 35 K with the QRFH, directional couplers, hybrids and LNAs attached to the cold stage (9 K). It has a 0.5mm thickness 319mm diameter Mylar window, a polystyrene foam IR filter (3 layers of 2.6mm each) and a dewar volume of circa 59 L.

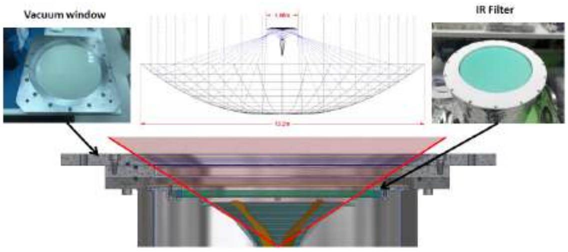

Fig. 7: Feed boresight inside the cryostat

The distance of the feed aperture to the vacuum window inside the cryostat is 45 mm, which gives a boresight angle of 58 degrees. This angle is defined as the half-angle of illumination from the feed phase center to the sub-reflector. The subtended half angle of the sub-reflector from the feed is 65 degrees, so in this design there is a slight blockage with the IR Filter and the vacuum window (Figure 7) which affects the noise temperature.

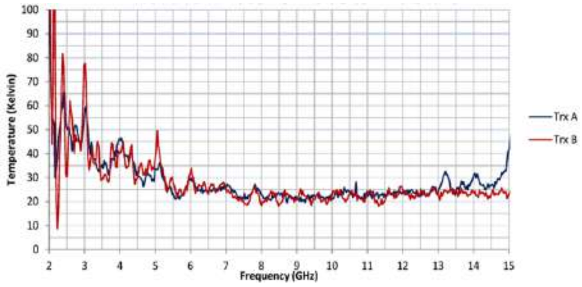

Fig. 8: Noise temperature of the first-generation front-end (red: single-ended, blue: balanced)

Figure 8 shows the noise temperature for a first-generation front-end prototype with both single-ended (red) and balanced (blue) configurations, one for each polarization channel. The figure shows higher noise and some artifacts at the edges of the band, specially at low frequencies with the single-ended configuration, mainly due to the higher return losses of the LNA and the QRFH. With the balanced configuration the noise at low frequencies decreases but there is a slight increment in the high end of the band (caused by the asymmetry of the QRFH return losses). Overall the noise is below 35K from 4.5 to 14GHz and better at low frequencies with the balanced configuration.

3 Second-generation VGOS front-ends

With all the knowledge acquired with the first-generation VGOS front-ends a new generation is currently being designed, putting the efforts on the improvement of the noise temperature (especially in the edges of the band), a size reduction, and better placement of the feed inside the cryostat.

A new feed is introduced for this second generation, the YQR-03-xxx (Figure 9) A. García et al. (2020) which improves the return losses of the previous version: below -10dB across the whole band as shown in Figure 10. Also both polarizations have a more similar behavior between them.

Fig. 9: Feed horn model YQR-03-002

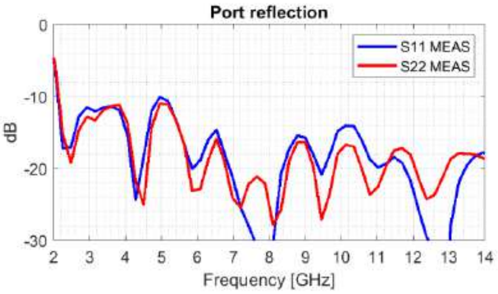

Fig. 10: YQR-03-002 return losses

The RF chain has also been reduced by connecting the directional couplers directly to the feed ports rather than with a SMA transition. This reduces the losses prior to the LNA and also makes more room in the cryostat for the installation of a HTS notch filter to mitigate RFI in the cases it is necessary.

Regarding the cryostat design, a reduction in volume, an increase of the vacuum window diameter, and a reduction of the distance between the feed aperture and the vacuum window have been implemented. These allow a better clearance angle for the feed (to fully illuminate the subreflector). The IR filter is also being redesigned. Table 3 shows the cryostat differences between the first and second generation.

Table 3: First-generation vs. second-generation cryostat

	1st gen.	2nd gen.
Vacumm window diameter	319 mm	>335 mm
Feed distance to window	45 mm	<37 mm
Clearance angle for feed	58 degree	>65 degree
IR filter	Polystyrene	TBD
Cryostat volume	59 L	49 L

Finally, some minor changes regarding the assembly of the cryostat have also been implemented, to make the assembly process easier and the whole construction more robust. Figure 11 shows a 3D design of the second-generation VGOS front-end.

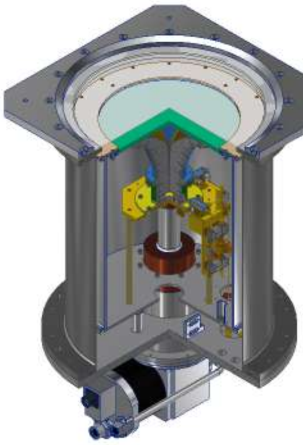

Fig. 11: Second-generation VGOS front-end with balanced LNA configuration

4 Conclusions and outlook

Since 2015, five VGOS receivers have been built and improved at Yebes laboratories based on feed, LNAs and cryostat with high performance in the middle band but with some artifacts in the edges, and concerns about the RFI environment getting worse.

New feed and cryostat designs combined with previous LNAs configurations will improve the noise performance of the receiver in the edges of the band in this new generation presented in this paper.

At least four new receivers are foreseen to be built in the next two years, one for Yebes, and the rest for other institutions.

References

Technical Report IT-CDT-2019-01 `https://icts-yebes.oan.es/reports/doc/IT-CDT-2019-1.pdf` 2

Technical Report IT-CDT 2020-11 `https://icts-yebes.oan.es/reports/doc/IT-CDT-2020-11.pdf` 3

I. Malo-Gomez, J. D. Gallego-Puyol, C. Diez-Gonzalez et al, ”Cryogenic Hybrid Coupler for Ultra- Low-Noise Radio Astronomy Balanced Amplifiers,” in IEEE TMTT, Dec. 2009

Technical Report IT-CDT-2020-26 `https://icts-yebes.oan.es/reports/doc/IT-CDT-2020-26.pdf` 4

J. A. López-Pérez, F. Tercero-Martínez, J. M. Serna-Puente et al, “A Tri-Band Cooled Receiver for Geodetic VLBI,” *Sensors*, vol. 21, no. 8, p. 2662, Apr. 2021. doi: 10.3390/s21082662. 3

F. Tercero, O. Garcia-Perez, J.M. Serna et al, ”Optimization of the Quad-Ridged Horn for the geodetic VGOS station of the Yebes Observatory” *12th European Conference on Antennas and Propagation (EuCAP 2018)*, 2018 page (5 pp.) doi: 10.1049/cp.2018.0818

J.A. López Pérez, P. de Vicente, J.A. López Fernández et al, ”Instrumentation Developments for VGOS at IGN Yebes Observatory” *Proceedings of the 24th European VLBI Group for Geodesy and Astrometry Working Meeting*, 17-19 March 2019, Las Palmas de Gran Canaria, Spain, Eds. R. Haas, S. Garcia-Espada, and J. A. López Fernández, ISBN: 978-84-416-5634-5, pp. 22-26

Advances in automatized schedule generation at the VLBI operation center DACH and introduction of the VLBI correlation center at Wettzell

C. Plötz, M. Schartner, J. Böhm, T. Schüler, B. Soja

Abstract Two newly established VLBI components, the Operation Center DACH and a new VLBI correlation facility are introduced.

The Geodetic Observatory Wettzell (GOW), jointly operated by the Federal Agency for Cartography and Geodesy (BKG) and the Technical University of Munich (TUM), was accepted as an IVS Operation Center (OC) on November 19, 2019. This addition complements BKG's substantial contribution to the IVS and its continuous and long-term VLBI observation programs. Recently, the OC in cooperation with ETH Zürich (ETHZ) and TU Wien (TUW) added automated schedule generation to its capabilities. This cooperation within the institutions operates now under the unified Operation Center with the abbreviation DACH, unifying BKG, ETHZ and TUW. The assigned VLBI schedules for this operation center are generated with an innovative approach consisting of a Python framework (VieSched++ AUTO), which allows to fully automate the generation of highly optimized schedules with VieSched++. The complete workflow is designed to gather and evaluate all master files, calling the VieSched++ scheduling application and also upload the selected schedule files to the IVS data centers. Additionally, a new website at BKG shows the complete history of all scheduled sessions, including quality oriented parameters with graphical comparisons.

Furthermore, an outline of the new VLBI correlation facility at the Geodetic Observatory Wettzell will be presented. This includes technical specifications, milestones and timelines.

Keywords automatization, VLBI schedules, operation center DACH

1 Introduction

In order to continue and complement the participation and contribution of BKG to the internationally coordinated VLBI observation programme of the International VLBI service (IVS) a new IVS Operation Center (OC) component was founded at the Geodetic Observatory Wettzell and approved officially on on November 19, 2019. The initial motivation for the new operation center was to adopt the assigned VLBI session types, which were supervised and serviced at the discontinued former VLBI Operation Center at the university of Bonn to provide a long-term and reliable infrastructure for the VLBI schedule generation. However, in 2019 there was the newly developed VLBI scheduling software VieSched++ (Schartner and Böhm , 2019) developed at a level to provide reliable usage and in particular promising improvements for the inclusion of VLBI stations, e.g. the German Antarctic Receiving Station (GARS) O'Higgins, in VLBI schedules with many participating stations. Therefore, the decision was taken to integrate the Technische Universität Wien, where VieSched++ was developed, and later on the ETH Zürich, with the change of the main developer there. Finally, the IVS Operation Center DACH was constituted and is nowadays in charge of many IVS

Christian Plötz[1], Matthias Schartner[2], Johannes Böhm[3], Torben Schüler[1], Benedikt Soja[2]

(1) Bundesamt für Kartographie und Geodäsie (BKG), Sackenrieder Str. 25, D-93444 Bad Kötzting, Germany

(2) Institute of Geodesy and Photogrammetry, ETH Zürich, Robert-Gnehm-Weg 15, CH-8093 Zürich, Switzerland

(3) Technische Universität Wien, Wiedner Hauptstraße/E120, A-1040 Wien, Austria

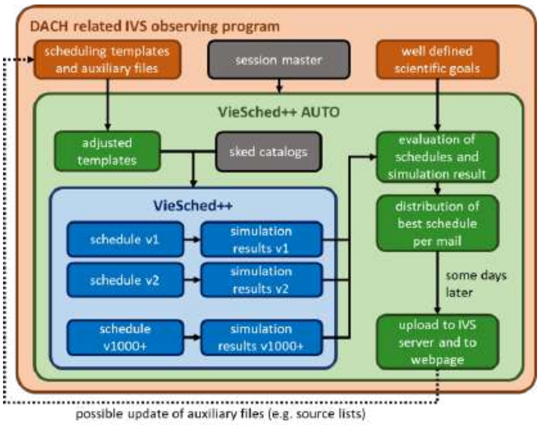

Fig. 1 Workflow for the automated VLBI schedule generation with VieSched++ AUTO.

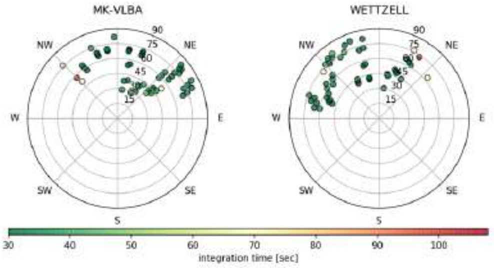

Fig. 2 Example of graphical material distributed via email for every generated schedule. Color coded integration time between of the observed radio sources between Wettzell and Mauna Kea for an Intensive session INT2.

VLBI session types. A main advantage of this approach is that the VLBI schedules are generated with a sophisticated combination of the core VLBI scheduling software VieSched++, yielding high quality state-of-the-art VLBI schedules and a Python software framework for a fully automatized scheduling workflow. In particular this workflow will be highlighted in this paper.

The constitution of the Operation Center DACH happened also in the context of the extension program of the Geodetic Observatory Wettzell. In this context a new correlation facility was planned and installed by the end of 2020. The initial purpose is to facilitate the data processing and evaluation of the in-house VLBI observation program. A main application is the DeltaUT1 determination of with AGGO and Wettzell, described in Plötz et al. (2019).

2 Scheduling

2.1 Method

The frontend for VieSched++ for automated VLBI schedule generation is a Python3 framework. The configuration and all run-time definitions are based on text files. No graphical user interface is necessary. The main advantage is that is is flexible, extendable and easy to configure. The script is executed once a day as registered cronjob on the Linux operating system. The complete software suite is open source and available on GitHub[1].

Figure 1 describes the workflow of a scheduling run. For every observing program, templates are provided describing the observing mode and schedule constraints as well as a combination of target parameters that should be optimized. In general, the schedule is generated 12 days prior to the session start and uploaded 9 days before the session is started. First, the latest catalogues and the session master files are downloaded. Then the script determines the upcoming sessions within the defined days prior the session start. Thereafter, the individual session are evaluated in sequence with preprocessing (e.g. add a downtime, adjust source list). The necessary preprocessing steps can be defined per observing program. Based on the templates, typically over 1000 schedules are generated for each session using different scheduling approaches and each of this schedule is simulated 1000 times for evaluating the repeatably metrics of the estimated geodetic parameters. Given the schedules target parameter, the best schedule is selected and some postprocessing is executed (e.g. incorporate special formatting/additions in the VEX file required by some stations). The postprocessing steps can also be defined per observing program. After the schedule is generated, it is distributed by email, along with statistics and session comparisons plots, see Figure 2 and 3 for examples. This allows for human inspection before the final schedule is uploaded automatically to the IVS servers some days later.

---

[1] https://github.com/TUW-VieVS/VieSchedpp_AUTO

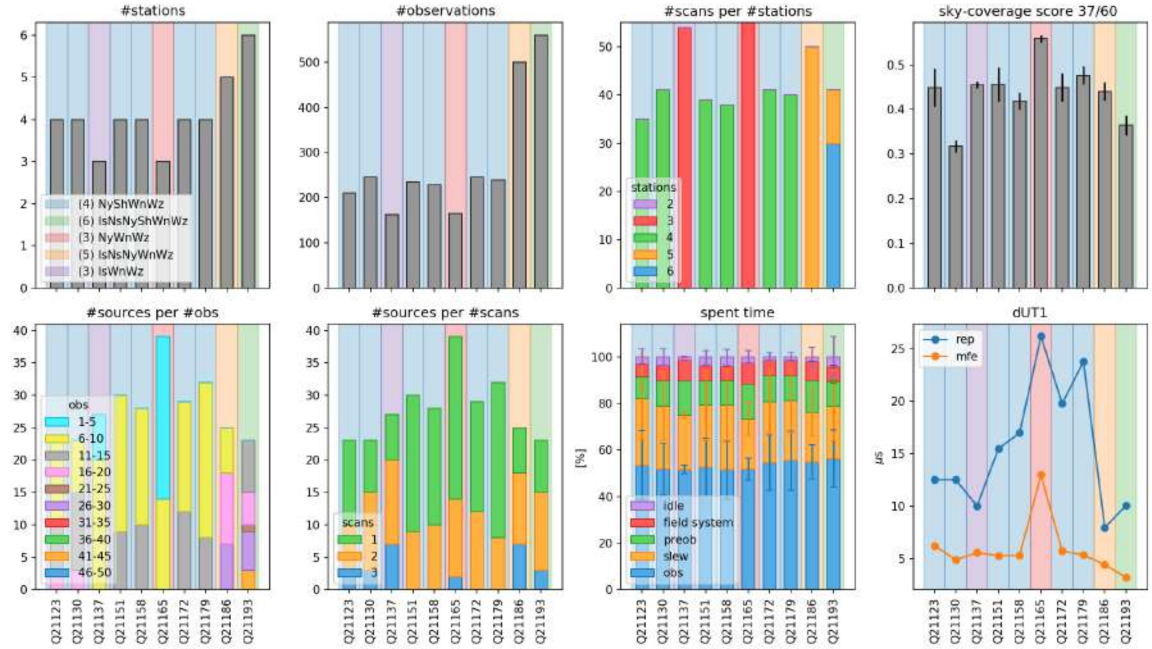

Fig. 3 Example of graphical material distributed via email for every generated schedule. Comparison of statistics for the ten most recent sessions within an observing program (here INT3). These plots allow for a quick human quality control. Different statistics are displayed for different observing programs.

The human supervision can be distinguished in a main operational task, which consists of checking the generated files, i.e. view statistics and comparisons in textual form, some logging information, check graphical attachments of the emails with sky-coverage and statistics in graphical form. Frequent additional task are maintain the templates, react on short notice adjustments and fix potential problems.

2.2 Results

Meanwhile there are a number of automatically generated VLBI schedules which are assigned to the DACH operation center. The main line of VLBI schedules consists of the officially assigned IVS VLBI observing programs:

- T2
- OHG
- INT2
- INT3
- AUA
- CRD
- CRF
- VGOS-B
- VGOS-C

Furthermore, there are In-house session regularly schedules like INT9 (Ag-Wn-Wz), local short baseline sessions (Wz-Wn-Ws), maximum baseline interferometry sessions (Ag-Oh-Wz) and SI-sessions (southern hemisphere Intensives between South Africa and Australia).

For evaluation and purpose, there are also test sessions generated for the INT1, R1, R4 and VO. Clearly, theses sessions are assigned to other Operation Centers and are intended only for evaluation and quality control of the VieSched++ AUTO software suite and not downloaded and observed by the stations.

3 Correlation

The installation of a VLBI correlation facility was mainly motivated by enhancing continuity, robustness and real-time capabilites at the Geodetic Observatory Wettzell (GOW). In particular, this allows the instantaneous correlation of in-house sessions like local VLBI tie sessions at the GOW Wettzell. Further VLBI sessions like Intensive's with Wettzell and AGGO are therefore also possible to process in close real-time in order to get DeltaUT1 measurement samples (Plötz et al. (2019)). The VLBI station in Antarctica, the German Antarctic Receiving Station (GARS) O'Higgins is also part of the in-house processed VLBI session types. In order to provide a solid basis for this activities a new VLBI correlator hardware was installed at the GOW Wettzell until December 2020. Thus, since January 2021 the HPC-cluster installation can be used and evaluated for VLBI correlation. The coarse specification of the High Performance Cluster (HPC) consists of 24 compute nodes (2x 12 CPU's per node = 576 cores). The individual components are connected with an Infiniband bus system with 100 Gbps throughput speed. The VLBI raw data storage is based on a BeeGFS system with 834 TB effective volume size. The current internet bandwidth capability is 6 Gbps transfer speed. An evaluation and stability testing, in particular with the in-house session with the VLBI stations of AGGO and Wettzell, is currently processed.

4 Conclusions and outlook

The newly established IVS VLBI operation center DACH realised a fully automated schedule generation based on modern state-of-the-art software methods. This allows to take full profit of the core scheduling software VieSched++ with Python3 framework for automated daily schedule generation. The automated approach enables a real large-scale scheduling and simulation for the optimal schedule to be deployed to the stations for the observation. The scheduling approach can be well defined in template files. This very helpful to concentrate on the sessions geodetic purpose. Additionally, the fully automated scheduling approach based on templates and well defined session goals help to diminish human biases in scheduling as well as to provide highest transparency.

In addition, the reliability is enhanced in terms that always the newest catalogues are available, daily updates are downloaded and through extensive statistics information it is possible to establish a quality control of the observed schedules. Furthermore, the schedule generation can be secured additionally by hardware redundancy, e.g. UPS, backup servers). The human workload is reduced by the automation and can be used to improve the scheduling process further.

References

Plötz et al.(2019): INT9 - UT1 Determination Between the Geodetic Observatories AGGO and Wettzell (2019) doi: 10.7419/162.08.2019.

Schartner and Böhm 2019: VieSched++: A new VLBI scheduling software for geodesy and astrometry. Publ Astron Soc Pac 131(1002):084501. doi: 10.1088/1538-3873/ab1820.

VLBI experiments with the dissemination of a common clock via a coherent optical fibre link

R. Ricci, M. Negusini, F. Perini, D. Calonico, C. Clivati, A. Mura, F. Levi, M. Siciliani de Cumis, L. Santamaria Amato, G. Bianco, M. Roma, C. Bortolotti, G. Maccaferri, M. Stagni, R. Ambrosini, R. Haas, B. Tercero, N. Iacolina, C. Migoni

Abstract Atomic clock synchronization plays an important role in both radio astronomical and geodetic Very Long Baseline Interferometry, as time and frequency standards are provided by station clocks. National metrological institutes have recently started disseminating frequency references from ultra-stable optical lattice clocks via optical fibre links. Optical clocks are already two order of magnitude more stable than the radio station H-masers. In this talk we will describe how the Italian Quantum Backbone (IQB) was used to carry out a series of VLBI experiments in which the Medicina and Matera radio stations were connected to the same remote clock located at the Italian Metrological institute in Turin. In the foreseeable future a European VLBI network of radio stations could be connected via optical fiber links to a single very high-performance clock hosted by a European Metrological institute.

Keywords frequency reference, optical fibre, VLBI

1 Introduction

Time and frequency optical fibre links are important for radioastronomy for various reasons. They can provide (i) faster operations via a better synchronizations of station clocks, (ii) better mm-VLBI phase stability above 100 GHz via the usage of highly performance atomic clocks (Rioja & Dodson , 2011; Rioja et al. , 2012), (iii) better study of compact structure in extragalactic radio sources and interstellar molecular clouds, as better angular resolutions can be achieved at increasing observing frequency if phase instability can be effectively mitigated. In geodetic Very Long Baseline Interferomery a 1-mm position accuracy as in the upcoming VGOS ntework (Schuh & Behrend (2012)) requires the ability of modelling the troposphere accurately but it also necessitates the availability of stable frequency references (Petrachenko et al., 2009; Niell et al., 2018). Moreover the study of pulsars requires accurate absolute time determinations (Lyne et al., 2016; Manchester et al., 2017).

Another field of research where highly performing optical atomic clocks play an important role is

---

Monia Negusini, Federico Perini, Mauro Roma, Claudio Bortolotti, Giuseppe Maccaferri, Matteo Stagni · Roberto Ambrosini
INAF-Istituto di Radioastronomia, Via Gobetti 101, Bologna (BO), I-40129 Italy

Roberto Ricci, Davide Calonico, Cecilia Clivati, Alberto Mura · Filippo Levi
Istituto Nazionale di Ricerche Metrologiche (INRiM), Strada delle Cacce 91, Torino (TO), I-10135 Italy

Mario Siciliani de Cumis, Luigi Santamaria Amato Giuseppe Bianco
Agenzia Spaziale Italiana - Centro di Geodesia Spaziale Località Terlecchia snc Matera (MT) I-75100 Italy

Ruediger Haas
Onsala Space Observatory (OSO) Chalmers University of Technology Gothenburg Sweden

Belen Tercero
Yebes Observatory National Geographic Institute (IGN) Yebes (Guadalajara) Spain

Noemi Iacolina
ASI-Sardinia Deep Space Antenna Pranusanguni San Basilio (CA) I-09040 Italy

Carlo Migoni
INAF-Osservatorio Astronomico di Cagliari Via della Scienza 5 Selargius (CA) I-09047 Italy

relativistic geodesy: the determination of absolute height between two reference points on Earth via the relativistic frequency shift caused by the difference in gravitational potential experienced by the optical clocks (see Grotti et al. (2018) for the usage of portable optical clocks and Mehlstäubler et al. (2018) for a comprehensive review). This technique, also called, chronometric levelling is complementary both to GNSS levelling method and to geometric geodesy which have a disagreement on the vertical datum of about 10 cm. With the usage of coherent wave optical fibre links (with frequency stability better than a few parts in 10^{-19}) connecting optical clocks with fractional frequency uncertainty down to 10^{-18} an absolute heigh difference of 1 cm could be achieved on integration times of a few thousand seconds, thus allowing the tracking of geodynamic effects such as the movement of fluid masses under the Earth surface (Bondarescu et al. (2015)), a measurement not obtainable by GNSS techniques.

Ultra-stable coherent optical fibre links are also important in time and frequency metrology per se, as they are used to perform optical clock comparison on continental scales (Lisdat et al. (2016)), in view of a redefinition of the SI second based on optical clock frequency standards (Riehle et al. (2017)).

In the following sections we will describe how the Italian Quantum Backbone optical fibre link (Calonico et al., 2014; Clivati et al., 2015) was used to perform a series of VLBI experiments in which two station antennas forming a baseline were utilizing the same remote frequency reference realizing a common-clock set-up on a scale length of 600 km.

2 Method

The Italian Quantum Backbone (IQB) is an optical fibre infrastructure serving seven reaserch institutes including INAF-IRA in Medicina, the European Lab for Non Linear Spectroscopy in Florence, the Institute of Optics in Pozzuli (Naples) and the ASI-Space Geodesy Centre in Matera, and also three industrial users (Galileo Telespazio facility, Thales Alenia and the Top-IX Consortium). IQB uses phase noise round-trip cancellation to minize phase noise to a stability level of 10^{-19} over 1000 s of integration time and optical frequency combs to up-/down-frequency convert the frequency reference from optical to RF and viceversa (details of electronic scheme and link characterization in Clivati et al. (2020)). The IQB link utilizes a dedicate 1800-km long dark fibre along the Italian peninsula and it is divided in four legs: INRiM/Torino-Medicina Radio station; Medicina Radio station-LENS/Florence; LENS/Florence-Institute of Optics/Pozzuoli; Institute of Optics/Pozzuoli-Space Geodesy Centre/Matera. At each leg terminal the fibre laser gets regenerated, fibre noise gets compensated and optical frequency combs allow for the 10 MHz RF to be extracted and used for scientific experiments. The IQB link reached Matera and saw the first light in November 2018 and since then it has been operating remotely from INRiM/Torino.

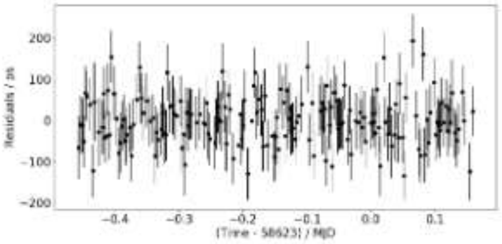

Fig. 1 Post-fit group delay residuals as a function of observing time for the geodetic VLBI experiment VI007 in which Matera and Medicina shared the *same* remote frequency reference from INRiM (Torino).

Table 1 Summary of the observations in the 2020-2021 VLBI clock timing campaign: project code, observing dates, stations involved, bands used and presence of remote clock are show.

Project code	Date	Stations	Band	rem clock?
VT010	20201129	Ma,Mc	X	No
VT011	20201209	Ma,Mc,Nt	X	No
VT012	20210213	Ma,Mc,Nt,Sr	X	Yes
VT013	20210224	Ma,Mc,Nt,Sr	X	No

3 Results

On May 19th-20th 2019 the first geodetic common-clock experiment was performed. The 24-hour S/X-band session involved the antennas of Matera, Medicina, Yebes and Onsala. Matera and Medicina received their frequency reference to be used in the receiver chain for time stamp and Local Oscillator signal remotely from an H-maser in INRiM/Torino via the IQB optical fibre link for the duration of the session. Data were transferred electronically to the Bologna DiFX (Deller et al. (2007)) software correlator, correlated and fringe fitted with HOPS Fourfit (Cappallo (2017)). The geodetic analysis was carried out using nuSolve (Bolotin et al. (2014)) with standard parametrization for troposphere and clock modelling. The presence of frequency reference unlocks during the session resulted in using a time interval of 15 hours in which no unlocks were present. The wrms on group delay post-fit residuals (Fig.1) on the Matera-Medicina baseline was 58 ps. The drift (CL1 parameter in the nuSolve model) of the Matera clock with respect to the Medicina clock, used as reference, was compatible with zero within 10^{-14} (s/s). This check reassured us that the frequency reference dissemination worked as expected. Details of the analysis are reported in Clivati et al. (2020). Further geodetic experiments were performed in Nov 2020 - January 2021 in order to make sure of the repeatibility of common-clock VLBI experiments and better characterize the effect on group delay residual statistics of baselines with common clock set-up with respect to hybrid baselines (remotely-locally distributed frequency reference) and totally local-clock baselines. Because of the presence of numerous frequence reference unlocks in the common-clock geodetic experiment performed in Jan 2021, its analysis is not final yet.

Another way of comparing remote clocks using VLBI antennas utilizes the scatter on the inteferometric phase (Krehlik et al. (2017)). For this reason a series of VLBI clock timing experiments were carried out with a network of stations including Matera, Medicina, Noto, Torun, Yebes and Metsahövi in January/February 2018 with geodetic S/X-band frequency set-up and in C-band low (5 GHz). In February 2019 a second series of phase scatter measurements was attempted with italian antennas at 6.7 GHz involving Medicina, Noto and the Sardinia Radio Telescope (SRT); for technical issues the antenna of Noto could not take part in the runs. The preliminary results of these initial timing tests were reported in EVGA 2019 conference proceedings (Ricci et al. (2019)). In the present report we will focus on the November 2020 – February 2021 campaign in which the antennas of Matera, Medicina, Noto and SRT were involved in 6-hour long runs at 8.4 GHz (see Table 1 for a summary of the observations). VT012 andVT013 were the first VLBI experiments involving *all* the four Italian antennas. It is worth notice also that Matera and Medicina in the VT012 experiment were in common-clock mode receiving both their frequency reference from an H-maser located at INRiM (Torino).

Many factors contribute to the deterioration of the interferometric phase stability: tropospheric fluctuations, gain elevation effects, unmodelled source structure, antenna thermal deformation, cable thermal dilation. These effects can contribute to mask the clock frequency reference behaviour. In order to minimize these effects the VLBI runs were performed, as much as possible, at night during the winter season on a couple of point-like target sources in 15-min long scans at medium/high antenna elevation in 3-hour observing arcs per source.

Table 2 RMS on the first difference of the interferometric phase based on Fourfit analysis for 1228+126: one of two sources observed in the 2020-2021 VLBI campaign. The measurement for each experiment baseline is expressed in term of time delay rms scatter $\Delta\tau_{\rm rms}$ in picoseconds. The sample number $N_{\rm samp}$ represents the number of phase pairs used in computing the rms statistics. The numbers in round brackets represent the measurement uncertainty in the last digit.

Project code	Baseline	$\Delta\tau_{\rm rms}[ps]$	$N_{\rm samp}$
VT010	MaMc	4.0(3)	180
VT011	MaMc	9.4(6)	181
VT011	McNt	10.0(8)	140
VT011	MaNt	6.3(6)	116
VT012	MaMc	14(1)	180
VT012	MaNt	9.4(7)	180
VT012	MaSr	4.9(4)	180
VT012	McNt	2.5(2)	220
VT012	McSr	2.8(2)	220
VT012	NtSr	3.3(2)	221
VT013	MaMc	1.7(1)	177
VT013	MaNt	2.1(2)	162
VT013	MaSr	2.0(2)	163
VT013	McNt	1.15(8)	200
VT013	McSr	1.7(1)	201
VT013	NtSr	1.6(1)	200

The observations were specifically carried out at 8.4 GHz to allow both SRT and Matera to take part in the runs. The Italian Space Agency operates a 8.4 GHz narrow-band (40-MHz wide) receiver at SRT to be used mostly for satellite tracking purposes; thus this was the only frequency overlap with the S/X-band system mounted in Matera. The X-band observations were performed using a radio astronomical 2-bit sampling frequency set-up: a 40 MHz bandwidth was split into 8 contiguous sub-bands (four Upper Side Band and four Lower Side Band) of 4-MHz bandwidth with 32 frequency channels in each sub-band. The Bologna DiFX correlator was used to correlate the e-transfered VDIF (for Mc, Nt and Sr) and Mark5b (for Ma) data which were then fringe fitted via HOPS Fourfit. The Fourfit output was then used to extract the interferometric phase information source by source, baseline by baseline, scan by scan for all the four experiments together with SNRs and fringe delay rates for each scan. DiFX output data were also transformed into FITS files and read into AIPS (Greisen et al. (2003)) where they were independently fringe fitted with the AIPS task FRING. Visibility amplitude/phase tables were then extracted using the AIPS task UVPRT. The statistics on the interferometric phase scatter for each source separately (3-hour observing arcs) were then computed using the same method described in Krehlik et al. (2017) namely the root-mean-square of the first difference in the interferoemtric phases. The Fourfit derived phases have a time samplimg of 22 seconds and phase resolution of 4 deg, while the AIPS processed phases have a finer sampling of 1 second and 1 deg. The central 80% of each sub-band was used in the AIPS analysis, thus removing the less sensitive sloping wings. The time scatter was computed using the formula:

$$\Delta\tau_{\mathrm{rms}} = \frac{\Delta\phi_{\mathrm{rms}}}{2\pi\nu_0}$$

where $\Delta\tau$ is the rms time scatter, $\Delta\phi_{\mathrm{rms}}$ is the rms phase noise and ν_0 is the sky centre frequency in each sub-band. Preliminary results of VT010-VT013 VLBI experiments obtained by the Fourfit analysis are shown in Tab. 2. The Fourfit results are in good agreement with the AIPS ones and they clearly show that the tropospheric phase instabilities are dominating the rms time scatter: the $\Delta\tau_{\mathrm{rms}}$ values span between 1.6 ps in VT013 in the best weather conditions (on baseline Nt-Sr) and 14 ps in VT012 in the worst weather conditions (on baseline Ma-Mc). The characterization of the different contributions to the rms phase noise is ongoing: clock fractional frequency differences and its uncertainty with respect a reference clock will be evaluated as a function of phase delay derivates by taking into account the tropospheric, ionospheric, geometric, source structure, cable and electronic delay terms.

4 Conclusions and outlook

The Italian Quantum Backbone infrastructure is able to deliver a frequency reference signal from the Italian Metrological Institute (INRiM) to remote locations via an optical fiber link with unprecedented stability (of the order of a few parts in 10^{-19} in 1000 s integration time based on Allan standard deviation) obtained by round-trip phase noise cancellation.

The IQB optical fibre link was used to perform a geodetic VLBI experiment in which the ASI-Centre for Space Geodesy Matera station and the INAF-IRA Medicina radio station received the *same* remote frequency reference from INRiM (Torino). The clock drift of Matera station with respect to Medicina (used as a reference) was found compatible with zero within 10^{-14} (s/s) from the geodetic analysis. This demostrates that a common-clock architecture can work for VLBI observations.

RMS stastistics on the interferometric phase noise was tested in clock timing experiments utilizing the VLBI technique. For the first time on Feb 13th, 2021 *all* the four Italian antennas took part in a VLBI experiment. Medicina and Matera received their frequency reference remotely from INRiM (Torino). Even if the phase noise statistics were completely dominated by tropospheric phase instabilities on the Ma-Mc baseline, this experiment opens a new possibity for clock fractional frequency comparison and testing for the common-clock architecture.

In the near future the following developments are planned:

- a VLBI vs GPS frequency stability analysis in the CONT14 and CONT17 campaigns focusing in particular on the co-located stations of Matera and Onsala compared to Wettzell;
- characterization of the different contributions (troposphere, ionosphere, source structure, cable, antenna deformations and clock) to the interferomet-

ric phase scatter in VLBI clock timing experiments with and without common-clock set-up

- usage of interplanetary space probe tones and the ΔDOR (Differential One-way Ranging) technique to compare clocks at two receiving radio stations;
- usage of the IQB link for future VLBI timing experiments between the Italian INRiM and Korean KRISS optical clocks

Acknowledgements We thank the VLBI partners from Yebes Observatory (B. Tercero Martinez, J. Gonzalez Garcia, P. de Vicente), Torun (A. Marecki, P. Wolak, M. Gavronski), Metsahoövi Observatory (J. Kullanki, J. Tammi), Effelsberg Observatory (A. Kraus, U. Bach), Matera CSG (G. Colucci, M. Paradiso, F. Schiavone), Noto radio station (P. Cassaro, S. Buttaccio), Onsala Space Observatory (R. Haas, J. Yang, M. Lindqvist), Sardinia Radio Telescope (S. Poppi, G Surcis) and the staff of the Medicina radio station for their support during the VLBI runs.

References

Bolotin S, Baver K, Gipson J, Gordon D, MacMillan D (2014) The VLBI Data Analysis Software νSolve: Development Progress and Plans for the Future. In proceedings of the *International VLBI Service for Geodesy and Astrometry 2014 General Meeting*, Science Press (Beijing), 253–257, doi: ISBN 978-7-03-042974-2.

Bondarescu R. *et al.* (2015) Ground-based optical atomic clocks as a tool to monitor vertical surface motion. *Geophysical Journal International*, Volume 202, Issue 3, p.1770-1774, doi: 10.1093/gji/ggv246.

Calonico D., Bertacco EK, Calosso CE, Clivati C, Costanzo GA (2014) High-accuracy coherent optical frequency transfer over a doubled 642-km fibre link. *Appl. Phys. B*, 117, 979–986, doi: xxx.

Cappallo R (2017) HOPS fourfit user's manual Version 1.0. *HOPS web page: https://www.haystack.mit.edu/tech/vlbi/hops.html*, doi: xxx.

Clivati C, Costanzo GA, Frittelli M, Levi F, Mura A, *et al.* (2015) A coherent fibre-optic link for Very Long Baseline Interferometry. *IEEE Trans. on Ultrason. Ferroel. Freq. Contr.*, 62, 1907–1912, doi: xxx.

Clivati C. *et al.* (2020) Common-clock very long baseline interferometry using a coherent optical fiber link. *Optica* Vol. 7, Issue 8, pp. 1031-1037, doi: 10.1364/OPTICA.393356.

Deller AT, Tingay SJ, Bailes M, West C (2007) DiFX: A Software Correlator for VLBI Using Multiprocessor Computing Environments. *Publications of the Astronomical Society of the Pacific*, 119, 318–336, doi: 10.1086/513572.

Greisen E and Heck A, editors (2003) AIPS, the VLA, and the VLBA. *Information Handling in Astronomy - Historical Vistas*, p. 114, doi: xxx.

Grotti J, Koller S, Vogt S, Haefner S, Sterr U, *et al* (2018) Geodesy and metrology with a transportable optical clock. *Nature Physics*, 14, 437–441, doi: 10.1038/s41567-017-0042-3.

Krehlik P, Buczek L, Kolodziej J, Lipiński M, Sliwczynski L (2017) Fibre-optic delivery of time and frequency to VLBI station. *Astronomy & Astrophysics*, 603, 48, doi: 10.1051/0004-6361/201730615.

Lisdat C, Grosche G, Quintin Q, Shi C, Raupach SMF *et al* (2016) A clock network for geodesy and fundamental science. *Nature Communications*, 7, 1–7, doi: 10.1038/ncomms12443.

Lyne A. *et al.* (2016) The formation, life and uses of pulsars - nature's finest cosmic clocks. *Proceedings of 2016 European Frequency and Time Forum*, doi: ISBN: 9781509007219.

Manchester R.N., Guo L., Hobbs G., Coles W.A. (2017) Pulsars: Celestial Clocks. In: Arias E., Combrinck L., Gabor P., Hohenkerk C., Seidelmann P. (eds) The Science of Time 2016. *Astrophysics and Space Science Proceedings*, vol 50. Springer, Cham. doi: 10.1007/978-3-319-59909-0_30.

Mehlstäubler T.E. *et al.* (2018) Atomic clocks for geodesy. *Reports on Progress in Physics*, Volume 81, Issue 6, article id. 064401, doi: 10.1088/1361-6633/aab409.

Niell A. *et al.* (2018) Demonstration of a Broadband Very Long Baseline Interferometer System: A New Instrument for High-Precision Space Geodesy . *Radio Science*, Volume 53, Issue 10, pp. 1269-1291 doi: 10.1029/2018RS006617.

Petrachenko B. *et al.* (2009) Design Aspects of the VLBI2010 System. Progress Report of the IVS VLBI2010 Committee, June 2009. *NASA/TM-2009-214180*, 2009, 62 pages, doi: xxx.

Ricci R. *et al.* (2019) Optical fiber links used in VLBI networks and remote clock comparisons: the LIFT/MetGesp project. In: Haas R., Garci-Espada S., & Lopez Fernandez J.A. (eds) EVGA2019. *Proceedings of 24th European VLBI Group for Geodesy and Astrometry Working Meeting*, pg. 47. CNIG, Madrid, Spain. doi: 10.7419/162.08.2019.

Riehle F (2017) Optical clock networks. *Nature Photonics*, 11, 25–31, doi: 10.1038/nphoton.2016.235.

Rioja M & Dodson R (2011) HIGH-PRECISION ASTROMETRIC MILLIMETER VERY LONG BASELINE INTERFEROMETRY USING A NEW METHOD FOR ATMOSPHERIC CALIBRATION. *Astronomical Journal*, 141, 114, doi: 10.1088/0004-6256/141/4/114.

Rioja M, Dodson R, Asaki Y, Harnett J, Tingay S (2012) The impact of Frequency Standards on Coherence in VLBI at the Highest Frequencies. *Astronomical Journal*, 144, 121, doi: 10.1088/0004-6256/144/121.

Schuh H. & Behrend D. (2012) VLBI: A fascinating technique for geodesy and astrometry. *Journal of Geodynamics*, Volume 61, p. 68-80 doi: 10.1016/j.jog.2012.07.007.

EU-VGOS activities in Vienna

F. Jaron, S. Bernhart, J. Böhm, J. González García, J. Gruber, Y. K. Choi, I. Martí-Vidal, M. Schartner, B. Soja, J. Wagner, E. Varenius, H. Verkouter, on behalf of the EU-VGOS collaboration

Abstract The EU-VGOS collaboration carries out observational sessions on a regular basis, some of them being correlated at TU Wien. This is a progress report on aspects of data processing from e-transfer to fringe-fitting. We compare two approaches of handling dual linear polarization: combining all four linear polarization products to pseudo Stokes *I*, and conversion from linear to circular polarization using PolConvert. Our results so far seem to indicate that the latter approach gives a higher signal to noise ratio than the former.

Frédéric Jaron · Johannes Böhm · Jakob Gruber
Department of Geodesy and Geoinformation, TU Wien, Wiedner Hauptstraße 8, A-1040 Vienna, Austria
`frederic.jaron@tuwien.ac.at`

Simone Bernhart · Yoon Kyung Choi
Reichert GmbH, Hittorfstraße 26, DE-53129 Bonn, Germany

Javier González García
Observatorio de Yebes (IGN), Apartado 148, 19181, Yebes, Spain

Ivan Martí-Vidal
Departament d'Astronomia i Astrofísica, Universitat de València, C. Dr. Moliner 50, 46100, Burjassot, València, Spain; Observatori Astronòmic, Universitat de València, Parc Científic, C. Catedràtico José Beltrán 2, 46980, Paterna, València, Spain

Matthias Schartner · Benedikt Soja
Institute of Geodesy and Photogrammetry, ETH Zürich, 8093, Zurich, Switzerland

Jan Wagner · Frédéric Jaron
Max-Planck-Institut für Radioastronomie, Auf dem Hügel 69, D-53121 Bonn, Germany

Eskil Varenius
Department of Space, Earth and Environment, Chalmers University of Technology, Onsala Space Observatory, SE-439 92, Onsala, Sweden

Harro Verkouter
Joint Institute for VLBI ERIC, Dwingeloo, Netherlands

Keywords VGOS, E-transfer, Correlation, Fringe-fitting, Polarization

1 Introduction

The EU-VGOS project was started in 2018 by Alef et al. (2019) with the aim to find a way for post-processing VGOS data alternate to the way implemented by the Haystack group within the *HOPS* package (Niell et al., 2018, and references therein). The idea is to exploit a *CASA* (McMullin et al., 2007) based *Python* pipeline that includes the *PolConvert* (Martí-Vidal et al., 2016) software, makes use of phase-cal tones, is able to correct ionospheric dispersion, and allows Stokes *I* fringe-fitting of the data. For this purpose, the EU-VGOS collaboration carries out research and development sessions with a network of VGOS stations, mainly located in Europe but also beyond. Here we report on the processing of EU-VGOS data at the VLBI correlator of TU Wien, from e-transfer to fringe-fitting.

The TU Wien VLBI correlator is operated by the working group of Higher Geodesy at the Department of Geodesy and Geoinformation. Correlations are being carried out by J. Gruber and F. Jaron. For data storage and processing we use the infrastructure of the Vienna Scientific Cluster[1], where we can use up to ten compute nodes simultaneously. Each of these nodes is equipped with 2 CPUs with 24 cores each, resulting in 48 cores per node. We have 1 PB of disk space reserved exclusively for VLBI. We are connected to the GÉANT network via a 10 Gbit/s link which is, however, shared with other users. For correlation we use the

---

[1] `http://www.vsc.ac.at`

DiFX-2 software correlator (Deller et al., 2011) in various sub-versions. For fringe-fitting we currently use *HOPS/fourfit* in its version 3.22. We have also *PIMA* (Petrov et al., 2011) installed on our system.

2 Short-scan experiments

Here we report on the processing of five[2] EU-VGOS sessions: ev0287, ev0303, ev0314, ev0328, ev0345. These experiments were scheduled by M. Schartner using his software *VieSched*++ (Schartner & Böhm, 2019). One special feature of the sessions is that shorter integration times were tested. Currently, all IVS-VGOS sessions utilize a fixed 30 s integration time, independent of the source brightness. In contrast, within the sessions considered here, integration times between 10 and 20 s were examined. Therefore, each session was divided into blocks and each block was scheduled with a different integration time. In addition, calibrator scans were included with durations of 2 to 3 min each. To ensure a reasonable signal to noise ratio (SNR) for the short scans, the theoretical SNR was computed during scheduling. Although this is standard for S/X observations, it is currently not utilized in the IVS-VGOS sessions due to the lack of station system equivalent flux density (SEFD) and source flux density information in the scheduling catalogs for the VGOS frequencies. To overcome this issue, the SEFD information was directly provided by the stations and the source flux densities were interpolated and extrapolated based on their S and X band flux densities. Similar to scheduling standard S/X observations, the SNRs were computed for each band individually and different thresholds between 8 and 20 per band were used. In these five sessions the participating stations were the two Onsala telescopes (ONSA13NE and -SW), Wettzell (WETTZ13S), Yebes (RAEGYEB), and in ev0345 also Ishioka (ISHIOKA) in Japan.

The frequency setup of these sessions (Fig. 1) is identical to the one currently used for global VGOS experiments, with four bands distributed between 3 and 11 GHz. The observations, each six hours in duration, were carried out in dual linear polarization. The polarizations were labeled “X” and “Y” in the VEX files. It is important to point out that these are local horizontals/verticals at the telescopes and (without a field rotator) are not aligned with the celestial X and Y coordinates, and are subject to changes in the parallactic angle. Hence, “H” and “V” might be a better choice for these labels. The sampling rate per channel was 64 Msamples/s (and 32 Msamples/s for Yebes I/Q sampling) with 2-bit quantization, resulting in a net data rate of 8.192 Gbit/s per antenna. All stations are equipped with phase-cal units, most of them inject tones every 5 MHz, except for Yebes, which has tones every 10 MHz. Most of the stations have DBBC backends (Tuccari et al., 2018), providing real-valued data, only Yebes has an RDBE (Ruszczyk et al., 2012) and the data are complex-valued. Stations record their data onto Mark 6 modules or onto FlexBuff recorders, except for ISHIOKA, who use an ADS3000+ sampler and a K5VSI recording system.

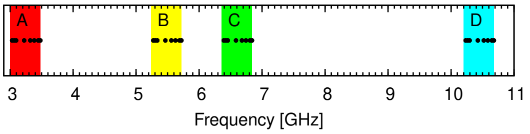

Fig. 1 Frequency setup. Each of the four bands (A-D) has a width of 480 MHz and contains 8 channels, each 32 MHz wide.

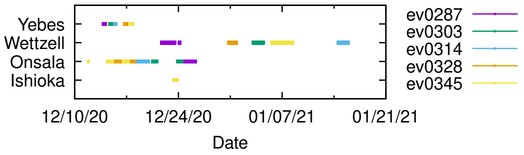

Fig. 2 E-transfer of five EU-VGOS sessions.

3 E-transfer

The TU Wien correlator does not have any Mark 6 units at its disposal, so data have to be transferred electronically. We used *m5copy* and *jive5ab* for the data transfers[3]. It took approximately one month to complete all transfers with a total volume of 115 TB (Fig. 2). When comparing the transfer duration of the individual stations, one has to keep in mind that Onsala had to transfer twice the amount of data (having two VGOS tele-

---

[2] This number is continuously growing. Currently ten of these sessions are being processed in Vienna, but we restrict ourselves to these five experiments as representative examples.

[3] `https://github.com/jive-vlbi/jive5ab`

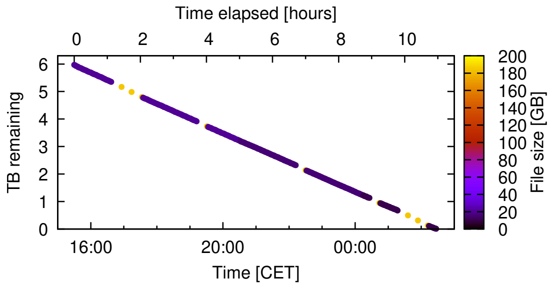

Fig. 3 E-transfer of ev0303 from Yebes to Vienna. Remaining data volume is plotted against time. The file size is color coded.

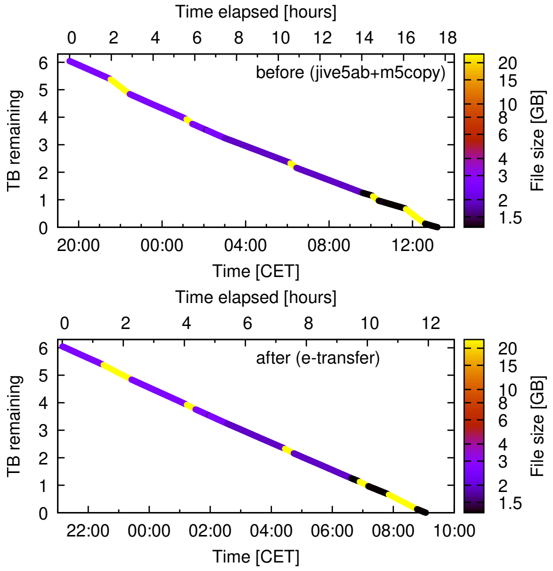

Fig. 4 E-transfer of ev0303 from Onsala to Vienna. **Top:** There is a strong dependence of transfer rate on file size. **Bottom:** Using the e-transfer daemon/client pair almost completely removes the file size dependence.

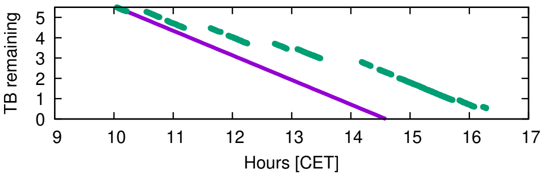

Fig. 5 Conversion from multi- to single-thread using *vmux* on Wettzell data of session ev0303. Remaining data volume is plotted against time. Gaps that follow the linear trend correspond to larger files being converted. Horizontal gaps are related to *vmux* being stuck in an infinite loop of error messages. The purple line is an extrapolation of the initial linear trend that would have been continued in the absence of errors.

scopes), and Ishioka participated in only one (ev0345) out of these five sessions.

As an example of a smooth transfer, Fig. 3 shows a plot for Yebes. The curve of remaining data volume plotted against time is a straight line without any dependence on file size. The average transfer rate in this case was 1.2 Gbit/s. The situation was initially very different for the transfers from Onsala. The plot in the top panel of Fig. 4 reveals a strong dependence of transfer rate on file size. Onsala recorded the data in multi-file format, resulting in many files with relatively small sizes of a few GB each. Only the few larger calibrator scans reached the full speed of 1.3 Gbit/s. The small files came at only half that speed. After discussing the issue with the author of *jive5ab* it became clear that this is the result of a large-ish constant per-file delay between transfers that the *jive5ab+m5copy* approach suffers from, causing the experienced transmission time of a small file to be (significantly) larger than the physical transfer time of the content itself. H. Verkouter suggested trying the e-transfer daemon/client pair[4] – a server/client file transfer utility that, like *jive5ab* but without its overheads, is capable of using the UDT data transfer protocol (Gu & Grossman, 2007) for fast data transfer over long, fat links where the TCP protocol significantly underperforms. We tested the new toolchain by repeating the same transfer. The resulting plot (bottom panel of Fig. 4) confirms that the file size dependence has almost been removed. In this way the total transfer duration could be reduced from initially 18 down to 12 hours.

4 Correlation

4.1 Converting multi- to single-thread

The *DiFX* software correlator adopted also for VGOS can process recordings that are multi-threaded VDIF (e.g., from the VLBA) or multi-threaded multi-datastream VDIF (e.g., Phased NOEMA in the EHT and GMVA). However, only single-threaded VDIF and the older *DiFX* version 2.5.3 have been validated for VGOS so far. In addition, the *difx2mark4* converter in 2.5.3 and in versions prior to 2.6.2 does not correctly handle PCal entries from multi-datastream recordings.

---

[4] `https://github.com/jive-vlbi/etransfer`

Thus any recordings not present in a VGOS-validated layout should be converted prior to correlation in *DiFX*-2.5.3.

For the five sessions that are subject of this article, Wettzell recorded the data in multi-threaded VDIF format. Conversion is done using the tool *vmux* that is part of the *DiFX* distribution[5]. Unfortunately, converting the data took very long, as shown in Fig. 5. The conversion of six hours of data from one station alone took approximately as long as the observation. This, however, includes time during which *vmux* was outputting error messages[6] in an infinite loop which had to be manually interrupted. Another consequence of these errors is that about 5 % of the data could not be converted, with calibrator scans being especially affected.

We have by now implemented a script which automatically interrupts and restarts the process when such error messages occur, eliminating this overhead. Nevertheless, *vmux* still takes very long compared to the actual observing time and will dominate the processing time if many stations deliver the data in multi-thread format. Attempts to parallelize the process on a cluster have not been successful so far. One possible reason could be that the process is I/O-limited.

4.2 DiFX for VGOS

Currently there has not been any official *DiFX* release which correlates VGOS data without any problems. Correlator centers have to apply various patches to their installations. Aiming at a *DiFX* version for VGOS, we discussed the issue within the EU-VGOS collaboration. As a result, at MPIfR Bonn we backported a specific set of EU-VGOS-relevant patches from the more recent *DiFX*-2.6 series into the *DiFX*-2.5 development base. In addition, MIT Haystack updated the included *HOPS* package from 3.19 to the current 3.22 vendor release used in VGOS processing. This development base, including HOPS 3.22, will be released as *DiFX*-2.5.4 after completion of an open testing phase in the *DiFX* user community[7]. At Vienna we used this version to correlate ev0303, and the results are shown in the following.

5 Calibration and fringe-fitting

We focus on two options for fringe-fitting:

1. Combine the four linear polarization products to pseudo Stokes *I* without any actual polarization calibration (cf. Eq. 2 in Cappallo 2014). This is implemented in the *HOPS/fourfit* software suite and is described in the MIT Haystack VGOS manual[8].

2. Convert visibilities from linear to a circular polarization basis, including a proper cross-polarization complex gain calibration (Martí-Vidal et al., 2016). Using a preliminary version of *PolConvert* for VGOS, we estimate the cross-polarization gain in a least squares method and apply the estimates in the conversion process. *PolConvert* also takes care of the differential parallactic angle correction to be introduced between polarization products in the visibilities. After this, we are ready to tell fourfit[9] to combine the two parallel hand circular polarization products to form true Stokes *I*.

6 Results

Figure 6 shows two *fourfit* fringe-plots for one calibrator scan from ev0303. The plot in the top panel shows the result for pseudo Stokes *I*, and the bottom panel for the polconverted data. For this example scan pseudo Stokes *I* yields an SNR of 525.4 while the polconverted data give a considerably higher SNR of 607.7. An inspection of other scans confirmed a tendency of higher SNR for polconverted data.

7 Conclusions and outlook

We have presented a work in progress. These are our conclusions so far:

1. E-transfer to Vienna works smoothly. An initial drop in transfer rate for small files could be fixed by using a different file transfer utility.

---

[5] If you have Mark 6 units, another possibility is to use the tool *mk6vmux* to convert the data directly off Mark 6 modules.

[6] Messages of the type: “desync, frame delta 15796, fps 31250”

[7] `https://deki.mpifr-bonn.mpg.de/Cooperations/EU-VGOS_P-o-C/VGOS_DiFX_Versions`

[8] `https://www.haystack.mit.edu/wp-content/uploads/2020/07/docs_hops_000_vgos-data-processing.pdf`

[9] Command line option -P RR+LL

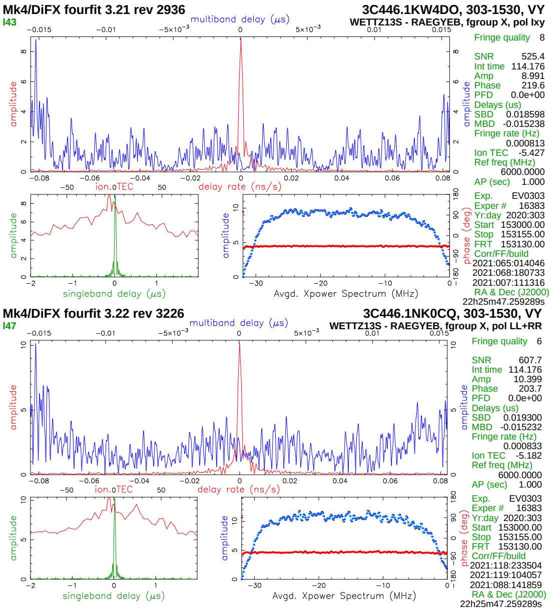

Fig. 6 Fourfit fringe-plot. **Top:** Pseudo Stokes I. **Bottom:** Polconverted data.

2. Converting multi-thread VDIF data to single-thread, using the tool *vmux*, takes very long and will become a significant overhead for experiments with larger networks.
3. In order to avoid locally patched *DiFX* installations for VGOS, Bonn and MIT Haystack have put together *DiFX*-2.5.0. This version is in a testing phase now and needs to be approved by the *DiFX* and VGOS communities to become version 2.5.4.
4. First results from fringe-fitting polconverted data indicate that SNR seems to be systematically higher than for pseudo Stokes I. This is expected, because *PolConvert* does a proper cross-polarization complex gain calibration.

Until now, the gain estimates in *PolConvert* come from only one calibrator scan selected from the whole experiment. Further development of the tool has already shown that many scans can be used in the least squares adjustment to generate more accurate solutions, and the current status of the development is concentrated on being able to apply this functionality to any of the EU-VGOS session setups.

Algorithms for fringe-fitting dual linear polarization broadband data have now been implemented in PIMA. We plan to include this option in the future.

Note added in proof: DiFX-2.5.4 officially released. With the *HOPS* configuration optimized for short scans, SNR for pseudo Stokes I is in general close to and sometimes greater than for *PolConvert*.

Acknowledgements

We thank Alan Roy of the MPIfR Bonn for carefully reading the manuscript and providing useful comments. The computational results presented have been achieved in part using the Vienna Scientific Cluster (VSC). This research was funded in part by the Austrian Science Fund (FWF) [P31625].

References

Alef W, Anderson JM, Bernhart S et al. (2015) The EUropean-VGOS Project. *Proceedings of the 24th European VLBI Group for Geodesy and Astrometry Working Meeting*, pp. 107-111

Deller AT, Brisken WF, Phillips CJ et al. (2011) DiFX-2: A More Flexible, Efficient, Robust, and Powerful Software Correlator. *PASP*, 123, 901, pp. 2752, doi:10.1086/658907

Cappallo R (2014) Correlating and Fringe-fitting Broadband VGOS Data. *IVS 2014 General Meeting Proceedings*, p. 91-96, ISBN 978-7-03-042974-2

Gu Y, Grossman RL (2007) UDT: UDP-based data transfer for high-speed wide area networks. *Computer Networks*, 51, 7, p. 1777-1799, doi:10.1016/j.comnet.2006.11.009

Martí-Vidal I, Roy A, Conway J, Zensus JA (2016) Calibration of mixed-polarization interferometric observations. *A&A*, 587, A143, 8 pp., doi:10.1051/0004-6361/201526063

McMullin JP, Waters B, Schiebel D et al. (2007) CASA Architecture and Applications. *Astronomical Data Analysis Software and Systems XVI ASP Conference Series*, 376, p.127

Niell A, Barrett J, Burns A et al. (2018) Demonstration of a Broadband Very Long Baseline Interferometer System: A New Instrument for High-Precision Space Geodesy. *Radio Science*, 53, 10, pp. 1269-1291, doi:10.1029/2018RS006617

Petrov L, Kovalev YY, Fomalont EB, Gordon D (2011) The Very Long Baseline Array Galactic Plane Survey – VGaPS. *AJ*, 142, 2, 35, 23 pp., doi:10.1088/0004-6256/142/2/35

Ruszczyk C, McWhirter R, Beaudoin C et al. (2012) VLBI2010 using the RDBE and Mark 5C. *Seventh General Meeting (GM2012) of the international VLBI Service for Geodesy and Astrometry (IVS)*, p. 81-85

Schartner M, Böhm J (2019) VieSched++: A New VLBI Scheduling Software for Geodesy and Astrometry. *PASP*, 131, 1002, pp. 084501, doi:10.1088/1538-3873/ab1820

Tuccari G, Alef W, Dornbusch S et al. (2018) DBBC3 the new wide-band backend for VLBI. *14th European VLBI Network Symposium & Users Meeting.* Online at `https://pos.sissa.it/cgi-bin/reader/conf.cgi?confid=344`, id.140

A superconductor filter installed in the broadband feed of Ishioka VLBI station

Y. Takagi, H. Ueshiba, T. Nakakuki, S. Matsumoto, K. Hayashi, T. Yutsudo, K. Mori, T. Kobayashi, M. Sekido,
J. McCallum, F. Shu

Abstract At the Ishioka VLBI Station, we installed a new superconductor filter in the broadband feed which was designed to mitigate the strong RFI around S-band so that the Ishioka station can observe S-band with the broadband feed. The survey of the signal after the installation of the filter revealed that the strong RFI was mitigated as expected. In addition, fringes were detected for both S- and X-bands in some test VLBI observations with domestic and international stations.

Keywords RFI, broadband feed, superconductor filter

1 Introduction

The Ishioka VLBI station, located in Ishioka-city, Japan, has a 13.2-m radio telescope which fulfils the VGOS requirement. It has participated in S/X sessions using a tri-band feed and VGOS sessions using a QRFH or broadband feed based on the master schedule of International VLBI Service for Geodesy and Astrometry (IVS). Due to the strong RFI around Ishioka station, signal below 3 GHz had been cut using high-pass filter when observing with the broadband feed. However, there are some advantages if S-band can be observed with the broadband feed. One is that it can participate in mixed-mode sessions with the broadband feed. Other is that it can pave the way for legacy S/X observations with the broadband feed. Once it is achieved, there will be no need to change feeds to participate in different types of observations. From these reasons, we developed and installed a superconductor filter to mitigate the RFI and to observe

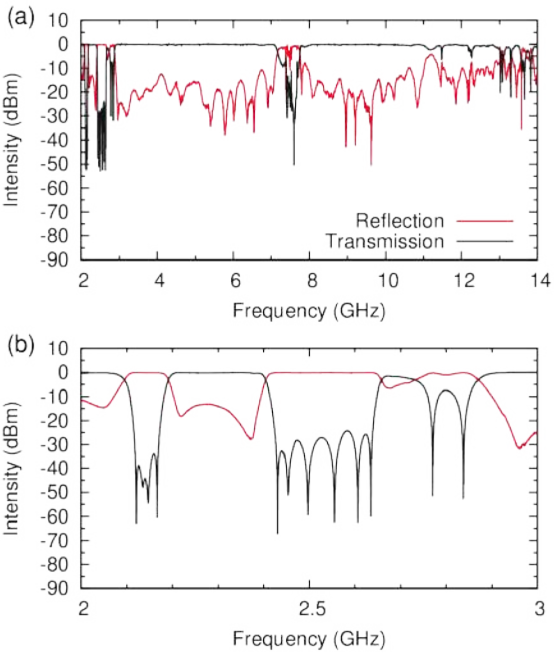

Fig. 1 Transmission (black) and reflection (red) characteristic of the superconductor filter. (a) 2–14 GHz. (b) 2–3 GHz.

Yu Takagi · Haruka Ueshiba · Tomokazu Nakakuki · Saho Matsumoto · Kyonosuke Hayashi · Toru Yutsudo · Katsuhiro Mori · Tomokazu Kobayashi
Geospatial Information Authority of Japan, 1 Kitasato, Tsukuba city, Ibaraki prefecture, 305-0811 Japan

Mamoru Sekido
National Institute of Information and Communications Technology, Koganei, Japan

Jamie McCallum
University of Tasmania, Hobart, Australia

Fengchun Shu
Shanghai Astronomical Observatory, Shanghai, Chaina

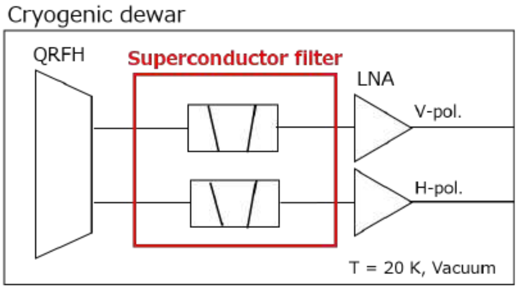

Fig. 2 Schematic diagram of cryogenic dewar. The filter was installed before LNA.

S-band with the broadband feed. After installing the filter, we investigated the signal that passed through the filter and conducted some VLBI test observations with domestic and international stations.

This paper reports their results and gives some discussion on the effect of the phase characteristic of the filter.

2 Frequency characteristics of the installed filter

Based on the results of the survey conducted in 2019 (Nakakuki et al., 2020), a superconductor filter was designed to mitigate only the RFI around S-band. We adopted the superconductor filter because it can realize a steep cut-off characteristic without enhancement of receiver noise temperature. Figure 1 shows the transmission and reflection characteristic of the filter. It is designed to attenuate only RFI around 2–3 GHz while it keeps the amplitude of the frequency range used for the observations (2.2–2.4 GHz). It should be noted that the signal around 7–8 GHz is also attenuated so as to realize the steep characteristic around 2–3 GHz, although this frequency range is not used for VGOS observations at present (Niell, 2017). The filter was installed before the Low Noise Amplifier (LNA) as show in Fig. 2.

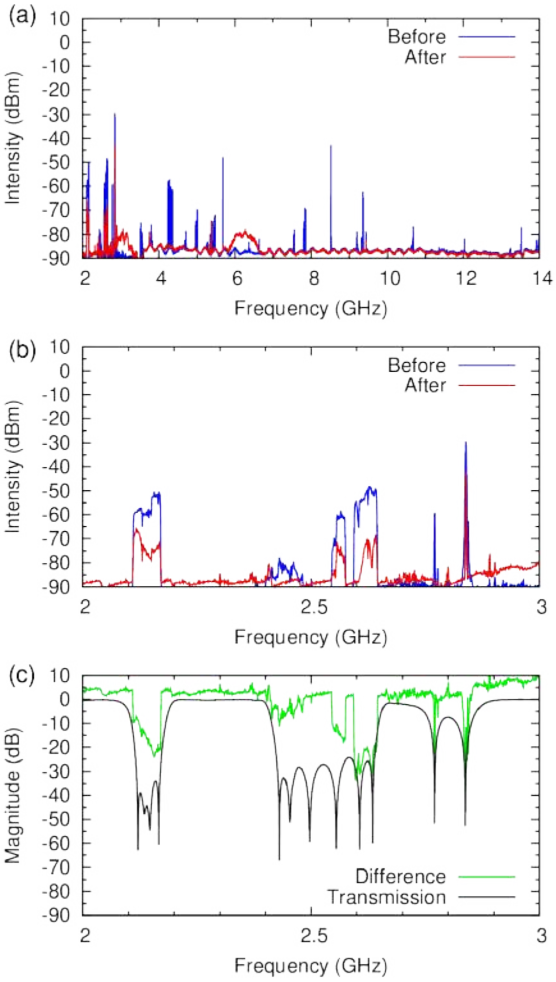

Fig. 3 Signal amplitude measured by the spectrum analyser. Blue and red curves represent the signal before and after installing the filter. (a) 2–14 GHz. (b) 2–3 GHz. (c) The difference between before and after installation is represented in green curve. Black curve shows the transmission characteristic.

3 Investigation of the filter performance

3.1 Amplitude of the signal after passing through the filter

After installing the filter, we investigated the amplitude of the output of LNA using a spectrum analyser. The spectrum was measured while changing the azimuth and elevation angles of the antenna. The result for the azimuth of 90 degrees and elevation of 5 degrees is shown in Fig. 3 with the result before the installation. It is the direction of the centre of Ishioka-city, where a large RFI was observed. As shown in Fig. 3(a), higher harmonics caused by the saturation seen before the installation dissapeared after the installation (Fig. 3(a)). In addition, the RFI around S-band was mitigated while the signal used for the observations was preserved (Fig. 3(b), (c)). Although RFI is still visible to some extent, it is not a serious problem because saturation does not occur as described above. These results indicate that the filter works well.

3.2 *Fringe tests*

After we confirmed that the filter suppressed the RFI, we conducted some test VLBI observations with cooperation of domestic and international stations in order to check fringe detection. All of the sessions were one-hour ones and their details are shown in Table 2. Fringes were detected for all of the baseline between both domestic and international stations. The fourfit output for S-band between HOBART12 and ISHIOKA is shown in Fig. 4. The result for the test observations shows that observations can be done with the installed filter.

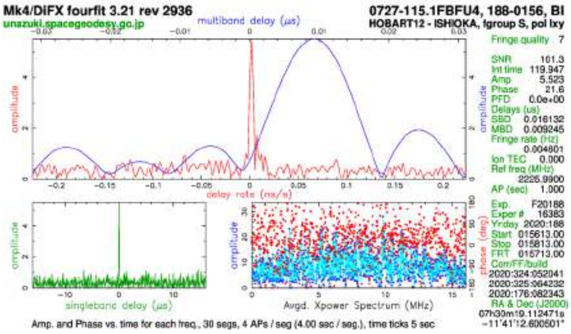

```
Mk4/DiFX fourfit 3.21 rev 2936                0727-115.1FBFU4, 188-0156, BI
unazuki.spacegeodesy.go.jp              HOBART12 - ISHIOKA, fgroup S, pol lxy
Fringe quality  7
SNR          101.3
Int time   119.947
Amp          5.523
Phase         21.6
PFD       0.0e+00
Delays (us)
SBD      0.016132
MBD      0.009245
Fringe rate (Hz)
         0.004601
Ion TEC     0.000
Ref freq (MHz)
        2225.9900
AP (sec)    1.000
Exp.       F20188
Exper #     16383
Yr:day   2020:188
Start   015613.00
Stop    015813.00
FRT     015713.00
Corr/FF/build
2020:324:052041
2020:325:064232
2020:176:082343
RA & Dec (J2000)
07h30m19.112471s
-11°41'12.600501"
Amp. and Phase vs. time for each freq., 30 segs, 4 APs / seg (4.00 sec / seg.), time ticks 5 sec
```

Fig. 4 Fourfit output for S-band fringe between HOBART12 and ISHIOKA in F20188.

4 Effect of the phase characteristic on VLBI observations

In the previous section, we confirmed that the filter attenuated the RFI and that fringes were detected. This section describes the estimation of the effect of the phase characteristic of the filter. Figure 5 shows the phase transmission characteristic of the filter. The slopes, which correspond to the group delays, for S- and X-band are different and we evaluated its influence to delay observable of a VLBI observation. The delay between S- and X-band was calculated to be -4.2 and -2.2 nanoseconds, respectively, by fitting linear functions to frequency range of 2.25–2.38 GHz and 8–10 GHz. We obtained the delay difference of 2.2 nanoseconds. This offset may affect TEC offset, but is not significant problem for geodesy. In addition, we estimated the coherence using the following equation:

$$\frac{\sin(\pi\tau B)}{\pi\tau B}, \tag{1}$$

where τ and B represent the delay and the bandwidth, respectively. With the delay $\tau = 2.2$ nanoseconds and $B = 32$ MHz, eq. (1) gives the coherence of 99%. Thus, it is also negligible. These estimations indicate that the difference in the slopes of the phase characteristic has little effect on the observation.

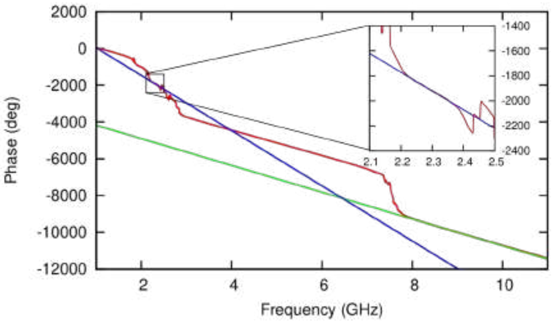

Fig. 5 Phase characteristic of the filter (red). Blue and green lines are fitting functions obtained by least mean square method in the range of 2.2–2.38 GHz and 8.2–9.0 GHz, respectively.

Table 1 Details of the test VLBI observations

	F20181	F20184	F20188
Antennae	ISHIOKA & KOGANEI	ISHIOKA, HOBART12, KATH12M & SESHAN25	ISHIOKA, HOBART12, KATH12M, YARRA12M & SESHAN25
Date & Time	June 29th, 2020 5:00–6:00UT	July 2nd, 2020 5:00–6:00UT	July 6th, 2020 1:00–2:00UT
Frequency	X-band (10 channels) and S-band (6 channels)		
Sources	29 sources including 3C273B, 3C84 & 4C39.25	7 sources including 0727-115, 0851+202 & 0458-020	9 sources including 0727-115, 0851+202 & 0458-020
Correlation	NICT & GSI processed using K5 correlator	UTAS and GSI processed using DiFX and HOPS software	UTAS and GSI processed using DiFX and HOPS software

5 Summary

We investigated and installed a superconductor filter that attenuates the RFI around S-band into the broadband receiver so that S-band can be observed with the broadband feed. After installation, we investigated the signal passed through the filter and conducted some test observations. In addition, the effect of the phase transmission characteristic was estimated. From the results of these investigations, we can say that the filter reduces the RFI effectively and that observations including S-band can be carried out using the broadband feed with the filter.

In order to participate in legacy S/X observations with the broadband feed, it is necessary to convert polariztions because the broadband receiver records linear polarizations while circular polarized signal is used for the legacy S/X sessions. This is to be the future work.

Acknowledgements We are grateful to Dr. Brian Corey of MIT Haystack Observatory for useful discussion on the effect of phase characteristic of the filter. This study made use of Koganei 11m antenna maintained by Space-Time Standards Laboratory of NICT, AuScope VLBI infrastructure operated by the University of Tasmania, and Seshan25 VLBI station operated by Shanghai Astronomical Observatory of Chinese Academy of Sciences. AuScope Ltd is funded under the National Collaborative Research Infrastructure Strategy (NCRIS), an Australian Commonwealth Government Programme.

References

Nakakuki T, Hayashi K, Ishikura N, et al. (2020) Radio Frequency Interference reseach around Ishioka VLBI station using VGOS broadband receiver. Japan VLBI Consortium 2019 proceedings, 66–69. (in Japanese) URL: `https://www2.nict.go.jp/sts/stmg/vcon/symposium2019/vcon19/Vcon2019Proc_all.pdf`

Niell A, (2017) VGOS Band and Channel Frequency Configuration. VLBI Broadband Memo Series (VGOS), #44. URL: `https://www.haystack.mit.edu/wp-content/uploads/2020/07/memo_VGOS_044.pdf`

Simulation of VGOS observations at the raw data level with VieRDS

J. Gruber, J. Böhm, F. Jaron, A. Nothnagel

Abstract Broadband observations of the VGOS system reveal new systematic influences within the interferometric magnitudes and phases that must be taken into account in the VLBI processing chain. These include, for example, the characteristic frequency response of the station or the nonlinear group delay contribution due to the ionosphere. Especially the correlation and fringe fitting analysis stages are affected by these systematics. In this publication, we present a novel software realization, called VieRDS, that simulates broadband VLBI observations at the raw data level. The approach is in contrast to existing simulation software packages that simulate at the group delay level. This presentation focuses on simulating the characteristic station frequency response of real VGOS telescopes and simulating the telescopes' phase calibration signal. The simulation of alternative frequency sequences for VGOS will also be shown and analyzed in the VLBI processing chain.

1 Introduction

To run an experiment with the technique known as Very Long Baseline Interferometry (VLBI), a process chain of several elements must be executed. The process chain is commonly structured into scheduling, observations, transfer, correlation, fringe-fitting, and geodetic parameter estimation. The data produced by the VLBI stations within the observations element represent the filtered, down-converted, sampled, and quantized electric field strength measurements of the radio telescopes.

There exist several terms to term the output data generated by the VLBI radio telescopes. Since the signal is down-converted from radio frequencies (RF) to the base of the frequency spectrum, the data is referred to as baseband data. According to a IVS resolution from 2019, the data is also called level-0 data[1]. Some VLBI scientists also use the term raw data to describe the data provided by the stations, which is then further processed by the correlator. For the descriptions in this text, we use the term raw data.

From a technical point of view, the raw data is characterized by the sampling frequency, the number of bits used for quantization, the number of baseband channels, and the number of recorded polarization components. Stations of the VLBI Global Observing System (VGOS) sample the analog data with 64 MHz and quantize with two-bit resolution. Additionally, 32 channels with two linear polarization components per channel are acquired. Most commonly, the VLBI Data Interchange Format (VDIF) is used to store the data.

Processing raw VLBI data at the correlator is essential to obtain group delays and estimate accurate geodetic parameters. However, the simulation of raw data is a new research field for VLBI with a variety of potential applications. In Gruber et al. (2021) a new software package implemented in MATLAB is presented that can simulate raw telescope data for VLBI. The software is called VieRDS and features tools to simulate a delay, a delay rate, a phase offset, and a frequency response of arbitrary magnitude for each channel of the telescope data stream. The signal model consists of a radio source component of selectable flux density, a

---

Jakob Gruber · Johannes Böhm · Frédéric Jaron · Axel Nothnagel
Department of Geodesy and Geoinformation, TU Wien, Wiedner Hauptstraße 8, A-1040 Vienna, Austria

[1] https://ivscc.gsfc.nasa.gov/about/resolutions/IVS-Res-2019-02-AnalysisLevels.pdf

system noise component, and a phase calibration signal. VieRDS is distributed within the umbrella of the Vienna VLBI and Satellite Software (VieVS, Böhm et al. (2018)) and can be downloaded from `https://github.com/TUW-VieVS/VieRDS`.

The great advantage of the simulation at the raw data level, as VieRDS can achieve it, arises from the fact that systematic and random effects can be directly accessed and isolated at the observation and raw data level. This contrasts with existing simulation software packages that simulate at the group delay level where these effects are already vanished due to the correlation and fringe-fitting process. This article analyzes the correlation results obtained by the application of VieRDS to simulate the phase calibration signal, station-specific frequency response, and alternative frequency sequences.

2 Processing chain of simulated data

An essential feature of VieRDS is the capability to provide the simulated data in the VDIF format. Hence, it is possible to process simulated data in the processing chain of real data. For the studies shown in this article, the simulated VDIF files are correlated by DiFX 2.5 (Deller et al., 2011) and fringe-fitted by HOPS-3.22[2]. It should be emphasized here, that the data provided by VieRDS can be processed by any other VDIF compatible VLBI correlator. It is not restricted to a dedicated software correlator or fringe-fitting program. The process chain used for these studies and alternative paths is depicted in Fig. 1.

3 Power of the phase calibration signal

The VLBI radio telescope represents a sophisticated interconnection of electronic devices, introducing instrumental phase and delay errors in the recorded raw data. In order to monitor and calibrate these systematic influences, a phase calibration (PCAL) signal is injected near the feed horn of the VLBI antenna. The PCAL signal is extracted in the correlation processes and is then applied in the fringe-fitting process to align the interferometric phases to obtain a coherent group delay. The PCAL signal is of great importance for the VGOS system due to its large spanned bandwidth, making it more difficult to find a coherent group delay of all channels in the broadband frequency setup.

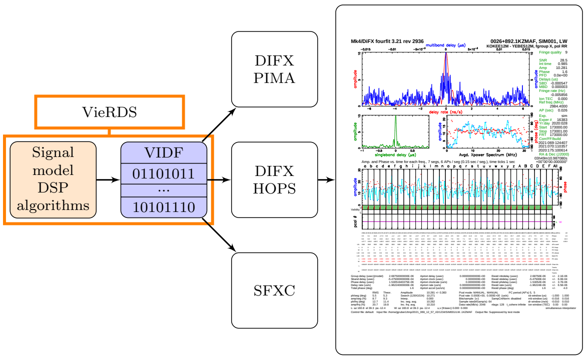

Fig. 1 Processing chain for simulated raw data of VieRDS using Digital Signal Processing (DSP) algorithms and an exemplary picture provided by the program fourfit from HOPS.

The PCAL signal is a comparably simple signal which can be visualized as a periodic sequence of short pulses. VieRDS features a tool to simulate such a PCAL signal which is superimposed onto the other signal components. These are the source signal and the system signal. In VieRDS, the PCAL signal is parameterized with two parameters. On the one hand, the amplitude can be controlled by setting the relative power of the PCAL signal ($p_{cal,rel}$), which is defined as,

$$p_{cal,rel} = \frac{P_{pcal}}{P_{tot}}. \tag{1}$$

The total power P_{tot} is the sum of the power of all signal components. On the other hand, the repetition rate (Hz) of the tones of the PCAL signal can be directly set by the user of VieRDS. For a detailed description of the signal model of the PCAL signal in VieRDS, see Gruber et al. (2021).

It is expected that $p_{cal,rel}$ relates to the quality of the fringe-fitting results in two ways. If $p_{cal,rel}$ falls below a specific limit, the detection algorithm of the correlator cannot extract a reliable PCAL phase and magnitude measurement, and an error will be introduced. If $p_{cal,rel}$ exceeds a specific limit, the additional signal power leads to a loss of Signal to Noise Ratio (SNR) for the source signal. In order to investigate this behavior, a study using VieRDS is carried out.

---

[2] https://www.haystack.mit.edu/haystack-observatory-postprocessing-system-hops/

In this study, 30 different $p_{cal,rel}$ levels ranging from 0.01% to 10.0% are simulated, and the PCAL phase error and the fourfit SNR values are analyzed. The PCAL phase error is the difference between the simulated input and detected output phases applied in fourfit. The simulation setups include legacy S/X observations with 8 and 16 MHz bandwidth, one and two-bit quantization, and a PCAL tone frequency spacing of 1 MHz. Furthermore, a VGOS observation scenario is also simulated for a channel with 32 MHz bandwidth, two-bit quantization and 5 MHz PCAL tone frequency spacing. The results of the PCAL phase error and relative SNR are shown in Fig. 2.

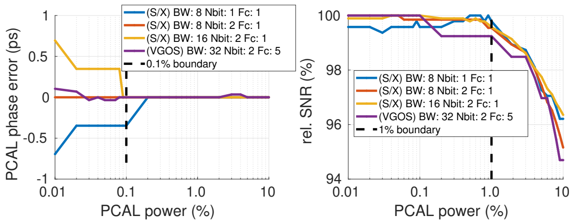

Fig. 2 Thirty relative power levels of the PCAL signal are simulated with VieRDS and the corresponding PCAL phase error at a frequency of 6 GHz (top), and relative SNR of the quasar noise (bottom) are depicted.

As can be seen in Fig. 2, there is no PCAL phase error introduced for $p_{pcal,rel}$ levels between 0.1% and 10.0%. Below 0.1% a PCAL phase error in the order of several fractions of picoseconds for a reference frequency of 6 GHz can be seen for all VLBI observation scenarios. In contrast, the SNR of the VLBI observable remains unchanged for low $p_{pcal,rel}$ levels. However, above 1.0% $p_{pcal,rel}$ a significant decrease in the SNR due to the additional power introduced by the PCAL signal can be seen for the group delay estimation.

From these results, we can identify two interesting thresholds at 0.1% and 1.0%. The PCAL phase measurements show significant errors below 0.1%. Above 1.0%, the SNR of the quasar noise signal is decreased. Consequently, we can define a 'sweet area' of $p_{pcal,rel}$ between 0.1% and 1.0% and suggest not to exceed and fall below these thresholds for the PCAL signal power configuration at the VLBI stations.

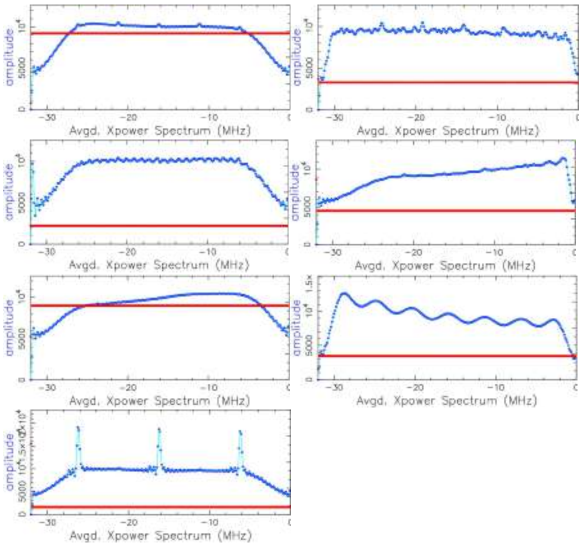

Fig. 3 Frequency response of VGOS telescopes: Gs, K2, Wf and Ys (first column), and Is, Oe, and Ws (second column) of experiment VO1021. In blue color the amplitudes of the autocorrelation spectra is shown and in red the corresponding phases.

4 VGOS station frequency response

Low noise amplifiers (LNA), couplers, distributors, up-down converters, and digital baseband converters are part of each VGOS telescope. However, each station has its unique internal structure and cabling and uses different products of these devices. Since each electronic device has a particular frequency response which reflects the system characteristics, also the frequency response of the entire signal chain is different between VGOS telescopes. In order to illustrate the difference in the system structures, the auto-correlation plots of the seven VGOS telescopes of channel 26 (10.26440 GHz), which participated in session VO1021 on 22/01/2021 is shown in Fig. 3.

The frequency responses shown in Fig. 3 reflect the system characteristics of each VGOS telescope. Since this natural frequency response deviates from the ideal case, which is a flat amplitude response for the entire 32 MHz spectrum, it is expected that sensitivity is lost compared to the ideal case. The SNR loss can also be explained by the fact that less bandwidth due to the amplitude drop at the bandpass edges is available for fringe-fitting, which decreases the SNR. In order to investigate this deviation from the ideal case, a simulation study with VieRDS is carried out.

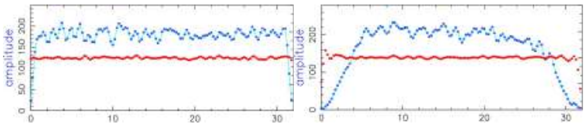

Fig. 4 Auto-correlation function for the ideal bandpass (left) and the simulated station specific K2 bandpass (right).

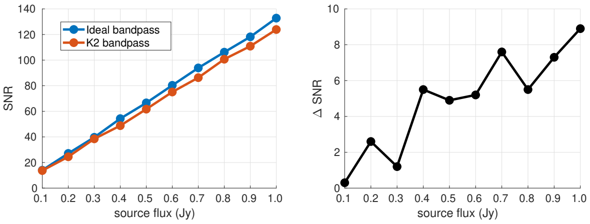

Fig. 5 SNR values shown for different source fluxes for the ideal bandpass (blue color) and for the K2 specific station frequency response (red color). The difference between the datasets is depicted in the right plot.

VieRDS features an arbitrary magnitude filter algorithm which can be applied to any of the signal components, but also to the final superimposed signal as well. The mathematical background and a demonstration of this feature can be found in Gruber et al. (2021). Furthermore, it has already been successfully used to simulate an artificial radio signal on a GNSS satellite (Jaradat et al., 2021).

In this article, only the frequency response of a single channel of K2 is investigated as an example. In the simulation setup, a VGOS channel bandwidth of 32 MHz and two-bit quantization is chosen. First, the ideal case with a flat amplitude response is simulated. This setup is referred to as an ideal bandpass. Second, the K2-specific frequency response is simulated and compared to the ideal case. The auto-correlation functions provided by HOPS for those two cases are shown in Fig. 4.

For this purpose, the amplitude values of the auto-correlation visibility function provided by DiFX are extracted and then handed over as input for the arbitrary magnitude filter toolbox of VieRDS. The K2-specific bandpass filter is then applied to the superimposed signal consisting of the source and system signal. Ten different source fluxes from 0.1 to 1.0 Jy are simulated to obtain a function of SNR versus source flux for the ideal case and the K2 case. The simulated data are processed by DiFX and HOPS, as described in Sect. 2. The SNR values provided by HOPS with respect to source flux are plotted in Fig. 5.

From the data depicted in Fig. 5, one can see that the SNR difference between the ideal and the K2 specific frequency response increases with increasing SNR values. From that, we can conclude that for fringe-detections with low SNR, the deviation from the ideal case is less significant than for higher SNR values. Nevertheless, the SNR discrepancy increases linearly in the plotted SNR range with increasing SNR. A maximum SNR difference of approximately ten can be found for fringes with 120 SNR. We suggest considering this characteristic for more efficient SNR calculations in the scheduling process in future.

5 Alternative VGOS frequency setups

Four widely spaced bands in the frequency range from 2-14 GHz characterize the VGOS system. This so-called broadband delay concept was developed to achieve the goal of 4 ps delay measurement precision (Petrachenko et al., 2009). Following up the latest discussions led by H. Hase and B. Petrachenko to re-think the allocation of the four bands introduced in 2008, simulations with VieRDS are carried out to test these alternative VGOS frequency setups in the real processing chain of DiFX and HOPS (Sect. 2).

Four different frequency setups are considered in this simulation which B. Petrachenko kindly provides. The first frequency sequence comes from the attempt to reproduce the original VGOS setup. The second sequence represents the currently used frequency setup for VGOS sessions. The third and fourth setup are sequences that go up to the Ku band at 14 GHz. The Ku frequency sequences differ in the spanned bandwidth for each single band. One Ku sequence operates with 512 MHz bandwidth for each single band, and the other one uses 1024 MHz bandwidth for each single band. Figure 6 shows the four different frequency sequences which are considered in this study.

To study the impact on the group delay precision of these four different frequency sequences, VieRDS is used to simulate them on the raw data level. Since VieRDS features multi-channel simulations, the frequency sequences provided by B. Petrachenko can be conveniently simulated with VieRDS and processed

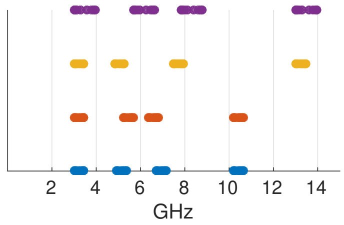

Fig. 6 Four different frequency sequences for VGOS are depicted.

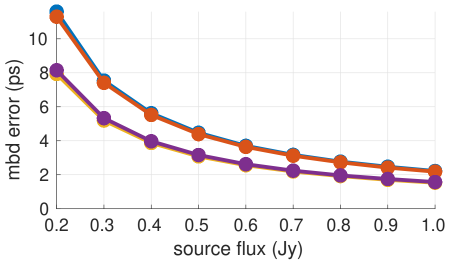

Fig. 7 The multi band delay (mbd) error for four different VGOS frequency sequences are plotted for several source flux densities between 0.2 1.0 Jy.

by the DiFX and HOPS. For this study, nine different source fluxes ranging from 0.2 to 1.0 Jy are simulated for each frequency sequence. Each of the 32 channels is generated based on a bandwidth of 32 MHz and two-bit quantization. The multi-band delay (mbd) error provided by HOPS is used to investigate the simulation results.

Figure 7 shows the mbd error for the four different frequency sequences. A significant improvement for sequences that go up to Ku band can be seen in comparison to the original VGOS setup and the attempt to reproduce it. No significant improvement can be found for the Ku sequences when expanding the single band bandwidth from 512 to 1024 MHz. Expanding the bandwidth of the four single bands of the Ku setups from 512 to 1024 MHz does not show any significant improvement. We can conclude that the Ku frequency sequences, when used in an isolated environment by VieRDS, significantly improve the mbd error provided by the fringe-fitting of HOPS.

6 Conclusions and outlook

In this article, we show three studies using the raw data simulator called VieRDS. The simulated data is stored in VDIF format and can be conveniently used in the processing chain of DiFX and HOPS. In the first study, the impact of the power of the phase calibration signal on phase detection error and SNR loss is investigated. Two interesting thresholds at 0.1% and 1.0% can be found. Below the 0.1% limit, a significant phase detection error can be seen, and if the power exceeds the upper 1.0% threshold, SNR is lost due to the significant additional power contribution of the phase calibration signal besides the system power. In the second study, VieRDS is used to evaluate the SNR loss due to the station characteristic frequency response of the VGOS antennas. Comparing an ideal bandpass with a bandpass approximation of the natural frequency response of K2 shows a significant decrease in SNR. The SNR loss is less significant for fringe detection with lower SNR than for higher SNR values. In the third study, alternative frequency sequences provided by B. Petrachenko are tested in the real processing chain, and the multiband delay error is analyzed. It can be seen that expanding the frequency range to Ku band shows a significant improvement in terms of group delay precision. However, extending the bandwidth of a single band from 512 to 1024 MHz does not show any significant improvement. In the future, we will create follow-up studies of the described topics in this text. These studies will include Monte-Carlo simulations to obtain more statistical quantities. In addition, we plan to implement a new feature for the simulation of source structure into VieRDS.

Acknowledgements

The authors are grateful to the Austrian Science Fund (FWF) for supporting this work with the project P31625 (VGOS Squared). The computational results presented have been achieved in part using the Vienna Scientific Cluster (VSC).

References

Böhm J, Böhm S, Boisits J, Girdiuk A, Gruber J, Hellerschmied A, Krásná H, Landskron D, Madzak M, Mayer D, McCallum J, McCallum L, Schartner M, Teke K (2018) Vienna VLBI and Satellite Software (VieVS) for Geodesy and Astrometry. *Publications of the Astronomical Society of the Pacific*, doi:10.1088/1538-3873/aaa22b

Deller A, Brisken W, Phillips C, Morgan J, Alef W, Cappallo R, Middelberg E, Romney J, Rottmann H, Tingay S (2011) DiFX-2: A More Flexible, Efficient, Robust, and Powerful Software Correlator. *Publications of the Astronomical Society of the Pacific*, doi:http://dx.doi.org/10.1086/658907.

Gruber J, Nothnagel A, Böhm J (2021) VieRDS: A Software to Simulate Raw Telescope Data for very Long Baseline Interferometry. *Publications of the Astronomical Society of the Pacific*, doi:10.1088/1538-3873/abeca4.

Jaradat A, Jaron F, Gruber J, Nothnagel A (2021) Considerations of VLBI transmitters on Galileo satellites. *Advances in Space Research*, doi:https://doi.org/10.1016/j.asr.2021.04.048.

Petrachenko B, Niell A, Behrend D, Corey B, Böhm J, Charlot P, Collioud A, Gipson J, Haas R, Hobiger T, Koyama Y, MacMillan D, Malkin Z, Nilsson T, Pany A, Tuccari G, Whitney A, Wresnik J (2009) Design Aspects of the VLBI2010 System. *IVS 2008 Annual Report, ed. by Behrend d, Baver KD, NASA/TP-2008-214183, p. 13-67*

On the selection of prospective sources for ICRF extension

Z. Malkin

Abstract Despite continuous increasing of the number of ICRF sources, their sky coverage is still not satisfactory. The goal of this study is to discuss some new considerations for extending the ICRF source list. Statistical analysis of the ICRF catalog allows us to identify less populated sky regions where new ICRF sources or additional observations of the current ICRF sources are most desirable to improve both the uniformity of the source distribution and the uniformity of the distribution of the position errors. It is also desirable to include more sources with high redshift in the ICRF list. These sources may be of interest for astrophysics. To select prospective new ICRF sources, the OCARS catalog is used. The number of sources in OCARS is about three times greater than in the ICRF3, which gives us an opportunity to select new ICRF sources that have already be tested and detected in astrometric and geodetic VLBI experiments.

Keywords ICRF, VLBI, OCARS, SREAG

1 Introduction

The International Celestial Reference Frame (ICRF) is the standard of the celestial reference frame recommended by the International Astronomical Union (IAU) for scientific researches and practical applications in various fields. The third ICRF realization, ICRF3 (Charlot et al., 2020) approved by the IAU in 2018 is currently in use. It contains positions of 4588 sources included in three catalogs ICRF3-SX, ICRF3-XKa, and ICRF3-K containing source positions determined from observations at three radio frequency bands. The ICRF3-SX catalog containing of 4536 sources observed at the *S*/*X* band is most complete and it is currently used to link ICRF and *Gaia*-CRF catalogs.

Although the number of sources in the ICRF catalog is continuously increased with time and the accuracy of their positions is continuously improved, the sky coverage by the ICRF sources, its density and uniformity, as well as the sky distribution of the source position errors, are still not satisfactory. For this reason, several institutions are considering new observing programs aimed at improving the ICRF. Statistical analysis of the ICRF catalog allows us to identify less populated sky regions where new ICRF sources or additional observations of the current ICRF sources are most desirable to improve both the uniformity of the source distribution and the uniformity of the distribution of the position errors. One more consideration for extending the ICRF list is including of sources with high redshift. These sources may be of interest for astrophysics.

The main goal of this work is to discuss new approaches for improving the source list for further ICRF extensions. Especial attention will be given to formalization and quantification of some criteria (mostly known) for the selection of new sources for future ICRF extensions, as well as identification of the ICRF sources that need more observations to provide more uniform sky distribution of the position errors.

To select prospective new ICRF sources, the catalog OCARS (Optical Characteristics of Astrometric Radio Sources) (Malkin, 2018)) is used. The current version of the OCARS catalog includes more

---

Zinovy Malkin
Pulkovo Observatory, Pulkovskoe Sh. 65, St. Petersburg 196140, Russia

than 13 thousand sources which is about three times greater than the ICRF3 catalog. The OCARS non-ICRF sources mostly have lower position accuracy compared to ICRF, but these sources have already been tested and detected in VLBI experiments. This gives us an opportunity to select new ICRF sources from the OCARS list without resource consuming detection tests, which are necessary if new sources are pre-selected from general radio surveys.

2 Analysis of possibilities for improving ICRF source list

This study is based on the analysis of the sky distribution of the ICRF3 and *Gaia* catalogs, and position errors of the ICRF3 sources. To quantify the uniformity of the source sky distribution a method of pixelization of the spherical surface SREAG (Spherical Rectangular Equal-Area Grid) (Malkin, 2019, 2020)) is used. It provides rectangular equal area cells with wide range of resolutions from ∼45° to ∼16″ (for 31-bit integer arithmetic). Fortran routines to perform basic operations with the SREAG pixelization are provided[1]. Table. 1 shows basic parameters of several grids that looks most relevant for ICRF studies. In this paper, the grid with N_{ring}=10 (128 cells) has been used for plots of the sky distribution of the ICRF3-SX, *Gaia*, and OCARS sources, and the grid with N_{ring}=18 (412 cells) has been used for plots of the sky distribution of the ICRF3 defining sources.

Table 1 SREAG grid parameters as a function of the number of rings N_{ring}.

N_{ring}	N_{cell}	Cell area [sq. deg]
4	20	2063
6	46	897
8	82	503
10	128	322
12	184	224
14	250	165
16	326	127
18	412	100
20	508	81

Figure 1 shows the sky distribution of the ICRF3-SX and OCARS sources. The upper panel of this plot allows us not only to see the well-known weakness of the ICRF3 catalog in the south, but also to identify the sky regions where the ICRF list should be enriched with new sources to obtain more even source distribution over the sky, in particular, the region of the Galactic plane. It can be seen that the number of sources in the poorly populated cells in the OCARS catalog is two-four times larger than in the ICRF3-SX catalog, which opens a new opportunity to select new ICRF sources from the OCARS source list.

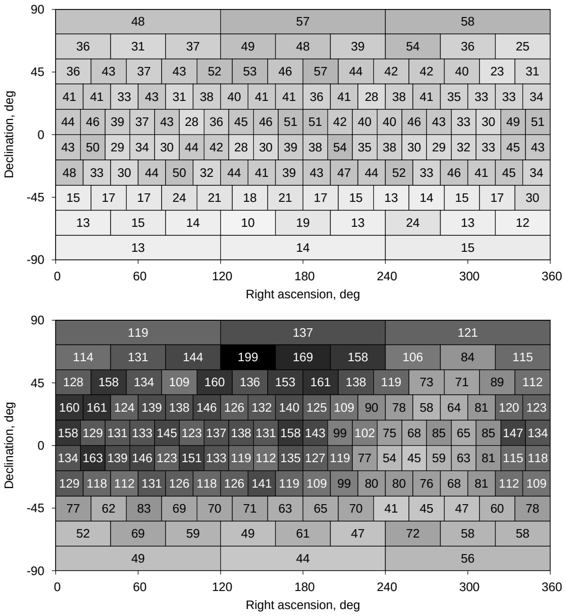

Fig. 1 Sky distribution of sources for ICRF3-SX (top, 4536 sources) and OCARS (bottom, 13560 sources).

Similar situation can be observed when analyzing the sky distribution of common ICRF3-SX and *Gaia* sources (Fig. 2). In this work, the *Gaia* EDR3 astrometric catalog (Lindegren et al., 2020) was used. One can see again the source deficiency in the south and near the Galactic plane. The number of cross-identified sources between the *Gaia* EDR3 and OCARS catalogs is more than twice as much as the number of cross-identified sources between the *Gaia* EDR3 and ICRF3-SX catalogs. Therefore, the selection of new ICRF sources from the list of cross-identified *Gaia*/OCARS sources will allow us to improve the uniformity of the source distribution of common ICRF/*Gaia* sources and thus

---

[1] http://www.gaoran.ru/english/as/ac_vlbi/

improve the accuracy, both systematic and stochastic, of the ICRF/*Gaia* link. It should be noted that uneven distribution of common sources may cause problems with analysis of the coordinate differences ICRF minus *Gaia* by means of spherical harmonics.

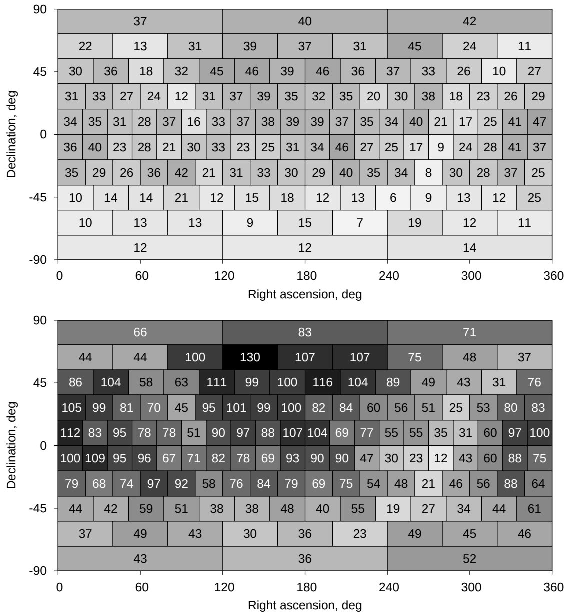

Fig. 2 Sky distribution of sources cross-identified with *Gaia* EDR3 for ICRF3-SX (top, 3485 sources) and OCARS (bottom, 8707 sources) catalogs.

It is important for ICRF not only to have even source distribution over the sky but also even sky distribution of the position error. Figure 3 shows the sky distribution of the ICRF3-SX sources with the position errors less than 1 mas and less than 0.2 mas. For this work, the source position error is computed as the semi-major axis of the error ellipse. This analysis allows us to identify the sky regions were additional observations of ICRF sources should be primarily planned.

An important characteristics of the ICRF catalog is the number of defining sources and how evenly they are distributed over the sky. The nearest goal may be to have ≈400 ICRF4 defining sources (one per 100 sq. deg). Figure 4 shows the sky distribution of the ICRF3 defining sources. One can see that there are many cells that lack defining sources. So, the future ICRF release should take this into account. Similar analysis was made earlier by Basu et al. (2018).

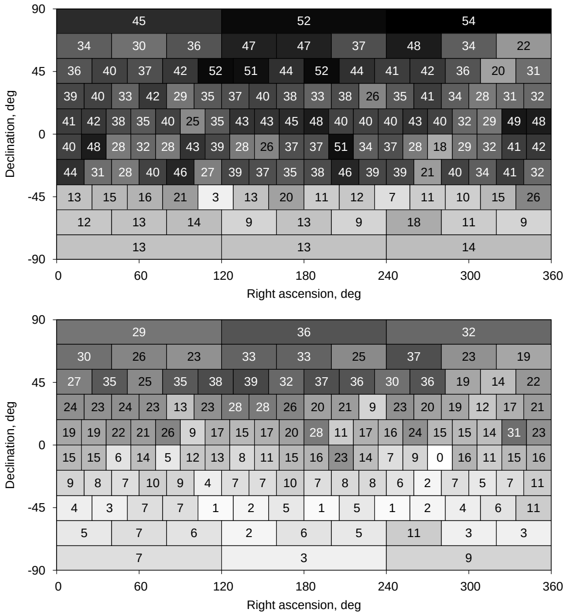

Fig. 3 Sky distribution of the ICRF3-SX sources with the position errors less than 1 mas (top, 4177 sources) and less than 0.2 mas (bottom, 2023 sources).

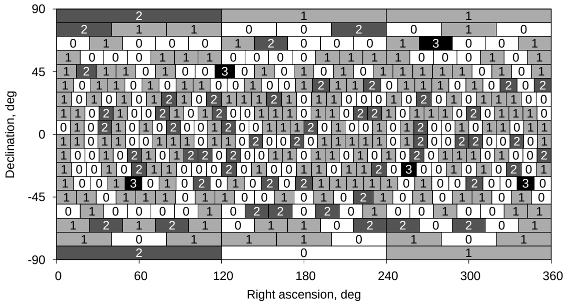

Fig. 4 Sky distribution of the ICRF3 defining sources.

Another consideration which is worth bearing in mind is having more ICRF sources with high redshift. These sources are important for astrophysical and cosmological studies Coppejans et al. (2017). Therefore this makes sense to include the redshift as a criterion for source selection for the ICRF extension. OCARS provides redshift info for about 58% of the sources. Table 2 shows the number of sources with high redshift in the ICRF3 and OCARS catalogs. The number of high-z sources in the OCARS catalog is about two-four times larger that in the ICRF3 catalog. So, inclusion of additional high-z sources from OCARS will make the future ICRF releases more useful for non-astrometric astronomical studies.

Table 2 Number of sources with high redshift in the ICRF3 and OCARS catalogs.

Catalog	Redshift			
	all	≤ 3	≤ 4	≤ 5
ICRF3	3382	106	15	3
OCARS	7967	213	58	13

Increasing the number of observations of prospective ICRF sources requires either to involve supplement network resources, which is not always possible, or to improve the scheduling strategy. A possible way to make more observations of CRF sources was discussed and tested in Malkin et al. (2013).

We started with actual schedule for IVS session R1591 that involved the 11-station network. In the original (actual) IVS schedule for the R1541 session, 60 sources were observed including 7 southern sources with declination less than -40°. For comparisons, the supplementary southern sources were added to the original source list and three experimental schedules were obtained to evaluate the trade-off between the number of southern sources and the accuracy of geodetic products. Schedule ‘R1’ was obtained with the original R1591 source list. Schedule ‘R1+’ includes three more southern sources, and schedule ‘R1++’ includes six more southern sources as compared with the original R1541 schedule. The three schedules for 24-hour continuous observations were generated with VieVS scheduling package (Sun et al., 2011).

For Monte Carlo simulation, 50 sessions were generated using the same 24-hour schedule but different realizations of noise delays, each time creating new values for wet zenith delay, clocks and white noise to simulate observations as realistic as possible. The simulated NGS data files were entered into the software package VieVS (Böhm et al. 2012), which computes a classical least squares solution. The source coordinates were fixed to the ICRF2 positions, and only Earth orientation parameters (EOP) and station positions were estimated. The standard deviation of the 50 EOP estimates and mean formal uncertainties obtained in our computations are listed in Table 3. One can see that we found no overall degradation of the EOP accuracy after the inclusion of supplement southern sources. Errors in some EOP became even smaller with inclusion of more southern sources, and some EOP showed minor degradation in the accuracy.

Table 3 Repeatability and standard deviation of EOP for the IVS R1541 and two experimental schedules R1+ and R1++ (Malkin et al. 2013).

Parameter		R1	R1+	R1++
Number of scans		1258	1351	1375
Number of observations		3905	3813	3997
EOP repeatability	Xp	143.2	125.5	98.2
[μas, μs]	Yp	98.2	79.1	96.8
	UT1	5.6	4.6	5.9
	dX	36.2	42.8	39.1
	dY	45.0	39.5	37.2
Mean EOP uncertainty	Xp	94.8	95.6	93.4
[μas, μs]	Yp	77.2	77.3	74.8
	UT1	4.4	4.6	4.7
	dX	29.8	30.9	29.5
	dY	29.1	29.6	28.1

As to the baseline length repeatability, it was found that for the baselines shorter than ∼5,000 km the R1 schedule shows the best result, and R1+ and R1++ schedules shows worse repeatability, whereas for longer baselines the R1++ schedule is the best, and R1 is the worst. However, in fact, the results obtained with the three schedules are close to each other. The mean baseline length repeatability derived from R1, R1+, and R1++ schedules are 13.5 mm, 12.4 mm, and 11.9 mm, respectively. In other words, increasing of the number of southern sources (cf. R++ and R+ schedules) leads to a small degradation of baseline length repeatability for short baselines, and small improvement for long baselines. However, an overall improvement in the baseline length repeatability was found after inclusion more southern sources in the schedule.

Summarizing the results of this simulation experiment, one can conclude that the inclusion of targeted southern sources in regular IVS sessions such as R1 and R4 can help to increase substantially the number of ICRF southern sources with accurate positions. Suppose, we want to add 100 new sources in the south observed each 100 times (to obtain sub-mas position error) during one year. Then we need to make ∼200 observations of these sources per week (cf. current ∼10K observations in R1+R4 weekly schedule), which would not significantly influence the normal IVS operations, and might even provide some improvement in obtained geodetic parameters.

3 Conclusion

In this paper, an approach is discussed to select new sources for ICRF extension and identify sources already included in the ICRF that preferably need more observations to improve their position. It is suggested that the OCARS catalog (Malkin, 2018)) can be used as an initial (candidate) list of already VLBI-detected sources to enrich ICRF.

Of course, some sources selected from OCARS using sky coverage criterion discussed in this paper may be too weak and/or may have a bad structure index (SI) to be used in the regular geodetic observing programs aimed at EOP and TRF monitoring. However, both source SI and flux are often variable and change with time (Charlot, 2008; Charlot et al., 2010). So, currently “bad” source can become a “good” one and vice versa.

It should be emphasized that the ICRF is not only needed for geodesy. Many other scientific and practical applications, from navigation to astrophysics and cosmology, will appreciate a dense and highly accurate catalog of radio source positions evenly distributed over the sky. Low flux radio sources are also important for astronomy, especially those sources that are cross-identified with objects in other wave bands such as optics, X-ray or gamma-ray. Such cross-identification is also provided by OCARS.

It should be also noted that increasing the number of ICRF sources evenly distributed over the sky is important for improving the link between ICRF and *Gaia*-CRF. Therefore, inclusion of radio weak but optically bright sources in ICRF will be of mutual benefit. OCARS provides optical and NIR magnitudes for about 78% of the sources, which can be used for source selection. The selection of candidate sources for ICRF extension that can be used for the ICRF–*Gaia* link can be made even simpler because OCARS provides the cross-identification table with the *Gaia* catalog.

Therefore it is worth spending efforts to enrich the next ICRF catalogs not only with sources “convenient” for solving say IERS- and GGOS-related tasks, but also with other sources that would improve general ICRF quality. In particular, observations of weak radio sources for ICRF can be performed in cooperation with other VLBI networks, which include large antennas.

4 Acknowledgments

This research has made use of the SAO/NASA Astrophysics Data System[2] (ADS). The figures were prepared using `gnuplot`[3].

References

Basu S, de Witt A, Quick J, Malkin Z (2018) Multi-epoch VLBI images to study the ICRF-3 Defining Sources in the Southern Hemisphere. In: *14th European VLBI Network Symposium & Users Meeting. 8-11 October. Granada, Spain*, PoS(EVN2018)135, doi: 10.22323/1.344.0135

Charlot P (2008) Astrophysical Stability of Radio Sources and Implication for the Realization of the Next ICRF. In: A. Finkelstein and D. Behrend (eds.) *5th IVS General Meeting Proceedings, St. Petersburg, Russia, 2008*, 345–354

Charlot P, Boboltz DA, Fey AL, *et al.* (2010) The celestial reference frame at 24 and 43 GHz. II. Imaging. *AJ*, 139, 1713, doi: 10.1088/0004-6256/139/5/1713

Charlot P, Jacobs CS, Gordon D, *et al.* (2020) The third realization of the International Celestial Reference Frame by very long baseline interferometry. *A&A*, 644, 159, doi: 10.1051/0004-6361/202038368

Coppejans R, van Velzen S; Intema HT, *et al.* (2020) Radio spectra of bright compact sources at z $>$ 4.5. *MNRAS*, 467, 2039 doi: 10.1093/mnras/stx215

Lindegren L, Klioner SA, Hernandez J, *et al.* (2020) *Gaia* Early Data Release 3: The astrometric solution. *A&A*, doi: 10.1051/0004-6361/202039709

Malkin Z, Sun J, Böhm J, Böhm S, Krásná H (2013) Searching for an Optimal Strategy to Intensify Observations of the Southern ICRF sources in the framework of the regular IVS observing programs. In: N. Zubko and M. Poutanen (eds.) *21st Meeting of the European VLBI Group for Geodesy and Astronomy, Espoo, Finland, March 5–8, 2013*, 199–204

Malkin Z (2020) A New Version of the OCARS Catalog of Optical Characteristics of Astrometric Radio Sources. *AJ*, 239, 20, doi: 10.3847/1538-4365/aae777

Malkin Z (2019) A New Equal-area Isolatitudinal Grid on a Spherical Surface. *AJ*, 158, 158, doi: 10.3847/1538-3881/ab3a44

Malkin Z (2020) Spherical Rectangular Equal-Area Grid (SREAG)–Some features. In: C. Bizouard (ed.) *Proc. Journees 2019 Astrometry, Earth Rotation, and Reference Systems in the GAIA era*, 55–59

---

[2] https://ui.adsabs.harvard.edu/

[3] http://www.gnuplot.info/

Towards the determination of the geodetic position of non-geodetic EVN antennas

M. E. Gomez, P. Charlot, R. M. Campbell, M. Kettenis, A. Keimpema

Abstract One of the goals of the EC Horizon 2020 project JUMPING JIVE was to establish a geodetic path at the European VLBI Network (EVN) correlator at JIVE (SFXC). This was successfully implemented in 2019, and since then we have conducted two EVN geodetic-type experiments at K-band, EC065 and EC076, taking advantage of this new capability. The two experiments exercised all aspects of the new geodetic path, from correlation to data export in MK4 format and post-processing, using standard geodetic analysis tools. These were carried out in 2018 and 2020, and involved both geodetic and non-geodetic EVN antennas, including Sardinia, Torun, and the Jodrell Mark2 telescope, along with the e-MERLIN outstations and KVN (Korean VLBI Network) telescopes. The main goal is to obtain precise geodetic coordinates for these antennas. The project will also consider the results from similar experiments conducted previously, going back to 2000, to allow for the estimation of the station velocity. This contribution presents the current state of the project.

Keywords JUMPING JIVE, EVN, VLBI

1 Introduction

In the last three years, as part of the JUMPING JIVE project, the EVN software correlator at JIVE (SFXC) was upgraded to be able to correlate geodetic experiments. This capability allows one to obtain positions of telescopes but also Earth's orientation parameters (EOP) and source positions from SFXC through a fully-validated geodetic path. Besides the usual geodetic applications, a precise knowledge of the geodetic coordinates of the telescopes is also important for phase-referencing when observing weak sources, and therefore of benefit to astrophysics.

The upgrade of the SFXC includes the handling of sessions with sub-netting and guarantees that the correlator output data can be post-processed and analyzed in a geodetic standard way. To validate the procedure, we correlated, post-processed and analyzed an IVS-R1 session whose methodology and results were published in Gomez et al. (2019).

Once the geodetic path was successfully implemented and checked, we performed two EVN experiments: EC065 in 2018 and EC076 in 2020. EC065 has been correlated, post-processed and analyzed following the mentioned geodetic path while EC076 is currently under processing.

Although these are the first geodetic experiments correlated by the SFXC, this is not the first time that geodetic experiments are conducted with the EVN. Previous experiments include TP001, carried out in 2000 and correlated in Bonn, which provided initial VLBI coordinates for the EVN non-geodetic telescopes (Charlot et al., 2001).

As EC076 is still in the post-processing stage, we focus here on the results achieved for EC065 and the comparison of the estimated coordinates for the non-geodetic telescopes from these data with those obtained from TP001.

M. Eugenia Gomez · Patrick Charlot
Laboratoire d'Astrophysique de Bordeaux, Pessac, France

Robert M. Campbell · Mark Kettenis · Aard Keimpema
Joint Institute for VLBI-ERIC, Dwingeloo, The Netherlands

Exp. /Station	Bd	Cm	Da	Ef	Hb	Hh	Jb	Kn	Kt	Ku	Ky	Mc	Mh	Nt	O6	Pi	Sr	Sv	T6	Tr	Ur	Yb	Zc
EC065	✓			✓		✓	✓				✓	✓	✓	✓	✓		✓	✓		✓		✓	✓
EC076	✓		✓	✓	✓	✓		✓	✓	✓	✓	✓	✓		✓	✓	✓	✓	✓	✓	✓	✓	✓

Table 1: Data availability for EC065 and EC076 (see the full names of EVN stations on the EVN web site at `http://www.evlbi.org`).

2 EVN observations

Since the geodetic path was established, two geodetic-type EVN experiments, EC065 in 2018 and EC076 in 2020, have been carried out. These were conducted in K-band and involved geodetic telescopes as well as non-geodetic ones, including Sardinia, Torun, the Jodrell Mark2 telescope, the e-MERLIN out-stations and the KVN antennas. The main goal of these experiments was to determine the geodetic coordinates of the mentioned non-geodetic telescopes.

EC065 was carried out on June 13, 2018, with a total of 20 telescopes scheduled, including the e-MERLIN out-stations and the Korean telescopes of Yonsei, Ulsan and Tamma. Unfortunately, reconstruction of the total delays for the e-MERLIN turned out not to be possible because of fibre-delay corrections applied to the data prior to its eventual sampling and recording (this situation has been addressed prior to EC076). This led us to abandon correlation for these stations. Additionally, two of the Korean telescopes failed to participate, hence leaving a total of 14 telescopes out of the initial 20 scheduled, with only Jodrell Bank, Sardinia, Torun and KVN-Yonsei left as non-geodetic telescopes, the latter observing for only 12 hours. During the experiment, 62 ICRF3 sources (among which 28 defining) were observed, with 478 scans scheduled over the 24-hour duration of the experiment.

EC076 was carried out on October 23, 2020, and included Tianma65 and Urumqi besides the antennas that participated in EC065, while Noto could not join. Additionally, Hobart 26, which is not part of the EVN, was also arranged to improve the geometry in the southern hemisphere. Fringes have been obtained for 20 out of the 22 scheduled antennas. This was also a 24-hour experiment and all sources observed were ICRF3 defining sources. The stations that participated in these two EVN experiments are listed in Table 1.

3 Modeling and analysis strategy

EC065 was correlated with SXFC and post-processed with HOPS following the established path. The analysis was done with VieVS (Böhm et al., 2018) in a standard way based on the modeling presented in Table 2. As only a single frequency was observed, it is mandatory to model ionospheric effects. For this purpose, we tested the use of CODE and JPL maps. The resulting differences were insignificant, which is in agreement with the findings of Lanyi et al. (2010), and the final solution was obtained by using a CODE map.

Data/Models	Comments
Ephemeris	JPL421
Earth Orientation Parameters	IERS C04
Terrestrial Reference Frame	ITRF2014
Celestial Reference Frame	ICRF3(K)
Ocean Tide Loading	FES2012
Ionospheric correction	CODE
Galactic Acceleration	YES
Tropospheric hydrostatic model	Saastamoinen
Tidal atmospheric loading	Vienna
Non-tidal atmospheric loading	Vienna
Tropospheric Mapping function	VMF3

Table 2: Models (non-exhaustive list) used for the analysis of the EC065 experiment.

The datum was defined by not-net-rotation and no-net-translation constraints with respect to ITRF2014. Source coordinates were treated as fixed, while station coordinates and EOP were estimated together with clocks and tropospheric parameters. The last three were estimated as piecewise linear functions with time interval of 24 hr for EOP (rel. constr. of 0.1 μas), 30 minutes for the zenith wet delay (rel. constr. 1.5 cm) and 60 minutes for the clock interval (rel. constr. 1.3 cm). In this case we considered one rate and one quadratic term per clock.

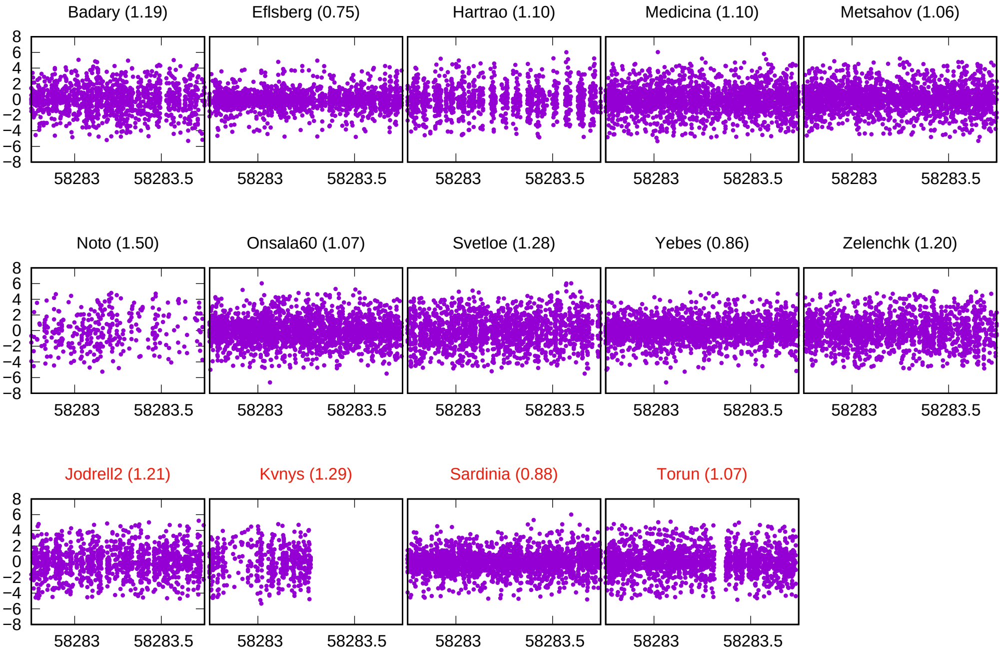

Fig. 1: Post-fit residuals per station in cm and weighted RMS in parenthesis. Each point represents an observation on a baseline that includes the mentioned station.

Station	$\sigma_{pos}[cm]$
Jodrell2	1.31
KVNYS	2.10
Sardinia	0.60
Torun	0.89

Table 3: Position uncertainties for the four non-geodetic EVN telescopes that observed in EC065.

4 Results

The post-fit residuals per station obtained after the analysis with VieVS are plotted in Figure 1. It can be appreciated that non-geodetic and geodetic antennas show residuals of the same order (about 1 cm) and as expected, the lowest values relate to the biggest antennas (Efflsberg, Sardinia and Yebes).

Regarding the coordinates of Jodrell2, KVN-YONSEI (KVNYS), Sardinia and Torun, Table 3 shows the uncertainty on the estimated positions for these stations. The values obtained are consistent with the quality of the observations and the post-fit residuals shown in Figure 1.

As mentioned in the introduction, this geodetic-type experiment was not the first one that involved EVN telescopes. Geodetic positions of Jodrell2 and Torun were first determined from a dedicated experiment run by the EVN in November 2000 (TP001, Charlot et al., 2001) with an accuracy of about 5 cm. Taking into account that almost two decades have passed since then, one can derive the velocity for Jodrell2 and Torun by comparing the results of TP001 and EC065. In order to compute these velocities, the coordinates obtained from TP001 were transformed into ITRF2014 by applying the procedure and transformation parameters given on the ITRF web page [1].. Figure 2 shows

---

[1] `http://itrf.ensg.ign.fr/doc_ITRF/Transfo-ITRF2014_ITRFs.txt`

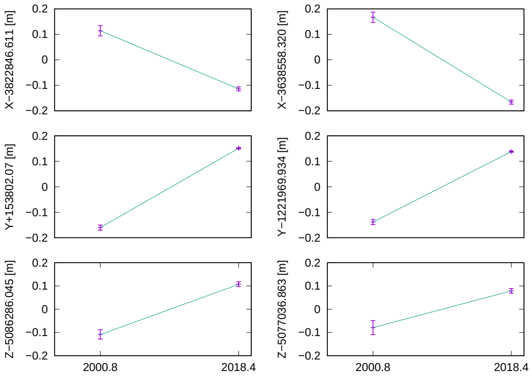

Fig. 2: Velocity components estimated for Jodrell2 (left) and Torun (right).

the (X, Y, Z) components of the velocities for Jodrell2 and Torun. The magnitude of these, 25-30 mm/yr, is in agreement with the motions derived from plate tectonic models for Europe.

5 Conclusions and Perspectives

Two non-standard geodetic-type experiments, EC065 and EC076, have been carried out with the EVN, correlated at JIVE, and post-processed by using a newly-established geodetic path developed under JUMPING JIVE. The post-fit residuals obtained after the analysis of EC065 are at the level of 1 cm for both the geodetic and non-geodetic telescopes. Position uncertainties for the non-geodetic antennas are at the same level. A comparison with the coordinates of Jodrell2 and Torun for TP001 (in 2000) and EC065 (in 2018) indicates velocities of 25-30 mm/yr. The magnitude and direction of these is in agreement with motions predicted from plate tectonic models fro Europe.

In the future, we expect to combine the results of EC065 and EC076 and to include previous experiments in the analysis.

6 Acknowledgement

We are grateful to the team in Hobart for agreeing to participate in EC076. The research leading to these results has received funding from the European Commission Horizon 2020 Research and Innovation Programmes Jumping JIVE (grant agreement No. 730884) and RadioNet (grant agreement No. 730562) We also thank to RadioNet for its support.

References

Böhm J, Böhm S, Boisits J, Girdiuk A, Gruber J, Hellerschmied A, Krásná H, Landskron D, Madzak M, Mayer D, McCallum J, McCallum L, Schartner M, Teke K (2018) Vienna VLBI and Satellite Software (VieVS) for Geodesy and Astrometry. Publications of the Astronomical Society of the Pacific. Vol. 130(986), 044503, 2018.

Charlot P, Campbell R, Alef W, Borkowski K, Conway J E, Foley T, Garrington S T, Kraus A, Nothnagel A, Sovers O J, Trigilio C, Venturi T, Xinyong H (2001) ITRF2000 Position of non-geodetic telescopes in European VLBI Network. In: D. Behrend and A. Rius (Eds.): Proceedings of the 15th Working Meeting on European VLBI for Geodesy and Astrometry, Institut d'Estudis Espacials de Catalunya, Consejo Superior de Investigaciones Cientificas, pp. 194–200.

Colomer F, Campbell R, Kettenis M, Charlot P, Szomoru A (2018) Geodetic capabilities of the JIVE SFXC correlator. In: K. L. Armstrong, K. D. Baver and Dirk Behrend (Eds.): Proceedings of the IVS 2018 General Meeting, NASA/CP2019-219039.

Gomez M E, Kettenis M, Charlot P., Campbell R M, Keimpema A (2019) Implentation of a geodetic path at the JIVE correlator. In: R. Haas, S. Garcia-Espada and J.A. López Fernández (Eds.): Proceedings of the 24th European VLBI Group for Geodesy and Astrometry Working Meeting, CNIG-Madrid, pp. 112–115.

Lanyi G E et al. (2010) AJ, 139, 1695.

Spectrum Management for the VGOS

H. Hase, J.A. López-Pérez, M. Bautista-Duran, J. Kallunki, P. Kupiszewski, V. Tornatore, W. Madkour, M. Lindqvist, B. Winkel

Abstract Spectrum management for the VLBI Global Observing System (VGOS) is an important task to keep radio frequency interference as absent as possible from observation sites. Protection can only be granted, if national and international authorities are made aware of the activities and operations at VLBI observing sites. To begin with spectrum management for the VGOS, it means two things: to be registered at the ITU-R as a Radio Astronomy Service site and try to get the requirements of VGOS into an official ITU-R document, so that further regulation actions can refer to an official document, e.g. for compatibility studies.

Keywords VGOS, geodetic VLBI, ITU-R, WP7D, RAS, RFI, ITU registration

1 International Telecommunication Union - Radiocommunication Sector (ITU-R)

The need for coordination of international communication dates back to the 19th century when the precessor of the ITU, the International Telegraph Union was founded in 1865. Today, one of the three ITU-divisions covers radio communication, ITU-R. Its main mission is to facilitate seamless and interference free operation of radio communication services between member states. The coordination started among service providers with active transmitters.

Radio astronomy, as a passive receiver of cosmic noise, was recognized with its needs only later (during the 1930s, when historically radio astronomy was born). The Radio Regulations (RR) are the main references in spectrum management. In RR Article 4.6 it is recognized that *'the Radio Astronomy Service (RAS) can be regarded as a radio communication service within the ITU-R for the purpose of protecting its operation from harmful interference'*. This means, that Radio Astronomy is equally considered with its requirements as any other (active) service. This is very important for spectrum management for VLBI as a radio astronomy technique.

Hayo Hase
Bundesamt für Kartographie und Geodäsie, BKG Wettzell-AGGO, Sackenrieder Str. 25, D-93444 Bad Kötzting, Germany

José Antonio López-Pérez
Instituto Geográfico Nacional, Observatorio Yebes, Cerro de la Palera sn, E-19141 Yebes, Guadalajara, Spain

Marta Bautista-Duran
Universidad de Alcalá de Henares, Pza. San Diego, s/n, E-28801 - Alcalá de Henares (Madrid), Spain

Juha Kallunki
Aalto University, Metsähovi Radio Observatory, Metsähovintie 114 , FI-02540 Kylmälä, Finland

Piotr Kupiszewski
Norwegian Mapping Authority, Geodetic Earth Observatory, N-9173 Ny-Ålesund, Norway

Vincenza Tornatore
Politecnico Milano, Piazza Leonardo da Vinci 32, I-20133 Milano, Italy

Waleed Madkour
Joint Institute for VLBI ERIC, Oude Hoogeveensedijk 4, NL-7991 PD Dwingeloo, The Netherlands

Michael Lindqvist
Department of Space, Earth and Environment, Chalmers University of Technology, Onsala Space Observatory, S-439 92 Onsala, Sweden

Benjamin Winkel
Max-Planck-Institut für Radioastronomie, Auf dem Hügel 69, D-53121 Bonn, Germany

Fig. 1 The Radio Regulations are binding in international law and are the 'bible' in spectrum management. `https://www.itu.int/pub/R-REG-RR`

It is important to note, that the RR have the status of an international treaty among member states, binding in international law. Consequently, most national spectrum authorities practise national spectral use in a way adherent to the international RR. The RR are constantly updated by decisions at the World Radio Conferences, every four years (next in 2023).

The Radiocommunications Bureau is hosted within the ITU-R (ITU-R BR). It holds the *'Master International Frequency Register'* - or in short *'Master Register'* - which contains *frequency assignments* and a database of the *radiocommunication stations*. With the recognition of radio astronomy as a service, radiotelescope sites count as 'radiocommunication station' and can be registered. The RR Article 11.12 reads: *Any frequency to be used for reception by a particular radio astronomy station may be notified if it is desired that such data be included in the Master Register.*

2 The process of registration of a radio telescope at ITU-R

The registration of a radio telescope site is done in 3 steps (Fig. 2).

1. The radio telescope station owner notifies its national spectrum authority about its (passive) use of radio spectrum as a RAS site. The national spectrum authority cannot know on its own, that a new radio telescope had been built. Only the owner knows about it and has to take the first step.
2. The national spectrum authority is the only entity which can request to the international entity a recording of the notification from the RAS site on its territory. As this registration procedures does not happen very frequently, it might take time to push the issue forward.
3. Once the completed forms have reached the ITU-R BR in the correct format, the request from the country will be evaluated, the location and the spectral use (the receiver capabilities) will be verified. Upon approval, the RAS site is registered.

There are benefits of a registration. In the coordination of spectrum a *chronological priority* is applied. It counts the date of registration, not the date of radio telescope construction. Therefore, the earlier the telescope is registered the better for the site protection.

A registered RAS station has to be considered by compatibility studies by those planning new transmitters in its vicinity or in space. Missions installing new transmitters in space have to follow special procedures at ITU-R in order to get permission for spectral use. For the avoidance of harmful interference the Master Register is an important resource for the mission planning.

The international registration is also important for RAS sites located near borders which then require bilateral coordination.

If the RAS station employs a new receiver with previously uncovered (and therefore unregistered) spectral bands, the Master Register should be updated following the same 3 steps mentioned earlier.

As it can be seen in Table 1 the registration process has been mainly initiated by ITU-Region 1 stations (Europe-Africa), but not in Region 2 (Americas) and 3 (Asia-Australia). For the global network of VGOS stations it would be an advantage to argue on the international level with the global network instead of individual national stations. The authors recognize actions already taken to improve the registration situation and are aware that the process is slow and needs to be triggered by questioning for the actual status.

Fig. 2 Registration process. The initiative must come from the VLBI station.

Table 1 Registration of VGOS sites at ITU-R, status March 2021. The status *'completed'* means that the registration process has finished successfully; *'in progress'* means that the request for registration has been received, evaluation did not finish yet; *'empty space'* means that it is unclear whether any action had been taken or if the file got stuck at the national spectrum authority or at ITU-R BR; '–' no action taken yet (due to project planning phase).

ITU-Region	Country	Station	N-Latitude	E-Longitude	Reflector	ITU-Status
R1	Finland	Metsähovi	60°13'04.8"	24°23'38.4"	13.2	in progress
R1	France	Tahiti	-17°31'04.8"	-149°26'13.2"	project	–
R1	Germany	Wettzell North	49°08'38.4"	12°52'40.8"	13.2	in progress
R1	Germany	Wettzell South	49°08'34.8"	12°52'40.8"	13.2	completed
R1	Italy	Matera	40°38'56.4"	16°42'18.0"	project	–
R1	Norway	Ny Alesund North	78°56'34.8"	11°51'18.0"	13.2	
R1	Norway	Ny Alesund South	78°56'34.8"	11°51'18.0"	13.2	
R1	Portugal	Flores	39°28'01.2"	-31°13'37.2"	project	–
R1	Portugal	Santa Maria	36°59'07.2"	-25°07'33.4"	13.2	in progress
R1	Russia	Badary	51°46'12.0"	102°14'02.4"	13.2	in progress
R1	Russia	Svetloe	60°31'48.0"	29°46'48.0"	13.2	in progress
R1	Russia	Zelenchukskaya	43°47'16.8"	41°33'54.0"	13.2	in progress
R1	South Africa	Hartebeesthoek	-25°53'16.8"	27°41'09.6"	13.2	completed
R1	Spain	Gran Canaria	28°01'33.6"	-15°40'15.6"	project	–
R1	Spain	Yebes	40°31'22.8"	-03°05'16.8"	13.2	in progress
R1	Sweden	Onsala NE	57°23'38.4"	11°55'12.0"	13.2	completed
R1	Sweden	Onsala SW	57°23'34.8"	11°55'08.4"	13.2	completed
R2	Brazil	Fortaleza			project	–
R2	USA	GGAO	39°01'19.2"	-76°49'37.2"	12.0	
R2	USA	Kokee	22°07'33.6"	-159°39'54.0"	12.0	
R2	USA	McDonald	30°40'48.0"	-104°01'26.4"	12.0	
R2	USA	Westford	42°36'46.8"	-71°29'38.4"	12.0	
R3	Australia	Hobart	-42°48'21.6"	147°26'16.8"	12.0	
R3	Australia	Katherine	-14°22'30.0"	132°09'07.2"	12.0	
R3	Australia	Yarragadee	-29°02'49.2"	115°20'45.6"	12.0	
R3	China	Seshan13	31°05'56.4"	121°11'56.4"	13.0	
R3	China	Tianma13	31°05'27.6"	121°08'13.2"	13.0	
R3	China	Urumqi13	43°28'16.0"	87°10'40.0"	13.2	
R3	Japan	Ishioka	36°06'10.8"	140°05'20.4"	13.2	
R3	Thailand	Chiang Mai	18°51'56.0"	99°13'03.4"	project	–

3 Protection by Regulation

How does the ITU-R regulate the spectrum? The Master File contains all spectral bands and lists the allocated services to a given band, defined by a start and a stop frequency, e.g. 4990-5000 MHz. The RR distinguishes two categories and restrictions to the spectral bands by footnotes.

- **PRIMARY allocations** give legal protection from interference, but they are not necessarily exclusive if more than one service shares the same primary allocation. Services allocated to a band are written in capital letters.

- **Secondary allocations** do not provide protection from primary users in the same band. Secondary users shall not cause interference to primary users of that band, nor can they claim protection against detrimental interference from primary users of that band.
- **Footnotes** regulate special attention to specific bands used e.g. by RAS. Two footnotes are of major importance to RAS:
  - **Footnote 5.149** urges administrations to take all practical steps to protect RAS from harmful interference. It notes that emissions from spaceborne and airborne stations can be particularly serious sources of interference to RAS.
  - **Footnote 5.340** lists frequency bands in which *'all emissions are prohibited'*. This gives the maximum protection for the passive RAS.

The current RAS-spectra in the 2-14 GHz VGOS range are shown in Table 2. It can be seen in the table, that the entire RAS spectrum covers only 220.9 MHz, whereas VGOS observes in 32 bands of 32 MHz bandwidth each, resulting in a demand of a total 1024 MHz bandwidth. The allocated bandwidth for RAS is insufficient and its distribution is not optimized for geodetic VLBI. However, when arguing for more spectrum to be protected for VGOS some of the RAS-bands could be covered in order to have a stronger argument.

At this point, where the actual RAS spectrum is insufficient, one might ask, whether geodetic VLBI might fit better to other services which might own more spectrum. The answer is that most services are active and when using the targeted VGOS spectrum of 2-14 GHz interfering to the observation. The RR Article 1 Nos. 13 and 58 defines *radio astronomy* and *radio astronomy service* as being astronomy based on the **reception of cosmic radio waves**. Geodetic VLBI receives cosmic radio waves. Therefore, geodetic VLBI might trigger more spectrum to be made available to RAS at the VGOS sites. The advantage to treat geodetic VLBI as RAS is that the ITU-R Recommendation RA.769 on the *'Protection criteria used for radio astronomical measurements'* which contains the protection levels also for VLBI measurements apply and can be used immediately (instead of pushing something similar for geodetic VLBI through the World Radio Conference cycle).

4 How to achieve protection?

The European Committee on Radio Astronomy Frequencies (CRAF) has been tasked with RAS spectrum management in Europe resp. ITU-Region 1. A VGOS-Working Group has formed in which strategies and actions are being discussed. In 2020 this group started an initiative to raise *'Questions on VGOS'* within the Working Party 7D (Radio Astronomy) of the ITU-R. These questions had been supported by the following countries: Finland, France, Germany, Norway, Spain, Switzerland; and CRAF as an European entity. Recently, this document had been accepted by the representatives in WP7D and

1. What are the technical and operational characteristics of geodetic VLBI?
2. How does geodetic VLBI use radio spectrum to achieve the accuracy needed to fulfil its mission?

needs to be approved by the Study Group 7 (Science). If agreed, a study on these question will be drafted and may result in a Report or a Recommendation, which shall be finished within 2021/22. If of particular importance, the subject might enter as an Agenda Item (AI) to the World Radio Conference 2027. The US-delegation at WP7D provided a *'Working document towards a preliminary draft new Report ond Geodetic VLBI'* which is a base for the answers to the questions. Input to answer these questions is welcome!

5 Difficulties of Spectrum Management for VGOS

The task of spectrum management for RAS is not easy. If successful, nobody will recognize that RFI is missing! In addition to that, it is a permanent task because the modern world is wireless and spectrum is a limited resource. To satisfy the demand, models of bandwidth sharing in time and in space are already in practice. Just as the telecommunication industry increases its demands for a better service, the geodetic VLBI also requires more bandwidth to provide the accuracy required for geodetic tasks.

Several difficulties have been encountered with spectrum management for the VGOS:

Table 2 RAS Spectra in the VGOS-spectrum range of 2-14 GHz. The demand for bandwidth VGOS is about 5-times higher than what is allocated to RAS.

Frequency band	Bandwidth	Allocated	Footnotes
2655-2670 MHz	25 MHz	secondary	5.149, 5.208B
2670-2690 MHz	20 MHz	secondary	5.149, 5.208B
2690-2700 MHz	10 MHz	PRIMARY	5.340, 5.413, 5.208B
3260-3267 MHz	7 MHz		5.149
3332-3339 MHz	7 MHz		5.149
3345.8-3352.5 MHz	6.7 MHz		5.149
4825-4835 MHz	10 MHz	secondary	5.149
4990-5000 MHz	10 MHz	PRIMARY	5.149, 5.402, 5.443B
6650-6675.2 MHz	25.2 MHz		5.149, 5.458A
10600-10680 MHz	80 MHz	PRIMARY	
10680-10700 MHz	20 MHz	PRIMARY	5.340
Σ= 220.9 MHz			
VGOS is using 32-times 32 MHz bandwidth/channel, Σ= 1024 MHz.			

- The increased bandwidth of VGOS shall lead to the global 1 mm accuracy in the global geodetic reference frame. The first VGOS observations demonstrate its potential. However, the observed VGOS frequency bands are not yet fixed, but kept flexible. For spectrum management it will be essential that sooner rather than later the different configurations of the system are fixed. Each 32MHz channel has a start and stop frequency, which is the base for the RR. We might argue for footnotes for each 32 MHz subband at globally distributed VGOS sites. But then they should be fixed, not flexible.
- VGOS does not make use of the allocated RAS spectrum, but it is asking for more bands.
- If regulation provided a coordination zone around an observatory site for a given spectral band, then the spectral band must be used by the observatory.
- Existing VGOS infrastructure cannot be moved to more radio quiet zones (e.g. ALMA, SKA). For new VGOS stations it might be an option, however a certain infrastructure is necessary to comply with the timeliness of processing the results and finding experts to run the observatory.
- Commercialization of space will probably have an impact on VGOS through new missions (Starlink, OneWeb, SAR).
- Geodetic VLBI for Earth monitoring as a RAS method is widely unknown and in the spectrum world should not be confused with methods used by Earth Exploring Satellite Service (EESS).
- The lack of professional spectrum management for VGOS compared to companies who present their issues using dedicated staff (engineers and lawyers).

6 Conclusion

During the decade 2020-2030 the electro-magnetic spectrum will be exploited in a way, which was difficult to foresee when the first ideas of VGOS had been discussed and at a time when the smartphone was not yet invented. In addition to the widespread wireless communication, the commercialization of space will lead to thousands of transmitting satellites in the sky. Geodetic VLBI needs access to the cold sky to catch the cosmic rays from far and faint radio sources. The perspective of loosing observable spectrum for geodetic VLBI demands action.

The VGOS radio telescope stations should all be registered at ITU-R with their receiver capabilities, so that potential interferers could know in advance where the VGOS sites are.

Geodetic VLBI is essential to the Global Geodetic Reference Frame and is covered by UN-General Assembly Resolution 69/266. The consequence of the resolution has to be reflected in the spectrum management. The first steps are undertaken with Questions to ITU-R. The geodetic community has to focus on this issue in order to enable geodetic VLBI also in the future.

References

CRAF-Handbook for Radio Astronomy, 2005
`https://craf.eu/wp-content/uploads/2015/02/CRAFhandbook3.pdf`

On the Impact of the Coordinate Representation onto the Estimates in Least-Squares Adjustment

M. Lösler, C. Eschelbach, C. Holst

Abstract In geodesy and metrology several coordinate representations are known. The most important representations are polar coordinates and Cartesian coordinates. The coordinate representations are rigorously convertible into each other. Such functional relations are well-known as the direct (first) and the inverse (second) geodetic problem. Instruments like e. g. total station, laser scanner, or laser tracker are polar measurement systems. It is common practise especially in surface analysis, e. g. deformation analysis of the VLBI main reflector, to initially convert the obtained polar coordinates into their Cartesian representations. Instead of the polar measurements, the converted Cartesian coordinates are introduced to the least-squares adjustment. In this investigation, the impact of the chosen coordinate representation onto the estimates is studied. It is shown that the adequate transformation of the functional model and the stochastic model of the least-squares adjustment is not sufficient to obtain identical estimates.

Keywords Paraboloid, Least-Squares Adjustment, Sequential Quadratic Programming, Surface Analysis, Cartesian Coordinates, Polar Coordinates, GeoMetre

---

Michael Lösler · Cornelia Eschelbach
Frankfurt University of Applied Sciences, Faculty 1: Architecture – Civil engineering – Geomatics, Laboratory for Industrial Metrology, Nibelungenplatz 1, 60318 Frankfurt am Main, Germany (michael.loesler@fb1.fra-uas.de, cornelia.eschelbach@fb1.fra-uas.de)

Christoph Holst
Technical University of Munich, Chair of Geodesy, Department of Aerospace and Geodesy, Arcisstr. 21, 80333 Munich, Germany (christoph.holst@tum.de)

1 Introduction

In geodesy and metrology different coordinate representations are in use, like e. g. polar or Cartesian coordinates. These representations are rigorously convertible into each other, known as the direct (first) and the inverse (second) geodetic problem. In most metrology applications, one has to deal with two coordinate representations, i. e., the representation of the observation space and the representation of the parameter space. Whereas the first one is related to the raw observations obtained by the measurement instrument, the second one relates to the target coordinate system of the parameters to be estimated.

For instance, a total station used for reference point determination at VLBI radio telescopes is a polar measurement instrument (e. g. Lösler et al., 2013; Kallio et al., 2016). The polar observations spans the observation space. However, the estimated coordinates of the reference point are usually related to a Cartesian coordinate system. Obviously, the coordinate representation of the observation space differs from the coordinate representation of the parameter space.

A further example comes from surface analysis, e. g., measuring the main reflector of a VLBI radio telescope (e. g. Sarti et al., 2009; Holst et al., 2017). If a laser scanner is used, the observation space is spanned by a polar system, because the physical measurement principle of the instrument provides the slope distance, the azimuth angle, and the zenith angle of an observed position. The parameters to be estimated, e. g. the focal length and the position of the apex, are usually specified in a Cartesian coordinate system. Again, the representations of both spaces differ from each other.

Since rigorous conversions exist to interchange between coordinate representations, such conversions can take place in the observation space but also in the parameter space. In several metrology applications, it is common practise to initially convert the obtained polar coordinates into their Cartesian representations (cf. Holst et al., 2012; Lösler et al., 2016). Thus, the polar representation of the observation space is converted to its Cartesian representation, including the coordinates of the observed positions as well as the related measurement uncertainties. The later one is usually converted by applying the propagation of uncertainty.

In a least-squares adjustment, the functional model connects the observation space and the parameter space. For that reason, the functional model has to be specified depending on the chosen coordinate representations of both spaces. The parameters to be estimated are derived by minimising the weighted squared observational residuals, and, thus, the objective function *may* depend on the chosen coordinate representation of the observations.

In this contribution, the impact of the chosen coordinate representation of the observation space onto the estimates is studied. The assumption whether the estimates remain unaffected by interchanging the coordinate representation is investigated, exemplified at the best-fit paraboloid. Moreover, the impact of the point distribution onto the estimates is studied.

Section 2 introduces the Sequential Quadratic Programming (SQP) as an universal solving approach, which is recommended for nonlinear constraint optimisation problems. Section 3 deals with the least-squares adjustment of a paraboloid. The functional model, the stochastic model, and the objective function are derived for polar observations and Cartesian coordinates, respectively. Based on synthetically generated data, the impact of the coordinate representation is studied in detail by means of Monte-Carlo simulations. Finally, Sect. 4 concludes our investigations.

2 Sequential Quadratic Programming

The Sequential Quadratic Programming (SQP) is a common solving approach in numerical optimisation. The SQP is recommended for optimisation problems with nonlinear constraint functions (Nocedal and Wright, 2006, p. 530f), i. e.,

$$\min \Omega\left(\mathbf{u}\right) \tag{1a}$$

subject to

$$f\left(\mathbf{u}\right) = \mathbf{0}. \tag{1b}$$

The Lagrangian function $\mathscr{L} = \frac{1}{2}\Omega + \lambda^{\mathrm{T}} f$ is introduced to combine the objective function Ω and the constraint functions f. The unknown parameters $\mathbf{u}$ are estimated iteratively by solving a sequence of quadratic programming subproblems. The optimization problem of the k-th iteration step reads (Lösler, 2021, p. 42)

$$\min \frac{1}{2}\nabla\Omega_k^{\mathrm{T}}\Delta\mathbf{u} + \frac{1}{2}\Delta\mathbf{u}^{\mathrm{T}}\nabla^2_{\mathbf{uu}}\mathscr{L}_k\Delta\mathbf{u} \tag{2a}$$

subject to the linear approximation of the constraint functions

$$\mathbf{J}_k\Delta\mathbf{u} + f_k = \mathbf{0}, \tag{2b}$$

where

$$\nabla^2_{\mathbf{uu}}\mathscr{L} = \frac{1}{2}\nabla^2\Omega + \sum_{i=1}\lambda^{(i)}\mathbf{H}^{(i)}$$

denotes the Hessian of the Lagrangian function, and λ are the Lagrange multipliers. Matrices $\mathbf{J}$ and $\mathbf{H}$ are the Jacobian and the Hessian of the constraint functions, respectively. $\nabla\Omega$ and $\nabla^2\Omega$ denote the gradient and the Hessian of the objective function, respectively. The new iterates $\hat{\mathbf{u}} = \mathbf{u}_k + \Delta\mathbf{u}$ are obtained by solving the quadratic programming subproblem given by Eqs. (2), i. e.,

$$\begin{bmatrix} \nabla^2_{\mathbf{uu}}\mathscr{L} & \mathbf{J}^{\mathrm{T}} \\ \mathbf{J} & \mathbf{0} \end{bmatrix} \begin{bmatrix} \Delta\mathbf{u} \\ \hat{\lambda} \end{bmatrix} = - \begin{bmatrix} \frac{1}{2}\nabla\Omega \\ f \end{bmatrix}. \tag{3}$$

As shown by Lösler (2021, p. 45ff) the models frequently used in geodetic sciences, i. e., the model of conditional adjustment, the Gauß-Helmert model, or the Gauß-Markov model, are quadratic programs, which can be interpreted as special cases of the SQP.

3 Best-fit paraboloid

To study the impact of the chosen coordinate representation of the observations onto the estimates, a rotational symmetric paraboloid is adjusted using polar coordinates as well as corresponding Cartesian coordinates.

3.1 Functional model

The functional model describes the relation between the observations space and the parameter space. To keep our investigation as simple as possible, but without loosing of generally, we restrict ourselves to the canonical form of a paraboloid given by

$$a\left\{u_i^2+v_i^2\right\}-w_i=0. \tag{4}$$

The apex and the principal axis of the paraboloid correspond to the origin and the w-axis of the frame, respectively. The Parameter a is a scale parameter that defines the opening of the paraboloid, and the coordinates $\begin{pmatrix} u & v & w \end{pmatrix}_i^{\mathrm{T}}$ refer to an arbitrary position lying on the surface. The commonly used focal length reads

$$F(a)=\frac{1}{4a}. \tag{5}$$

Substituting

$$u_i=x_i-e_{x_i} \tag{6a}$$
$$v_i=y_i-e_{y_i} \tag{6b}$$
$$w_i=z_i-e_{z_i}, \tag{6c}$$

into Eq. (4) yields the constraint function in Eq. (1b) having Cartesian observations $\begin{pmatrix} x & y & z \end{pmatrix}_i^{\mathrm{T}}$ and corresponding residuals $\begin{pmatrix} e_x & e_y & e_z \end{pmatrix}_i^{\mathrm{T}}$. If Cartesian coordinates are used as observations, the vector of unknown parameters reads [1]

$$\mathbf{u}_{\mathrm{c}}^{\mathrm{T}}=\begin{bmatrix} a_{\mathrm{c}} & \mathbf{e}_{\mathrm{c}}^{\mathrm{T}} \end{bmatrix}=\begin{bmatrix} a_{\mathrm{c}} & e_{x_1} & \ldots & e_{x_i} & e_{y_i} & e_{z_i} & \ldots & e_{z_n} \end{bmatrix}. \tag{7}$$

Analogously, one found the constraint function in Eq. (1b) having polar observations $\begin{pmatrix} s & \phi & \zeta \end{pmatrix}_i^{\mathrm{T}}$ and corresponding residuals $\begin{pmatrix} e_s & e_\phi & e_\zeta \end{pmatrix}_i^{\mathrm{T}}$ by setting

$$u_i=(s_i-e_{s_i})\sin(\zeta_i-e_{\zeta_i})\cos(\phi_i-e_{\phi_i}) \tag{8a}$$
$$v_i=(s_i-e_{s_i})\sin(\zeta_i-e_{\zeta_i})\sin(\phi_i-e_{\phi_i}) \tag{8b}$$
$$w_i=(s_i-e_{s_i})\cos(\zeta_i-e_{\zeta_i}), \tag{8c}$$

where s, ϕ, and ζ are the slope distance, the azimuth angle, and the zenith angle of the i-th position, respectively. If polar observations are used, the vector of unknown parameters reads

$$\mathbf{u}_{\mathrm{p}}^{\mathrm{T}}=\begin{bmatrix} a_{\mathrm{p}} & \mathbf{e}_{\mathrm{p}}^{\mathrm{T}} \end{bmatrix}=\begin{bmatrix} a_{\mathrm{p}} & e_{s_1} & \ldots & e_{s_i} & e_{\phi_i} & e_{\zeta_i} & \ldots & e_{\zeta_n} \end{bmatrix}. \tag{9}$$

Obviously, the functional model of Eq. (4) can rigorously be expressed for Cartesian coordinates as well as for polar coordinates.

3.2 Stochastic model

The stochastic model characterises the dispersion of observations by a positive-definite dispersion matrix Σ. If the coordinate representation is changed within the observation space, the stochastic model has to be adapted, using, for instance, the propagation of uncertainty or any other *invertible* method.

Let Σ_{p} be the dispersion of polar observations, and $\mathbf{F}$ be the coefficient matrix that describes the linearized conversion between polar and Cartesian coordinates, the dispersion of the converted Cartesian observations is obtained by

$$\Sigma_{\mathrm{c}}=\mathbf{F}\Sigma_{\mathrm{p}}\mathbf{F}^{\mathrm{T}}. \tag{10a}$$

Since $\mathbf{F}^{-1}$ exists, the backward conversion reads

$$\Sigma_{\mathrm{p}}=\mathbf{F}^{-1}\Sigma_{\mathrm{c}}(\mathbf{F}^{-1})^{\mathrm{T}}. \tag{10b}$$

Even if Σ is a sparse matrix, for instance, the diagonal variance matrix of the polar observations, i. e.

$$\Sigma_{\mathrm{p},i}=\operatorname{diag}\begin{pmatrix} \sigma_s^2 & \sigma_\phi^2 & \sigma_\zeta^2 \end{pmatrix}_i, \tag{11a}$$

the converted dispersion matrix of the i-th Cartesian point is usually fully populated, and Σ_{c} becomes a block diagonal structure,

$$\Sigma_{\mathrm{c}}=\operatorname{blkdiag}\begin{pmatrix} \Sigma_{\mathrm{c},1} & \ldots & \Sigma_{\mathrm{c},i} & \ldots & \Sigma_{\mathrm{c},n} \end{pmatrix}. \tag{11b}$$

Having Eqs. (10), a proper method is available to interchange between the dispersion of the coordinate representation of the observations, which is treated as stochastic model.

3.3 Objective function

The objective function is the function that has to be minimised, subjected to the constraint functions. It pro-

---

[1] A subscript c and p denote the Cartesian and polar observation space, respectively.

vides a global measure of quality of the estimates, because the function increases if the estimates are inadequate. In sense of a least-squares adjustment, the well-known objective function in Eq. (1a) reads

$$\Omega = \mathbf{u}^{\mathrm{T}}\mathbf{W}\mathbf{u} = \mathbf{e}^{\mathrm{T}}\Sigma^{-1}\mathbf{e} \tag{12}$$

where the vector of parameters to be estimated $\mathbf{u}^{\mathrm{T}} = \begin{bmatrix}\mathbf{x}^{\mathrm{T}} & \mathbf{e}^{\mathrm{T}}\end{bmatrix}$ is separated into the model parameters $\mathbf{x}$ and the observational residuals $\mathbf{e}$, Σ is the known positive-definite dispersion matrix of the residuals $\mathbf{e} \sim N(\mathbf{0}, \Sigma)$, and

$$\mathbf{W} = \begin{bmatrix}\mathbf{0} & \mathbf{0}\\ \mathbf{0} & \Sigma^{-1}\end{bmatrix}.$$

Obviously, the SQP does not differ between $\mathbf{e}$ and $\mathbf{x}$. Both are treated as unknowns within the optimisation, and are explicitly estimated (Lösler and Eschelbach, 2020).

The objective function using polar coordinates reads

$$\Omega_{\mathrm{p}} = \mathbf{e}_{\mathrm{p}}^{\mathrm{T}}\Sigma_{\mathrm{p}}^{-1}\mathbf{e}_{\mathrm{p}}, \tag{13}$$

and the commonly used objective function using Cartesian coordinates is given by

$$\Omega_{\mathrm{c}} = \mathbf{e}_{\mathrm{c}}^{\mathrm{T}}\Sigma_{\mathrm{c}}^{-1}\mathbf{e}_{\mathrm{c}}. \tag{14}$$

As shown by Eqs. (10), the stochastic models are interchangeable. However, equating Eq. (7) with Eq. (9) yields $\mathbf{e}_{\mathrm{c}} = \varepsilon(\bar{\mathbf{e}}_{\mathrm{p}})$ as the nonlinear function of the polar coordinates (Lösler, 2020), i. e.,

$$\begin{aligned}
e_{x_i} &= s_i \sin\zeta_i \cos\phi_i \qquad\qquad \text{(15a)}\\
&\quad - (s_i - \bar{e}_{s_i})\sin(\zeta_i - \bar{e}_{\zeta_i})\cos(\phi_i - \bar{e}_{\phi_i})\\
e_{y_i} &= s_i \sin\zeta_i \sin\phi_i \qquad\qquad \text{(15b)}\\
&\quad - (s_i - \bar{e}_{s_i})\sin(\zeta_i - \bar{e}_{\zeta_i})\sin(\phi_i - \bar{e}_{\phi_i})\\
e_{z_i} &= s_i \cos\zeta_i - (s_i - \bar{e}_{s_i})\cos(\zeta_i - \bar{e}_{\zeta_i}). \qquad \text{(15c)}
\end{aligned}$$

Inserting Eq. (15) into Eq. (14) yields the Cartesian objective function rigorously expressed by polar coordinates, i. e.,

$$\bar{\Omega}_{\mathrm{p}} = \varepsilon(\bar{\mathbf{e}}_{\mathrm{p}})^{\mathrm{T}}\Sigma_{\mathrm{c}}^{-1}\varepsilon(\bar{\mathbf{e}}_{\mathrm{p}}). \tag{16}$$

Figure 1 depicts the condition that must hold for polar residuals and Cartesian residuals, if both representations refer to the identical optimization problem.

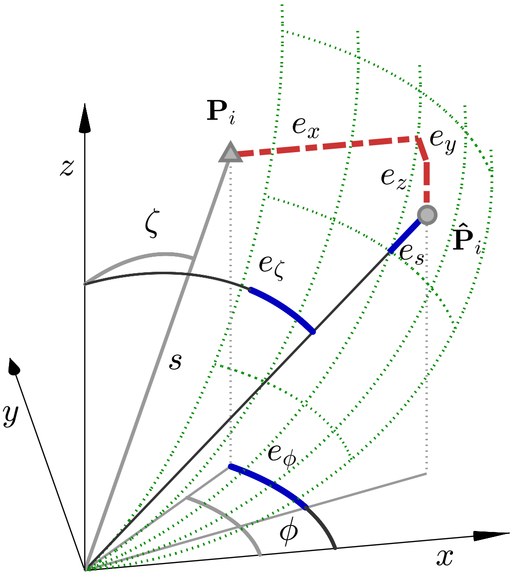

Fig. 1 Condition between polar residuals (blue) and Cartesian residuals (red), if both coordinate representations parametrize the identical optimization problem. $\mathbf{P}$ is the observed position and $\hat{\mathbf{P}}$ is the adjusted position, lying on the estimated surface of the paraboloid (green).

Applying the equation of the inverse geodetic problem yields $\mathbf{e}_{\mathrm{p}} = \varepsilon^{-1}(\bar{\mathbf{e}}_{\mathrm{c}})$ as the nonlinear function of the Cartesian coordinates (Lösler, 2020), i. e.,

$$\begin{aligned}
e_{s_i} &= \sqrt{x_i^2 + y_i^2 + z_i^2} \qquad\qquad \text{(17a)}\\
&\quad - \sqrt{(x_i - \bar{e}_{x_i})^2 + (y_i - \bar{e}_{y_i})^2 + (z_i - \bar{e}_{z_i})^2}\\
e_{\phi_i} &= \arctan\frac{y_i}{x_i} - \arctan\frac{y_i - \bar{e}_{y_i}}{x_i - \bar{e}_{x_i}} \qquad \text{(17b)}\\
e_{\zeta_i} &= \arctan\frac{\sqrt{x_i^2 + y_i^2}}{z_i} \qquad\qquad \text{(17c)}\\
&\quad - \arctan\frac{\sqrt{(x_i - \bar{e}_{x_i})^2 + (y_i - \bar{e}_{y_i})^2}}{(z_i - \bar{e}_{z_i})}.
\end{aligned}$$

The polar objective function rigorously expressed by Cartesian coordinates follows from Eqs. (13), (17), i. e.,

$$\bar{\Omega}_{\mathrm{c}} = \varepsilon^{-1}(\bar{\mathbf{e}}_{\mathrm{c}})^{\mathrm{T}}\Sigma_{\mathrm{p}}^{-1}\varepsilon^{-1}(\bar{\mathbf{e}}_{\mathrm{c}}). \tag{18}$$

In general, the following inequality holds

$$\Omega_{\mathrm{p}} = \bar{\Omega}_{\mathrm{c}} \neq \Omega_{\mathrm{c}} = \bar{\Omega}_{\mathrm{p}}, \tag{19}$$

and the results differ (Lösler and Eschelbach, 2020).

3.4 Example

To demonstrate the impact of the objective function, $n = 60$ points are simulated from Eq. (4), perfectly lying on the surface of the paraboloid. The surface parameter is set to $\tilde{a} = \frac{1}{4}$. The circular distribution of the points is depicted in Fig. 2.

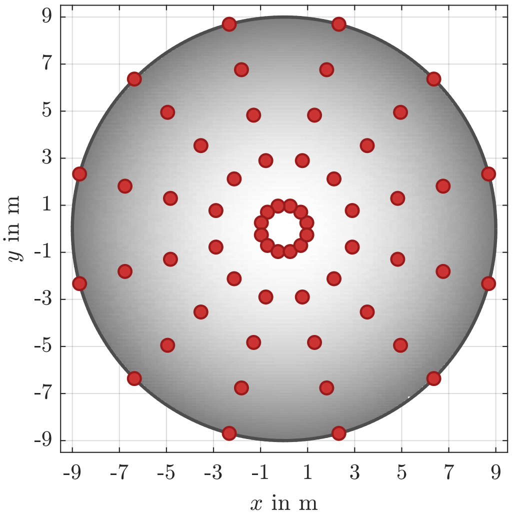

Fig. 2 Topview of the circular distribution of the $n = 60$ simulated points (red dots) lying on the surface of the paraboloid.

Let the measurement instrument be a polar instrument having specified uncertainties $\sigma_s = 5\,\text{mm}$, $\sigma_\phi = \sigma_\zeta = 5\,\text{mgon}$, forming the stochastic model via Eq. (11a). The instrument is located in the origin. Such a configuration is already used for surface analyses of VLBI radio telescopes (e. g. Sarti et al., 2009; Bleiders, 2020). The coordinate components of the n points are noised by normally distributed measurement errors $\nabla \sim N(\mathbf{0}, \sigma_0 \mathbf{I})$, where $\mathbf{I}$ is the identity matrix. It should be noted, ∇ cumulates random measurement errors of the instrument but also unknown systematic errors caused by surface deviations (cf. Holst et al., 2015; Lösler et al., 2018).

Polar and Cartesian coordinate components are derived referring to identical point positions. The dispersion of the Cartesian coordinates is obtained by Eq. (10a), and yields a block diagonal matrix, cf. Eq. (11b). Best-fit paraboloids are adjusted treating the $n = 60$ polar and Cartesian coordinates as observations, respectively, as well as the corresponding stochastic model. Four different objective functions are used given by Eqs. (13), (14), (16), (18).

Table 1 summarizes the obtained results of a single random experiment, which confirm the inequality given by Eq. (19). The estimates are only identical, if the objective functions are referred to the same optimization problem. This condition is fulfilled for $\Omega_\text{p} = \bar{\Omega}_\text{c}$ and $\Omega_\text{c} = \bar{\Omega}_\text{p}$ yielding $\hat{F}_\text{p} = \hat{\hat{F}}_\text{c}$ and $\hat{F}_\text{c} = \hat{\hat{F}}_\text{p}$, respectively.

Table 1 Comparison of estimated focal lengths F using polar and Cartesian coordinates as observations, and four different objective functions. The randomly drawn measurement errors ∇ corresponds to $\sigma_0 = 10\,\text{cm}$. For demonstration purpose, an increased number of digits is chosen. Results are given in m.

$\hat{F}_\text{p}$	$\hat{\hat{F}}_\text{c}$	$\hat{F}_\text{c}$	$\hat{\hat{F}}_\text{p}$
0.998 323	0.998 323	0.997 973	0.997 973

Certainly, the reason for the differences in F comes from the used objective functions, which describe different optimization problems. The size of the differences, however, depends on the size of the measurement errors ∇. To demonstrate these dependencies between $\hat{F}_\text{c} - \hat{F}_\text{p}$ and the size of the introduced measurement errors $\nabla \sim N(\mathbf{0}, \sigma_0 \mathbf{I})$, a Monte-Carlo simulation is performed using $m = 20\,000$ samples. Within the simulation, the range of σ_0 is set from 0 cm to 10 cm, using a step size of 1 cm.

Figure 3 depicts the obtained differences $\hat{F}_\text{c} - \hat{F}_\text{p}$ for various scaled measurement errors ∇. As expected, the differences increase as the measurement errors get large. However, the maximum difference does not exceed 0.5 % of the measurement error.

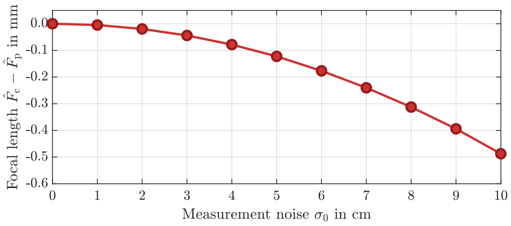

Fig. 3 Dependency between $\hat{F}_\text{c} - \hat{F}_\text{p}$ and the size of the measurement errors $\nabla \sim N(\mathbf{0}, \sigma_0 \mathbf{I})$ for circular distributed surface points.

Nothnagel et al. (2013) study the influence of the distribution of the points on the surface onto the estimates. The authors conclude that a prominent concentration of the points near the apex, also shown in Fig. 2, dominates the estimated focal length, and a uniform distribution is recommended (Holst et al., 2015). For that reason, the $n = 60$ points are rearranged in a regular rectangular grid, leading to the configuration depicted in Fig. 4.

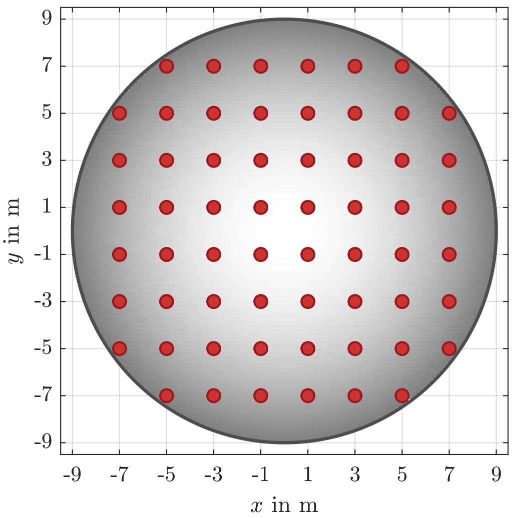

Fig. 4 Topview of the rectangular distribution of the $n = 60$ simulated points (red dots) lying on the surface of the paraboloid.

Measurement errors ∇ are added to the points, and polar and rigorous converted Cartesian coordinates are derived referring to identical point positions of the new configuration. Whereas the stochastic model of the polar observations in Eq. (11a) keeps unchanged, the stochastic model of the Cartesian coordinates is derived by Eq. (10a), and yields a block diagonal matrix, cf. Eq. (11b).

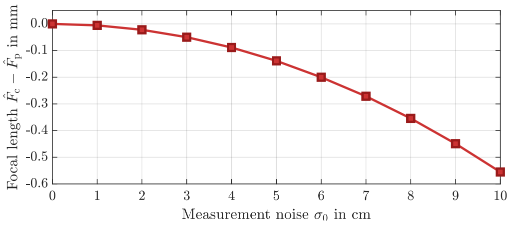

Fig. 5 Dependency between $\hat{F}_c - \hat{F}_p$ and the size of the measurement errors $\nabla \sim N(\mathbf{0}, \sigma_0 \mathbf{I})$ for rectangular distributed surface points.

Figure 5 depicts the dependencies between $\hat{F}_c - \hat{F}_p$ and the measurement errors $\nabla \sim N(\mathbf{0}, \sigma_0 \mathbf{I})$, obtained by a Monte-Carlo simulation, using $m = 20\,000$ samples. The range of σ_0 is set from 0 cm to 10 cm, using a step size of 1 cm. The curve indicates a similar behavior as already shown in Fig. 3. If the measurement errors get large, the differences also increase. Identical results are obtained if and only if $\nabla = \mathbf{0}$.

The chosen distribution of the observed positions on the surface has only a marginal effect onto the estimates. Even for $\sigma_0 = 10$ cm, the differences between the estimated focal lengths are <1 mm, as summarized in Table 2. The differences between the estimated focal lengths and the true value $F(\tilde{a}) = 1$ m result from the nonlinearity of the functional model (Lösler et al., 2020). The smallest bias is obtained for the rectangular distributed surface points and $\hat{F}_p$, and confirms the recommendation given by Holst et al. (2015).

Table 2 Estimated focal lengths $\hat{F}$ for circular and rectangular distributed surface points, respectively. Estimates are derived from polar observations as well as Cartesian coordinates, using Monte-Carlo simulations and varying measurement errors, indicated by σ_0. Focal lengths $\hat{F}$ are given in m, σ_0 is given in cm.

	Circular		Rectangular	
σ_0	$\hat{F}_c$	$\hat{F}_p$	$\hat{F}_c$	$\hat{F}_p$
0	1.0000	1.0000	1.0000	1.0000
1	1.0000	1.0000	1.0000	1.0000
2	0.9999	0.9999	0.9999	1.0000
3	0.9999	0.9999	0.9999	1.0000
4	0.9997	0.9998	0.9998	0.9999
5	0.9996	0.9997	0.9997	0.9998
6	0.9993	0.9995	0.9996	0.9998
7	0.9992	0.9994	0.9994	0.9997
8	0.9990	0.9993	0.9993	0.9996
9	0.9987	0.9991	0.9991	0.9996
10	0.9985	0.9989	0.9988	0.9994

The recommendation for the surface accuracy of a VGOS radio telescope is specified by <0.2 mm (Petrachenko et al., 2009, p. 24), and, thus, fifty-times smaller than the maximum simulated errors. The differences between the chosen objective functions, and the differences between the point distributions under consideration are on the same order of magnitude. If both, the deviations of the surface and the measurement uncertainties of the instrument, are small, all approaches yield comparable results.

4 Conclusion

The parameters of synthetically generated paraboloids were adjusted, using different coordinate representations. For this purpose, the functional model, the stochastic model, and the objective function were derived for polar observations and for rigorous converted Cartesian coordinates, respectively. The impact of the coordinate representation of the observation space onto the parameters to be estimated was studied in detail.

Using Sequential Quadratic Programming, it has been shown that the proper transformation of the functional and the stochastic model is not sufficient to obtain identical results, because also an adapted objective function is required to get corresponding estimates. Moreover, the impact of the point distribution onto the estimates was investigated by means of Monte-Carlo simulations. The focal lengths, obtained by a circular distribution, were compared to the focal lengths, derived by a rectangular distribution. Both, the realized configuration and the chosen objective function affect the parameters to be estimated. However, if the residuals are quite small, these differences are usually negligible.

Acknowledgements

This project 18SIB01 GeoMetre has received funding from the EMPIR programme co-financed by the Participating States and from the European Union's Horizon 2020 research and innovation programme.

References

Bleiders M (2020) Electromagnetic Model of Dual Reflector Radio Telescope based on Laser Scanning Survey. In: *2020 IEEE Microwave Theory and Techniques in Wireless Communications*, 217–221, Riga, Latvia. doi:10.1109/mttw51045.2020.9245071.

Holst C, Zeimetz P, Nothnagel A, Schauerte W, Kuhlmann H (2012) Estimation of Focal Length Variations of a 100-m Radio Telescope's Main Reflector by Laser Scanner Measurements. *J. Surv. Eng.*, 138(3):126–135. doi:10.1061/(asce)su.1943-5428.0000082.

Holst C, Nothnagel A, Blome M, Becker P, Eichborn M, Kuhlmann H (2015) Improved area-based deformation analysis of a radio telescope's main reflector based on terrestrial laser scanning. *J. Appl. Geod.*, 9(1):1–13. doi:10.1515/jag-2014-0018.

Holst C, Schunck D, Nothnagel A, Haas R, Wennerbäck L, Olofsson H, Hammargren R, Kuhlmann H (2017) Terrestrial Laser Scanner Two-Face Measurements for Analyzing the Elevation-Dependent Deformation of the Onsala Space Observatory 20-m Radio Telescope's Main Reflector in a Bundle Adjustment. *Sensors*, 17(8):1833. doi:10.3390/s17081833.

Kallio U, Lösler M, Bergstrand S, Haas R, Eschelbach C (2016) Automated simultaneous local ties with GNSS and robot tachymeter. In: Behrend D, Baver KD, Armstrong KL (eds), *Proceedings of the 9th IVS General Meeting 2016 – New Horizons with VGOS*, NASA/CP-2016-219016, 154–158.

Lösler M (2020) Zur Parameterschätzung mit unterschiedlichen Koordinatendarstellungen. *zfv*, 145(6):385–392. doi:10.12902/zfv-0319-2020.

Lösler M (2021) *Modellbildungen zur Signalweg- und in-situ Referenzpunktbestimmung von VLBI-Radioteleskopen*. Technische Universität Berlin, Institute of Geodesy and Geoinformation Science, Geodesy and Adjustment Theory. doi:10.14279/depositonce-11364.

Lösler M, Eschelbach C (2020) Orthogonale Regression — Realität oder Isotropie? *Tech. Mess.*, 87(10):637–646. doi:10.1515/teme-2020-0063.

Lösler M, Haas R, Eschelbach C (2013) Automated and continual determination of radio telescope reference points with sub-mm accuracy: results from a campaign at the Onsala Space Observatory. *J. Geod.*, 87(8):791–804. doi:10.1007/s00190-013-0647-y.

Lösler M, Haas R, Eschelbach C (2016) Terrestrial Monitoring of a Radio Telescope Reference Point Using Comprehensive Uncertainty Budgeting. *J. Geod.*, 90(5):467–486. doi:10.1007/s00190-016-0887-8.

Lösler M, Eschelbach C, Haas R (2018) Bestimmung von Messunsicherheiten mittels Bootstrapping in der Formanalyse. *zfv*, 143(4):224–232. doi:10.12902/zfv-0214-2018.

Lösler M, Lehmann R, Neitzel F, Eschelbach C (2020) Bias in Least-Squares Adjustment of Implicit Functional Models. *Surv. Rev.*, 1–12. doi:10.1080/00396265.2020.1715680.

Nocedal J, Wright SJ (2006) *Numerical Optimization*. Springer, New York, 2 ed. doi:10.1007/978-0-387-40065-5.

Nothnagel A, Eichborn M, Holst C (2013) Improved Focal Length Results of the Effelsberg 100 m Radio Telescope. In: Zubko N, Poutanen M (eds), *Proceedings of the 21th European VLBI for Geodesy and Astrometry (EVGA) Working Meeting*, 55–59. Reports of the Finnish Geodetic Institute. ISBN 978-951-711-296-3.

Petrachenko B, Niell A, Behrend D, Corey B, Böhm J, Charlot P, Collioud A, Gipson J, Haas R, Hobiger T, Koyama Y, MacMillan D, Malkin Z, Nilsson T, Pany A, Tuccari G, Whitney A, Wresnik J (2009) Design aspects of the VLBI2010 system. NASA/TM-2009-214180, Washington.

Sarti P, Vittuari L, Abbondanza C (2009) Laser Scanner and Terrestrial Surveying Applied to Gravitational Deformation Monitoring of Large VLBI Telescopes' Primary Reflector. *J. Surv. Eng.*, 135(4):136–148. doi:10.1061/(asce)su.1943-5428.0000008.

VLBI enhancement of the Bernese GNSS Software for multi-technique analysis at BKG

C. Flohrer, D. König, D. Thaller, C. Gattano, U. Meyer, R. Dach, U. Hugentobler

Abstract For many years the geodesy group at BKG (Federal Agency for Cartography and Geodesy) participates in IVS analyses and combination activities. It successfully operates an IVS analysis center and the IVS combination center. On the other hand, BKG also contributes to ILRS and IGS activities. It runs an ILRS analysis center and is partner of the CODE consortia, which runs the IGS analyses center CODE at the AIUB (Astronomical Institute of the University of Bern). AIUB is also the home of the Bernese GNSS Software, where it is developed and enhanced, continuously adapting to changing requirements and user needs. By this, the software is in use for global GNSS analysis at CODE since the beginning of the IGS, and it is used for global SLR analysis at BKG's ILRS analysis center since 2010. BKG has gained a long-standing experience in the analysis of the three geodetic techniques VLBI, SLR and GNSS. However, our focus is not only on the individual techniques but on the combination of the various observation techniques, in particular for the improvement of Earth rotation parameters. We would like to continue the multi-technique combined analysis using the Bernese GNSS Software and bring the efforts from earlier studies to operational implementations. We recently started an effort for the enhancement of the Bernese GNSS Software to enable also VLBI processing capabilities. Thus, we could use the Bernese GNSS Software for the processing of all three space-geodetic techniques in the near future. Eventually it will allow us to combine GNSS, VLBI and SLR data not only on SINEX level, but on the observation level.

Keywords Bernese GNSS Software, VLBI, EOP, combination at the observation level

1 Introduction

The geodesy group at BKG (Federal Agency for Cartography and Geodesy) is actively involved in the IVS since its establishment in 1999. We operate an IVS data center (Wojdziak and Thorandt, 2020), an IVS analysis center (Engelhardt et al., 2020), and an IVS combination center (Bachmann et al., 2020). In addition we are running an ILRS analysis center (König et al., 2020) for more than 20 years and being a partner of the CODE (Center for Orbit Determination in Europe) consortia since 1992.

The CODE consortia consists of the four institutions - Astronomical Institute of the University of Bern (AIUB) located in Switzerland, Federal Office of Topography swisstopo in Switzerland, Federal Agency of Cartography and Geodesy in Germany, and Institut für Astronomische und Physikalische Geodäsie at the Technical University of Munich (IAPG, TUM) in Germany. CODE participates as an IGS analysis center, which is actually operated by the AIUB in Bern (Villiger and Dach, 2019). AIUB is also the home of the Bernese GNSS Software (BSW). The

---

Claudia Flohrer[1], Daniel König[1], Daniela Thaller[1], César Gattano[2], Ulrich Meyer[2], Rolf Dach[2], Urs Hugentobler[3]

(1) Federal Agency for Cartography and Geodesy (BKG), Department Geodesy, Frankfurt am Main, Germany

(2) Astronomical Institute of the University of Bern, Bern, Switzerland

(3) Institute for Astronomical and Physical Geodesy, Technical University of Munich, Munich, Germany

Corresponding author: claudia.flohrer@bkg.bund.de

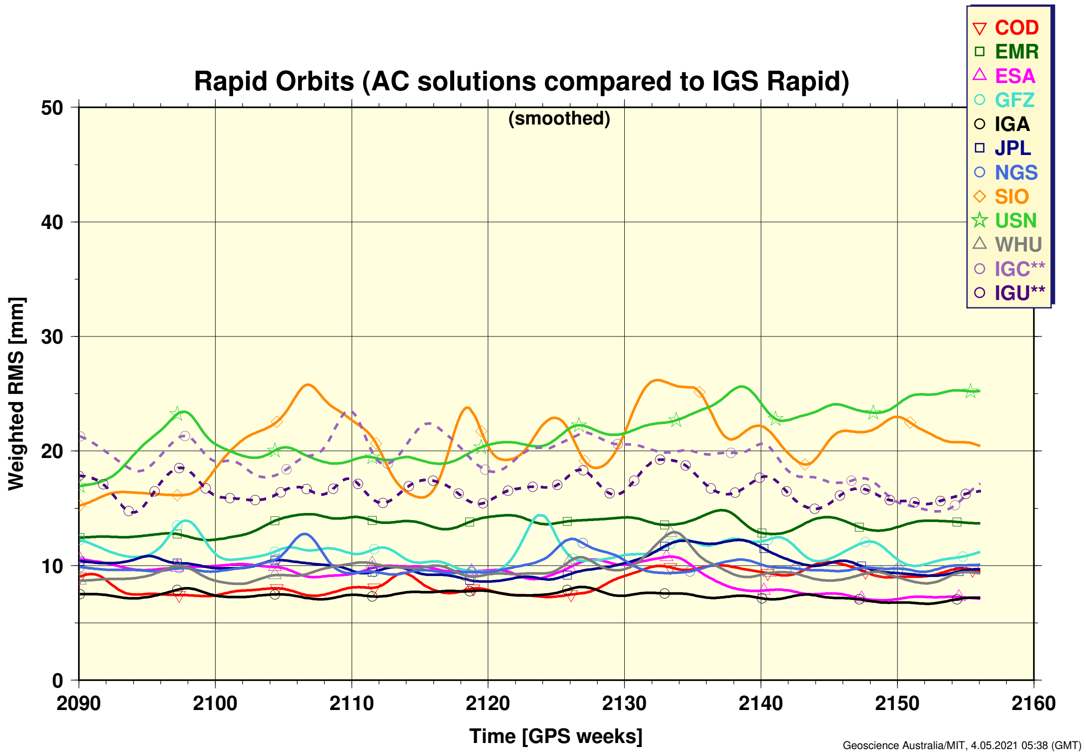

Fig. 1 Weighted RMS (mm) of the differences between the individual IGS AC rapid orbits and the combined IGS rapid orbit (picture taken from http://acc.igs.org/igsacc_rapid.html on May-04-2021).

BSW is used by CODE for its IGS analysis center activities since the very beginning of the IGS in 1994. It has an excellent reputation within the IGS scientific community as it delivers highly accurate products, which is demonstrated by IGS orbit comparisons provided at the IGS Analysis Center Coordinator web page (http://acc.igs.org). Taking the IGS rapid orbit products with a 24 hour latency as an example, CODE is consistent with the IGS combined solution at or even below the 1 cm level, see Figure 1.

Since 2010 BKG is also using the BSW for its ILRS analysis center activities. Figure 2 shows exemplarily the WRMS values of the coordinate differences between the individual ILRS analysis center solutions and the combined ILRS-A solution, demonstrating that the BKG solution (represented by the orange line) is well inline with the other analysis centers.

BKG has gained a long-standing experience in the analysis of the three geodetic techniques VLBI, SLR and GNSS. However, our focus is not only on the individual techniques but on the combination of the various observation techniques, in particular for the improvement of Earth rotation parameters. So far we use the BSW for SLR and GNSS combination studies only (Thaller, 2008). For the combination of VLBI and GNSS (Lengert et al., 2021) we use the DOGS-CS software package provided by DGFI-TUM (Gerstl et al., 2004). In order to enable the combination of all three techniques at the observation level within one single software package, we recently started an effort for the enhancement of the BSW for VLBI processing capabilities.

This paper presents the current software development activities for the VLBI enhancement of the BSW. We give a brief overview of the BSW, followed by a discussion of the different combination concepts. We present the current development status and address the challenges of the implementation. Finally, we give an outlook on BKG's combination activities with its focus on Earth rotation.

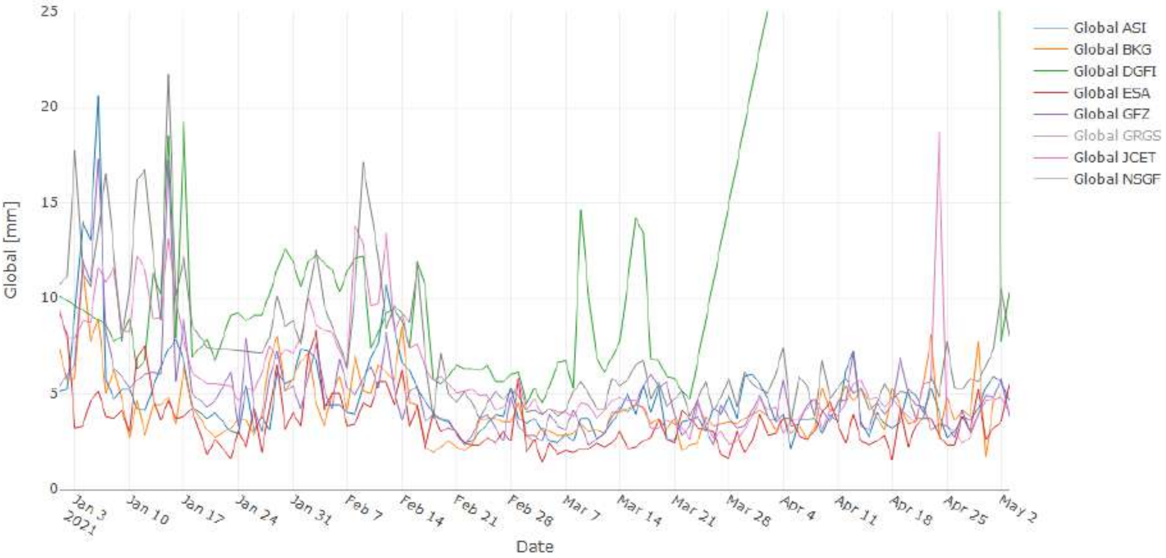

Fig. 2 Weighted RMS (in mm) of the coordinate differences between the individual ILRS AC solutions and the combined ILRS-A solution.

2 Bernese GNSS Software

The Bernese GNSS Software is a scientific, high-precision, multi-GNSS data processing software (Dach et al., 2015). It is developed and maintained at the AIUB in Switzerland. Currently the BSW is used by over 700 institutions from all over the world. As user requirements are changing all the time, the BSW is continuously adapted to respond to the user needs. Starting as a GPS-only processing software in 1998, it is today able to process the various GNSS as well as SLR observations. It is used for precise orbit determination (POD) of GNSS, SLR and Low Earth orbiting (LEO) satellites. The BSW allows for an automated processing of global permanent networks.

The processing is based on least-squares algorithm using normal equations. The BSW offers also the possibility to process normal equations from external sources (via SINEX files). It provides a full set of options to handle and manipulate normal equations, i.e. combination/stacking of normal equations, parameter transformation and pre-elimination, geodetic datum definition by minimum constraint network conditions. These features are of particular interest for our combination efforts, following, e.g., Thaller (2008).

3 Combination aspects

Global geodetic parameters, such as Earth Orientation Parameters (EOP), are derived from the combination of different space-geodetic techniques. The techniques complement each other using their individual strengths and sensitivity to Earth orientation. Satellite techniques are thus not able to determine the rotation of the Earth in an absolute sense, i.e. the parameter dUT1 cannot be separated from the motion of the orbital node of the satellite. As a consequence, VLBI is essential to determine the full set of EOPs.

Today we rely on the “Rapid Service/Prediction Centre” of the International Earth Rotation and Reference Systems Service (IERS), which provides the Bulletin A series, a rapid low-latency time series including predictions. This daily EOP product is based on the combination of individual space-geodetic technique solutions, generated by different analysis groups using different software packages dedicated to individual observation technique. Such a combination is a classical combination at the parameter level. Each parameter type is combined independently from other parameters. Thus, correlations between the different parameters are not considered. This approach represents the least rigorous combination method.

A more rigorous way for the combination of individual technique contributions is the combination at the normal equation level. Normal equations of each observation technique free of any constraints can be provided by different analysis groups using different software packages by using the SINEX format for exchanging the normal equations. These normal equations are stacked to one normal equation system before applying datum constraints and solving for all parameters. The resulting EOP are more consistent than those from the previous approach when combining on the parameter level, as the correlations between the parameters are considered and the very same underlying reference frame can be assured if station coordinates are combined along with the EOP. In fact, this approach offers the flexibility to change the geodetic datum definition, as this is applied after the normal equation stacking. Of course all parameter a priori values are transferred to the very same value for each combined parameter before stacking. Another benefit of the combination on normal equation level is the possibility for the combined parameters to impact other parameters. If, e.g., the stacked EOP would get improved through the combination process, there might also be a positive impact on satellite orbit parameters.

The most rigorous way of combination is the combination directly on observation level. All observations of the different space-geodetic techniques are processed in one single software package. This approach ensures the usage of the very same underlying models and the same parameterization. The observations can be screened for outliers based on the combination and a consistent observation weighting can be applied. All parameters are derived from the very same analysis taking into account all correlations. And all parameters are accessible, whereas in the normal equation approach entire parameter groups might be pre-eliminated to speed up the processing and save disk storage.

So far, no publicly available EOP time series is generated by using any of the last two approaches. As the combination on the observation level ensures the highest consistency for the EOP estimation we are going to enhance the BSW software package for VLBI, which will allow us to combine the GNSS, SLR and VLBI techniques on the observation level and to study the potential improvements w.r.t. the combination on parameter level.

4 Bernese GNSS Software enhancement for VLBI

BKG together with AIUB and TUM started an effort to enhance the Bernese GNSS Software also for VLBI processing. The implementation work is still on-going as several challenges had to be faced.

As the BSW is used by many external customers (mainly for GNSS processing) the existing software functionalities and performance requirements still have to be ensured. During the VLBI development phase there are other software developments for the GNSS and SLR techniques on-going in parallel. These parallel developments have to be aligned constantly. One major challenge are the necessary changes in the entire software design to cope with the requirements of a multi-technique and multi-frequency software package. Thus, a flexible space object structure was invented using modern Fortran programming techniques.

The current implementation status allows us to use the BSW for VLBI analysis based on a normal equation input (using SINEX files), see also Figure 3. The next step will enable also VLBI observation handling including the vgosDB format. The VLBI observation model is already implemented and successfully tested.

5 Outlook on BKG's combination activities

With the on-going VLBI developments we will be able to use the Bernese GNSS Software for the processing of all three space-geodetic techniques on the observation level within a time frame of about 2 years.

On a much shorter time scale (by the end of 2021) we are planning to set up an operational EOP product based on the combination of VLBI Intensives and

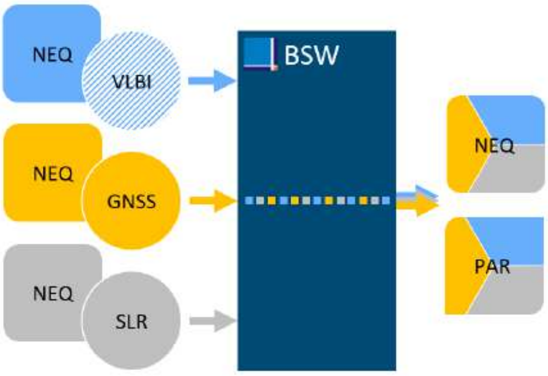

Fig. 3 Technique-specific BSW input and output overview. Input to the BSW are either normal equation files from all three techniques, or observation files from GNSS and SLR. VLBI observations are still to be implemented. After the combined analyses the BSW outputs normal equations and estimated parameters based on all techniques.

GNSS data using the DOGS-CS software package. This combination on the normal equation level was presented by Lengert et al. (2021) demonstrating the generation of a consistent, high-precision time series for polar motion and dUT1 with daily resolution and a very low latency. The combined processing shows a significant accuracy improvement for the dUT1 time series and a slight improvement for the pole coordinates time series, compared to the individual technique-specific parameters.

Furthermore we are extending the combination of GNSS and VLBI Intensives by adding VLBI 24-hour sessions. Beside the combination of EOP, we are also planning to use other common parameters for the combination of the techniques, as station coordinates, tropospheric parameters and satellite orbits through local ties, atmospheric ties and space ties.

References

Bachmann S, Bloßfeld M, Glomsda M, Thaller D (2020) BKG/DGFI-TUM Combination Center Biennial Report 2017+2018. In: International VLBI Service for Geodesy and Astrometry 2017+2018 Biennial Report, edited by Armstrong KL, Baver KD, Behrend D. *NASA/TP-2020-219041; NASA Goddard Space Flight Center, Greenbelt, MD, USA*, 189–193.

Dach R, Lutz S, Walser P, Fridez P (Eds) (2015) Bernese GNSS Software Version 5.2. *User manual, Astronomical Institute, University of Bern, Bern Open Publishing*, doi: 10.7892/boris.72297.

Engelhardt G, Thorandt V, Ullrich D, Girdiuk A, Halsig S, Iddink A, Jaron F, Karbon M, Nothnagel A (2020) BKG/IGGB VLBI Analysis Center. In: International VLBI Service for Geodesy and Astrometry 2017+2018 Biennial Report, edited by Armstrong KL, Baver KD, Behrend D. *NASA/TP-2020-219041; NASA Goddard Space Flight Center, Greenbelt, MD, USA*, 204–207.

Gerstl M, Kelm R, Müller H, Ehrnsperger W (2004) DOGS-CS: Kombination und Lösung großer Gleichungssysteme. *DGFI (Deutsches Geodätisches Forschungsinstitut) MG/01/1995/DGFI.*

König D, Thaller D, Grahs A, Meyer U (2020) ILRS Analysis Activities - BKG (Bundesamt für Kartographie und geodäsie), Germany. In: International Laser Ranging Service (ILRS) 2016-2019 Report, edited by Noll C, Pearlmann M. *NASA/TP-20205008530; NASA Goddard Space Flight Center, Greenbelt, MD, USA*, 7-6–7-9.

Lengert L, Flohrer C, Girdiuk A, Hellmers H, Thaller D (2021) Single- and Multi-day Combination of VLBI and GNSS Data for Consistent Estimation of Earth Rotation Parameters. *Proceedings of the 25th European VLBI for Geodesy and Astrometry Working Meeting*, March 14-18, 2021.

Thaller D (2008) Inter-technique combination based on homogeneous normal equation systems including station coordinates, Earth orientation and troposphere parameters. *Scientific Technical Report STR08/15; GFZ, Potsdam, Germany.*

Villiger A, Dach R (eds.) (2019) International GNSS Service Technical Report 2018 (IGS Annual Report). *IGS Central Bureau and University of Bern; Bern Open Publishing*, 31–46, doi: 10.7892/boris.130408.

Wojdziak R, Thorandt V (2020) BKG Data Center. In: International VLBI Service for Geodesy and Astrometry 2017+2018 Biennial Report, edited by Armstrong KL, Baver KD, Behrend D. *NASA/TP-2020-219041; NASA Goddard Space Flight Center, Greenbelt, MD, USA*, 165–166.

Combined IVS contribution to the ITRF2020

Hendrik Hellmers, Sadegh Modiri, Sabine Bachmann, Daniela Thaller, Mathis Bloßfeld, Manuela Seitz, John Gipson

Abstract The ITRF2020 will be the next official solution of the International Terrestrial Reference Frame and the successor of the currently used frame, i.e., ITRF2014. Based on an inter-technique combination of the four space geodetic techniques VLBI, GNSS, SLR, and DORIS, contributions from different international institutions lead to the global ITRF2020 solution. The IVS Combination Centre generates the final contribution of the International VLBI Service for Geodesy and Astrometry (IVS). Thereby, an intra-technique combination utilizing the individual contributions of multiple Analysis Centres is applied. For the contribution to the upcoming ITRF2020, sessions containing 24h VLBI observations from the last 40 years are processed by 11 Analysis Centres and submitted to the IVS Combination Centre. The required SINEX format enables a combination on the level of normal equations. This contribution gives an overview of the IVS combination procedure for ITRF2020 and shows the first results of the evaluation of estimated Earth Orientation Parameters and station coordinates.

Keywords ITRF2020, IVS Combination Centre, VLBI

Hendrik Hellmers · Sadegh Modiri · Sabine Bachmann · Daniela Thaller
Federal Agency for Cartography and Geodesy (BKG), Department Geodesy, Frankfurt am Main, Germany

Mathis Bloßfeld · Manuela Seitz
Deutsches Geodätisches Forschungsinstitut (DGFI-TUM), Technische Universität München, Munich, Germany

John Gipson
Planetary Geodynamics Laboratory, Goddard Space Flight Center, Greenbelt, Maryland, USA

1 Introduction

The International Terrestrial Reference Frame (ITRF) as the realization of the International Terrestrial Reference System (ITRS) is the official global reference frame. The ITRF includes positions and velocities of globally distributed geodetic observing stations. Applications using this product are manifold, e.g., for positioning and navigation as well as for scientific research concerning, e.g., climate change, global sea level rise or earthquakes (Métivier et al., 2014). A new ITRF solution is computed in different intervals, in recent years, about every five to six years. This is essential to ensure a high validity of the ITRF by considering new observation data, including new stations, providing high-precise station positions and velocities for stations affected by earthquakes and ensuring that the ITRF is based on up-to-date models. The ITRF is provided by the ITRS Centre of the International Earth Rotation and Reference System Service (IERS) and is based on the mathematical foundations, physical constants and models provided by the IERS 2010 Conventions (Petit and Luzum, 2010). The upcoming ITRF2020 is the successor of the ITRF2014 (Altamimi et al., 2016) and represents the next official realization of the ITRS. With considering different individual strengths in view of the determination of geodetic parameters, the ITRF is based on an inter-technique combination of four space-geodetic observation techniques (Thaller, 2008). The Global Navigation Satellite System (GNSS), the Satellite Laser Ranging (SLR), and the Doppler Orbitography and Radiopositioning Integrated by Satellite (DORIS) deliver the information to realize an Earth-centered, Earth-fixed reference system. As a complement, the Very Long Baseline Interferometry (VLBI) as the only technology observing extragalactic objects (radio sources), enables the determination of the orientation of the Earth in inertial space, and consequently delivers the full set of Earth Orientation Parameters (EOP).

The Combination Centre of the International VLBI Service for Geodesy and Astrometry (IVS) (Nothnagel et al., 2016) - operated by the Federal Agency for Cartography and Geodesy (BKG, Germany) in close cooperation with the Deutsches Geodätisches Forschungsinstitut (DGFI-TUM, Germany) – is responsible for the final VLBI contribution to the ITRF (Schlüter and Behrend, 2007). Thereby, an intra-technique combination utilizing the individual contributions of multiple Analysis Centres (AC) is realized on the level of normal equations (NEQs) (Vennebusch et al., 2007), (Böckmann et al., 2010). The DOGS-CS software is used for the IVS combination. The IVS contribution to the ITRF2014 is explained in Bachmann et al. (2016).

For the contribution to the upcoming ITRF2020, sessions containing 24h VLBI observations from 1979 until the end of 2020 are processed and submitted by 11 ACs. The required SINEX format[1] includes datum-free normal equations containing station coordinates and source positions as well as a full set of EOPs, including polar motion (-rates), dUT1, LOD and nutation parameters[2]. A linear transformation to equal epochs as well as to similar a priori values of the EOPs and the station coordinates ensures consistency of the individual contributions. The combined solution is based on a session-wise addition of the available NEQs, where EOPs and station coordinates are stacked. In the current state of the combination process for ITRF2020, the source coordinates are fixed to the ICRF3 (Charlot et al., 2020) and eliminated from the NEQ. The first results of adding source positions to the IVS combination are given in Bachmann and Thaller (2017). Finally, the IVS contribution to the ITRF2020 consists of session-wise normal equations which include combined station coordinates and EOP and are provided in SINEX format.

For verifying the quality of the combination and the consistency among the individual AC contributions, the time series of EOPs and station coordinates have been evaluated. Additionally, a VLBI-only Terrestrial Reference Frame (VTRF) and a Celestial Reference Frame (CRF) (Kwak et al., 2018) can be generated and further investigated. In order to assess the quality of the AC contributions, internal as well as external comparisons of the estimated EOPs were carried out as a first step. Thereby, the determined combined solution as well as external time series (e.g. IERS Bulletin A) serve as a reference. This paper presents the evaluation of the individual contributions by the ACs, the combination procedure and the results of the combined solution for station coordinates and EOPs.

2 IVS AC contributions to ITRF2020

A regular update of the ITRS realization becomes necessary approximately every five to six years (see above). Compared to the IVS contribution to ITRF2014, the contribution to ITRF2020 contains more stations and considers new models, e.g., the Galactic Aberration (MacMillan et al., 2018), a new secular pole model, gravitational deformation for some of the antennas[3] and a new high-frequency EOP model[4]. In addition, for the first time, sessions observed by the VLBI Global Observing System (VGOS) station network are considered. VGOS is established for improving VLBI data to meet the increasingly demanding requirements[5].

Figure 1 shows the total number of sessions submitted by each AC (green bar). Thereby 6,100 sessions (including VGOS) are combined from 1979 until the end of 2020 and contributed using the SINEX format. In addition, the yellow bar shows the number of invertible NEQs, and the red bar illustrates the successful contributions to the combination (status as of March 2021).

Almost every AC contributes a total number of approximately 6,500 sessions. Due to poor station configuration in the early 1980s – most sessions include only three or four stations – the number of successful combinations is only in the range of 6,100. Because the full set of EOPs is estimated constraint-free, an adequate station network (minimum of five datum stations) is re-

---

[1] https://ccivs.bkg.bund.de/data/sinex_v202.pdf

[2] https://ivscc.gsfc.nasa.gov/IVS_AC/ITRF2020/ITRF2020_checklist_v2020Jan13.pdf

[3] https://ivscc.gsfc.nasa.gov/IVS_AC/apriori/gravity_deform_model_v2019Nov21.txt

[4] https://ivscc.gsfc.nasa.gov/hfeop_wg/

[5] https://earth.gsfc.nasa.gov/geo/instruments/vlbi-global-observing-system-vgos

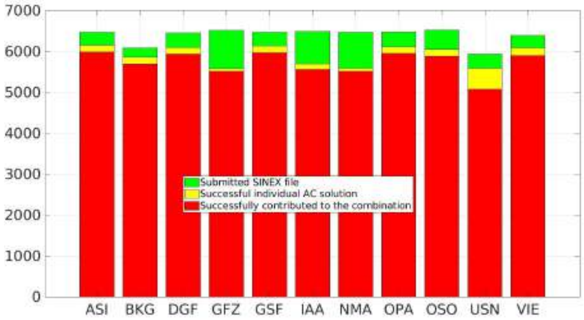

Fig. 1 Number of Sessions contributed to the combination

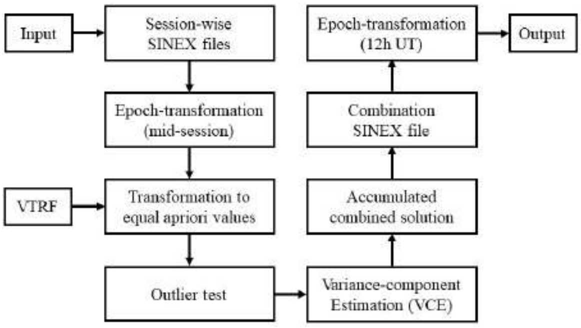

Fig. 2 Sketch of combination procedure

quired for the combination process. For the small network sessions further investigations are still ongoing to find the optimal way to include these sessions in the final contribution of the IVS combination to ITRF2020.

3 IVS Combination procedure

The goal of a session-wise combination is stability improvement compared to the individual AC solutions. Because the 11 contributing ACs are using 7 different software packages for their VLBI analysis, the single AC solutions are computed by specific pre-assumptions, leading to an increased variety of the input used as a basis for the combined product. The inputs for the combination process are session-wise SINEX files by the individual ACs, including a full set of EOPs, station coordinates and source positions. In order to realize consistency between all individual contibutions a transformation to equal epochs (middle of 24h observation interval) as well as to equal a priori values is carried out. Therefore, the latest IVS Quarterly solution (2020/Q2) serves as a priori TRF. For realizing individual AC solutions, the source coordinates are fixed to the ICRF3 and the station coordinates are estimated by applying No-Net-Rotation and No-Net-Translation conditions (NNR/NNT) w.r.t. the a priori TRF. The EOPs are estimated as free parameters. For detecting bad contributions or sessions that do not behave well and should be excluded from the combination, an outlier test w.r.t. station coordinates and EOPs is carried out. Finally, the combined normal equation consists of the accumulated individual NEQs. Thereby, specific weighting factors – resulting from a variance component estimation (VCE) (Bähr, 2007) – are applied for each single NEQ. After eliminating the source coordinates, the combined product includes only station coordinates and the full EOP set. Two series of combined session-wise SINEX files are provided to the ITRF combination centers: one series with parameters given at the mid-epoch of each VLBI session (i.e., the best VLBI-only solutions), and a second series with all parameters transformed to 12:00 UTC in order to be consistent with the other space-geodetic techniques. Figure 2 shows a simplified sketch of the combination process.

A comparison of different combination strategies for terrestrial reference frames and geodetic parameter series is shown in (Seitz, 2012)

4 Results of the IVS combination

For assessing the quality of the combined product, an evaluation of the combination and the consistency between the individual AC solutions are performed w.r.t.

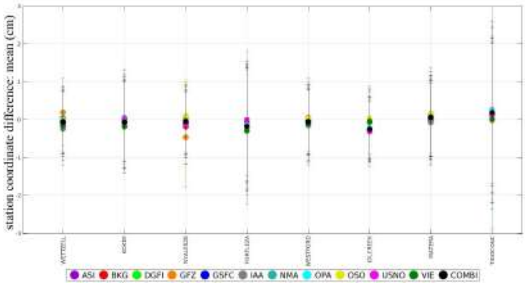

Fig. 3 Accuracy of station coordinate (H component)

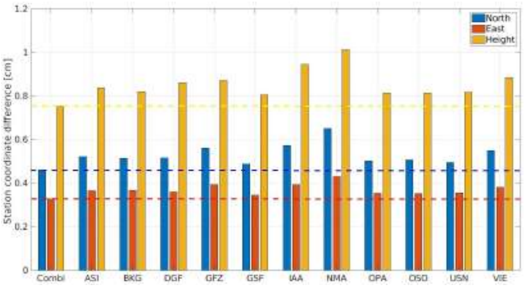

Fig. 4 WRMS of station Wettzell

both parameter groups: the station coordinates and the EOPs.

Figure 3 shows the eight best-performing VLBI stations as an example for the mean difference of the different solutions and the IVS Quarterly 2020/Q2. Beneath the individual ACs also the combination is depicted. In this case, the illustration is limited to the height component. The combined estimates represent the weighted mean of the single AC estimates and are well within the range spanned by the individual solutions. Beneath an alignment to the reference, also an enhancement of the precision – illustrated by the error bars – can be reached. A more detailed summary of the station coordinate estimation is shown in Figure 4. The Weighted Root Mean Square (WRMS) of the station Wettzell (Germany) is shown for the combined and the individual AC solutions.

The decrease of the WRMS level of the combined solution compared to all individual AC solutions confirms the improvement reached by the combination process for all three components. In addition to the station coordinates, Figure 5 shows the external validation of the ERPs. Polar Motion and dUT1 are thereby compared to the IERS Bulletin A time series.

Fig. 5 WRMS of ERP (Bulletin A - ACs and combination)

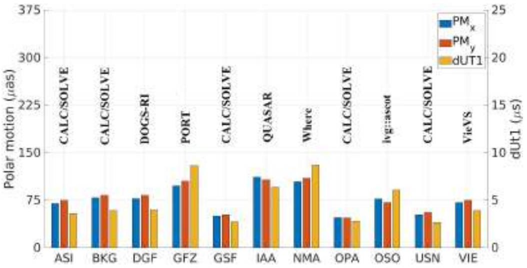

Fig. 6 WRMS of ERP (ACs - combination)

The combination decreases the WRMS level of all parameters. Finally, Figure 6 shows the internal validation of the ERP estimates. Concerning the combined solution the WRMS deviations of each AC are depicted. In the VIE contribution the EOP are presented by piece-wise linear parameterization by offsets and drifts. Nevertheless, compared to the other ACs, there is no significant degradation of the contribution by VIE visible. Although almost half of the ACs are using the CALC/Solve software – meaning that these contributions cannot be denoted as completely independent – the combination does not seem to be dominated by those ACs. However, the influence of the different software packages on the combination will be further investigated in the near future.

5 Conclusions and outlook

This paper presents the preliminary combined contribution of the IVS to the ITRF2020. Thereby, the individual contributions of 11 Analysis Centres serve as input for a combination on the level of normal equations. In a preparatory step, the EOP of all AC contributions are transformed to equal epochs (epoch transformation) and the station positions and EOP are transformed to the same a priori values (a priori value transformation). This ensures the consistency of the different NEQs, which is necessary for their combination. The atmospheric loading corrections are not applied (in contrast to the operational IVS solutions), and if contributions by ACs still contain the loading corrections, these are added back to the NEQ before starting the combination process. Applying individual weighting factors derived from a variance component estimation leads to an unbiased combination with an improved accuracy w.r.t. the single solutions. The method of combining normal equations fully respects the correlations between all parameters (including the prereduced ones). As an observation technique, which provides the link to the inertial space, VLBI is sensitive for the full set of EOP and enables their estimation as free parameters without any constraints. In this case, the geodetic datum of the station network is defined by applying NNR and NNT conditions w.r.t. the VTRF realized by the current quarterly solution. The source positions are fixed to the ICRF3.

The results of the investigations presented here have shown a significant improvement of the combined estimates in comparison to the individual AC solutions. The station coordinates as well as the ERPs are characterized by a decreased WRMS w.r.t. external references (IVS Quarterly solution 2020/Q2, IERS Bulletin A). Furthermore, the VCE and the outlier detection deliver realistic weighting factors for unbiased estimations. As of now (i.e. April 2021), a number of almost 6,100 session-wise combined SINEX files are submitted as preliminary IVS contribution to the ITRS Combination Centres. Sessions with small and regional networks are not yet submitted in this preliminary IVS combination as they are not suitable for EOP determination. The investigation of these sessions as well as the handling of the source coordinates in the combination will be the focus of the IVS Combination Centre in the near future. The final combined IVS contribution to ITRF2020 will also contain the small network sessions.

References

Altamimi, Z., Rebischung, P., Métivier, L., and Collilieux, X.: ITRF2014: A new release of the International Terrestrial Reference Frame modeling nonlinear station motions. Journal of Geophysical Research: Solid Earth, Volume 121, pp 6109–6131, doi:10.1002/2016JB013098, 2016.

Bachmann, S., Thaller, D., Roggenbuck, O., Lösler, M., and Messerschmitt, L.: IVS contribution to ITRF2014. Journal of Geodesy, Volume 90(7), pp 631-654. Doi: 10.1007/s00190-016-0899-4, 2016

Bachmann, S., Thaller, D.: Adding source positions to the IVS combination – First results. Journal of Geodesy, Vol. 91, pp 743-753. Doi: 10.1007/s00190-016-0979-5, 2017

Bähr, H., Altamimi, Z., Heck, B.: Variance Component Estimation for Combination of Terrestrial Reference Frames. Schriftenreihe des Studiengangs Geodäsie und Geoinformatik, Universität Karlsruhe (TH) (2007)

Böckmann, S., Artz, T, Nothnagel, A.: A VLBI terrestrial reference frame contributions to ITRF2008. J Geod 84(3):201–219. doi:10.1007/s00190-009-0357-7

Charlot, P., Jacobs, C. S., Gordon, D., Lambert, S., de Witt, A., Böhm, J., Fey, A. L., Heinkelmann, R., Skurikhina, E., Titov, O., Arias, E. F., Bolotin, S., Bourda, G., Mal, C., Malkin, Z., Nothnagel, A., Mayer, D., MacMillan, D. S., Nilsson, T. and Gaume, R.: The third realization of the International Celestial Reference Frame by very long baseline interferometry. In: Astronomy and Astrophysics, Section Celestial mechanics and astrometry, Volume 644, December 2020, https://doi.org/10.1051/0004-6361/202038368

Kwak, Y., Bloßfeld, M., Angermann, D., Gerstl, M. and Seitz, M.: Consistent realization of Celestial and Terrestrial Reference Frames. J Geod 92, 1047–1061 (2018). https://doi.org/10.1007/s00190-018-1130-6

MacMillan, D, Fey, A., Gipson, J., Gordon D., Jacobs, C., Krásná, H., Lambert, S., Ma, C., Malkin, Z., Titov, O., Wang, G., Xu, M.,Zacharias, Z.: Final Report of the IVS Working Group 8 (WG8) on Galactic Aberration, IVS General Meeting, Svalbard June 5, 2018

Métivier, L., Collilieux, X., Altamimi, Z., Lercier, D.: The ITRF and its scientific applications. Proceedings of the Journées 2013 ”Systèmes de référence spatio-temporels”: Scientific developments from highly accurate space-time reference systems, Observatoire de Paris, 16-18 September 2013, Edited by Nicole Capitaine, ISBN 978-2-901057-69-7, p. 3-6

Nothnagel, A., Artz, T., Behrend, D., Malkin Z.:International VLBI Service for Geodesy and Astrometry - Delivering high-quality products and embarking on observations of the next generation. Journal of Geodesy volume 91, pages 711–721 (2017)

Petit, G., Luzum, B. (eds.): IERS Conventions 2010. IERS Technical Note No. 36. Frankfurt am Main: Verlag des Bundesamts für Kartographie und Geodäsie, 2010. p. 132-131

Schlüter, W., Behrend D., The international VLBI service for geodesy and astrometry (IVS): current capabilities and future prospects. J Geod 81(6–8):379–387. doi:10.1007/s00190-006-0131-z

Seitz, M., Comparison of Different Combination Strategies Applied for the Computation of Terrestrial Reference Frames and Geodetic Parameter Series. In: Kutterer H., Seitz F., Alkhatib H., Schmidt M. (eds), The 1st International Workshop on the Quality of Geodetic Observation and Monitoring Systems (QuGOMS'11). International Association of Geodesy Symposia, vol. 140., Springer, Cham, 2012

Thaller, D.: Inter-technique combination based on homogeneous normal equation systems including station coordinates, Earth orientation and troposphere parameters. Dissertation der Fakultät für Bauingenieur- und Vermessungswesen der Technischen Universität München, München 03/2008, ISSN 1610-0956, 2008

Vennebusch, M., Böckmann, S., Nothnagel, A.: The contribution of very long baseline interferometry to ITRF2005. J Geod 81(6–8):553–564. doi:10.1007/s00190-006-0117-x

Intensives and 24-hour session data reprocessing for BKG AC 2020a solutions

A. Girdiuk, G. Engelhardt, D. Ullrich, D. Thaller, H. Hellmers

Abstract We present the newest BKG series of intensives and 24-hour VLBI session solutions. The data reprocessing includes almost all sessions since 1984 up to now. The parameterization of 24-hour sessions is aligned with ITRF2020 requirements. The differences from the previous BKG 2014 solution are new mean pole tide model, new recommendation for the high-frequency Earth Rotation variations – the tide corrections derived from TPXO8-based model, galactic aberration and corrections for the gravitational deformation of VLBI antennas. The a priori station positions are set to the ITRF2014 with corresponding post-seismic deformation corrections. For a few stations which are not included in the ITRF2014, the combined VTRF2020b built by the IVS Combination Center and the internal BKG solution are chosen. Among the others a priori station positions for new VGOS stations are adjusted internally as well. The source positions are aligned with the last realization of the celestial reference frame ICRF3. Applied models and reductions are updated for 1-hour solution correspondingly. This results in new 24-hour session series of consistently estimated EOPs, station coordinates and troposphere parameters. While intensives allow for the routine dUT1 estimation only, they are observed also on long baselines as most of 24-hour sessions. The growing number of intensive sessions observed on 3-4 stations facilitate to collect at least twice as much observations and, thus, more accurate dUT1 estimates. This data reprocessing is focused on the quality and consistency of the obtained geodetic products. In particular, we are interested in the consistency between dUT1 estimates derived from intensives and 24-hour sessions. This work is aimed to pinpoint challenges and feasibility of the united analysis of intensives and 24-hour experiments.

Keywords VLBI data reprocessing, sesionwise and global solutions, BKG AC, ITRF2020 contribution

1 Introduction

The BKG Analysis Center (AC) is the official IVS AC, what entails to carry out the routine VLBI data analysis as one of the main IVS AC responsibility. The results of the processed VLBI data are provided to the IVS community in the common form referred to as products: intensives and daily sinex files, EOP time series, dUT1 time series (as a result of intensive session processing), tropospheric data files, quarterly solutions for station and source positions. The BKG AC is capable to produce the entire set of the IVS products. The newest BKG solutions cover the gap induced by the experiments released in the vgosDb format only. The obtained results of the processed sessions R4 or INT3 since the middle of 2018 can be found now in the updated EOP time series. By this reason, some sessions, i.e. R4 sessions, were not included in the BKG last quarterly solutions. The BKG standard solution parameterization of 24-h experiments and applied reductions are modified to align with the ITRF2020 requirements (see Gipson (2020) and references hereinafter). In particular, station positions are utilized as provided by ITRF2014 (Altamini et al., 2016) and source positions by ICRF3 (Charlot et al., 2020). Also we updated

---

Anastasiia Girdiuk · Daniela Thaller · Dieter Ullrich · Gerald Engelhardt
Federal Agency for Cartography and Geodesy (BKG), Richard-Strauss-Allee 11, Frankfurt am Main, 60598 D-Germany

Table 1 The solution parameterization.

Parameter	A priori data source
Source positions	ICRF3
Galactic abberation	Working Group 8
Pole tides	IERS mean pole model, 2018
HF ERP	Desai&Sibois/Egbert
Troposphere	VMF3
Station positions and velocities	ITRF2014
Gravitational antenna deformations	by the courtesy of Axel Nothnagel
Episodic site motions	
Loadings	
Ocean tidal loading	TPXO7.2 by Scherneck
Atmosperic tidal and non-tidal loadings	by the courtesy of the Goddard group

Intensive solution setup accordingly. The substantial accuracy of dUT1 estimates is on the impartially comparable level with the dUT1 estimates as derived from 24-h and Intensives. Besides, we present a preliminary results of the implementation of the non-tidal atmospheric loading corrections (Wang et al., 2021) derived from the products provided by the Earth-System-Modelling group at GFZ (Dobslaw and Dill, 2018).

2 BKG AC solutions

The latest official key solution prepared by the BKG AC is called bkg2020a. The newest CALC/Solve version revised on 2020.01.23 is employed, so that the reprocessed data in vgosdb format are included in our products.

The BKG AC processes all VLBI observations starting with the so-called database 1. The database 1 is the correlated VLBI data provided by a correlator as the set of the single band delays. The CALC/Solve is employed at BKG to maintain the entrire analysis workflow: to process the single band delays, to resolve ambiguities and produce group delays. Finally, the geodetic parameters are evaluated based on the group delays calculated in this chain. After vgosDb have been accustomed at BKG AC, the old VLBI data were released, where the independently resolved ambiguities are included. These vgosDbs, which contain the wrapper files with 'iBKG', are available at the dedicated directory (ftp://ivs.bkg.bund.de/pub/vlbi/ivsdata/vgosdb_bkg/) at the BKG Data Center only.

Table 1 summarizes the a priori data sources and applied models. Note, that not all stations have the a priori coordinates in ITRF2014, so that the BKG internal or combined products Bachmann et al. (2016) are utilized. The high-frequency Earth Rotation Parameters (HF ERP) amplitude-corrections were updated for the first time since 2010. The corresponding corrections as derived from the model provided by Desai&Sibois/Egbert were validated within the analysis of the geodetic techniques: VLBI, GNSS and SLR, performed by the HF-EOP Working Group. The activities of the other working group, the IVS Working Group 8, resulted in the recommendation on the Galactic Aberration, which is modeled in the VLBI analysis for the first time. Furthermore, the gravitational antenna deformations are modeled for the first time as well. The appropriate corrections are systematized by Axel Nothnagel as well as episodic site motions and distributed in the frame of the ITRF2020 preparations on the IVS Analysis Coordinator website (see Gipson (2020) and hereinafter for the references to all applied reductions).

As a contribution to the ITRF2020 over 90% of the requested session were submitted. The obtained single session solutions are provided to the BKG Data Center in the unified SINEX format to suit the combination on the normal equation level. In this time, the solutions corrected for the tidal and non-tidal loading induced by the atmosphere are prepared along with the uncorrected solutions. As usual the station positions, source coordinates, polar motion, polar motion rates, dUT1 and LOD as well as celestial pole offsets are estimated. Besides, the stochastic parameters, namely clock polynomials by order 3, zenith wet delays and session-wise gradients as well as baseline clocks, are estimated, but they are not distributed via SINEX files.

The other BKG solution is the internal combination of the single session solutions contributed to the ITRF2020 referred to as the global solution. The global solution is required to build in order to derive the EOP time series evaluated as the local parameters. The station positions are estimated as global parameters only for the sites listed in the y axis of Figure 1. Additionally, about 40 station positions are treated as the local parameters, if any significant discontinuities are observed, i.e. Conception or the observed time series is too short, i.e. AGGO or new VGOS antennas. The selected source positions with at least 2 observations are estimated as global parameters ($\sim$4600 sources) and local parameters (over 1000 sources). The crucial

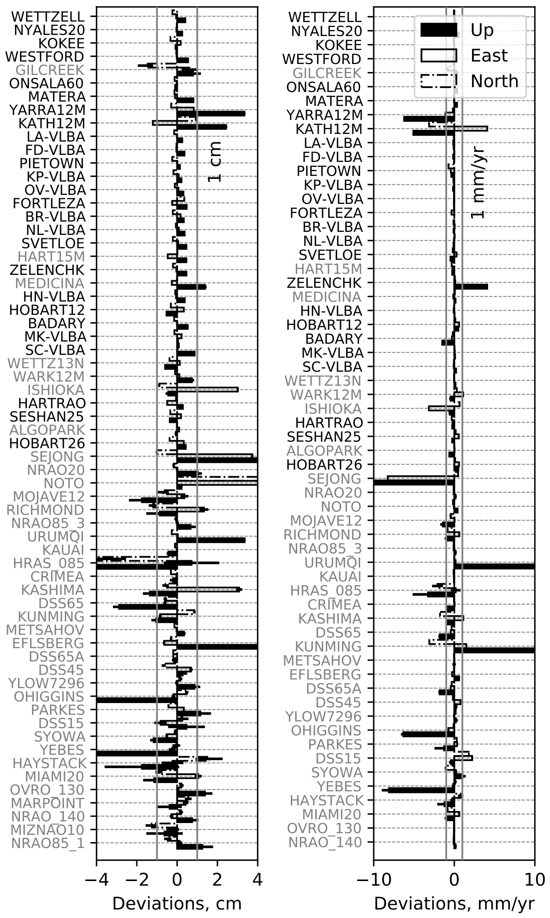

Fig. 1 The deviations of the evaluated station positions are plotted on the left side and velocities on the right side in the local horizontal coordinates (right-handed: Up, East and North) in mm and mm per year respectively. The datum stations are marked by black font color. The deviations of the station positions exceed the plot limits in the Up component: YEBES (-80 mm), OHIGGINGS (-50 mm), EFLESBERG (131 mm), HRAS 085 (-61 mm) and SEJONG (71 mm); in the East component: NOTO (105 mm); in the North component: HRAS 085 (-40 mm) and NOTO (97 mm). The deviations of the station velocities exceed the plot limits in the Up component: KUNMING (27 mm/yr), URUMQI (12 mm/yr), SEJONG (-15 mm/yr).

point of the global solution is the choice of the proper reference. The selected datum stations are highlighted in Figure 1 with black font color. The selected datum sources are assigned to the list of the ICRF3 defining sources (303 sources at frequency of 8.4 GHz in X band) except 0355-669 observed only once, thus excluded, and 0809-493 evaluated as the local parameter.

The Intensive session analysis produces the respectively designed daily solution to monitor the dUT1 variations. The corresponding solution is called eopi and limited to the stochastic clock estimates by the degree 3, zenith wet delay and dUT1. The provided SINEX files, however, include an extended solution where the station positions and the full set of EOP are evaluated for the further combination. The clock and tropospheric parameter estimates are reduced as well as in the case of 24-hour sessions.

3 Results

The obtained estimates of the stations positions and velocities are presented in the local horizontal coordinates in Figure 1. The most of the station positions deviations are achieved on the 1-cm-level, and only 2 Australian stations KATH12M and YARRA12M included in the datum exceed this level. A similar behavior can be seen in the velocity estimates. The obtained estimates are relatively large for the stations, which have either comparatively small number of observations (KUNMING, SEJONG, URUMQI) included in the solution or they observed mainly in 80e (HRAS 085). The considerably small deviations of the source positions are calculated mainly within 0.1 µas for the defining sources. The EOP time series estimated consistently with station and source positions in the global solution are represented by unbiased variations in x and y components of polar motion, dUT1 and celestial pole offsets. The comparison of polar motion and dUT1 with the conventional IERS C04 14 time series (Petit and Luzum, 2010) shows rather small deviations which expectedly larger in 80e (see Figure 2). The total values of the estimated celestial pole offsets illustrate in Figure 2 the anticipated nutation periodicity.

3.1 dUT1 variations

We compare the dUT1 variations on the time span, where our updated Intensive sessions are reprocessed. The Intensives are comprised by about 1700 sessions starting from 2017. About 600 different experiments of 24-h Sessions are observed over the same time. The results of the Intensive session analysis are juxtaposed

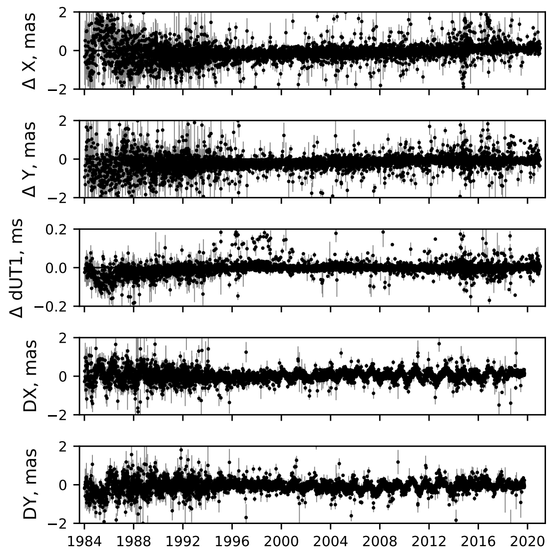

Fig. 2 The obtained deviations wrt IERS C04 14 time series in the x and y components of polar motion and dUT1 marked on panels from the top to the down as ΔX, ΔY and ΔdUT1 accordingly. The celestial pole offsets variations are ploted in the lowest two panels as DX and DY accordingly.

with the obtained dUT1 variations derived from the described global solution of 24-h Sessions (ses Figure 3). The overall weighted root-mean-square residuals (WRMS) is approximately 1.7 times larger for Intensives than for 24-h Sessions. The dUT1 standard deviations are obtained in the analysis of the Intesives are 2.5 to 5 times larger (for mean and median values respectively) than the standard variations calculated in the global solution of 24-h Sessions. The selection of INT3 experiments facilitates to improve the WRMS and standard deviations marginally. The selection of INT3 consisted of at least 4 stations, however, benefits by reduction of WRMS to 1.5 times. Moreover, the mean standard deviations of the Intensives and 24-h sessions are recognized on the approximately same level, and the median values of the Intensive standard deviations are calculated as twice of the 24-h Session size. We note, that the obtained single session solutions of Intensives and 24-h Sessions as well as the global solution of 24-h Sessions show also no bias wrt IERS C04 14 (Petit and Luzum, 2010). The bias, however, may appear due to the deficiency of the global solution, to suppress which the rigorous datum is required to be introduced.

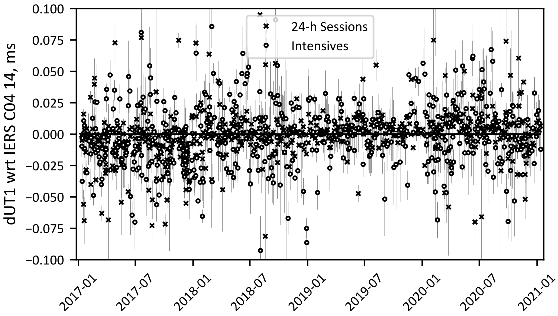

Fig. 3 The obtained deviations wrt IERS C04 14 time series in dUT1 derive from two independent solutions of the Intensives and 24-h Sessions. The corresponding estimates are unbiased.

3.2 GFZ Loading corrections

The RAMADDA repository supported by the Earth-System-Modelling group GFZ Section 1.3 (ESMGFZ) is considered (Dobslaw and Dill, 2018) as a source of the non-tidal atmospheric loading (NTAL) due to the discontinuance of the loading corrections provided by the Goddard group (the GSFC model). The GFSC model was calculated based on National Center for Environmental Prediction (NCEP) Reanalysis calculated at 6-h step with 2.5° resolution (Petrov, 2015). The RAMADDA repository for ESMGFZ products contains the loading data on a finer regular global grid 0.5°x0.5° with 3-h-step-NTAL. The Mass distribution is based on the European Centre for Medium-Range Weather Forecasts (ECMWF), the Max-Planck-Institute for Meteorology Ocean Model and the Land Surface Discharge Model. The NTAL corrections (the GFZ model) derived from the corresponding ESMGFZ product (Wang et al., 2021) are applied in the single 24-h session solution. The reference solution, in which no NTAL was applied, is compared with two corresponding solutions (see Figure 4) to demonstrate the loading impacts. The comparison is conducted in terms of the relative variance reduction (Girdiuk, 2017), which indicates that the corrections of the GFZ model advance the obtained solutions considerably.

4 Conclusions and outlook

The latest BKG AC solutions and the corresponding products are described in this paper. The accuracy of the obtained products are calculated on the expected 1 cm and 1 mm/yr level for the stations in the datum. Also the dUT1 variations derived from the intensive session analysis allow for the comparison with more accurate results of the 24-h Sessions. These dUT1 results are encouraging for the combination of Intensives and 24-hour sessions, in order to build a combined ERP time series. Besides, the considerable improvement induced by the applied NTAL corrections facilitates the further use of the ESMGFZ products in our routine VLBI analysis, i.e. non-tidal ocean loading.

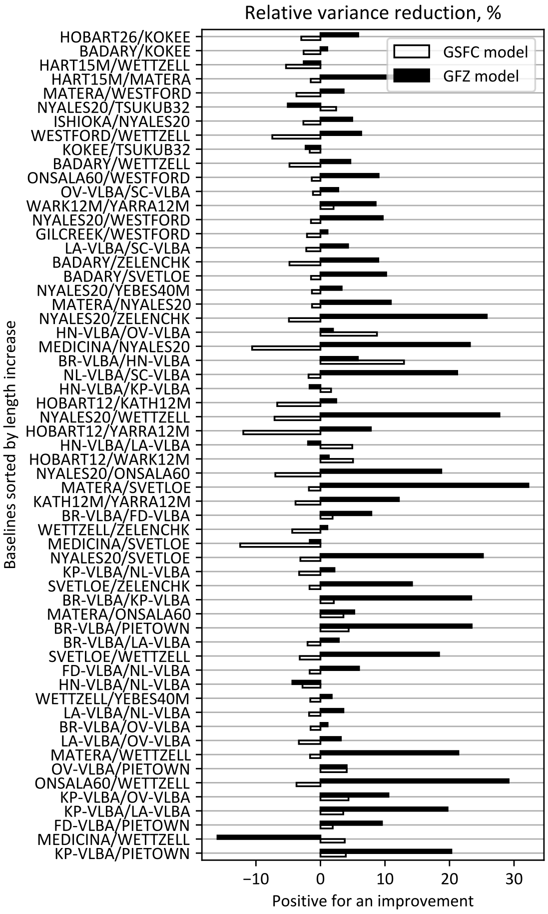

Fig. 4 The relative variance reduction is shown for the baselines where the obtained values exceed 1%. The positive values of the relative variance reduction indicate that the applied loading corrections facilitate to build a better stochastic model. The GSFC model stands for the NTAL corrections provided by the Goddard group. The ESMGFZ product used to calculated the NTAL corrections is referred to as the GFZ model. The baselines are ordered by the length decreasing from top to the bottom.

References

Altamini Z, Rebischung P, Métivier L, Collilieux X (2014) ITRF2014: A new release of the International Terrestrial Reference Frame modeling nonlinear station motions. Journal of Geophysical Research: Solid Earth, 121, 6109–6131, doi: 10.1002/2016JB013098.

Bachmann S, Thaller D, Roggenbuck O, Lösler M, and Messerschmitt L (2016) IVS contribution to ITRF2014. Current intra-technique combination is available: https://ccivs.bkg.bund.de/index.php?uri=quarterly/vtrf Journal of Geodesy, 90(7):631–654, doi: 10.1007/s00190-016-0899-4.

Böhm J, Boisits J (2020) re3data.org - Registry of Research Data Repositories. re3data.org: VMF Data Server; editing status 2020-12-14. http://doi.org/10.17616/R3RD2H.

Charlot P, Jacobs C S, Gordon D, Lambert S, de Witt A, Böhm J, Fey A L, Heinkelmann R, Skurikhina E, Titov O, Arias E F, Bolotin S, Bourda1 G, Ma11 C, Malkin Z, Nothnagel A, Mayer D, MacMillan D S, Nilsson T, and Gaume R (2020) The third realization of the International Celestial Reference Frame by very long baseline interferometry. Astron. Astrophys, http://hpiers.obspm.fr/icrs-pc/newwww/icrf/index.php.

Dobslaw H, Dill R (2018) Predicting Earth Orientation Changes from Global Forecasts of Atmosphere-Hydrosphere Dynamics. Adv. Space Res., 61(4), 1047-1054. doi: doi.org/10.1016/j.asr.2017.11.044.

Gipson J (2020) IVS Checklist for ITRF2020. IVS Analysis Coordinator website. `https://ivscc.gsfc.nasa.gov/IVS_AC/ITRF2020/ITRF2020_checklist_v2020Jan13.pdf`.

Girdiuk A (2017) Atmospheric tides in Earth rotation observed with VLBI. Thesis, Hochschulschrift. https://resolver.obvsg.at/urn:nbn:at:at-ubtuw:1-105235

Petit G, Luzum B (eds.)(2010) IERS Conventions (2010). IERS Technical Note, 36, Frankfurt am Main: Verlag des Bundesamts für Kartographie und Geodäsie.

Petrov L (2015) The International Mass Loading Service. MEMO:http://arxiv.org/abs/1503.00191.

Wang L, Thaller D, Susnik A, and Dach R (2021) Improving the products of global GNSS data analysis by correcting for loading displacements at the observation level. EGU General Assembly 2021, online, 19–30 Apr 2021, EGU21-12920. https://doi.org/10.5194/egusphere-egu21-12920, 2021.

The K Band Geodesy with the East Asian VLBI Network

S. Xu, T. Jike, T. Jung, F. Shu, L. Cui, A. Melnikov, J. McCallum, S. Yi, B. Zhang, N. Sakai, X. He, H. Imai, N. Kawaguchi, D. Sakai, C. Oh, P. Jiang, M. Xu, G. Wang

Abstract The East Asian VLBI Network (EAVN) is an international collaborative array, which consists of radio telescopes in China, Japan, and Korea. For the high precision astrometry, the EAVN astrometry working group has been conducting K-band geodetic observations by collaborating with several IVS stations (Quasar VLBI Network, Hobart and Sejong). Based on the first EAVN geodetic observation and the local tie measurement, the agreement of $\sim$ 1 - 3 cm (in terms of the ITRF) was achieved for the Korean VLBI Network (KVN). Such experiments will also contribute to the ICRF at K-band.

Shuangjing Xu[1,2], Takaaki Jike[3],Taehyun Jung[1], Fengchun Shu[2], Lang Cui[4], Alexey Melnikov[5], Jamie McCallum[6], Sang Oh Yi[7], Bo Zhang[2], Nobuyuki Sakai[1], Xuan He[2], Hiroshi Imai[8], Noriyuki Kawaguchi[3], Daisuke Sakai[3], Chungsik Oh[1], Pengfei Jiang[4], Minghui Xu[9], Guangli Wang[2]

(1) Korea Astronomy and Space Science Institute, 776 Daedeokdaero, Yuseong-gu, Daejeon 34055, Republic of Korea

(2) Shanghai Astronomical Observatory, Chinese Academy of Sciences, 80 Nandan Road,Shanghai 200030, China

(3) Mizusawa VLBI Observatory, National Astronomical Observatory of Japan, 2-12 Hoshigaoka, Mizusawa-ku, Oshu, Iwate 023-0861, Japan

(4) Xinjiang Astronomical Observatory, Chinese Academy of Sciences, 150 Science 1-Street, Urumqi, Xinjiang 830011, China

(5) Institute of Applied Astronomy of the Russian Academy of Sciences, Kutuzova Embankment 10, St. Petersburg, 191187, Russia

(6) University of Tasmania, Private Bag 37, Hobart, Tasmania 7001, Australia

(7) National Geographic Information Institute, Space Geodetic Observatory, Sejong, PO Box 30060, Republic of Korea

(8) Amanogawa Galaxy Astronomy Research Center, Graduate School of Science and Engineering, Kagoshima University, 1-21-35 Korimoto, Kagoshima 890-0065, Japan

(9) Aalto University Metsähovi Radio Observatory, Metsähovintie 114, 02540 Kylmälä, Finland

Keywords instrumentation: interferometers, geodesy, astrometry

1 Introduction

At present, EAVN[1] is operated using 15 telescopes for the open-use observations at 6.7 GHz (C-band), 22 GHz (K-band), and 43 GHz (Q-band), with the longest baseline length of $\sim$ 5100 km. In particular, EAVN provides the unique opportunity for observing in K/Q bands simultaneously (KaVA[2]+Nobeyama) (Han et al., 2013) or observing with dual-beam astrometry (only VERA) (Honma et al., 2008).

One of the primary goals is to make EAVN a high-accuracy astrometric array. To evaluate the astrometry performance, EAVN astrometry working group has conducted two repeat astrometric observations of (1) the parallax observations of W3OH (Xu et al., 2006; Hachisuka et al., 2006) and (2) the phased-referenced observation of QSO-QSO pairs (Fomalont et al., 2011). Also (3) geodetic observations at the K band are performed for improving the station positions of EAVN, which is fundamental for astrometry.

Among the EAVN antennas, the coordinates of KVN, VERA, and CVN (Chinese VLBI Network) are determined by different observations [3] and different methods on data reduction:

- VERA geodetic observations are carried out in the K-band and S/X-band (Jike et al., 2012). The S/X-

---

[1] EAVN website: `http://eavn.kasi.re.kr/`

[2] KaVA (KVN and VERA Array) is a combined VLBI array with KVN and VERA (VLBI Exploration of Radio Astrometry)

[3] `https://radio.kasi.re.kr/status_report/files/status_report_EAVN_2021B.pdf`

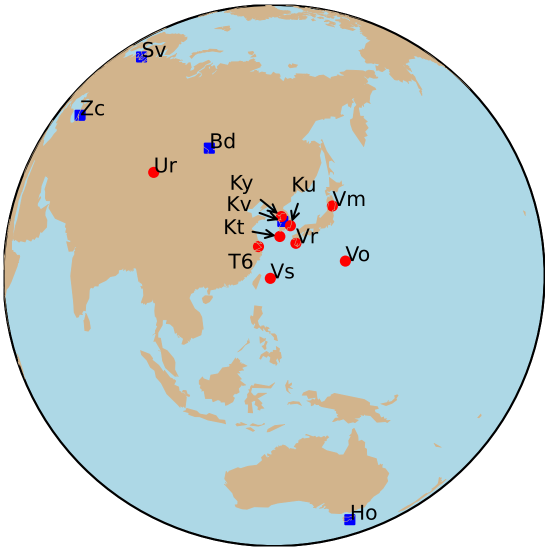

Fig. 1 The array configuration of EAVN Geodesy. Red dots are EAVN antennas and blue squares are the cooperative IVS sites.

bands are used in the IVS experiments and the domestic experiments with the Geographical Survey Institute of Japan.

- KVN has joined the VERA's K band sessions (eg. KaVA Geodesy) bimonthly since 2011.
- CVN antennas are the members of IVS, joining the international experiments at S/X-band regularly.

Meanwhile, there is a remained issue of KaVA Geodesy. The uncertainty of relative positions in the KaVA frame was in mm level, but the absolute position in the ITRF was in cm level. That's because the Mizusawa station has a non-linear post-seismic movement after the big earthquake in 2011, which is the only IVS station in KaVA. Therefore, EAVN Geodesy is curried out for connecting KaVA to ITRF directly with more IVS sites, which is important for EAVN astrometry.

2 Observation and Data Reduction

We started this work in 2019 by collaborating with several IVS stations, including the Quasar VLBI Network, Hobart and Sejong. The configuration of 14 participant antennas is shown in Figure 1.

A common frequency for all stations was selected with the total bandwidth of ~400 MHz (22102-22518 MHz) and a recording rate of 1 Gbps (8 IFs * 32 MHz). Since the data formats and soft-wares used in previous KaVA Geodesy are different with IVS, KaVA and IVS data can not be processed together. EAVN Geodesy would be consistent with IVS. As shown in Fig. 2, the independent methods would be performed at SHAO, NAOJ, and KASI, respectively.

Firstly, we performed one 2-hours session in 2019 for fringe detection and processing validation. After the successful test, two formal sessions were conducted as shown in Table 1.

Table 1 Conducted EAVN sessions

Date	Duration	Antennas
2019-11-19	2 h	VmVsVoVrKyKuKtT6UrBdSvZcHo—
2020-05-25	24 h	VmVsVoVrKyKuKt—UrBdSvZc——
2021-01-16	24 h	VmVsVoVrKyKuKtT6Ur———HoKv

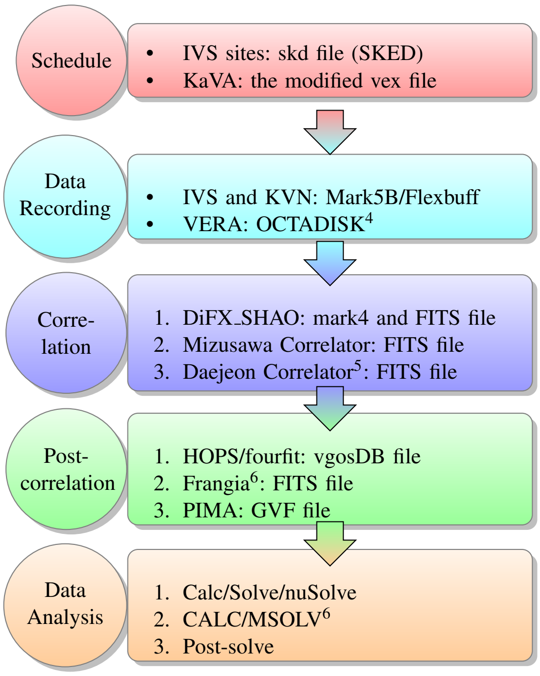

Fig. 2 Data-flow diagram of EAVN Geodesy

---

[4] The disk recorder of NAOJ compliant with VDIF specifications: https://ivscc.gsfc.nasa.gov/publications/gm2012/oyama.pdf

3 Results

Preliminarily, we present the results of the session in 2020MAY25 with the IVS standard processing way (eg, DiFX+HOPS+nuSolve), while the other data and methods are under investigation. In this session, 544 scans (2 min for each scan) were scheduled with 13 stations (VmVsVoVrKyKuKtT6UrBdSvZcHo) and 80 ICRF3_K sources (Charlot et al., 2020). In practice, Horbat and Tianma did not join, while Urumqi encountered an observing failure. The detection rates on ZELENCHK and VERA stations were relatively lower due to the bad weather conditions. The data quality of KVN, Svetloe, and Badary was excellent. In total, 13653 observations were scheduled, and 9112 observations (67%) were usable with the Quality Code (QC) >5.

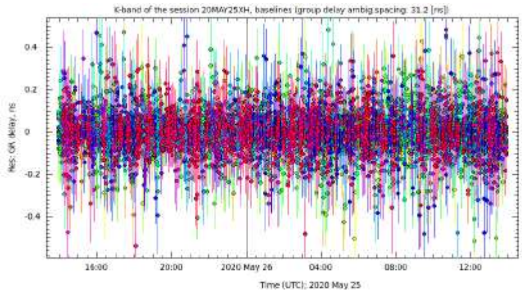

Fig. 3 Post-fit delay residuals of 2020MAY25

As shown in Fig.3, the weighted RMS residual of 47 ps is achieved using 8579 observations in the parameter estimation. The coordinates of IVS sites are referred to GSFC2019d solution and source positions are fixed to ICRF3. BADARY was used as the reference station to estimate the coordinates of KaVA stations with a formal error of 3-10 mm. Then we compared the results with the invariant point (IVP) measurements of KVN based on the GNSS (Yoo et al., 2018). When comparing at different epochs, the VLBI positions are propagated with the velocity estimated by the previous KaVA Geodesy. As shown in Table.2, the measured coordinates of IVP between VLBI and GNSS were consistent within 1∼3 cm level at the KVN.

Table 2 The difference of VLBI and GNSS coordinates of KVN

Station	Epoch	dX(mm)	dY(mm)	dZ(mm)
Ulsan	2017/11/23	0.3	11.5	11.9
	2018/05/02	1.0	19.6	13.0
	2018/11/03	-4.5	15.9	3.9
	2019/10/21	-7.8	17.5	10.1
	2020/09/19	-8.3	19.8	9.8
Tamna	2017/12/06	-10.3	31.0	19.8
	2018/03/25	-5.4	30.5	19.3
	2019/11/23	-8.0	26.6	15.5
	2020/05/28	-7.7	26.7	15.2

4 Conclusions and outlook

We have successfully conducted the K band geodesy with EAVN, and the absolute accuracy of ∼ 1 - 3 cm for KVN coordinates is achieved based on the first experiment.

As the outlook, we will improve the station positions of EAVN to mm-level with the advanced calibration and batch solution with new observations. Several regular sessions per year are necessary to trace the non-linear post-seismic movement of Mizusawa and other no-geodetic stations. We will also contribute to the ICRF at high frequency with the unique multi-frequency (K/Q/W bands) systems.

References

Charlot P., Jacobs C. S., Gordon D., Lambert S., de Witt A., Böhm J., Fey A. L., et al., 2020, A&A, 644, A159. doi:10.1051/0004-6361/202038368

Fomalont E., Johnston K., Fey A., Boboltz D., Oyama T., Honma M., 2011, AJ, 141, 91. doi:10.1088/0004-6256/141/3/91

Hachisuka K., Brunthaler A., Menten K. M., Reid M. J., Imai H., Hagiwara Y., Miyoshi M., et al., 2006, ApJ, 645, 337. doi:10.1086/502962

Han S.-T., Lee J.-W., Kang J., Oh C.-S., Byun D.-Y., Je D.-H., Chung M.-H., et al., 2013, PASP, 125, 539. doi:10.1086/671125

Honma M., Kijima M., Suda H., Kawaguchi N., Kobayashi H., Bushimata T., Shimizu R., et al., 2008, PASJ, 60, 935. doi:10.1093/pasj/60.5.935

Jike, T., Manabe, S., Tamura, Y. and Shizugami, M., (2012) VERA Geodetic Activities, *International VLBI Service for Geodesy and Astrometry*, p. 72.

Xu Y., Reid M. J., Zheng X. W., Menten K. M., 2006, Sci, 311, 54. doi:10.1126/science.1120914

Yoo S.-M., Jung T., Lee S.-M., Yoon H. S., Park H.-E., Chung J.-K., Roh K.-M., et al., 2018, JKAS, 51, 143. doi:10.5303/JKAS.2018.51.5.143

---

[5] `https://radio.kasi.re.kr/kjcc/main_kjcc.php`

[6] The VLBI processing software of NAOJ

A Broadband VLBI experiment with transportable stations between Japan and Italy with a new observation scheme using closure delay relation

M. Negusini, M. Sekido, K. Takefuji, H. Ujihara, T. Kondo, N. Nemitz, M. Tsutsumi, H. Hachisu, E. Kawai, M. Pizzocaro, C. Clivati, F. Perini, G. Maccaferri, R. Ricci, C. Bortolotti, M. Roma, J. Leute, G. Petit, D. Calonico and T. Ido

Abstract A broadband VLBI system inspired by the concept of VGOS was developed by NICT and implemented in the Kashima 34 m antenna and in two transportable stations utilizing 2.4 m diameter antennas. The transportable stations were conceived as a tool for intercontinental frequency comparison but are equally useful for geodesy. In the procedure of node-hub style (NHS) VLBI, the closure delay relation provides a virtual delay observable between 'node' stations, thanks to joint observation with a large, high sensitivity 'hub' antenna. This overcomes the limited sensitivity of the small diameter node antennas, while error sources associated with large diameter antennas (e.g., gravitational deformations) are eliminated. This scheme does not increase the sensitivity to radio source structure if the hub antenna is located at intermediate position between two nodes. We performed VLBI experiments utilizing this approach over 8700 km baselines among Medicina, Koganei, and Kashima, with the aim of comparing two remote optical clocks. We used the Vienna mapping function (VMF3) for atmospheric delay corrections including its anisotropic components. The performance of NHS VLBI scheme was evaluated to be comparable with IVS-R1 and R4 sessions via baseline length repeatability. The NHS VLBI scheme can be applied at VGOS observation stations, and it may become a tool for improving the global distribution of geodetic VLBI station and for co-location with other space geodetic techniques. Our measurements revealed signatures of structure effects in the correlation amplitude of several of the observed radio sources. We present a model of the frequency dependent source size for 1928+738 derived from correlation amplitude data observed in four frequency bands. Finally, this system demonstrated in intercontinental frequency comparison performance beyond satellite techniques and can potentially be used for future long-term stable international clock comparison that is fundamental to international timekeeping, global positioning and test of fundamental physics.

Keywords Broadband VLBI, Direct RF-sampling, Closure delay

Monia Negusini · Federico Perini · Giuseppe Maccaferri · Roberto Ricci · Claudio Bortolotti · Mauro Roma
Istituto Nazionale di Astrofisica, Istituto di Radioastronomia, Bologna, Italy

Mamoru Sekido · Hideki Ujihara · Masanori Tsutsumi · Eiji Kawai
National Institute of Information and Communications Technology, Kashima Space Technology Center, Kashima, Japan

Kazuhiro Takefuji
Japan Aerospace Exploration Agency, Usuda Deep Space Center, Saku, Japan

Tetsuro Kondo
Chinese Academy of Sciences, Shanghai Astronomical Observatory, Shanghai, China

Nils Nemitz · Hidekazu Hachisu · Tetsuya Ido
National Institute of Information and Communications Technology, Space-Time Standards Laboratory, Koganei, Japan

Marco Pizzocaro · Cecilia Clivati · Davide Calonico
Istituto Nazionale di Ricerca Metrologica, QN Metrologia quantistica e nanotecnologie, Torino, Italy

Julia Leute · Gérard Petit
Bureau International des Poids et Mesures, Time Section, Sevres, France

1 Introduction

Redefinition of the SI second as the unit of time is being discussed in the metrological community (Riehle, 2015), thanks to the development of high accuracy optical frequency standards reaching 10^{-18} accuracy (Riehle et al., 2018). Accurate frequency comparison between atomic clocks at distant locations is an important issue and requires accurate methods. Frequency transfer by optical fiber-link reaches uncertainties below 10^{-18} (Lopez et al., 2012; Predehl et al., 2012; Calonico et al., 2014), then, several attempts of intercontinental frequency link have been tried. Two-way satellite time and frequency transfer (TWSTFT) using signal's carrier phase has the potential to reach instabilities on the order of 10^{-17} (Fujieda et al., 2016). The availability of suitable communication satellites and the need to license radio transmissions limit its applicability. Precise Point Positioning (PPP) methods using the carrier phase of Global Navigation Satellite Systems (GNSS) are used to maintain time links between national time standards agencies. Integer-ambiguity techniques (IPPP) (Petit et al., 2015) can also reach instabilities of order 10^{-17}, but need continuous measurements over longer averaging durations.

VLBI application for time and frequency transfer has been investigated since the 1970s (e.g. (Counselman et al., 1977; Saburi, 1978; Clark et al., 1979(@)), and an uncertainty of $1.5 \cdot 10^{-15}$ for a time period of 1 day has been reported in an earlier study (Rieck et al., 2012). VLBI is not restricted by the availability of communication satellites or the requirement of licensed radio transmission and relies on observing extragalactic radio sources of the international celestial reference frame (ICRF).

The concept of broadband VLBI observation proposed as VLBI Global Observing System (VGOS) (Petrachenko et al., 2012; Niell et al., 2018) improves the delay measurement precision by one order of magnitude over conventional S/X-band VLBI, using a ten times wider bandwidth of observing radio frequency. A higher data acquisition rate contributes to improvement of observing sensitivity as well. We developed the broadband VLBI system named 'GALA-V' (Sekido et al., 2017) with the aim to enable intercontinental precise frequency comparison. Transportable broadband VLBI stations can be installed at selected locations, such as metrology institutes operating next-generation frequency standards. The 34 m antenna located at Kashima Space Technology Center provides the high sensitivity used to boost the SNR of observations.

2 Broadband VLBI System and NHS observations

NICT (National Institute of Information and Communications Technology) developed the NINJA feed system (Ujihara et al., 2019) to use existing Cassegrain antennas, which have narrower bean size with respect to VGOS stations (e.g., 34 ° for the Kashima 34 m antenna), for broadband observations (in the range of 3.2-14 GHz). It was installed on the Kashima 34 m antenna (Kas34) and two 2.4 m diameter antennas (MBL1 and MBL2). The receiver employs a room-temperature low noise amplifier rather than a cryogenic LNA to save cost and time for development, installation, and maintenance. The NINJA feed allows simultaneous observation of V and H linear polarization. Signals of both polarizations are acquired in Kas34, while the 2.4 m antennas only record the V-polarization signal. This is a compromise, in particular because data recorded at a remote site have to be transferred to the correlation center at the Kashima Space Technology Center. Although it was performed over high-speed research networks, the present data transfer rate is only about half of the data acquisition rate for a single polarization, therefore the acquisition of both polarization would result in doubling the turnaround time. Thus, single polarization observation were performed at the remote sites and the correlation data were synthesized to form an emulated polarization-aligned dataset.

Unlike VGOS, the received RF signal is amplified and separated into lower (0–8192 MHz) and upper ($>$ 8192 MHz) signals by a power divider and filters. Each of these signals is then directly digitized at 3-bit quantization by a high-speed sampler K6/GALAS (Takefuji et al., 2012; Sekido, 2015) with 16,384 MHz sampling rate. The sampler then extracts the four desired signals with 1024 MHz bandwidth per polarization at 6.0, 8.5, 10.4, and 13.3 GHz. This data acquisition process named RF-direct sampling (RFDS) digitizes the signal in early stage without analog frequency conversion. It reduces relative phase variation of the channels, consequently improves stability of group delay measurement. The RFDS technique brings large benefits for phase calibration, polarization synthesis, and wideband bandwidth synthesis in the signal processing.

Emulating the polarization aligned cross correlation products is formed by synthesizing two correlation products VH and VV by compensating the parallactic angle difference of the long baseline (see Sekido et al. (2021)). Then, group delay is derived by wideband bandwidth synthesis (WBWS) software 'komb' (Kondo and Takefuji (2016)). Differently from conventional S/X observation, the WBWS requires simultaneous estimation of differential ionospheric electron column density in the line of sight together with broadband group delay (e.g. Cappallo (2016)).

When applying VLBI for long-distance frequency comparisons, small 'node' stations are convenient for installation near the frequency standards, but it may be impossible to obtain the delay observable between the two due to reduced correlated flux for long baseline. Joint measurements with a high sensitivity 'hub' station overcome this problem by evaluating the closure relation for the full measurement network, in a scheme named 'Node Hub style' (NHS) VLBI. Thanks to the large effective bandwidth (2.7 GHz), the delay precision is achieved with minimum SNR. Besides flexibility and low cost, a small VLBI station also avoids gravitational antenna deformation and can help reduce temperature-dependent signal transmission cable length change. A delay observable in the NHS VLBI scheme is schematically depicted in Figure 1, where also Kas34, MLB1 and MLB2 antennas are displayed. A detailed discussion can be found in Sekido et al. (2021).

3 Optical clock comparison between Italy and Japan

The MBL2 antenna was installed at NICT Headquarters in Koganei and MBL1 was moved from Japan to Medicina Observatory in August 2018. The observed RF signal was converted to optical within the temperature controlled receiver box and then transferred to the Medicina VLBI station, over approximately 600 m of optical fiber placed in an underground trench, where the data acquisition system was placed. The purpose of the installation was to compare optical atomic frequency standards between NICT and INRiM (Istituto Nazionale di Ricerca Metrologica, Torino), connected to INAF via optical fiber link (Calonico et al., 2014). Several hydrogen maser frequency references were used as flywheels to bridge interruptions in operation of clocks and links. More details on the frequency link are described in Pizzocaro et al. (2021). A series of VLBI sessions during October 2018–February 2019 focused on comparing optical atomic frequency standards (the Yb clock at INRiM and the Sr clock at NICT) to a fractional uncertainty of only a few parts in 10^{-16}. In addition to the VLBI measurements, results from GPS data analysis, using improved integer ambiguity solution of Precise Point Positioning (IPPP) (Petit et al., 2015) were produced and compared, demonstrating consistent determination of differential clock behavior between two observation nodes across multiple VLBI sessions.

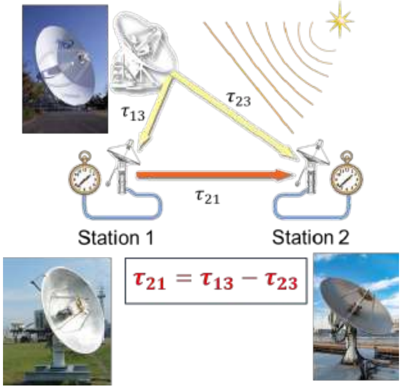

Fig. 1 NHS scheme and the three antennas involved in the project: above Kashima, on the left MLB1 installed at the Medicina Observatory and on the right MLB2 located in Koganei.

4 Evaluation of error source for NHS VLBI

The VLBI sessions were analyzed with Calc/Solve and the overall quality of the solutions can be stated with the WRMS of post-fit residuals of the single sessions of the order of a few tens of picoseconds. The use of Vienna Mapping Function (VMF3) (Landskron et al., 2018) to compute the a priori atmospheric delays included in data analysis contributed to overcome the problem of a single intercontinental baseline, which made it difficult to estimate anisotropic properties of the atmosphere, usually parameterized by atmospheric gradients. We examined baseline length repeatability (BLR) to evaluate the performance of NHS VLBI observations between the two small antennas and we found that the results are comparable to the IVS-R1 and R4 sessions using legacy S/X antennas (Figure 2). Moreover, IVS-R1 and R4 sessions take advantage of network observations with five to eleven stations, providing better sky coverage and a better estimation of atmospheric contributions, in particular the anisotropic component. The effectiveness of network observation with respect to single baseline is displayed for the two baselines: Wettzell(Wz)-Tsukuba(Ts) baseline (8840 km) and Wz-Kokee(Kk) baseline (10360 km), in Table 1. Using atmospheric gradients and network observation more effectively improves BLR for very long baselines. The group delay observable is affected by various factors, including instrumental delay and source structure effects. Table 2 gives an overview of the magnitude of uncertainty contributing to delay residual from each component, which are discussed separately in Sekido et al. (2021). We discussed how these effects affect the result of a single scan and the group delay instability is presented as a RMS-deviation from the mean.

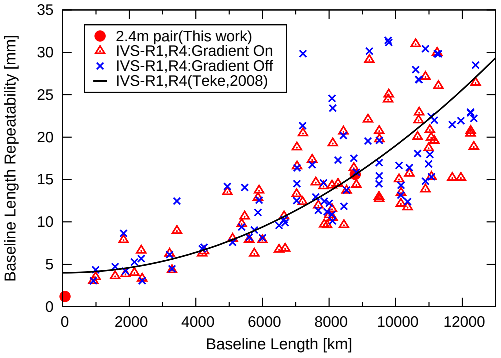

Fig. 2 BLR for NHS baselines (red circle) and our re-evaluation of IVS-R1 and R4 sessions during 2011–2013 with Gradients ON (red triangle) or OFF (blue cross). The solid line represents a regression function of BLR for IVS-R1 and R4 sessions presented in Teke et al. (2008).

Table 1 Baseline repeatability (BLR) for Wz-Ts and Wz-Kk baselines.

BLR (mm)	Atm. Grad. OFF		Atm. Grad. ON	
	Single	Network	Single	Network
Wz - Ts	12.8	12.1	12.4	9.9
Wz - Kk	48.3	12.4	37.2	11.7

Table 2 Group delay uncertainty for NHS VLBI.

Error Source	Uncertainty (ps)
Sensitivity ($\propto 1/\mathrm{SNR}$)	6.4
Instrumental	12.7
Troposphere	8.2
Ionosphere	1.7 - 17.2
Radio Source Structure	22.0 - 33.0

The influence of radio source structure on group delays has been investigated through closure delays (e.g. (Xu et al., 2019)). In our measurement, we did not achieve sufficient SNR on the baseline between the two small antennas. However, we found that the correlation data output of the Kas34-MBL1 baseline, after the polarization synthesis, provided information about radio source structure. Some high latitude sources have been observed through the NHS campaign. As an example, we present a simple ellipsoidal Gaussian model of 1928-738 derived from correlation amplitude data for each frequency band (Figure 3). Despite the limited sensitivity of the small antennas, the spatial resolution is sufficient to resolve sub-milliarcsecond structure. The data in Figure 3 show a larger deviation from the model at higher frequencies, suggesting that these frequencies better resolve the source structure. The observation of band-dependent source structure has additional implications for broadband VLBI. That can be an error source of broadband group delay determination by coupling with dispersive ionospheric phase delay contribution.

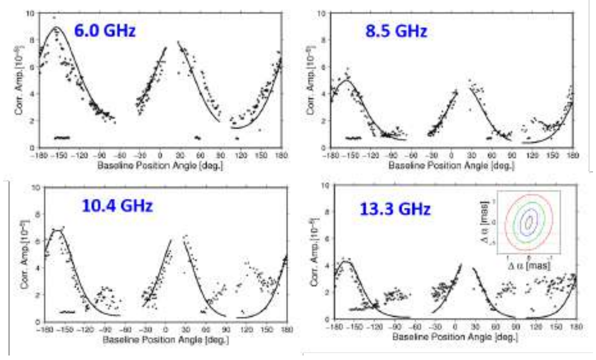

Fig. 3 Model of the frequency dependent source size for 1928+738.

5 Summary and outlook

Two transportable 2.4 m broadband VLBI stations were installed at Medicina and Koganei for a intercontinental frequency link experiment, using Kashima 34 m antenna in a Node-Hub Style scheme. Precise frequency comparison between the Yb lattice clock at INRiM and the Sr lattice clock at NICT has been performed with broadband VLBI sessions, carried out from October 2018 to February 2019. The experiments made use of signal processing for polarization and broadband bandwidth synthesis, and confirmed that the 2.4 m diameter size radio telescopes achieved a precision of few tens of picoseconds in NHS measurements over an intercontinental baseline.

The frequency ratio Yb/Sr between optical clocks was measured as +2.5(2.8) $\cdot$ 10^{-16} on 9000 km distance. Dominating delay error sources are ionospheric delay ($\approx$2-17 ps) and radio source structure (20-30 ps). NHS VLBI has potential to reduce structure effect in group delay observable.

Legacy (equipped with broadband systems) or VGOS antennas could be used as Hub stations in the NHS scheme. VLBI stations with coherent optical fiber links can play a role to compare optical clocks of National Metrology Institutes over intercontinental distances. High speed network for fast data transfer and dedicated resources for correlation processing will the required condition for it.

References

Calonico D., et al. (2014) High-accuracy coherent optical frequency transfer over a doubled 642-km fiber link. *Appl. Phys. B*, 117: 979-986.

Cappallo R. (2016) Delay and Phase Calibration in VGOS Post-Processing. *Proc. IVS-GM 2016*, pp.61-64.

Clark T.A., et al. (1979) Synchronization of clocks by very-long-baseline interferometry. *IEEE Trans Instrum Meas*, 28: 184–187.

Counselman C.C., et al. (1977) VLBI clock synchronization. *IEEE Proc*, 65: 1622–1623.

Fujieda M., et al. (2016) Advanced two-way satellite frequency transfer by carrier-phase and carrier-frequency measurements. *J. Phys. Conf. Ser.* 723.

Kondo, T., and K. Takefuji (2016), An algorithm of wideband bandwidth synthesis for geodetic VLBI. *Radio Sci.*, 51.

Landskron D., Böhm J. (2018) VMF3/GPT3: refined discrete and empirical troposphere mapping functions. *J Geod*, 92(4): 349–360.

Niell A., et al. (2018) Demonstration of a broadband very long baseline interferometer system: a new instrument for high-precision space geodesy. *Radio Sci*, 53(10): 1269–1291.

Lopez O., et al. (2012) Ultra-stable long distance optical frequency distribution using the Internet fiber network. *Opt Express*, 20(21): 23518.

Petrachenko W. T., et al. (2012) *VLBI2010: Next generation VLBI system for geodesy and astrometry*. *Int Ass Geod Symp*, 136, 999-1005.

Petit, G., et al. (2015) 1x10^{-16} frequency transfer by GPS PPP with integer ambiguity resolution. *Metrologia*, 52, 301-309.

Pizzocaro M., et al. (2021) Intercontinental comparison of optical atomic clocks via very long baseline interferometry. *Nat Phys.*, 17:223–227.

Predehl K., et al. (2012). A 920-kilometer optical fiber link for frequency metrology at the 19th decimal place. *Science*, 336(6080): 441.

Rieck C., et al. (2012) VLBI frequency transfer using CONT11. *In: 2012 European frequency and time forum*, pp 163–165.

Riehle F. (2015) Towards a redefinition of the second based on optical atomic clocks. *CR Phys*, 16(5): 506–515.

Riehle F., et al. (2018) The CIPM list of recommended frequency standard values: guidelines and procedures. *Metrologia*, 55, 188-200.

Saburi Y. (1978) Time synchronization by VLBI technique. *Radio Res Lab Rev*, 24: 597–601.

Sekido M. (2015) VGOS-related developments in Japan. *In: Notebook article of Eighth IVS technical operations workshop*, May 4–7, 2015 held at Haystack Observatory.

Sekido M., et al. (2017) Broadband VLBI System GALA-V and Its Application for Geodesy and Frequency Transfer. *In: R. Haas, G. Elgered (eds.): Proc. 23rd EVGA Working Meeting*, 5–9.

Sekido, M., et al. (2021) A broadband VLBI system using transportable stations for geodesy and metrology: an alternative approach to the VGOS concept. *J Geod*, 95, 41.

Takefuji K., et al. (2012) High order sampling techniques of aliased signals for very long baseline interferometry. *Publ Astron Soc Pac*, 124(920): 1105.

Teke K., et al. (2008) VLBI baseline length repeatability tests of IVS-R1 and IVS-R4 session types. *In: Finkelstein A, Baver KD (eds) IVS 2008 general meeting proceedings Measuring the future*, p 173.

Ujihara H., et al. (2019) Development of wideband Antennas. *International Symposium on Advancing Geodesy in a Changing World*, APR 2019.

Xu M.H., et al. (2019) Structure effects for 3417 celestial reference frame radio sources. *Astrophys J Suppl Ser*, 242(1): 5.

Single- and Multi-day Combination of VLBI and GNSS Data for Consistent Estimation of Earth Rotation Parameters

Lisa Lengert, Claudia Flohrer, Anastasiia Girdiuk, Hendrik Hellmers, and Daniela Thaller

Abstract The current activities of the Federal Agency for Cartography and Geodesy (BKG) towards a combined processing of VLBI and GNSS data on the normal equation level are presented. The main goal of the combined analyses of the two different space-geodetic techniques is the improvement of the consistency between the techniques through common parameters, i.e., mainly Earth Rotation Parameters (ERPs), but also station coordinates and tropospheric parameters through local ties and atmospheric ties, respectively. Based on the combination using GNSS Rapid and VLBI Intensive sessions on a daily and multi-day level, we generate a consistent, low-latency ERP time series with a regular daily resolution for polar motion and dUT1. We achieved in this way a significant improvement of the dUT1 time series and a slight improvement of the pole coordinates time series for the ERPs from the combined processing compared to the individual technique-specific ERPs. We extend the combination of GNSS and VLBI Intensive sessions by adding VLBI 24-hour sessions in order to exploit the benefit of the combination to its maximum extent.

Keywords Combination, VLBI, VLBI Intensives, GNSS, space-geodetic techniques, ERP, EOP, consistency

---

Lisa Lengert · Claudia Flohrer · Anastasiia Girdiuk · Hendrik Hellmers · Daniela Thaller
Federal Agency for Cartography and Geodesy, Section G1, Richard-Strauss-Allee 11, Frankfurt am Main, 60598 Germany

1 Introduction

The Earth Orientation Parameters (EOPs) describe the irregularities of the Earth's rotational axis in space. They are represented by the five following components, allowing the transformation between the International Celestial Reference Frame (ICRF) and the International Terrestrial Reference Frame (ITRF): the polar motion x_p and y_p, the difference dUT1 between Universal Time UT1 and Coordinated Universal Time UTC and the celestial pole offsets δX and δY. The Length-of-Day (LOD), which represents temporal changes of dUT1, plays an important role in our combination approach (Thaller , 2008; Blossfeld , 2015). A precise and rapid knowledge of the EOPs is required for a variety of different applications, for example the satellite orbit determination for the global navigation satellite systems.

Within the IERS, EOPs are derived by the combination of observation data from different space-geodetic techniques. The most important techniques are Global Navigation Satellite Systems (GNSS), Doppler Orbitography Integrated by Satellite (DORIS), Satellite Laser Ranging (SLR) and Very Long Baseline Interferometry (VLBI) (IERS Annual Report 2018 , 2020). The combination of the observation techniques can be performed on three different levels which are listed here in descending order according to their consistency with regard to the estimated parameters: the parameter level, the normal equation (NEQ) level and the observation level, which assures the highest consistency. (Thaller , 2008; Seitz , 2012; Blossfeld , 2015)

Hitherto publicly available low-latency EOP time series, the so-called *Bulletin A*, provided by the "Rapid Service/Prediction Centre" (RS/PC) of the

Table 1 Different contributions of GNSS as well as 24 h VLBI R1/R4 sessions and 1h VLBI INT sessions to the determination of EOPs.

	GNSS	VLBI INT	VLBI R1/R4
x_p, y_p	✓	✗	✓
$\dot{x}_p, \dot{y}_p$	✓	✗	✓
dUT1	✗	✓	✓
LOD	✓	✗	✓
δX, δY	✗	✗	✓

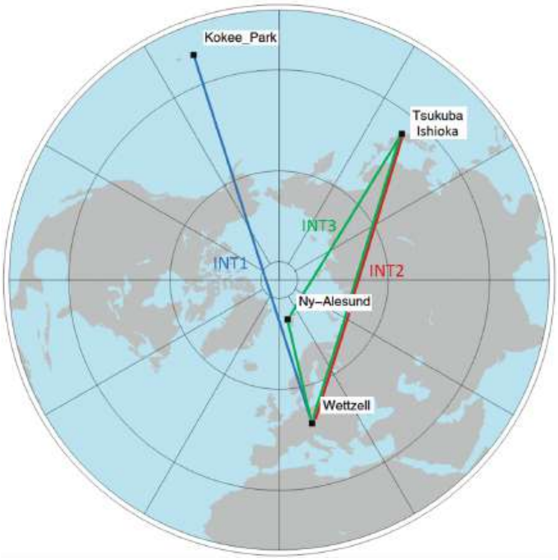

Fig. 1 Three network configurations of VLBI INT sessions for the daily monitoring of dUT1 (Luzum et al. in J Geod (2010) 84:399–402 DOI 10.1007/s00190-010-0372-8, own modifications added)

International Earth Rotation and Reference Systems Service (IERS) results from the combination of individual space-geodetic technique solutions, which represents the least rigorous combination method. (https://www.iers.org/IERS/EN/DataProducts/EarthOrientationData/eop.html, last access: 6 May 2021)

We want to use the combination at NEQ level for the generation of a consistent, high-precision ERP product, with a daily resolution and shortest possible latency of two days or less. Each of the space-geodetic techniques contributes differently to the estimation of geodetic parameters. In this paper we focus on the combination of VLBI and GNSS data.

As shown in Table 1, GNSS allows primarily the estimation of pole coordinates as well as LOD which can be derived with high internal accuracy (Meindl et al., 2014; Thaller et al. , 2014). The dUT1 parameter is the most variable quantity among the EOPs with significant unpredictable variations. These can only be measured with VLBI, which is the only space-fixed technique. (Thaller , 2008)

An similar approach for a rapid ERP determination by combining VLBI Intensive and GNSS sessions is given by Hellmers et al. (2020).

We use two different types of VLBI experiments. For the determination of all five components of the EOPs, the so-called IVS-Rapid 24-hour observation campaigns are organized every Monday (R1) and Thursday (R4), involving eight to ten globally distributed antennas. The latency of this session types can be up to 15 days (Nothnagel et al., 2017). Additionally, for the daily monitoring of dUT1, the IVS organizes daily sessions of 1 hour duration including two or three antennas. These baselines are characterized by a large east-west extension, which is sensitive to dUT1. Figure 1 shows the network configurations for the three different so-called VLBI Intensive (INT) session types (INT1, INT2 and INT3), which are currently conducted with a repeating schedule. The latency of the VLBI INT sessions is about two days or less. (Nothnagel et al., 2008, 2017; Dermanis et al., 1978)

In conclusion, the ERP sensitivities of GNSS and VLBI INT complement each other so a daily and consistent set of all ERPs with short latency can be estimated by combining data of both techniques (see Table 1). The additional combination with VLBI R1 and R4 sessions enables a stabilization of all ERPs two times a week.

In order to use past-day information to stabilize the estimates and minimize random deviations, multi-day intra- and inter-technique combinations are investigated. In this combination approach ERPs are estimated as continuous, up to seven day long, piece-wise linear polygons.

2 Method

In this research, SINEX (Solution INdependent EXchange format) files for the VLBI INT and R1/R4 as well as GNSS Rapid sessions in the period from June 3, 2014 to September 28, 2019 are used, provided by the

BKG IVS AC and CODE IGS AC, respectively (Engelhardt et al., 2020; Dach et al., 2016).

VLBI NEQs from the BKG SINEX files explicitly contain pole coordinates, dUT1 and the respective rates as well as station coordinates. The VLBI R1/R4 NEQs also include celestial pole offsets δX and δY and source coordinates. The ERPs are parameterized at the middle observation epoch (MOE) of the respective VLBI session (Thorandt et al., 2017). Additionally to all ERP offset components, the GNSS NEQs from the CODE SINEX files explicitly include station coordinates, geocenter coordinates and satellite phase center offsets in Z-direction. The ERP parameterization is a continuous piece-wise linear (PWL) polygon with offsets at the day boundaries including the GNSS observations of the current and the two previous days (Dach et al., 2016).

Figure 2 summarizes the processing steps and the combination procedure. The resulting solutions are labeled with “VLBI INT”, “n-VLBI INT”, ”VLBI R1/R4” “GNSS”, “n-GNSS”, ”COMBI” and “n-COMBI”, with “n” being the total number of combined days.

In the first step of the processing, each NEQs extracted from the respective technique-specific SINEX file undergo first several transformations to get a consistent datum-free input for the subsequent combination process. In case of VLBI, the incoming NEQs undergo first a parameter transformation step. The parameterization of the ERPs is transformed from offset/drift representation to a PWL representation with offsets at 0 h and 24 h. In the case of VLBI R1/R4, the day with the majority of observations is selected (usually Tuesday and Friday). In addition, the parameter a priori values of all technique-specific NEQs are transformed to a consistent set, which is used for all solutions in this study: *IERS 14 C04* and *ITRF2014* for the ERPs and station coordinates, respectively (Bizouard et al., 2018; Altamimi et al., 2016). If no ITRF coordinates are available, the a priori values provided in the SINEX are retained. In the case of GNSS, a LOD-bias correction must be performed in order to reduce the drift of the estimated GNSS dUT1 time series due to orbit model deficiencies of the GNSS satellites. Therefore the dUT1 parameters are corrected for the detected mean LOD bias of 7.7 $\mu s/d$. Furthermore, the ERPs of the first two days of the 3-day polygon are pre-eliminated.

In principle two independent inter-technique combination approaches are examined:

1. Combination of GNSS with VLBI INT only
2. Combination of GNSS with VLBI R1/R4

For the first combination approach, shown on the left side of Figure 2, multi-day inter-technique combined NEQs for VLBI INT and GNSS are computed, in which ERPs are stacked to generate continuous, up to seven day long, piece-wise linear polygons (n-VLBI INT, n-GNSS). In the next step, these n-VLBI INT and n-GNSS NEQs are stacked with an optimal weighting factor in order to obtain the inter-technique combined n-COMBI NEQs.

For the second combination approach, shown on the right side of Figure 2, the GNSS and VLBI R1/R4 NEQs are combined session-wise when both sessions are available (in an optimal case two times a week). These single-technique NEQs also have to be re-scaled before stacking.

With the aim to create a operational ERP product, we have chosen for all inter-technique combinations a constant scaling factor for the technique-specific NEQs, which nearly reflects the ratio of the observation times of both techniques (1 VLBI INT : 24 VLBI R1/R4 : 72 GNSS). The detailed procedure is described and evaluated in Lengert et al. (2021).

After applying constraints, all these datum-free NEQ systems can be solved for the estimated parameters and used for the internal validation of the combined ERP solutions. In summary, seven different solution types are obtained, which are listed in the last line of Figure 2.

For the combination procedure we use the ”Combination and Solution” library of the ”DGFI Orbit and Geodetic parameter estimation Software” (DOGS-CS), developed at DGFI-TUM (Deutsches Geodätisches Forschungsinstitut, Technische Universität München) (Gerstl et al., 2004).

3 Results

Figure 3 shows the WRMS of the six extracted dUT1 sub-series, resulting from the multi-day n-VLBI INT solution and inter-technique combinations n-COMBI with $n = 7$ w.r.t. *IERS Bulletin A* analyzed at 12 h

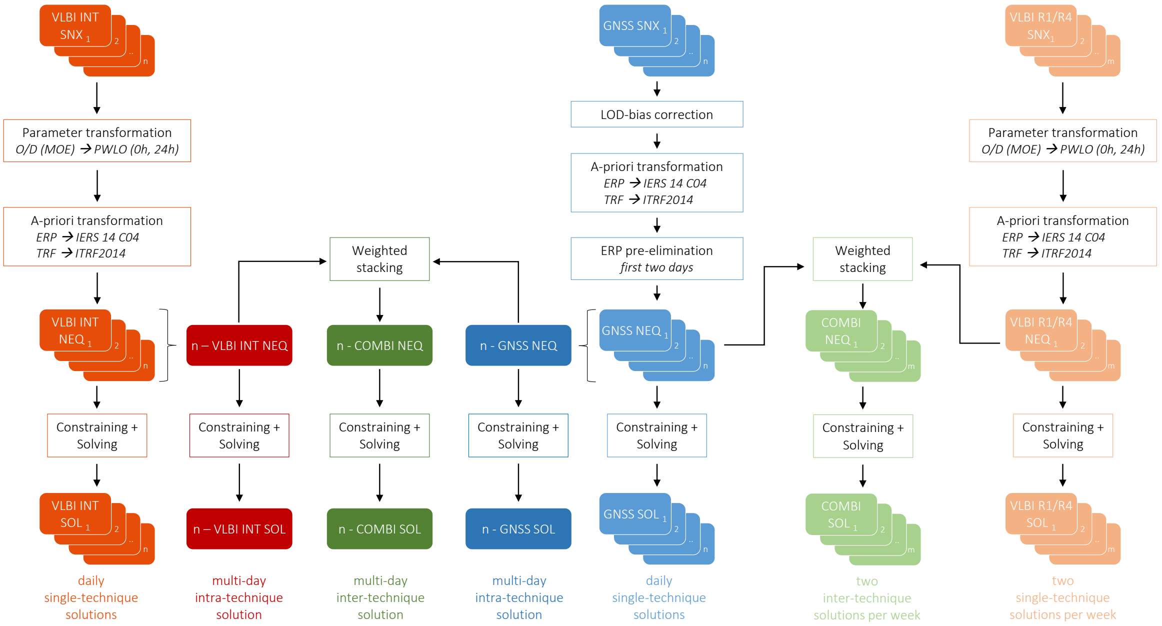

Fig. 2 Schematic representation of the entire combination strategy starting with the daily single-technique analysis of the VLBI INT, VLBI R1/R4 and GNSS RAP data (SINEX), followed by multi-day intra-technique combinations of both daily available techniques, and finally the weighted multi-day and session-wise inter-technique combinations. (from Lengert et al. (2021) with modifications)

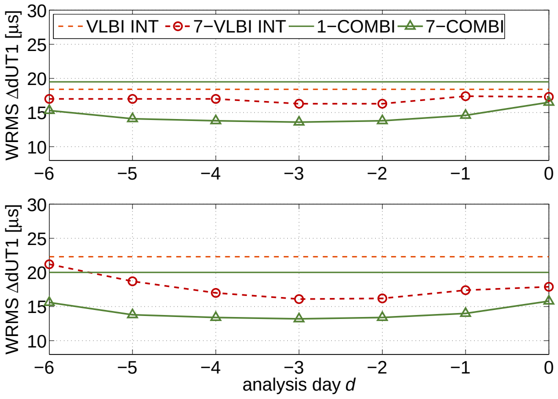

Fig. 3 WRMS of 1-day and 7-day VLBI-INT-only and inter-technique combined dUT1 series compared to *IERS Bulletin A* (top: INT MOE, bottom: 12 h epochs).

epochs (top) and INT MOEs (bottom) of each analysis day d ($d = 0,\ldots,-6$). The WRMS values of the single-day VLBI INT solution (VLBI INT) (with fixed LOD a priori values) and the session-wise inter-technique combination (1-COMBI) are depicted additionally. All WRMS values can be found additionally in Table 2.

An interpolation of the estimated dUT1 values to the MOEs of the INT sessions, see Figure 3 (top), shows an almost constant level of accuracy for all sub-series of the analysis day d. The WRMS values are slightly lower than that of the conventional daily single-technique solution VLBI INT. Accordingly, no significant improvement of the dUT1 parameter at INT MOEs can be achieved by stacking consecutive days.

When we focus on the 12-h series in Figure 3 (bottom), it can be recognized, that the WRMS values of ΔdUT1 are significantly lower than that of the single-technique solution.

The advantage of the multi-day solution is that no constraining of the LOD parameter is required in order to achieve at least the same precision level of dUT1. We also conclude that a significant improvement can be achieved for epochs laying outside the observation period of the VLBI INT sessions.

For the session-wise inter-technique combination of VLBI INT and GNSS (1-COMBI) a significant improvement can only be seen for epochs laying outside of the VLBI INT MOEs. In case of the multi-day inter-technique combination (7-COMBI), a significant improvement of the ΔdUT1 WRMS compared

Table 2 WRMS of the estimated ERPs w.r.t. the reference (*IERS Bulletin A* or *IERS 14 C04*) derived from the single-day and some selected 7-day VLBI, GNSS and COMBI solutions, analyzed at 12 h and INT MOE.

Solution ID	ΔdUT1 [μs] INT MOE	ΔdUT1 [μs] 12 h	Solution ID	Δx_p [μas] 12 h	Δy_p [μas] 12 h
VLBI INT	18.4	22.3	GNSS	49.4	42.3
7−VLBI(@0)	17.3	17.9	7−GNSS(@0)	47.6	42.3
7−VLBI(@-3)	16.3	16.1	7−GNSS(@-3)	43.9	35.2
7−VLBI(@-6)	17.0	21,2	7−GNSS(@-6)	44.9	34.9
1−COMBI	19.5	20.0	1−COMBI	48.7	41.9
7−COMBI(@0)	16.5	15.8	7−COMBI(@0)	46.0	42.2
7−COMBI(@-3)	13.6	13.2	7−COMBI(@-3)	43.5	35.3
7−COMBI(@-6)	15.3	15.6	7−COMBI(@-6)	44.4	34.7
VLBI R1/R4	-	9.5	VLBI R1/R4	126.0	126.8
COMBI	-	10.9	COMBI	49.8	42.3

to the single-day and multi-day single-technique solutions (VLBI INT, *n*-VLBI INT) as well as compared to the single-day combined multi-technique solution (1-COMBI) can be observed for INT MOEs as well as for 12-h epochs. We observe an almost symmetrical, parabolic behaviour of the WRMS with minimal values at the middle day.

The resulting WRMS of the second combination approach, the session-wise combination of VLBI R1/R4 and GNSS (COMBI), are summarized in Table 2. The WRMS of the combined dUT1 series w.r.t. *IERS Bulletin A* is 10.9 μs, thus, almost at the same level as the high-quality VLBI R1/R4 dUT1 with a WRMS of 9.5 μs.

The same behaviour can be detected for both pole coordinates. The WRMS values w.r.t. *IERS 14 C04* of the combined solution are 49.8 μas and 42.3 μas for x_p and y_p, respectively, and therefore almost at the same level as the high-quality GNSS pole coordinates with 48.7 μas and 41.9 μas.

4 Conclusions and outlook

So far, the publicly available ERP time series arise from the combination on parameter level. In this study, a more rigorous way for the combination, the combination on normal equation level, is used.

The combination of GNSS and VLBI based on homogenized, datum-free NEQs provides a full and consistent set of all ERPs.

Concerning the combination of GNSS and VLBI INT, the ability to determine polar motion and LOD with GNSS complements the estimation of dUT1 with VLBI INT. In conclusion, a daily and consistent set of all ERPs with a latency of 2 days or less can be determined by combining data of both techniques. Due to the daily resolution we are also able to stack the ERP of several consecutive days in order to stabilize the estimates. In case of the multi-day VLBI INT intra-technique solution, we can see a slight improvement of the dUT1 parameter at the middle observation epoch of the INT sessions and a significant improvement for epochs laying outside this period. In case of the multi-day inter-technique combined solution (7-COMBI), a significant improvement of the ΔdUT1 WRMS compared to the single-day and multi-day single-technique solutions (VLBI INT, *n*-VLBI INT) as well as to the single-day combined multi-technique solution (1-COMBI) can be achieved for INT MOEs and for 12 h epochs. In conclusion, merging of the continuous GNSS LOD and the high-quality, but limited to one hour per day, VLBI INT dUT1 results in a high-quality 24h-dUT1 product. Moreover, the accuracy is independent of the irregularity of the INT observation period.

Concerning the combination of GNSS and VLBI R1/R4, a consistent set of high-quality ERPs can be estimated two times a week.

In the following, we want to merge the strengths of all three session types, i.e., VLBI INT, VLBI R1/R4 and GNSS in one common combination approach. Based on the improved combination method, we want to generate a new operational BKG-EOP product. In this way, BKG will be the first institution (according to the current status) providing a complete and homogeneously combined EOP product with daily resolution and short latency (1-2 days) with open access for the international community.

References

Altamimi Z, Rebischung P, Métivier L, Collilieux X (2016) ITRF2014: A new release of the International Terrestrial Reference Frame modeling nonlinear station motions. *J. Geophys. Res.-Sol. Ea.*, 121, 6109—6131, https://doi.org/10.1002/2016JB013098.

Bizouard Ch, Lambert S, Gattano C, Becker O, Richard J.-Y. (2019) The IERS EOP 14C04 solution for Earth orientation parameters consistent with ITRF 2014. *J. Geodesy*, 93, https://doi.org/10.1007/s00190-018-1186-3.

Blossfeld M (2015) The key role of Satellite Laser Ranging towards the integrated estimation of geometry, rotation and gravitational field of the Earth. *Dissertation der Ingenieurfakultät Bau Geo Umwelt der Technischen Universität München, München 2015*, ISBN 978-3-7696-5157-7, 2015.

Dach R, Schaer S, Arnold D, Orliac E, Prange L; Susnik A, Villiger A, Grahsl A, Mervart L, Jäggi A, Beutler G, Brockmann E, Ineichen D, Lutz S, Wiget A, Rülke A, Thaller D, Habrich H, Söhne W, Ihde J et al. (2016) CODE Analysis center: Technical Report 2015. *Jean, Yoomin; Dach, Rolf (eds) IGS Technical Report 2015*, 25–43, Bern: IGS Central Bureau.

Dermanis A, Mueller I (1978) Earth rotation and network geometry optimization for very long baseline interferometers. *J B. Géod.*, 52, 131–158, https://doi.org/10.1007/BF02521695.

Engelhardt G, Thorandt V, Ullrich D, Girdiuk A, Halsig S, Iddink A, Jaron F, Karbon M, Nothnagel A (2020) BKG/IGGB VLBI Analysis Center. In: International VLBI Service for Geodesy and Astrometry 2017+2018 Biennial Report, edited by Armstrong KL, Baver KD, Behrend D. *NASA/TP-2020-219041; NASA Goddard Space Flight Center, Greenbelt, MD, USA*, 204–207.

Gerstl M, Kelm R, Müller H, Ehrnsperger W (2004) DOGS-CS: Kombination und Lösung großer Gleichungssysteme. *DGFI (Deutsches Geodätisches Forschungsinstitut) MG/01/1995/DGFI.*

Hellmers H, Thaller D, Blossfeld M, Kehm A, Girdiuk A (2020) Combination of VLBI Intensive Sessions with GNSS for generating Low latency Earth Rotation Parameters. *Adv. Geosci.*, 50, 49–56, https://doi.org/10.5194/adgeo-50-49-2019.

IERS (2020) Dick WR, Thaller D (eds) IERS Annual Report 2018. *International Earth Rotation and Reference Systems Service, Central Bureau. Frankfurt am Main: Verlag des Bundesamts für Kartographie und Geodäsie*, 207 pp., ISBN 978-3-86482-136-3.

Lengert L, Flohrer C, Girdiuk A, Hellmers H, Thaller D (2021) Single- and Multi-day Combination of VLBI and GNSS Data for Consistent Estimation of Low-Latency Earth Rotation Parameters. *To be submitted to JoG.*

Meindl M, Beutler G, Thaller D, Dach R, Schaer S, Jaeggi A (2014) A comment on the article “A collinearity diagnosis of the GNSS geocenter determination” by P. Rebischung, Z. Altamimi, and T. Springer. *J. Geodesy*, 89, 189—194, https://doi.org/10.1007/s00190-014-0765-1.

Nothnagel A, Schnell D (2008) The impact of errors in polar motion and nutation on UT1 determinations from VLBI Intensive observations. *J J. Geodesy*, 82, 863–869, https://doi.org/10.1007/s00190-008-0212-2.

Nothnagel A, Artz T, Behrend D, Malkin Z (2017) International VLBI Service for Geodesy and Astrometry: Delivering high-quality products and embarking on observations of the next generation. *J J. Geodesy*, 91, 711–721, https://doi.org/10.1007/s00190-016-0950-5.

Seitz M (2012) Comparison of Different Combination Strategies Applied for the Computation of Terrestrial Reference Frames and Geodetic Parameter Series. *The 1st International Workshop on the Quality of Geodetic Observation and Monitoring Systems (QuGOMS'11), International Association of Geodesy Symposia, edited by: Kutterer, H., Seitz, F., Alkhatib, H., and Schmidt, M., Springer, Cham,*, 140.

Thaller D (2008) Inter-technique combination based on homogeneous normal equation systems including station coordinates, Earth orientation and troposphere parameters, *Dissertation, Scientific TechnicalReport STR 08/15, Deutsches GeoForschungsZentrum*, ISSN 1610-0956, doi: 10.2312/GFZ.b103-08153.

Thaller D, Sosnica K, Dach R, Jaeggi A, Beutler G, Maraynen M, Richter B (2014) Geocenter coordinates from GNSS and combined GNSS-SLR solutions using satellite co-locations. *Earth on the Edge: Science for a Sustainable Planet, International Association of Geodesy Symposia. International Association of Geodesy Symposia*, 139, 129–134, doi: 10.1007/978-3-642-37222-3-16.

Thorandt V, Engelhardt G, Ullrich D, Arzt T, Halsig S, Holst C, Idding A, Jaron F, Nothnagel A (2017) BKG/IGGB VLBI Analysis Center. *International VLBI Service for Geodesy and Astrometry 2015+2016 Biennial Report, edited by: Baver, K. D., Behrend, D., and Armstrong, K. L.*, NASA/TP-2017-219021.

Improving the S/X Celestial Reference Frame in the South: A Status Update

A. de Witt, S. Basu, P. Charlot, D. Gordon, C. Jacobs, M. Johnson, H. Krásná, K. Le Bail, F. Shu, O. Titov,
M. Schartner

Abstract Catalogues of positions of compact extragalactic radio sources, including the ICRF-3, are generally weaker in the south by factors of 2 or more in both density and precision. In 2018 we started a campaign to improve the S/X celestial reference frame in the south by upgrading existing IVS astrometric observing programmes. Our efforts were mainly focused on the Celestial Reference Frame (CRF) and Celestial Reference Frame Deep South (CRDS) sessions, which are dedicated astrometric observing programmes of sources at mid- and southern declinations. In particular, the data rate of the CRF and CRDS sessions were increased from 256 Mbps to 1 Gbps and the pool of sources were increased by a factor of two. The scheduling was also optimised to allow for simultaneous astrometric and imaging observations, and the CRF network was revised for improved uv-coverage. We provide details of our efforts, to date, to improve both the density and precision of the southern celestial reference frame, as well as our efforts to map and monitor the sources to quantify non-point-like structure and measure jet directions. We also discuss planned changes and upgrades, noting that the Australian 12-m telescopes are transitioning to broadband and may not be available for S/X astrometric observing in future. We also present the ideas and role of the newly-established IVS-CRF committee to improve the celestial reference frame in the south.

Keywords Astrometry, VLBI, Celestial Reference Frame, Southern Hemisphere, quasars

1 Introduction

At present there are still only a few VLBI-capable radio telescopes in the Southern Hemisphere and even fewer that regularly participate in astrometric and geodetic VLBI experiments. For this reason current radio astrometric catalogues remain weak in the south, with a significant hemispheric disparity in source distribution, density, and source coordinate accuracy. The second realization of the International Celestial Reference Frame (ICRF-2, Ma et al., 2009) was dominated by data from the north, and despite many efforts in recent years to improve this imbalance, current radio astro-

---

Aletha de Witt · Sayan Basu
South African Radio Astronomy Observatory (SARAO),
Hartebeesthoek, South Africa

Patrick Charlot
Laboratoire d'astrophysique de Bordeaux, Univ. Bordeaux,
CNRS, France

David Gordon · Megan Johnson
United Stated Naval Observatory (USNO), United States

Christopher S. Jacobs
Jet Propulsion Laboratory,
California Institute of Technology/NASA, United States

Hana Krásná
Technische Universität Wien (Tu Wien), Austria
and Astronomical Institute of the Czech Academy
of Sciences, Czech Republic

Karine Le Bail
Onsala Space Observatory (OSO)/Chalmers University of
Technology, Sweden

Fengchun Shu
Shanghai Astronomical Observatory (SHAO), China

Oleg Titov
Geoscience Australia, Australia

Matthias Schartner
ETH Zurich, Switzerland

metric catalogues are still weaker in the south by factors of 2 or more in both density and precision.

The efforts toward the realisation of the third International Celestial Reference Frame (ICRF-3, Charlot et al., 2020), placed specific emphasis on improving the southern celestial reference frame. However, while the ICRF-3 shows significant improvements in the south, the south has not yet reached parity with the north. Various efforts are currently underway to correct this. In particular, a dedicated campaign was started in 2018 to improve the S/X celestial reference frame in the south by upgrading record rates and improving source lists and schedules for existing IVS astrometric observing programmes (e.g. de Witt et al., 2019). In future, the newly established IVS-CRF Committee[1] will coordinate these efforts to improve the celestial reference frame in the south.

It is also important to map the structures of the celestial reference frame sources on a regular basis, as the effect of source structure on astrometric VLBI positions can be significant and the structure and flux density variability are directly related to the precision of geodetic solutions (e.g. Charlot, 1990). Unfortunately there have only been a few imaging sessions of reference sources in the far south ($\lesssim -45^\circ$) and dedicated programmes to map and monitor source structure are difficult to obtain on astronomical VLBI networks. However, dedicated campaigns to map and monitor the sources in the far-south are underway, and efforts to image source structure from existing astrometric observations in the south have shown that dedicated imaging campaigns may indeed be possible for southern sources (e.g. Basu et al., 2018).

This paper provides an update on recent progress that was made towards improving the southern celestial reference frame, with specific emphasis on the progress made towards improving the southern astrometric IVS observing programmes, in particular the Celestial Reference Frame Deep South (CRDS) sessions. It also provides an update on the sources observed as part of the astrometric sessions of the Asia-Oceania VLBI group for Geodesy and Astrometry (AOV). An update on the progress towards improving the Celestial Reference Frame (CRF) sessions will be provided in a follow-up paper.

2 Current Status

The most recent S/X astrometric solution from August 2020 (sx-gsfc-200827, David Gordon) show some improvement over previous solutions (e.g. de Witt et al., 2019). However, the number of sources is still a factor of 2 less in the far-south ($\leq -30^\circ$), and while the number of sessions per source are roughly the same in the north and the south, the average number of observations per source is also factor of 2 less in the far-south. Figure 1 shows the sky coverage from the latest S/X astrometric solution, colour coded by the Right Ascension ($\alpha\cos(\delta)$) and declination (δ) precision. We find that the median σ in $\alpha\cos(\delta)$ is almost 1.5 times weaker in the far-south and that the median σ in δ is a factor of 2.53 weaker in the far-south. It is clear that not only do we need more southern baselines, but we also need more sources in the far-south, and we also need to improve the spatial coverage in the south. It should be noted that the declinations are consistently worse than the right ascensions, even at the equator, and it is clear that we also need more north-south baselines.

3 CRDS Sessions

The CRDS sessions (now abbreviated to CRD sessions) are part of an IVS astrometric program focussing on the Deep Southern Sky. In November 2013 the data rate of these sessions was increased from 128 to 256 Mbps. On 24 January 2018 (starting with CRDS-93), the data rate was further increased to 1 Gbps, which allowed for the detection of weaker sources and more efficient scheduling (for more details see de Witt et al., 2019). With the increase in the data rate to 1 Gbps, the frequency sequence was also revised and was optimised to avoid S-band RFI.

The CRDS source list was also updated to include an additional 216 southern sources (before CRDS-93 only ICRF-2 defining sources were included), which at the time were sources observed in less than 10 sessions and that had a flux density of > 350 mJy. Priority was given to the 124 sources from this list that are in the far-south and for which no VLBI images were available (note that CRDS-94 was a special session that was used to image and analyse potential defining sources for the ICRF-3). At the same time, the scheduling of these sessions was optimised for both astrometry and

---

[1] https://ivscc.gsfc.nasa.gov/about/com/crfc/index.html

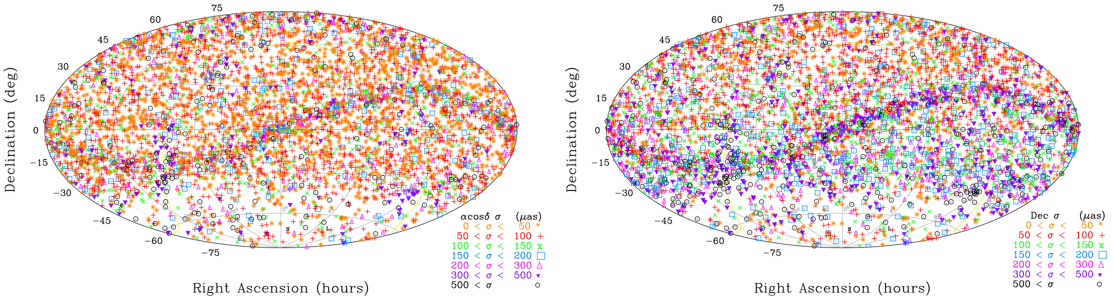

Fig. 1 The distribution of sources from the most recent S/X astrometric solution (sx-gsfc-200827) showing the formal uncertainties in $\alpha\cos(\delta)$ on the left and δ on the right.

imaging. The new schedules were generated using the NRAO scheduling software SCHED[2]. From June 2019 onward, starting with CRD-102, the schedules were generated using the new VLBI scheduling software for geodesy and astrometry, VieSched++ (Schartner and Böhm , 2019).

The CRDS network has always consisted of only a few stations, and prior to CRDS-89, there were six stations that regularly participated in the CRDS sessions. In July 2017 (CRDS-89), the Hobart 12-m antenna (Australia) was upgraded to a VGOS-style broadband receiver, leaving only five stations. More recently, in May 2019 (CRD-102) the O'Higgings 9-m antenna (Antarctica) was added to the CRDS network, but in June 2019 the Katherine 12-m antenna (Australia) was also converted for VGOS. In February 2020 (CRD-105) the Aggo 6-m antenna (Argentina) was added to the CRDS network, bringing the total number of stations back to six (see Figure 2), although at some point the Yarragadee 12-m antenna (Australia) will also move to broadband, However, both the Hobart and Katherine 12-m antennas have been used in locally organised mixed-mode observations together with the traditional S/X telescopes and hopefully the Australian 12-m antennas will re-join the CRDS sessions in the near future.

The statistics obtained from the IVS analysis reports for the CRDS sessions (e.g. the number of sources scheduled per session or the number of observations per source), provide valuable information in terms of the performance of these sessions. From CRDS-93 onward the statistics show that the majority of sources in a session were scheduled to be observed in at least 4 scans and with four or more stations per scan, to enable imaging. However, from a scheduling perspective, achieving at least 4 scans per source is a very hard scheduling constraint to achieve with a small network. One of the open problems, evident from the session statistics, is that only a small percentage of the observations from the CRDS sessions are actually used for analysis (on average $\sim 44\%$). However, closer inspection of the analysis reports show that the main contributor to this high failure rate is the long baseline observations to smaller antennas. The Aggo and O'Higgins antennas both have small dishes with large SEFD's (> 10000 Jy) and are mostly tagged along in CRDS schedules. Some proposed solutions to improve the CRDS sessions include:

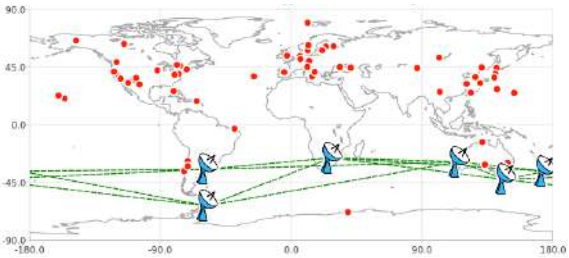

Fig. 2 The distribution of the six antennas that currently make up the CRDS network; the Aggo 6-m antenna in Argentina, the HartRAO 26-m antenna (Hh) in South Africa, the Hobart 26-m antenna (Ho) in Australia, the O'Higgins 9-m antenna (Oh) in Antarctica, the Warkworth 12-m antenna (Ww) in New Zealand, and the Yarragadee 12-m antenna (Yg) in Australia.

- increasing the scan length for weak sources (this has already been done for CRD-114 onward).
- moving to SNR based scheduling (only if correct flux information is available).
- increasing the data rate to 2 Gbps.
- adding more large, sensitive antennas.

---

[2] http://www.aoc.nrao.edu/software/sched/index.html

One of the biggest issues in moving to SNR based scheduling for the CRDS sessions, is that many of the southern sources have either unreliable or no flux density information available. Figure 3 shows an example of the flux density information available for the source 1424-418 at X-band. The available flux density information was obtained from the *sked* flux catalogue[3] (these values are empirical fluxes based on the individual IVS sessions' SNRs and averaged over time). The *sked* flux catalogue is currently used for SNR-based scheduling of all IVS geodetic and astrometric sessions. Flux density information was also obtained from available images of 0424-418 in the Bordeaux VLBI Imaging Database[4] (BVID) and from the CRDS imaging campaign (one epoch only). The flux time series in Figure 3 shows some big differences between the IVS values and the flux densities obtained from the BVID (in particular after 2010), while the CRDS flux density values seem to agree well with the BVID. The source 1424-418 is an example of a well observed source with multi-epoch images, but for many sources further south there are very little or no images available and it is uncertain (as evident from this example) how accurate the available flux densities from the *sked* flux catalogue would be.

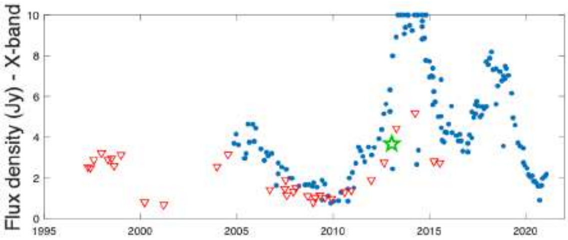

Fig. 3 Flux values in X-band of the source 1424-418 as reported in the *sked* flux catalogue (blue dots), and from the BVID (red triangles) and CRDS imaging campaign (green star).

A campaign to image southern celestial reference frame sources using the CRDS sessions started in January 2013 (see e.g. Basu et al., 2018), and the imaging of eleven CRDS sessions has been completed to date. Imaging of the older sessions, prior to CRDS-93, was challenging because of poor sensitivity and poor uv-coverage. Amplitude calibration is also difficult, in general, since system temperature and gain curve information is not available for all of the stations. In addition, because of the already small network, some sessions end up with only three or four participating stations (e.g. CRDS-93 and 99), and some these sessions are not useful for imaging. Figure 4 shows the contour maps for a representative sample of five sources, taken from more recent CRDS sessions that were observed during 2018 and 2019. Three of these sources, 0302-623, 0454-810 and 1925-610 are ICRF-2 defining sources. The source 0302-623 shows poor astrometric quality due to its extended structure and was subsequently removed as a defining source. The sources 0454-810 and 1925-610 are also ICRF-3 defining sources. However, the source 1925-610 shows a secondary component and its status as a defining source should be revisited in future, as indicated in the ICRF-3 paper.

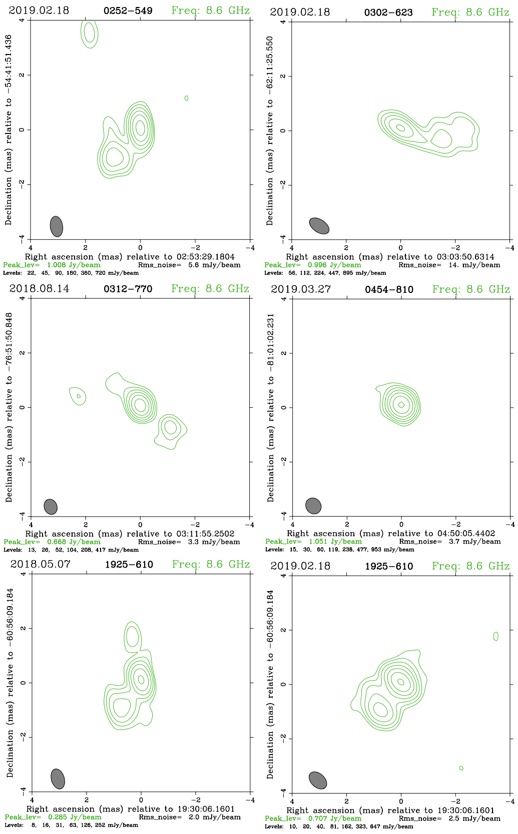

Fig. 4 Contour plots for sources 0252-549 and 0302-623 (top panel), 0312-770 and 0454-810 (middle panel), and 1925-610 (bottom panel) at 8.6 GHz from CRDS sessions between 2018 and 2019. North is Up and East is to the Left. The FWHM beamsize is graphically indicated in the bottom left corner.

---

[3] https://github.com/nvi-inc/sked_catalogs

[4] http://bvid.astrophy.u-bordeaux.fr/

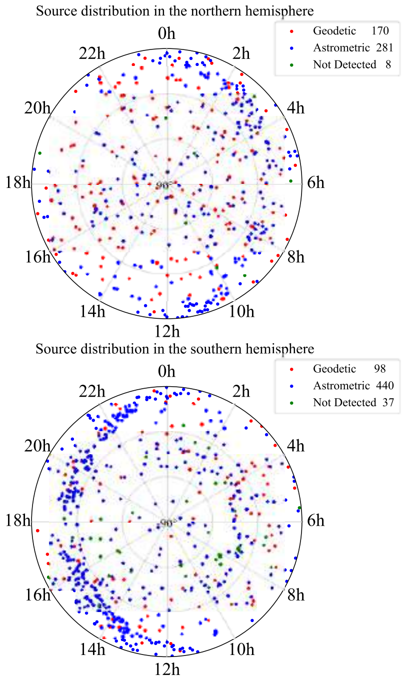

Fig. 5 Distribution of the 1034 sources observed as part of the AOV astrometric sessions. The astrometric sources that were detected are shown in blue, and the sources that were not detected are shown in green. The sources shown in red are sources that are listed as good geodetic sources in the *sked* source catalogue.

4 AOV Sessions

The AOV group is composed of 5 countries (New Zealand, Australia, Japan, China and South Korea) and 17 participating telescopes. The programme was launched in 2015 and one of the goals is the astrometry of weak sources with an emphasis on the ecliptic plane and Southern Hemisphere. All of the astrometric sessions were observed at a data rate of 1 Gbps. So far 1034 sources have been observed, including 861 ICRF-3 sources and a few radio stars. From the original 1034 sources a total of 989 were detected at S/X dual band. The median values of the flux densities are 0.26 Jy at X-band and 0.24 Jy at S-band. Figure 5 shows the Northern and Southern Hemisphere distribution of the 1034 sources observed as part of the AOV astrometric sessions. The AOV is now considering the source list for the next AOV astrometric sessions.

5 Conclusions and outlook

Our goal is to improve the S/X-band frame in the south by at least a factor of 2 in density and 2.5 in precision, in order to reach parity with the north. To achieve this, the IVS-CRF committee recommends these actions:

- Increase southern IVS session data rate to 2 Gbps.
- Increase the number of south-south but also north-south baseline observations.
- Image all southern sources to quantify non-pointlike structure and to measure jet directions.
- Expand the southern source list and improve spatial coverage following ICRF-3 recommendations.
- Add more sensitive antennas in the south e.g. the Tidbinbilla 70-m antenna in Australia, the VLBA Saint Croix and Mauna Kea 30-m antennas, and the Kunming 50-m antenna in China.
- Add the Warkworth 30-m antenna in New Zealand in single-frequency mode (X-band only and using external ionosphere data).
- Address RFI issue by using single-frequency mode for the Hobart 26-m antenna in Australia and other stations that suffer from severe S-band RFI issues.

Acknowledgements

AdW & SB thank the NRF for sponsorship. CSJ thanks US Gov. sponsorship under NASA contract. Copyright 2021. All rights reserved

References

Charlot P. (1990) Radio-source Structure in Astrometric and Geodetic Very Long Baseline Interferometry. *AJ*, 99, 1309.

Charlot P. et al. (2020) The 3rd realization of the International Celestial Reference Frame by VLBI. *A&A*, 644, A159.

de Witt A. et al. (2019) Improving the S/X Celestial Reference Frame in the South. *IVS 2018 GM*, Sep 2019, 189–193.

Basu S. et al. (2018) Multi-epoch VLBI images to study the ICRF-3 Defining Sources in the Southern Hemisphere. *14th EVN Network Symposium & Users Meeting*, Nov 2018, 135.

Ma C. et al. (2009) The Second Realization of the International-Celestial Reference Frame by Very Long Baseline Interferometry. *IERS Technical Note 35*, 29, 2009.

Schartner M. and Böhm J. (2019) VieSched++: A New VLBI Scheduling Software for Geodesy and Astrometry. *PASP*, 131, 1002.

Source flux-density monitoring in the VGOS era

K. Le Bail, E. Varenius, R. Haas

Abstract Source flux density is used to prepare optimal schedules of geodetic VLBI experiments in scheduling software packages such as *Sked* and *VieSched*++. It enters in the determination of the scan length to reach the signal-to-noise target to ensure successful radio-source detection. We present a comparison of different available catalogs and summarize the main current issues. We also present the first preliminary results of short-baseline (75 m) VGOS flux-density monitoring carried out in early 2021 using the Onsala Twin Telescopes.

Keywords Source flux density, monitoring, Onsala Twin Telescopes

1 Introduction

Source flux density is an essential parameter to optimally schedule geodetic experiments in software packages as *Sked* (Gipson, 2010, 2012) and *VieSched*++ (Schartner and Böhm, 2019). Flux-density variations, although interesting in themselves for astrophysical reasons, may also be coupled to structure variations, which in turn may lead to variations in the effective source positions assumed for geodetic parameter estimation. However there is no regular flux-density monitoring project currently conducted in the IVS[1]. This paper presents an overview of how source flux-density monitoring is performed at Onsala Space Observatory using the Onsala Twin Telescopes: ONSA13NE (Oe) and ONSA13SW (Ow).

We first discuss the importance of regularly monitoring source flux density, particularly in the VGOS[2] era (Section 2). Three flux-density catalogs currently used in the VLBI community are compared in Section 3 focusing on three different radio-sources. We also reflect on a few reasons for the discrepancies we see in between these three catalogs. Finally, our preliminary results on flux-density monitoring on the short-baseline Oe to Ow is presented in Section 4.

2 Importance of source flux-density monitoring in the VGOS era

When scheduling geodetic experiments using *Sked*, the length of a scan[3] is calculated using the following equation (see Gipson (2012) for more details):

$$SNR = \frac{Flux}{\sqrt{SEFD_1 \times SEFD_2}} \sqrt{(CST \times ScanLen)} \times \eta \tag{1}$$

where *ScanLen* is the scan length, $Flux$ is the flux density of the observed radio-source as given in the catalog used for the scheduling, $SEFD_1$ and $SEFD_2$ are the System Equivalent Flux Density (SEFD) for each participating antenna, *SNR* is the Signal to Noise Ratio, *CST* is the product of the sample rate and the number of channels, and η is a factor that accounts for the number of bits sampled and how the correlation is done.

K. Le Bail, E. Varenius, R. Haas
Onsala Space Observatory, Chalmers University of Technology, Observatorievägen 90, 439 92 Onsala, Sweden

[1] International VLBI Service for Geodesy and Astrometry

[2] VLBI Global Observing System

[3] a scan is defined by the observation of a radio-source by several antennas during the same period

For S/X experiments, the target *SNR* is usually 20 for the X-band and 15 for the S-band. This corresponds to the minimum *SNR* value that the term on the right side of Equation 1 should reach.

Thus the optimal scan length depends, among other parameters, on flux density of the observed radio-source. If the flux density is larger than the actual one, the length of the scan will be larger too: the antennas will spend more time than necessary observing this given radio-source. In the case of a too short scan length, the observation of the given radio-source may lead to the non-detection since the necessary *SNR* may not be reached.

Another reason why we should closely look into source flux density is to derive source information from source flux-density variation. It brings information on the nature of the source.

3 Comparisons of current flux-density catalogs used in the VLBI community

For our comparisons, we focused on flux density from three origins:

- Individual IVS experiments: After each IVS experiment, flux-density values on the S-band and the X-band are re-evaluated for each radio-source of the experiment from a priori values. This data is not publicly available but it could be obtained from the VLBI group at Goddard Space Flight Center which is in charge of its maintenance, as well as the *Sked* flux catalog. The flux-density values corresponding to this data is called IVS/GSFC in the following text and IVS in the Figures legends.
- *Sked* flux.cat: This catalog contains the most current flux-density values derived from previously mentioned IVS/GSFC values and is used for scheduling purposes. It is publicly available on the *Sked* Git repository[4], maintained by the VLBI group mentioned above.
- BVID: The Bordeaux VLBI Image Database[5] provides flux-density values derived from VLBI images. BVID computes these images from a subset of experiments, mostly the IVS Research and Development with the VLBA (RDV) experiments.

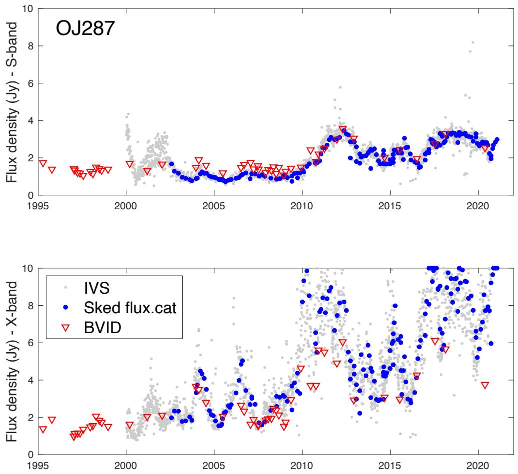

Fig. 1 Source flux density in Jy on the S-band (upper plot) and the X-band (lower plot) for the radio-source OJ287 as provided by IVS/GSFC (small grey circles), the *Sked* flux catalog (large blue circles) and BVID (red triangles) over the period 1995 to now.

Other VLBI catalogs we have not used but that should be mentioned are the Astrogeo Radio Fundamental Catalog (RFC[6]) and the USNO Radio Reference Frame Image Database (RRFID[7]).

This work focused on three sources : OJ287, 0059+581, and 3C418. These sources are all in the source catalog used to schedule geodetic experiments and are among the most observed in the IVS. In the following we compare the source flux-density values on the S-band and the X-band for each of these radio-sources as provided by IVS/GSFC, the *Sked* flux catalog, and BVID.

3.1 *OJ287*

Figure 1 shows the agreement between the flux-density values time series of the radio-source OJ287 given by IVS/GSFC, the *Sked* flux catalog, and BVID.

For the S-band, there is a very good agreement over the entire period. However a discrepancy can be seen beginning 2010 for the X-band between the IVS/GSFC time series and the BVID time series. The latest flux-

---

[4] https://github.com/nvi-inc/sked_catalogs/

[5] http://bvid.astrophy.u-bordeaux.fr/

[6] http://astrogeo.org/rfc/

[7] https://www.usno.navy.mil/USNO/astrometry/vlbi-products/rrfid

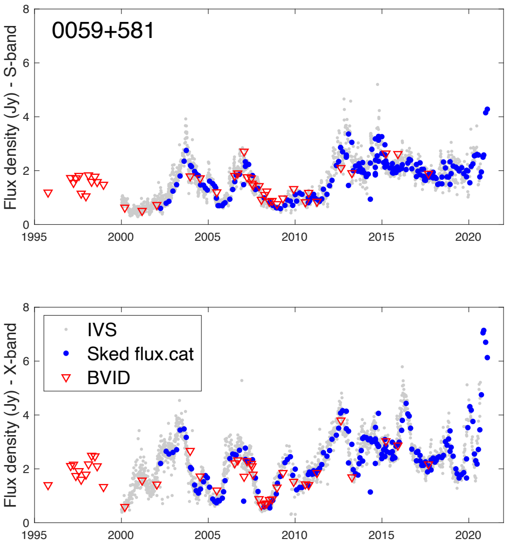

Fig. 2 Source flux density in Jy on the S-band (upper plot) and the X-band (lower plot) for the source 0059+581 as provided by the IVS/GSFC (small grey circles), the *Sked* flux catalog (large blue circles) and BVID (red triangles) over the period 1995 to now.

density value given by BVID, 3.76 Jy, was derived from data of the experiment RV140 (date 2020-05-19). For the same experiment, the IVS/GSFC value is 6.09 Jy.

If we take into account the flux-density value from the IVS/GSFC series, the radio-source OJ287 is stronger than for BVID which means the scan length calculated using the value from IVS/GSFC will be shorter than the scan length calculated using the value from BVID.

3.2 0059+581

As seen in Figure 2, there is a very good general agreement for the radio-source 0059+581 for all flux-density values presented. Let's note however that the latest values from BVID correspond to the experiment RV126 that happened on 2017-09-06. The values are 2.17 Jy for the X-band and 1.89 Jy for the S-band. The latest values available from IVS/GSFC is for R1962 on 2020-08-31: 5.21 Jy in X-band and 2.25 Jy in S-band.

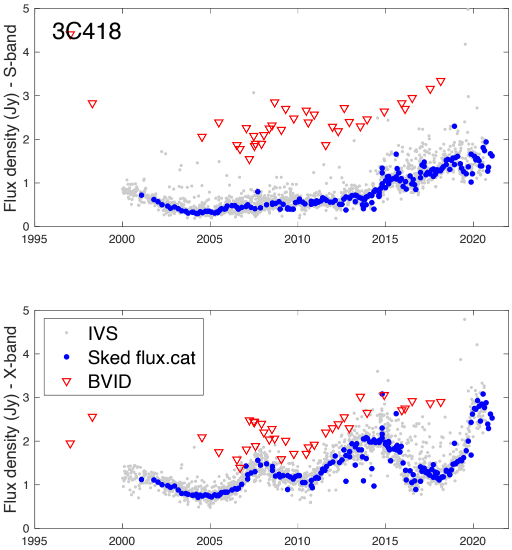

Fig. 3 Source flux density in Jy on the S-band (upper plot) and the X-band (lower plot) for the source 3C418 as provided by IVS/GSFC (small grey circles), the *Sked* flux catalog (large blue circles) and BVID (red triangles) over the period 1995 to now.

3.3 3C418

For the radio-source 3C418, there is a significant offset between the IVS/GSFC and *Sked* flux catalog values, and the BVID values on both bands (see Figure 3). The offset on the S-band is at a level of 1.5 Jy and on the X-band at a level of 0.5 Jy. The radio-source systematically appears stronger for BVID.

3.4 Discrepancies

The significant discrepancies between the flux-density values as given by IVS/GSFC and the *Sked* flux catalog, and the flux-density values given by BVID could be explained in various ways. First of all, it is necessary to mention that the two methods to compute the flux-density values are fundamentally different.

The BVID flux-density values are derived from images obtained from a very specific type of experiments (mostly RDV sessions in the past years).

For IVS/GSFC and the *Sked* flux catalog, the flux-density values are derived from re-evaluation of apriori values after observations and are used for scheduling purposes only. The values are scaled depending on other observation parameters, assuming the flux density of the source is constant during the experiment and the SEFDs of the antennas are only dependent on the elevation during the experiment.

Another plausible explanation for the offset between the different methods can also be the different effective UV-coverage and weighting used when obtaining the flux-density value. IVS observations are often long baselines, on which relatively large-scale structure is resolved out by the fringe pattern. Imaging observations, on the other hand, also include relatively shorter baselines, and if larger-scale structure is present, the total flux density obtained on short and long baselines will be different. Other plausible reasons may reside in calibration uncertainties and errors.

4 VGOS flux-density monitoring at Onsala Space Observatory

The VGOS-B experiments are a series of 1 h long observing sessions that were scheduled over the period December 2019 to February 2020. They were designed to be similar to the S/X Intensive sessions of the IVS but observing on the VGOS frequency bands. Three antennas were involved in the observations: Ishioka in Japan, Oe and Ow in Sweden. The experiments were scheduled with *VieSched*++ (Schartner and Böhm, 2019). More details can be found in Haas et al. (2021).

To monitor flux density, we focus on the short baseline Oe to Ow (75 m) for the experiment B21035 that observed on February 4, 2021. No results will be shown for the band A which was excluded due to local radio frequency interference (RFI). The data analysis was performed using the NRAO Astronomical Image Processing System (AIPS[8]).

The results focus on the three sources illustrated in Section 3 and are shown in Figure 4. The three plots of this Figure show the flux-density values in Jy in function of the frequency in GHz. The points in green correspond to the data calculated in this work: there are the flux densities in bands B, C and D, for each of the three sources, derived from the B21035 experiment, with an estimated error bar of 20%.

We compare these flux-density values with the flux-density values from the time series described in Section 3, using the most recent points (see Figures 1 to 3). For the IVS/GSFC time series (in grey), the most recent point is from September 2020 for the source OJ287, August 2020 for the source 3C418, and September 2020 for the source 3C418. The dates are indicated on the plots in the same color than the corresponding markers. In the same manner, the plots contain data from the *Sked* flux catalog in blue and the BVID in red. As an indicator at a higher frequency, we included data from the MOJAVE project (Lister et al., 2018) in black.

The values we are comparing are derived using different methods, different experiments and also corresponds to different epochs (within four years between IVS/GSFC, *Sked* flux catalog, BVID and the results of this work, within 8 years if we include MOJAVE data points).

However our results seem consistent with the different values we are comparing with. For the radio-source OJ287, our results show a very good agreement with all other values. For the source 0059+581, our results are the most consistent with the IVS/GSFC and the *Sked* flux catalog values. For 3C418, our results seem to diverge for the higher frequency. The source 3C418 is however a source that has shown some significant changes in the past five years so comparing with more recent values would be more representative.

5 Conclusions and outlook

The source flux density can evolve quite rapidly as seen in Figures 1 to 3, which has an impact on schedules and thus on actual observations (possibility of non detection for certain radio-sources). In the VGOS era, constantly monitoring source flux densities would be crucial to reach the levels of accuracy expected. Having special sessions dedicated to monitor flux density could be an appropriate solution to closely monitor radio-sources. However, in the long term, all IVS stations should obtain continuous system temperature measurements during all observations. This will allow flux-density measurements of all sources in all experiments, mapping of the structure of all sources which is one of the main sources of uncertainty in current geodetic parameter estimation, and optimal dual-linear-to-

---

[8] http://www.aips.nrao.edu/cook.html

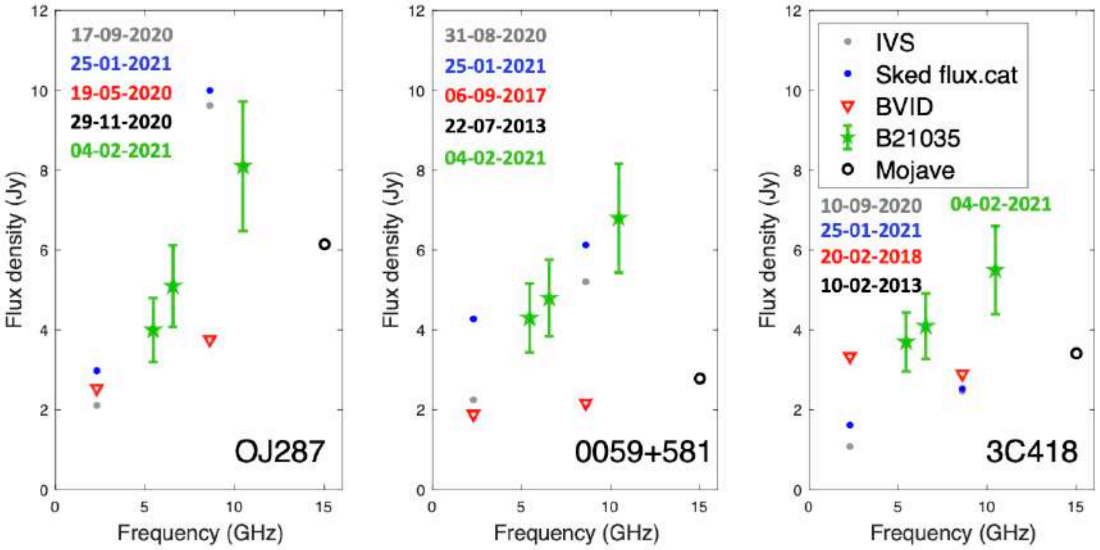

Fig. 4 Flux-density values in Jy of radio-sources OJ287 (left), 0059+581 (center), and 3C418 (right) in function of the observation frequency in GHz. Green points and dates correspond to the results of this work with estimated error bars at the level of 20 %. Grey, blue and red points and dates correspond to the latest flux-density values of IVS/GSFC, the *Sked* flux catalog and BVID respectively. See Section 3 for details on these values. Black points and dates correspond to the flux-density values given by the MOJAVE project (Lister et al., 2018).

circular-polarisation-conversion for modern antennas like VGOS.

In this work, we showed that it was possible to obtain reasonable flux densities for VGOS with apriori calibration for all bands, using methods discussed in Varenius (2021) (antenna calibration information for every station as a function of time). A publication detailing each step of this work, including calibration, is currently in progress.

6 Acknowledgements

This research has made use of data from the MOJAVE database that is maintained by the MOJAVE team (Lister et al., 2018).

References

Gipson J (2010) An Introduction to Sked. *IVS 2010 General Meeting Proceedings*, 77-84, D. Behrend and K. D. Baver (editors), NASA/CP-2010-215864.

Gipson J (2012) Sked: VLBI Scheduling Software. *Program Reference Manual, Goddard Space Flight Center*, https://ivscc.gsfc.nasa.gov/IVS_AC/sked_cat/SkedManual_v2018October12.pdf.

Haas R, Varenius E, Matsumoto S, Schartner M (2021) Observing UT1-UTC with VGOS. *Earth Planets Space*, 73:78, doi: 10.1186/s40623-021-01396-2.

Lister, M. L. and Aller, M. F. and Aller, H. D. and Hodge, M. A. and Homan, D. C. and Kovalev, Y. Y. and Pushkarev, A. B. and Savolainen, T. (2018) MOJAVE. XV. VLBA 15 GHz Total Intensity and Polarization Maps of 437 Parsec-scale AGN Jets from 1996 to 2017. *The Astrophysical Journal Supplement Series*, 234(1), doi: 10.3847/1538-4365/aa9c44.

Schartner M, Böhm J (2019) VieSched++: A New VLBI Scheduling Software for Geodesy and Astrometry. *Publications of the Astronomical Society of the Pacific*, 131, 084501, doi: 10.1088/1538-3873/ab1820.

Varenius E (2021) Station Amplitude Calibration: Why we need it and how to do it. *Seminar of the VGOS Technical Committee (VTC) meeting*, April 08, 2021, https://vlbi.org/2021/04/12/seminar-stations-amplitude-calibration/.

Improving the efficiency of the AuScope VLBI observations through dynamic observing

L. Chin Chuan, L. McCallum, J. McCallum, G. Molera Calvés, T. McCarthy

Abstract The AuScope VLBI network actively participates in the IVS S/X observing program and aims to achieve compatibility with the future geodetic VLBI system: VGOS. However, the realisation of VGOS is limited significantly by the current operational model, which relies heavily on manual inputs from the schedulers, operators and analysts. The dynamic observing programme aims to introduce more automation into the AuScope VLBI observation process and to improve observations with a feedback loop. We looked at the stations' performance and automatically determined the flux densities of sources to optimise the agreement between the observed and the scheduled signal-to-noise ratios (SNRs). This programme is used in semi-automated operations for small AuScope observing routines, such as regular fringe checks and mixed-mode observations.

Keywords Dynamic Observing, AuScope, mixed-mode

1 Introduction

The research on the feasibility of dynamic observing was initiated in 2016 by researchers at the University of Tasmania (UTAS) to reduce the significant labour and cost requirement for continuous observing (Lovell et al., 2016). The programme also aimed to allow full Earth Orientation Parameter (EOP) products to be available within 24 hours post-observations and 6 hours for UT1-UTC measurements. However, due to the limitation on the data transfer speed and correlation facility, complete geodetic data within 24 hours is still far too optimistic for the Australian VLBI array. The original study in 2016 showed the viability of short-notice scheduling with the minimum recommended 15 minutes duration (Iles et al., 2018). The project has now resumed and focuses on improving the efficiency and results of the mixed-mode observing. The dynamic observing programme (Dynob) aims to optimise available AuScope VLBI antenna idle time and correlation resources without requiring additional expenses to support this increase in observing time as we move toward continuous observing. A performance monitoring mechanism is also incorporated to consistently monitor and improve the agreement between the apriori and observed SNR.

2 Current AuScope Operations

This section describes the current mode of operation at UTAS for the IVS and AUSTRAL sessions. The motivation for the Dynob project is discussed based on the sequence of tasks: scheduling, observing, correlation and post-correlation analysis.

2.1 Scheduling

For the geodetic AUSTRAL sessions, the session dates and observing duration are decided at least a month in advance to ensure no conflict between astronomical,

---

Lim Chin Chuan · Lucia McCallum · Jamie McCallum · Guifré Molera Calvés · Tiege McCarthy
University of Tasmania, School of Natural Sciences, Private Bag 37, Hobart, 7001 TAS-Australia

geodetic and spacecraft tracking commitments. Additionally, advance notice allows allocation of observers if required. Dynamic scheduling aims to utilise the idle time, allowing for more observations when the telescopes become available at short notice.

2.2 Observing

Currently, the geodetic VLBI observation at UTAS requires observers to be on duty for the entire session and about 0.5 to 2 hours before the session starts. The observers' roles include configuring the hardware, checking the telescopes' condition and starting/stopping a session. Inspection of the system temperature, clock delays, weather and recordings is done every 2 hours if the observation runs smoothly. The remote observing method is quite mature at UTAS as the monitoring system is capable of error detection in real-time and notifies the observers through mobile phone messages if they are away from their computer (Neidhardt et al., 2009). An automated approach that starts the short-notice schedules and keeps track of the updates can allow observations to run continuously with minimum supervision.

2.3 Correlation

The dynamic scheduling test session in 2016 used short scheduling blocks of 15 minutes and relied on manual fringe-fitting to produce the databases (Lovell et al., 2016). The considerable overhead of setting up the correlator vex file and fringe-fitting of mixed-mode data are both fully automated in Dynob.

2.4 Performance monitoring

Currently, UTAS does not implement a method that analyses the SNR and monitors source flux densities continuously after each experiment. From SNR analysis (publication in preparation), using both the correct apriori antenna system equivalent flux density (SEFD) and source flux densities is vital to improving the match between the observed SNR and the scheduled SNR. Since 2020, UTAS started to monitor the SEFDs of these telescopes by using the correlator reports released to the IVS server. The re-estimation is done automatically by a script running on a web server, which performs the least-square calculation using the SNR_RATIOS within each session. However, this method is not very robust, especially with small networks and missing baselines. The error due to the inaccuracy of source flux can also significantly impact the calculation.

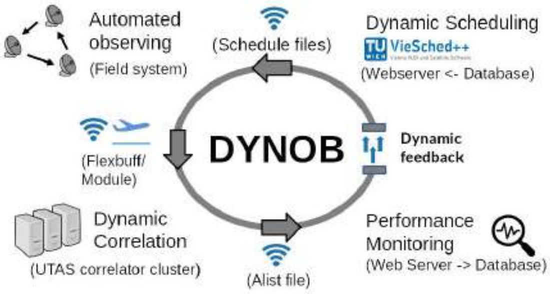

Fig. 1 Illustration of the Dynob process

3 The Implementation and application of Dynob

Dynob is a web-based tool, which centralises and controls all the operational procedures through PHP. This program is in the progress of replacing the "fringe finding" procedure at UTAS, wherein the operator can do a fringe check with multiple AuScope VLBI telescopes just by clicking a button. Dynob also allows the automatic creation of geodetic schedules when two or more stations become available. Although it is an automated looped process, manual interaction is possible at any stages for any non-typical sessions. Dynob focuses on mixed-mode observing but is working towards VGOS compatibility. Currently, three AUSTRAL programmes are using Dynob: 30 seconds fringe-checks, 24-hour sessions and short dynamic sessions.

As shown in figure 1, the Dynob process starts with Dynamic scheduling, which creates the schedule files, including the skd and vex files. These files are then transferred via Internet to the PC field system for observation. For the AuScope VLBI network, the observation can start automatically if the correct software is running. After the session, stations either send the data over the Internet or by courier service to the UTAS correlator. When all data has arrived and is stored on RAID arrays, the operator initiates the Dynob correlation, which runs automatically until the alist program (part of the MIT Haystack Observatory Post-processing System (HOPS) software) collects fringe-fitting results. The Dynob performance monitoring mechanism on the coordinating web server then grabs the alist file from the correlator and calculates the SNR performance, antenna SEFD and source flux density.

3.1 Scheduling

The scheduler runs on the same web server as the Dynob, which allows Dynob to automatically invoke the VieSched++ (Schartner et al., 2019) to generate schedules when two or more stations become available. We can also easily interrupt these ”filler observations” for the maintenance of telescopes and other infrastructure. Dynob uses the session-based optimisation mechanism in VieSched++ to select the best schedule, which is proven to yield 10% more observations than the manually created schedules for IVS experiments (Schartner, 2021). The drawback is higher computational power when the telescope network is large. For smaller size network such as the AUSTRAL sessions, which typically involves only 3 to 5 stations, the effect of this disadvantage is minimised.

The non-AuScope VLBI stations can download the created schedules from the webserver, while the AuScope stations automatically receive the files and start the observing (provided that the system is correctly set up). Since Dynob is a web tool, stations can change their observing commitment at any time through a unique web page.

3.2 Observations

For the AuScope VLBI network, tuneable digital baseband converters (DBBCs) are used together with flexbuff (Lindquist et al., 2014) and mark5B recorder, which allows the recording frequencies to be automatically set based on the $CODES section in an skd file. Before starting the schedule, the Dynob invokes a Python script on the computer field system to extract the sky frequencies from the skd file. Dynob can configure the DBBC automatically if the necessary software is running. The automation of observing is only applicable to the AuScope VLBI telescopes, which means that other participating stations operate their infrastructure and maintain their observing practises. Within the AuScope VLBI network, the automated observation of multiple short schedules is possible. For short fringe-check sessions, the data can be transferred directly from Yarragadee and Katherine to UTAS over the Internet. For a 24-hour session, the data from these two stations are shipped to Hobart in the forms of Mark5B modules or USB hard disks.

3.3 Correlation

At the moment, the mixed-mode AUSTRAL schedules are created in a similar way to legacy sessions. This results in the mode, IF, freq, BBC and tracks parameters in the created vex file not being correct. Dynob uses a template vex file combined with the original vex file for the session. If the recording mode differs, such as in the observed sky frequencies, only the template file needs to be modified. Dynob also automatically downloads and parses the observing logs and usno_final.erp file to get the clock delays and the EOP.

If multiple interrupted blocks of schedules over 24 hours exist, Dynob collates and assembles these schedules into a 24-hour vex file for correlation. Combining these blocks is necessary for analysis and producing good geodetic results. Compared with the previous correlation method, Dynob enormously reduces the time and manual interaction required during pre-correlation.

For the correlation, Dynob scans through all the data storing RAID arrays (which can be added or removed via the interface), then uses a scan-wise approach for correlation to allow progress tracking and resuming if an unexpected interruption happens. In the future, the correlation progress can be monitored through a web interface in real-time.

To date, Dynob has successfully correlated more than ten 24-hour mixed-mode sessions involving the three AuScope VLBI telescopes and the Warkworth telescope. In theory, the Dynob correlation would work with any correlation cluster running the DiFX (Deller et al., 2011) software. However, its compatibility outside the UTAS geodetic correlator cluster has not been tested..

3.4 Post-correlation and performance monitoring

After the correlation, Dynob automatically performs an initial fringe fitting, selecting a calibrator source scan as the reference for manual phase-cal. Manual assignment of the reference scan is also possible with Dynob to further reduce time overhead when finding the reference scan. Dynob then generates a control file dynamically with the delay and phase models to fringe-fit the entire session.

When the fringe-fitting ends, Dynob generates the ”alist file”, which is the foundation for the post-correlation performance check. For the fringe-check sessions, a very rough estimation of the antennas SEFD is calculated using the catalogued source flux. Whereas, for the 24-hour sessions, Dynob re-calculates the SEFDs of antennas using the mean of five selected sources defined in the configuration file. Using these SEFD values, Dynob calculates the flux densities for all the sources observed during the session and stores them in the database.

The reasons to re-calculate the SEFD from the SNR instead of measuring it directly from the system temperature are: 1) the re-calculated SEFD represents the more realistic situation because non-temperature related factors can sometimes contribute to the SNR losses. 2) In the absence of noise-cal, such as at Hobart and Katherine, re-calculating the SEFD from the SNR is the easiest way to monitor the antennas' performance. In the future, the re-calculated SEFDs can be used to improve the AUSTRAL SNR performance.

4 Fringe-checks

More than 20 fringe-checks have been carried out on the AuScope VLBI array (Hb, Ke, Yg) from June 2020 in parallel with the Dynob development. Data transfer to Hobart commences immediately, and the Dynob iteration time depends mostly on the data transfer rate and data size. The fastest is about 30 minutes for a 30-second scan after the data transfer speed improved from $\sim$1Mbps to $\sim$30Mbps. The fringe-check currently runs every Monday in order to give a quick estimation of the antennas' health and sensitivities but aims to run every day, replacing the obsolete and non-functioning fringe-check routine at the beginning of a session. These routines should also act as good indicators that everything is correctly set up and ready for the following experiments.

4.1 Operation

The current fringe-checking works with the flexbuff recorders and rigid frequencies. Ultimately, the fringe-checking will become part of the AuScope IVS operation routine. The Dynob workflow is shown in figure 2. A set of global parameters, including the variable telescope network, template files for scheduling/correlations, and a config file that includes the definition for the Fourfit station codes, sources for SEFD calculation, and the list of VGOS stations, must be defined. Then, Dynob runs all the ”yellow processes” dynamically, based on the automatically generated files (green boxes). The process ends by storing the SNR performance, re-calculated SEFD and flux density to the database.

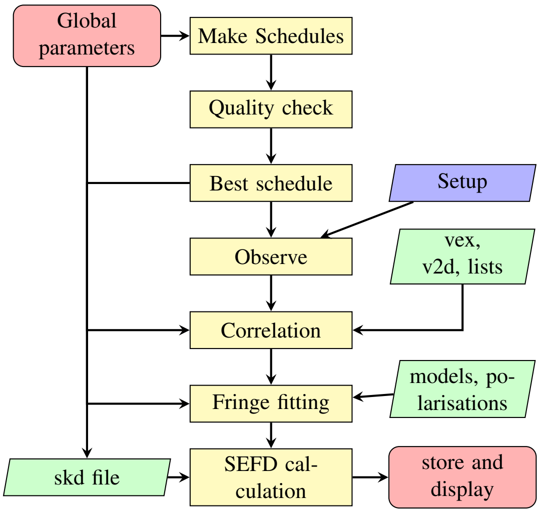

Fig. 2 Dynob fringe-check workflow. All yellow processes, green inputs and the end process are automated.

4.2 Results

The re-calculation of SEFD from SNR is done by solving the simultaneous equation, which is only possible when at least three observations exist within a scan. As seen from Fig. 3, the SEFD re-calculated from one source based on one scan is unreliable. Many open issues contribute to the high degree of fluctuation, such as the polarisation combination for mixed-mode, inaccuracy of the catalogued flux densities, etc.

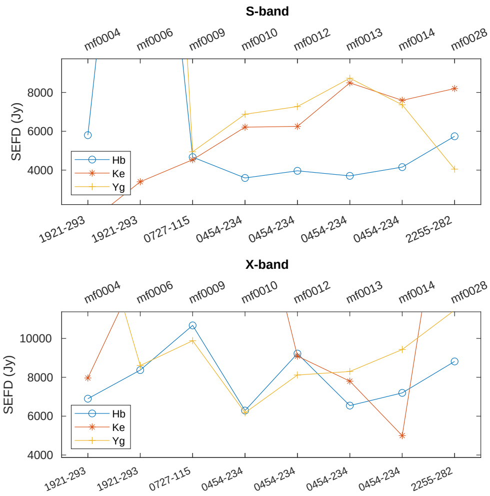

Fig. 3 Re-calculated SEFDs from the fringe-checks that involved all three AuScope VLBI telescopes.

The fringe checks have proven that the Dynob process is functional. The current plan is to increase the number and duration of these observations gradually to produce valuable results that can be used to monitor the telescopes performance and sources.

5 Conclusions

With the progressive improvement to Dynob, short one-scan fringe finding sessions are run as a testing ground and showcasing platform for "one-click observation". The fringe checking usually involves all three 12-meter AuScope VLBI telescopes with 20 to 30 seconds of integration time to test the stations' health and give a rough estimation of each antennas' sensitivity. The current weekly fringe checks allow the determination of any issue at the start of a week, and it minimises unexpected failures during or right before an IVS session. The goal is to use Dynob for fringe checking every day in the future. For the typical 24-hour sessions involving non-AuScope VLBI stations, Dynob will make data processing more efficient.

Dynob is developed to work with mixed-mode observing and aims for VGOS compatibility, however, it is not a solution to all the open questions for mixed-mode VLBI. Instead, it uses the currently available hardware and software to improve the operational efficiency, allowing for a higher cadence of observations. Dynob will consistently be updated in parallel with the improvements to the processing of mixed-mode and VGOS data. The scope for Dynob is only limited to the Australian VLBI sessions because there is currently no rigid procedure that all other correlator and post-processing sites adhere to, but it shows that Australia is ready for the transition to continuous observing in terms of the cost and data handling efficiency.

References

Deller A. T, Brisken W. F, Phillips C. J, Morgan J, Alef W, Cappallo R, Wayth R (2011) DiFX-2: a more flexible, efficient, robust, and powerful software correlator. *Publications of the Astronomical Society of the Pacific*, 123(901), 275.

Iles E. J, McCallum L, Lovell J. E. J, McCallum J. N (2018) Automated and dynamic scheduling for geodetic VLBI–A simulation study for AuScope and global networks. *Advances in Space Research*, 61(3), 962–973. doi: https://doi.org/10.1016/j.asr.2017.11.012

Lindquist M, Szomuru A (2014) Present status and technical directions of the EVN. *Proceedings of the 12th European VLBI Network Symposium and Users Meeting, 031*

Lovell J, Plank L, McCallum J, Shabala S, Mayer D (2016) Prototyping automation and dynamic observing with the AuScope array. *International VLBI service for geodesy and astrometry*, 92–95. `http://ivscc.bkg.bund.de/publications/gm2016/017_lovell_etal.pdf`

Neidhardt A, Ettl M, Plötz C, Mühlbauer M, Dassing R, Hase H, Himwich E (2009). e-control: new concepts for remote control of VLBI-telescopes and first experiences at Wettzell. *In Proceedings of Science (PoS)-The 8th International e-VLBI Workshop*, Vol. EXPReS09, EID PoS (EXPReS09) (Vol. 38).

Schartner M, Böhm J (2019). VieSched++: a new VLBI scheduling software for geodesy and astrometry. *Publications of the Astronomical Society of the Pacific*, 131(1002), 084501.

Schartner M (2021) Automated VLBI scheduling utilizing Artificial Intelligence based parameter optimization *European VLBI Group for Geodesy and Astrometry (EVGA) meeting*

HartRAO weather data

M. Nickola, A. de Witt, R.C. Botha, P. van Zyl

Abstract Accurate and continuous meteorological data are of great importance in geodetic and astrometric VLBI processing and analysis as well as in the processing and analysis of data from other space geodetic techniques and from astronomical single-dish and VLBI observations. The meteorological sensors at the Hartebeesthoek Radio Astronomy Observatory (HartRAO) provide *in-situ* measurements of barometric pressure, ambient temperature and relative humidity. These sensors, which are utilised in conjunction with HartRAO 15-m and 26-m antenna observations, have not been calibrated or upgraded for at least 10 years. We investigate the quality of historical and current meteorological data from the HartRAO sensors, and its possible degradation over time.

Keywords VLBI, weather data, *in-situ* meteorological measurements

1 Introduction

High-quality meteorological data are of great importance for astrometric and geodetic VLBI processing and analysis. Accurate and continuous meteorological data are required for accurate determination of troposphere delay and antenna thermal deformation. For troposphere delay, surface measurements of barometric pressure are used to determine the *a priori* zenith hydrostatic delay. A pressure change of 1 mbar corresponds to a path delay of $\sim$2.3 mm (Teke et al., 2013). For sub-mm accuracy of the zenith hydrostatic delay, an accuracy of 0.1 mbar in the measurement of surface pressure is required. An error in pressure of 3 mbar results in an error in the estimated station height of $\sim$1 mm (J. Böhm, private communication, 12 March 2021). Surface measurements of temperature are used to determine the structural deformation of antennas due to variations in the temperature. This causes variations in the height of the VLBI reference point ranging from 4-6 mm (Nothnagel, 2009). With regards to observations with the HartRAO antennas, surface meteorological data are also required for refraction correction for pointing purposes and for applying atmospheric opacity corrections to 22-GHz calibration data obtained with the 26-m antenna.

2 Meteorological sensors at HartRAO

A recent request by the IVS Network Coordinator for updated information regarding IVS station meteorological data, prompted an investigation of the meteorological sensors and data at HartRAO. The meteorological sensors providing *in-situ* measurements of ambient temperature, relative humidity, barometric pressure as well as wind speed and direction for astrometric and geodetic VLBI (as well as astronomical single-dish and VLBI observations) are listed in Table 1. The on-site location of the instruments are shown in Figure 1. These sensors have not been calibrated or upgraded for

---

Marisa Nickola · Aletha de Witt · Roelof C. Botha · Pfesi van Zyl
Hartebeesthoek Radio Astronomy Observatory (HartRAO), PO Box 443, Krugersdorp 1740, South Africa

Marisa Nickola
University of Pretoria (UP), Private Bag X20, Hatfield 0028, South Africa

Table 1 HartRAO meteorological sensors providing *in-situ wx* measurements for astrometric/geodetic VLBI

Parameter	Manu-facturer	Model	Sensor	Accuracy	Calibrated (c) Replaced (r)	Height above ground level	Height above (a) /below (b) antenna reference point
Air Temp. & Rel. Humidity	Huato	HE400-EX	External	± 0.5 °C ± 0.5%	2011-09-02 (r)	~1 m	15m: ~5.5 m (b) 26m: ~12.0 m (b)
Air Pressure	Setra	270	Variable capacitance	± 0.05% (full-scale)	2011-09-05 (c)	~3.5 m	15m: ~2.9 m (b) 26m: ~9.2 m (b)
Wind	RM Young	05103L	Mechanical	Speed: ± 0.3 m/s Direction: ±3°	Unknown	~10 m	15m: ~3.5 m (a) 26m: ~3.0 m (b)

Fig. 1 Location of HartRAO meteorological sensors and MET3 and MET4 units with respect to the 15-m and 26-m antennas.

the past 10 years. At the beginning of September 2011, just before the start of the CONT11 campaign, the temperature and humidity sensors were replaced and the pressure sensor calibrated. The temperature and humidity sensors are enclosed in a Stevenson screen located on the lawn between the control room building and the 26-m antenna, the pressure sensor is located in the control room, and the anemometer is located on the roof of the control room building. Sensors are located ~50 m from the 26-m antenna and ~100 m from the 15-m antenna.

During a geodetic or astrometric VLBI session, the temperature, pressure and relative humidity values are recorded in the station log file in response to the FS 'wx' command for each observation.

3 Meteorological sensors and MET3 comparison

The quality of historical and current meteorological data from the HartRAO sensors, and its possible degradation over time, were investigated by comparison with long-term meteorological data provided by the Paroscientific MET3 of the IGS GNSS reference station HRAO. The MET3 was installed on the roof of the main buidling at a height of ~6 m above ground level in 2005 (see Figure 2). It is located ~2.5 m above the barometer in the control room at a distance of ~30 m. It is located ~5 m above the temperature and pressure sensors in the Stevenson screen at a distance of ~50 m. Accuracies of ± 0.5 °C, ± 0.1 mbar and ± 2% are quoted in the IGS station log file for temperature, pressure and relative humidity, respectively. The difference between the MET3 and HartRAO sensor values for both temperature and pressure displays a near-

Fig. 2 The Paroscientific MET3 unit of the HRAO IGS GNSS station used in the comparison is located on the roof of the main building. The new MET4 is temporarily installed ∼12 m behind the MET3, in the direction of the 26-m antenna in the background.

linear instrumental offset and drift for the period just before and shortly after replacement of the temperature sensor and calibration and re-installation of the pressure sensor at the end of August / beginning of September 2011 (see Figures 3 and 4). For the pressure, a minimum resolution granularity due to data collection and storage – a resolution of 0.1 mbar for 'wx' and also for GNSS RINEX format – is apparent. MET3 and MET4 pressure sensors are able to provide a much higher data resolution. The HartRAO relative humidity sensor persisted with an incorrect lower ceiling value, reaching a new low after sensor replacement in 2011, followed by a sudden rise in ceiling value in June of 2015 (see Figure 5). Sulphur from on-site diesel generators might be responsible for sensor contamination. Nevertheless, the relative humidity sensor has never reached full-scale. It needs to be investigated whether this is due to a data collection circuit problem or a problem with the sensor itself. After the 2011 sensor replacement, a gap also appears in the data at ∼70%, which could possibly be ascribed to electronic scaling and/or faulty analogue-to-digital conversion.

4 Meteorological sensors and MET4 comparison

Data sets of the HartRAO sensors and the MET3 were also compared to short-term data from a new Paroscientific MET4 test installation, used as a calibrator. At the start of December 2020, the MET4 was installed on the roof of the main building in the vicinity of the MET3 (∼12 m distant) and at a height of ∼5 m above ground level. Accuracies of ± 0.5 °C, ± 0.08 mbar and ± 1% are indicated for temperature, pressure and relative humidity, respectively. The differential offsets in temperature between the HartRAO sensor and the MET4, as displayed in Figure 6, may be due to roof heating and radiation, caused by the temporary location of the MET4. The slight offset in pressure between the HartRAO sensor and the MET4 can be explained by the difference in height above ground level (∼4 m). The HartRAO relative humidity sensor persisted in displaying a lower ceiling value, possibly due to a combination of effects (see Figure 7).

5 Conclusions and outlook

The investigation of HartRAO meteorological sensors/data revealed the need for calibration, upgrade or replacement. The installation of a full scientific-level meteorological sensor set and high-accuracy pressure sensors is being planned. Pressure laboratory standards will be acquired to enable in-house calibration of sensors.

Discussions are still underway regarding the best location for the new MET4 unit. It will in all likelihood be installed at the reference height of the VGOS antenna whilst the Paroscientific pressure sensors will be installed at the reference heights of the 15-m and 26-m antennas. WMO standards for siting of meteorological equipment will be used as guidelines for the installations. The HartRAO meteorological sensor set that is currently being used for astrometric and geodetic VLBI will either be replaced entirely or calibrated.

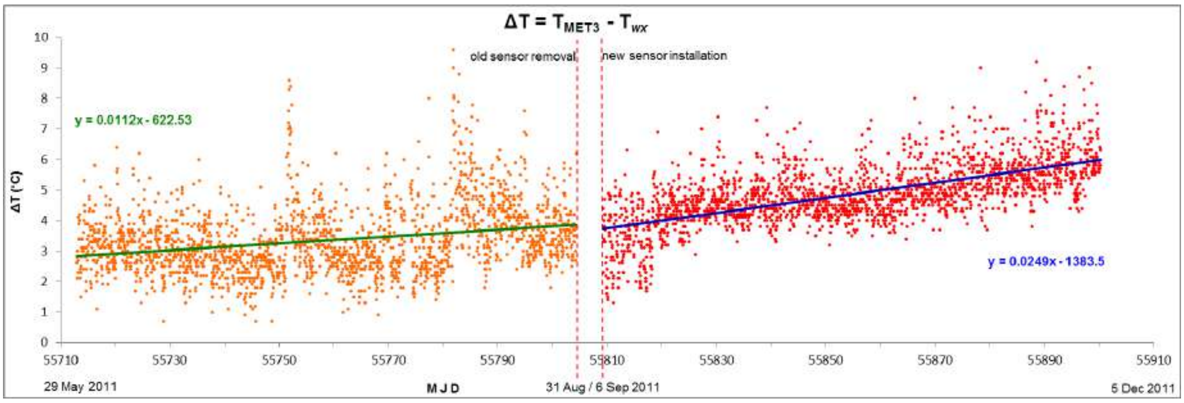

Fig. 3 The temperature difference between the IGS GNSS MET3 and HartRAO on-site sensor (*wx*) displays a near-linear instrumental offset and drift for the period before and after sensor replacement in 2011.

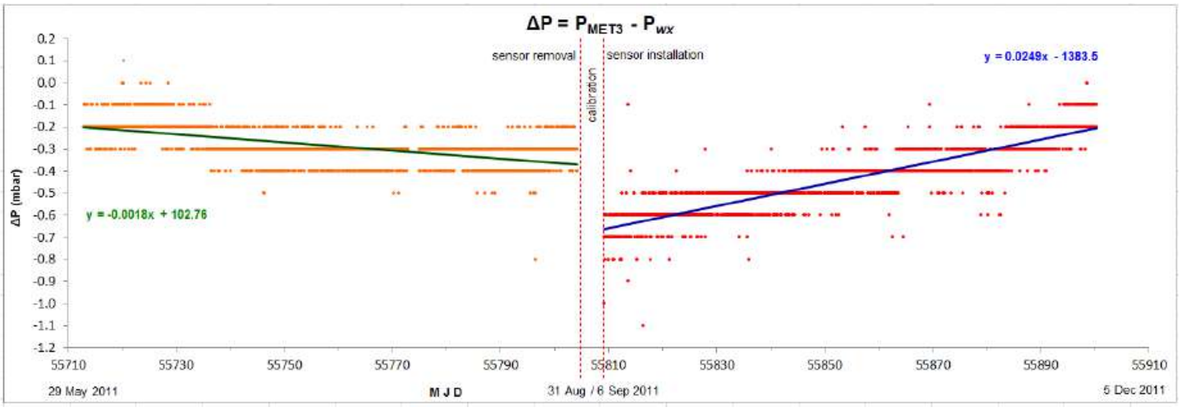

Fig. 4 The pressure difference between the IGS GNSS MET3 and HartRAO on-site sensor (*wx*) also displays a near-linear instrumental offset and drift for the period before and after sensor calibration in 2011.

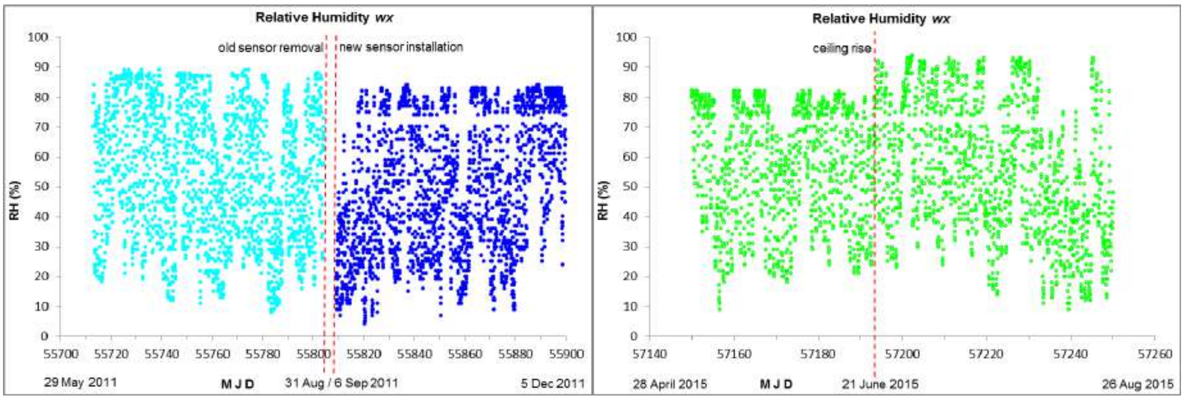

Fig. 5 Left: The relative humidity from the on-site sensor (*wx*) displays an incorrect lower ceiling value before and after replacement in 2011 and also a gap in the data at ∼70% after replacement. Right: During 2015, the persistent lower ceiling value increased to ∼90%.

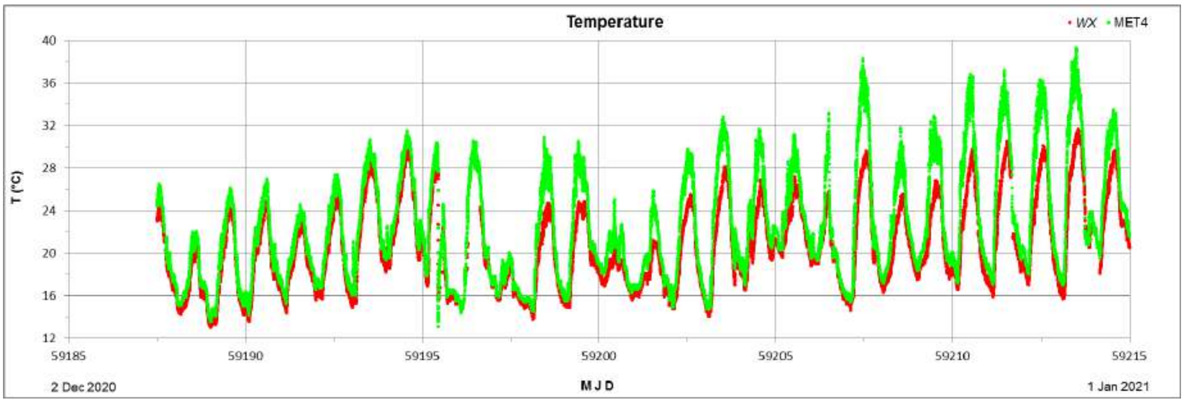

Fig. 6 The non-linear temperature offset between the new MET4 unit and on-site sensor (*wx*) may be caused by heating and radiation due to the MET4's temporary location on the roof of the facility.

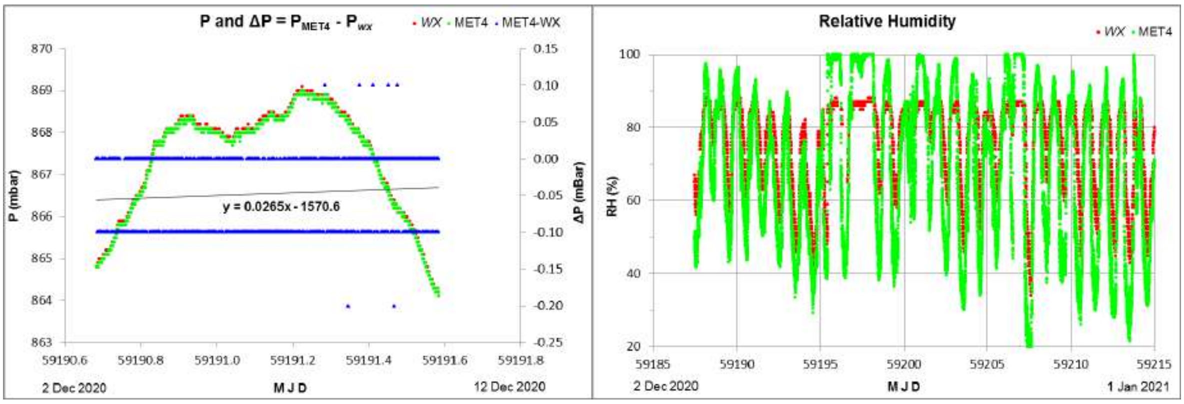

Fig. 7 Left: The slight pressure difference between the MET4 and on-site sensor (*wx*) could be due to a difference in height between the two instruments. Right: Relative humidity readings from the on-site humidity sensor (*wx*) are clearly topping out when comparing it with readings from the new MET4 unit.

Following the advice from the scientific community, a further month-long comparison of the current HartRAO meteorological sensors with the new MET4 will be run in the interim. The MET4 unit is to be installed on a pole located next to the Stevenson screen at the height of the barometer in the control room. Subsequently, the MET4 will also be installed next to the meteorological systems of all on-site collocated space geodetic techniques (GNSS MET3, NASA and Roscosmos SLR MET4s) for a month-long comparison with each. The exact position of all on-site meteorological systems will be determined in order to account for the height difference between the pressure sensors being compared and also to determine the meteorological system's height relative to its space geodesy instrument's reference point. Henceforth, all on-site meteorological data will be monitored and compared continuously.

References

Nothnagel A (2009) Conventions on thermal expansion modelling of radio telescopes for geodetic and astrometric VLBI. *J Geod*, 83, 787-792, doi: 10.1007/s00190-008-0284-z.

Teke K, Nilsson T, Böhm J et al. (2013) Troposphere delays from space geodetic techniques, water vapor radiometers, and numerical weather models over a series of continuous VLBI campaigns. *J Geod*, 87, 981–1001, doi: 10.1007/s00190-013-0662-z.

Source structure and position stability of celestial reference frame sources in the Deep South

S. Basu, A. de Witt, C. Gattano

Abstract Very long baseline interferometric (VLBI) observations in the Southern Hemisphere have always been more difficult than in the north, and in the past, there have been no dedicated imaging observations of celestial reference frame sources at declinations below $\sim -45°$. In 2013 we started an imaging campaign to map, monitor, and study the structure of southern celestial reference frame sources using data from routine astrometric observations in the south. These observations are coordinated through the IVS as part of the Celestial Reference Frame Deep South (CRDS) sessions. In 2018, we increased the data rate (and thus sensitivity) of the CRDS sessions to allow for more and weaker sources to be observed. We also optimised the scheduling for improved *uv*-coverage for imaging. To date, we have produced images for 164 sources from ten CRDS sessions at both 2.3 and 8.4 GHz. We now have multi-epoch images of 96 sources, allowing us to study the structural variability over time. We present the most recent results from our imaging campaign, in particular from recent CRDS that included the O'Higgins antenna in Antarctica. We also present an analysis of the source astrometric positions estimated from the CRDS sessions in the prospect of assessing the link between individual astrometric variation and structure changes.

Keywords astrometry, ICRF, quasar, IVS, CRDS

Sayan Basu and Aletha de Witt
South African Radio Astronomy Observatory, Hartebeesthoek, Farm 502 Q Hartebeesthoek, Broederstroom Road, Krugersdorp, South Africa

Cesar Gattano
Astronomical Institute of the University of Bern, Sidlerstrasse 5, 3012 Bern, Switzerland

1 Introduction

High precision very long baseline interferometric (VLBI) measurements of extra-galactic radio source positions are used to define and maintain the International Celestial Reference Frame (ICRF) with sub-mas accuracy. The present realisation of the ICRF, the ICRF-3 (Charlot et al., 2020) contains VLBI positions of 4,536 radio sources at 2.3 (S-band) and 8.4 GHz (X-band) with only 256 source located in the far-south ($< -45°$ declination). The ICRF has always been much weaker in the south than in the north, both in the number and distribution of sources and the accuracy of the source positions. Therefore, in order to reach parity with the north, more efforts are needed in the south.

The radio sources that make up the ICRF are mainly quasars which ideally should have a compact or core-dominated structure on mas scales at radio frequencies. However, in practice, many of these sources exhibit spatially extended intrinsic source structures which may vary with time, frequency and baseline projection. Such structure can introduce significant errors in the VLBI measurements thereby degrading the accuracy of the estimated source positions and thus the stability of the celestial reference frame (Charlot, 1990). It is therefore important to map and monitor the structure of the ICRF sources and to assess the astrometric suitability of these sources on a regular basis.

Unfortunately there have only been a few of observations to image the celestial reference frame sources in the far-south and dedicated observations to map and monitor source structure have proven difficult to obtain. However, in 2013 we started a campaign to image source structure from existing, routine astrometric and geodetic VLBI observations, coordinated through the International VLBI Service for Geodesy and Astrometry (IVS), in the south. Our success in producing images using the astrometric observations from the Celestial Reference Frame Deep South (CRDS) programme (e.g., Basu et al., 2018), have shown that dedicated imaging campaigns in the far-south may indeed be possible.

In this paper, we present our most recent imaging results and astrometric quality assessment of the celestial reference frame sources observed in the CRDS sessions between March 21, 2018 and May 06, 2019. In addition, we also present our analysis of the source position time-series for these sources and we discuss the results from our study to investigate the link between the astrometric variation and source structure variability.

2 CRDS sessions

The CRDS[1] sessions (abbreviated as CRD from session 100 onwards) are dedicated astrometric observations coordinated through the IVS to strengthen the density of the celestial reference frame in the far-south. There are five to six CRDS sessions per year (roughly once every second month), and each source is observed two or three times per year in approximately four-month intervals.

To date, we have imaged a total of eleven CRDS sessions between 2013 and 2019. As part of our pilot programme we imaged three session form 2013 (CRDS-63, 66 and 68), and the results were reported in Basu et al. (2018). However, imaging of these older sessions were difficult both because of the poor sensitivity and poor *uv*-coverage, and therefore the remainder of the sessions between CRDS-68 and CRDS-93 were not considered for imaging.

On 24 January 2018 (starting with CRDS-93), the data rate of the CRDS sessions was increased from 256 Mbps to 1 Gbps, and subsequently the source list was also updated to include more and weaker sources. The scheduling was also optimised for both astrometry and imaging (e.g. adding additional scheduling constraints which requires at least 4 stations per scan and at least 4 scans per source). We have now imaged an additional five sessions from 2018 (CRDS-94, 95, 96, 97 and 98), and three sessions from 2019 (CRD-100, 101 and 102). Two of the sessions were not considered for imaging; CRDS-93 had no useable data for the HartRAO 26-m antenna, and thus no long-baselines observations, and CRDS-99 had only three participating antennas.

The CRDS sessions are 24-hour VLBI observations recorded in right circular polarization (RCP) with 8-baseband channels at X-band and 6-baseband channels at S-band with a bandwidth of 16 MHz per baseband channel (from CRDS-93 onwards). The CRDS network for the 2018 and 2019 sessions consisted of an initial five antennas; the HartRAO 26-m antenna in South Africa, the Yarragadee 12-m, Katherine 12-m, and the Hobart 26-m antennas in Australia, and the Warkworth 12-m antenna in New Zealand. In May 2019 (CRD-102) the O'Higgins 9-m antenna in Antarctica was added to the CRDS network (see Figure 1).

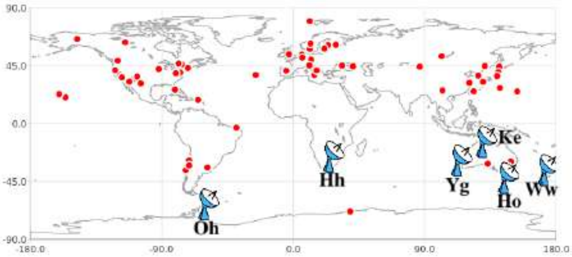

Fig. 1: The distribution of the antennas that participated in the CRDS network for sessions that were observed in 2018 and 2019; the HartRAO 26-m (Hh) in South Africa, the Yarragadee (Yg) 12-m, Katherine (Ke) 12-m, and the Hobart (Ho) 26-m antennas in Australia, the Warkworth (Ww) 12-m in New Zealand, and the O'Higgins (Oh) 9-m antenna in Antarctica.

3 Image analysis

The visibility data were calibrated using the Astronomical Image Processing System (AIPS; Greisen, 1998) and the self-calibration and imaging were done using DIFMAP (Shepherd, 1997). Details of the calibration steps that were followed can be found in Basu (2019).

---

[1] *http://ivscc.gsfc.nasa.gov*

To date, we have imaged a total of 123 sources observed in the CRDS sessions between 2018 and 2019. In Figure 2 we show the X-band multi-epoch contour maps for a representative sample of three sources that all show some extended emission. The source 0302-623 and 1251-713 show extended emission in the second and third epoch maps, while the source 1657-562 shows a bright second component in all three of the epochs.

We also present the results from our image analysis to determine the amount of source structure and it's variation over time. The source compactness (SC) was calculated by taking the ratio of the core flux density (the sum of the CLEAN components within and area of radius 0.85 mas from the brightest pixel in the map) to the total image flux density (the sum of all the CLEAN components), where a value of 1.0 would represent a compact source, where all of the flux is within core. The CLEAN component models were also used to calculate the source structure index (SI) based on the median value of the structure delay corrections, as described in Charlot (1990). An SI of 1 or 2 is indicative of a source with excellent or good structure, while an SI of 3 and 4 would indicate a source with significant or very bad structure. In Table 1 we list the peak flux, the total CLEAN flux density, the SI and SC for each of the three sources at each of the epochs shown in Figure 2.

All three of the sources show extended structure which agrees well with the results from the image analysis. It is recommended that these sources be imaged on a regular basis to assess the astrometric quality over time.

Table 1: Results of the image analysis for each of the three sources shown in Figure 2.

Source Name	Epoch (yy-mm-dd)	Peak Flux (Jy Beam^{-1})	Total Flux (Jy)	SI	SC
0302-623	18-06-20	0.819	0.908	1.90	0.90
	19-02-18	0.996	2.169	3.49	0.46
	19-05-06	0.467	0.850	3.79	0.55
1251-713	18-08-14	0.922	1.245	3.04	0.74
	19-02-18	0.833	1.542	3.42	0.54
	19-05-06	0.429	0.891	3.52	0.48
1657-562	18-03-21	1.050	1.400	3.10	0.75
	18-08-14	1.039	1.332	3.18	0.78
	19-02-18	1.306	2.009	3.03	0.65

4 Source position time-series analysis

We also derived a position time series for each of the 104 sources observed in the CRDS sessions between March 02, 2004 and May 07, 2018. The position time series were extracted from a composition of ten solutions based on the full set of dual-frequency S/X-band sessions present in the IVS observation database and by using the NASA software package CALC-SOLVE. In each of the ten individual solutions one-tenth of the set of sources have their position estimated session-wise, while the remaining sources have their position estimated globally. This ensures a quasi-similar celestial reference frame constraint within each individual solution. The position time series for source 0302-623, 1251-713 and 1657-562 are shown in Figure 3.

For all our solutions, we used the same astronomical and geophysical modelling as recommended by the International Earth rotation and Reference system Service (IERS; Petit et al., 2010). Our analysis strategy is detailed in § 2 of Gattano et al. (2018), with the only difference being that the a-priori source positions was taken from the ICRF-3 catalogue, including their prescription for the galactic aberration correction.

From the derived position time series we assessed the quality of the CRDS sessions by investigating the repeatability of the position estimation based on each CRDS session. This is done by deriving the range of values within which 50% of the CRDS session-wise coordinate estimations are scattered (25% above the median value, and 25% below). In Table 2 we present the results for the the source 0302-623, 1251-713 and 1657-562. The same statistics are computed from all the IVS sessions for comparison.

All IVS sessions considered, the interquartile range is often better than 0.6 mas in $\Delta\alpha\cos(\delta)$ and better than 1 mas in $\Delta\delta$. In the case of the CRDS sessions only, the interquartile range is often better than 1 mas in $\Delta\alpha\cos(\delta)$ and better than 2 mas in $\Delta\delta$. The east-west baseline orientation favoured in CRDS sessions is most probably the reason for the differences between the right ascension and declination.

5 Case study: 1657-562

The statistical results in § 4 were made based on the hypothesis that the position of a source remains the same

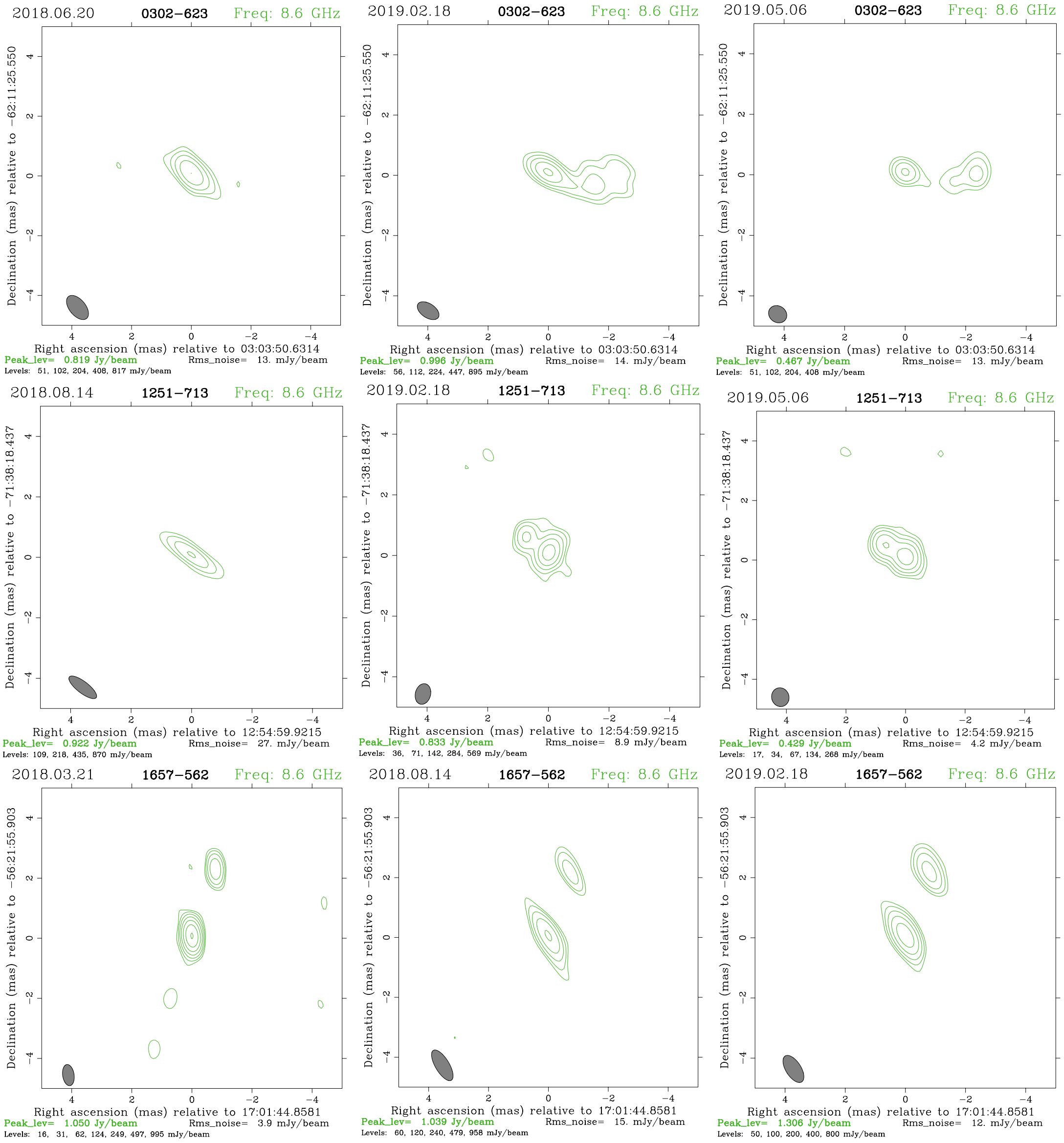

Fig. 2: Multi-epoch contour maps of the source 0302-623 (top panel), 1251-713 (middle panel) and 1657-562 (bottom panel). North is Up and East is to the Left. The FWHM beam size is indicated in the bottom left corner of each map.

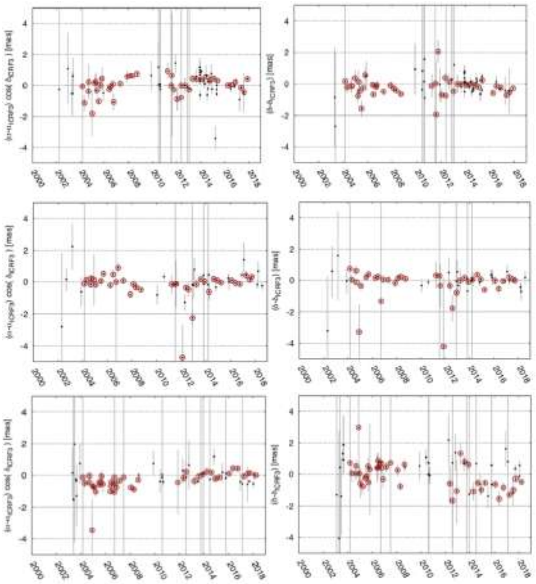

Fig. 3: The equatorial coordinate time series for source 0302-623 (top panel), 1251-713 (middle panel) and 1657-562 (bottom panel). The coordinates are shown as the offsets $\Delta\alpha\cos(\delta)$ and $\Delta\delta$ from the position recorded in the ICRF-3 catalog. CRDS sessions are highlighted by red circles.

Table 2: The statistical dispersion (in mas) of the coordinate time series, for the source 0302-623, 1251-713 and 1657-562, computed for all IVS sessions (Col. 2–3) and for the subset of points derived from the CRDS sessions only (Col. 4–5).

Source name	$\alpha\cos(\delta)$ (IVS)	δ (IVS)	$\alpha\cos(\delta)$ (CRDS)	δ (CRDS)
0302-623	0.787	0.633	0.691	0.488
1251-713	0.630	0.563	0.333	0.553
1657-562	0.611	1.361	0.636	1.270

over time. However, it is clear from Figure 3 that this is not the always the case, as is evident from the position variations seen in the declination time series for the source 1657-562. We are interested in relating these source astrometric position variations with the structural changes observed in the muli-epoch VLBI images. A study of the source 1657-562 was conducted to estimate a preferred direction from the position variation. Instead of looking at the session-wise coordinates, we investigate the epoch-wise vectors connecting two successive positions from the time series. From the method detailed in Gattano and Charlot (2021), we derived the preferred directions of the source position variation. For the source 1657-562, we found a preferred direction of $-19.7 \pm 16.9°$. This value is in close agreement with the value obtained from the DIFMAP model-fitting which is $-19.343 \pm 0.955°$. Due to the dual structure of this source, the result is not very surprising but this preliminary study reveals the potential of our method to relate position variation and structure change.

6 Conclusions

We present multi-epoch VLBI images from the CRDS sessions observed between 2018 and 2019, showing that dedicated imaging campaigns using routine astrometric sessions is possible in the far-south. We also present the coordinate time-series of the sources observed in the CRDS sessions. Statistically, the performance from the solely CRDS sessions are often better than 1 mas in right ascension and 2 mas in declination, allowing us to investigate the correlation between the source position and structure changes.

References

Basu S. et al. (2018) Multi-epoch VLBI images to study the ICRF-3 Defining Sources in the Southern Hemisphere. *14th EVN Symposium & Users Meeting*, 135.

Basu S. (2019) VLBI Imaging of ICRF Sources in the Southern Hemisphere. *Ph.D Thesis.*

Charlot P. (1990) Radio-Source Structure in Astrometric and Geodetic Very Long Baseline Interferometry. *AJ*, 99, 1309.

Charlot P. et al. (2020) The third realization of the International Celestial Reference Frame by very long baseline interferometry. *A&A*, 644, A159.

Gattano C. et al. (2018) Extragalactic radio source stability and VLBI celestial reference frame: insights from the Allan standard deviation. *A&A*, 618, A80.

Gattano C. and Charlot P. (2021) Characterizing the astrometric instability of extragalactic radio source positions measured with geodetic VLBI. *A&A*, 648, A125.

Greisen E. W. (1998) Recent Developments in Experimental AIPS. *ASP Conf. Series*, 145, p204.

Petit G. et al. (2010) IERS Conventions (2010). *IERS Technical Note*, 36.

Shepherd M. C. (1997) Difmap: an Interactive Program for Synthesis Imaging. *Astronomical Data Analysis Software and Systems VI*, 125, p77.

Small scale atmospheric variations sensed with very short baseline interferometry (VSBI) and microwave radiometry

G. Elgered and R. Haas

Abstract We have compared differential zenith wet delays, estimated between the 20 m telescope and the twin telescopes at Onsala, with linear horizontal gradients from a water vapour radiometer (WVR). The east and north gradients from the WVR are projected on to the baseline between the telescopes. The formal errors of the estimated differential zenith delays are comparable to the size of the estimated values. We obtain correlation coefficients for specific 24 h experiments in the range from 0 to 0.2, and the overall correlation is 0.1. Although the correlations are low, we use simulations to verify that they are in the expected range.

Keywords wet delay, horizontal gradients, microwave radiometry

1 Introduction

Three telescopes at the Onsala Space Observatory are regularly used in geodetic VLBI experiments: the 20 m radome enclosed telescope (ON) and the twin telescopes (OE and OW). The distance between the twin telescopes is approximately 75 m and they are in turn approximately 500 m southwest of the 20 m telescope, see Figure 1. The location of the Onsala telescopes close to the coast line suggests that there may occasionally be significant local horizontal gradients in the atmospheric water vapour content. Horizontal gradients estimated by collocated GNSS stations and a Water Vapour Radiometer (WVR) frequently reach a size of several millimetres (Elgered et al., 2019). In this study we address if it is reasonable to estimate the differential equivalent zenith wet delay (ΔZWD) between the 20 m telescope and the OTT telescopes. A series of 25 local Very Short Baseline Interferometry (VSBI) experiments has been carried out with these three telescopes in 2019 and 2020 (Varenius et al., 2021).

The ΔZWD relates to the horizontal linear gradient, G, projected on to the baseline, $\bar{b}$, between the telescopes via the scale height, h_s, of the wet refractivity and the distance between the telescopes:

$$\Delta \mathrm{ZWD} = \frac{|\bar{b}|}{h_s} \cdot G \tag{1}$$

Elósegui et al. (1999) and Zus et al. (2019) have estimated the scale height to be in the range from 1 to 3 km. Assuming a scale height of 2 km a typical gradient size inferred from the WVR observations of 1 mm, then corresponds to a ΔZWD of 0.25 mm over the approximately 500 m baseline between the telescopes. With this in mind we compare the horizontal gradients inferred from the data WVR with the ΔZWD estimated in the analysis using the interferometry data from the 20 m and the OTT telescopes.

In Section 2 we describe the VSBI and WVR data processing. In Section 3 we present the comparisons between the ΔZWD estimated from the interferometer data with the horizontal gradients estimated from the WVR data, and in Section 4 we assess the quality of the results using simulations based on the estimated observed parameters and their formal errors. Finally, the conclusions are given in Section 5.

G. Elgered and R. Haas
Chalmers University of Technology, Onsala Space Observatory, SE-439 92 Onsala, Sweden

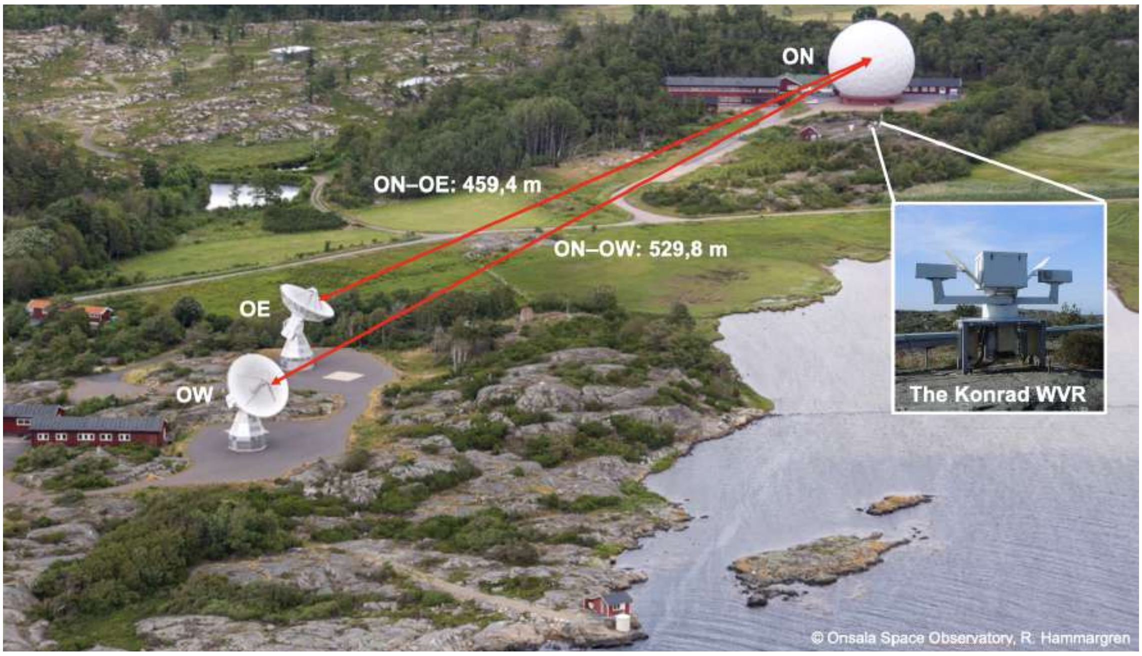

Fig. 1 The three telescopes used for geodetic VLBI at Onsala: the 20 m radome enclosed telescope and the twin telescopes. The WVR is located close to the 20 m telescope.

2 Input data

The VSBI data analysis was carried out using the ASCOT software (Artz et al., 2016) as follows:

- A group delay analysis was performed.
- The station coordinates were fixed for the 20 m telescope (ON) on VTRF2020b, but estimated for the twin telescopes (OW and OE).
- The reference clock was ON. Clock parameters for OE and OW were estimated every hour.
- The ZWD was fixed at OE and OW, based on the ground pressure referred to the reference points, and estimated for ON as a continuous piece-wise linear function updated every 5 min. We tested to carry out the analysis with different constraints for the ZWD, from 50 ps/h to 350 ps/h. All observations down to an elevation angle of 5° were used.
- EOP and radio sources were fixed according to IERS C04 and ICRF3.

The WVR data were analysed with our in house software as described by Elgered et al. (2019). However, the observing schedule was different during 2019 and 2020. The WVR was operated according to a 5 min long cycle, during which 52 observations were distributed over the sky at elevation angles from 25° and above (see Figure 2). This means that we had a good sky coverage in order to estimate linear horizontal gradients with a temporal resolution of 5 min. The reason for the high elevation cutoff angle was to avoid ground noise pickup. A drawback of the WVR is that data acquired during rain, or when the equivalent zenith liquid water content is larger than 0.7 mm, are inaccurate and therefore ignored. There were also several periods during the VSBI experiments when the WVR was unstable and these data were also deleted. A final requirement was that there had to be at least 40 of the scheduled 52 observations in a 5 min period in order to estimate gradients.

Both the WVR gradients and the differential zenith delays, ΔZWD, were estimated every 5 min. However, they were not synchronized, and as mentioned above there are also many data gaps in the WVR gradient time series. Therefore, in order to be used in the comparison, we required a maximum difference between the time epochs of the samples of ±2.5 min. Finally, out of the original 6414 ΔZWD estimates, from the 25 experiments, we had 3044 matching gradients from the WVR for the comparison.

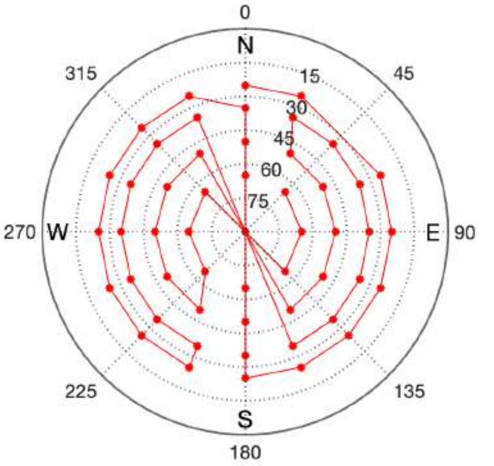

Fig. 2 One measurement cycle of the WVR consists of 52 observations. The cycle starts in the north direction with an elevation angle of 25° and is repeated every 5 min. The zenith point is only measured once, the first time it passes over zenith direction.

3 Results

The results presented are based on the 3044 data pairs of projected WVR gradients and the ΔZWD from the VSBI experiments if nothing else is stated.

The estimated values and their formal uncertainties are summarised in Table 1. The formal uncertainties of the ΔZWD, from the VSBI analysis, are typically larger than the estimated values and the effect of course increase when the constraint is weaker. The uncertainties of the WVR gradients are scaled meaning that if the true wet delays in the different directions have deviations from the linear gradient model the uncertainties increase. Such deviations will be common during convection processes and the assumption of linear changes of the wet refractivity in a layered atmosphere will not be accurate.

The correlations for the whole dataset of 25 experiments and 3044 data points between the ΔZWD and the WVR gradient projected on to the OTT–ON averaged baseline are calculated for the three cases with different applied constraints. The correlation coeficients are 0.077, 0.109, and 0.098 for the constraints of 50 ps/h, 200 ps/h, and 350 ps/h, respectively. Given the small relative size of the atmospheric signal compared to the uncertainties we do not regard these differences as significant.

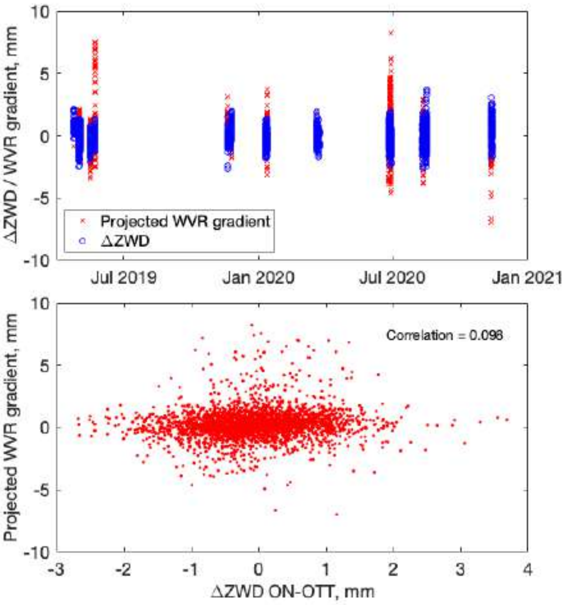

Fig. 3 All estimated projected WVR gradients and ΔZWD obtained when the constraint of 350 ps/h is applied in the VSBI analysis. Time series of the individual experiments (top) and a correlation plot (bottom).

We find, as expected, that both the differential ΔZWD between the 20 m telescope and the OTT telescopes and the gradients estimated from the WVR are slightly larger during the warmer season when there is a higher water vapour content in the atmosphere. The time series and the correlation plot are shown in Figure 3 for the case when a constraint of 350 ps/h is applied.

The effect of using different constraints is further illustrated in Figure 4 where we present the data from two experiments, each one with a duration of 24 h, that show one of the highest correlations. A tighter constraint reduce the noise, but at the same time the possibility to catch and follow rapid changes are decreased. An overall result for all the experiments studied is that weakening the constraint results in larger ΔZWD values and more noise. In this specific case also the correlation decreases when the constraint is weaker but for the whole data set it seems as the advantage of being able to track short term variations is balanced by the increased noise.

Table 1 Statistics of ΔZWD and the WVR gradients projected on to the OTT–ON average baseline

ΔZWD constraint (ps/h)	Mean absolute (mm)	Maximum absolute (mm)	Mean formal error (mm)	Maximum formal error (mm)
50	0.34	1.70	0.36	0.98
200	0.49	3.09	0.61	1.59
350	0.58	3.91	0.76	2.01
WVR gradient (no constraint)	0.80	8.21	0.09	0.84

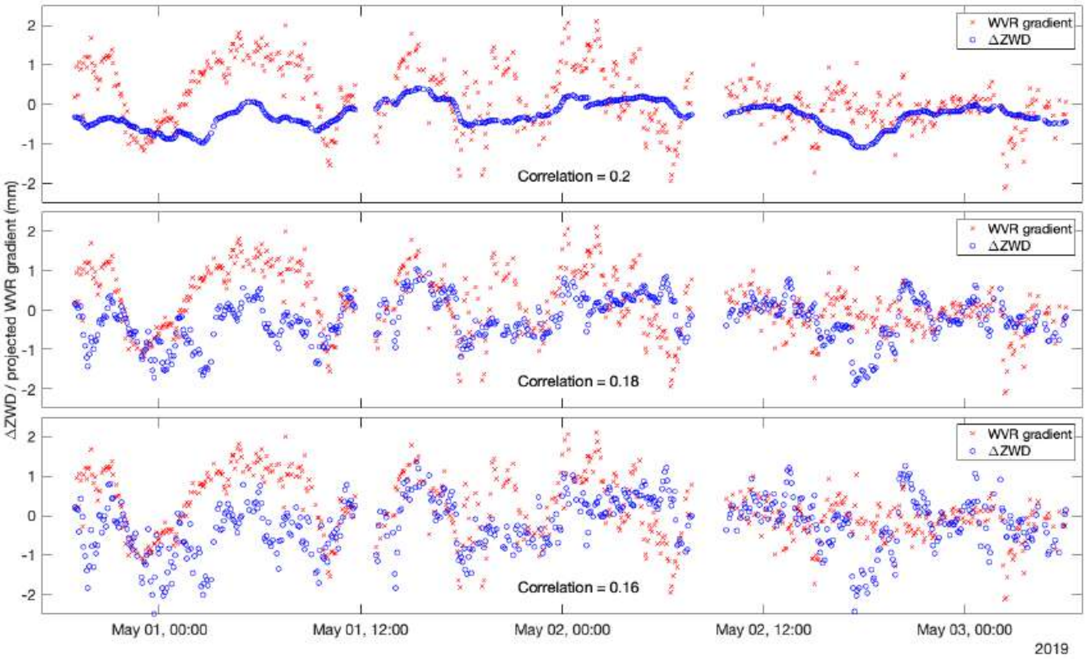

Fig. 4 An example of estimated ΔZWD (ON–OTT) and WVR gradients projected on to the ON–OTT baseline for two contiguous experiments (19APR30VB and 19MAY02VB). The applied constraints are 50 ps/h (top), 200 ps/h (middle), and 350 ps/h (bottom).

4 Simulations

In order to assess the results we carried out a couple simple simulations as follows.

- We generated a time series of projected WVR gradients with a mean value of zero and a gaussian distribution with a standard deviation (SD) equal to 0.5 mm.
- Using Eq. (1 with a scale height of 2 km and a baseline length of 500 m we calculated the corresponding time series of ΔZWD. These simulated time series of true values are then of course perfectly correlated.
- Gaussian noise with an SD of 0.1 mm was added to the WVR gradient time series and three different time series adding different SD were generated for the ΔZWD (0.3, 0.6, and 0.8 mm, based on the three different constraints in Table 1).
- The resulting correlation coefficients were 0.35, 0.18, and 0.15.

We note that the correlation obtained based on the values corresponding to the constraint of 350 ps/h is closest to the observed values. Our preliminary interpretation is that using a the tighter constraint, acting as a low pass filter, means that the temporal resolution shall be significantly lower than 5 min, which in turn means that the assumed size of the true WVR gradients shall also be smaller.

This is illustrated by another simulation. When reducing the SD of the assumed true WVR gradients from 0.5 mm to 0.2 mm, reducing the SD of the WVR gradient noise from 0.1 mm to 0.05 mm, and adding the ΔZWD noise of 0.3 mm (corresponding to the 50 ps/h constraint), the correlation becomes 0.14.

5 Conclusions and future work

Given the relative large values of the uncertainties compared to the estimated values, a relevant question is if it is motivated to solve for a ΔZWD when the baselines between the telescopes are as short as 500 m. Of course, the short baselines between the telescopes implicates that no large differences in the differential zenith delays are expected. Although the estimated differences are most of the time very small they may also absorb other errors in the observations and uncertainties in the models used, thereby hiding the possibility to identify the origin of such problems. This motivates the operation of a co-located WVR in order to estimate independent ZWD and gradients. These can than be used to search for large differences compared to the corresponding expected ΔZWD in order to identify and eliminate problems that are not necessarily caused by the atmosphere.

In this study we focused on the highest possible temporal resolution, defined by the gradients inferred from the WVR data. The primary goal was to assess if it would be meaningful to estimate differential zenith delays between the the Onsala 20 m telescope and the twin telescopes telescopes. However, from a geodetic point of view, i.e. in terms of the accuracy of the estimated geodetic parameters, a lower temporal resolution is possibly a better strategy. We have not yet addressed this question.

Future work in order to assess the modelling of the wet atmosphere is proposed to also analyse experiments where the Onsala telescopes are included in long baseline experiments, allowing estimates of the ZWD for each telescope, or for a combination of telescopes.

References

Artz T, Halsig S, Iddink A, Nothnagel A (2016) ivg::ASCOT: Development of a new VLBI software package. In: Behrend D, Baver KD, Armstrong KL (eds) IVS 2016 General Meeting Proceedings ”New Horizons with VGOS”, NASA/CP-2016-219016, 217–221, `https://ivscc.gsfc.nasa.gov/publications/gm2016/045_artz_etal.pdf`

Elgered, G, Ning, T, Forkman, P, and Haas R (2019) On the information content in linear horizontal delay gradients estimated from space geodesy observations, Atmos Meas Tech, 12, 3805–3823, doi:10.5194/amt-12-3805-2019

Elósegui P, Davis JL, Gradinarsky LP, Elgered G, Johansson JM, Tahmoush DA, and Rius A (1999) Sensing atmospheric structure using small-scale space geodetic networks. Geophys Res Lett, 26, 2445–2448, doi:10.1029/1999GL900585

Varenius E, Haas R, and Nilsson T (2021) Short-baseline interferometry local-tie experiments at the Onsala Space Observatory, J Geod, 95:54, doi:10.1007/s00190-021-01509-5

Zus F, Douša J, Kačmařík M, Václavovic P, Dick G. and Wickert J. (2019) Estimating the impact of global navigation satellite system horizontal delay gradients in variational data assimilation, Remote Sens, 11(1), 41, doi:10.3390/rs11010041

First results from the new station NYALE13S

A-S. Kirkvik, M., Dähnn, I. Fausk

Abstract In February 2020 the new VLBI station NYALE13S had its first successful 24 hour session with a tri-band receiver. The goal is to have at least one and a half year of parallel observations with NYALE13S and NYALES20. The purpose of the legacy observations is to be able to transfer the long time series from NYALES20 to the new station NYALE13S and compare the results with the local tie measurements. The length of the NYALES20-NYALE13S baseline is approximately 1.5 kilometers. There are at the moment 17 sessions available with observations from both NYALE13S and NYALES20. These and future parallel observations will be very useful for connecting future VGOS observations with the legacy network. The baseline length estimated from VLBI observations agree well with the local tie measurements, but the uncertainty is high. The number of available observations is significantly less than scheduled due to problems with the equipment both at the new and old station. The results are therefore very preliminary and hopefully more sessions will be observed in the near future.

Keywords VLBI, Baseline length, Ny-Ålesund

1 Introduction

The road from the inauguration of the new geodetic observatory in Ny-Ålesund in June 2018 to making the first successful analysis of recorded data has been long and filled with problems. But the station NYALE13S is finally recording usable data. The station is equipped with a tri-band receiver and will participate in R1 and R4 sessions together with NYALES20 before NYALES20 is dismantled and NYALE13S is equipped with a broadband receiver.

NYALE13S joined as tag-along for R1 sessions in July 2019 but the first fringe was not found until December 2019. And it was not until February 2020 multiple fringes were found and the data could be analysed. These first few sessions with data from both the new station NYALE13S (Ns) and the old station NYALES20 (Ny) have been analyzed and results are compared to the preliminary results from the local tie measurements.

2 Data

On the 17th of February 2020 the new station NYALE13S had its first successful 24 hour session. The week before some data was successfully correlated, but since it was only 88 observations spanning 3 hours the station was not included in the official database. There is still only a limited number of sessions available with observations from both NYALE13S and NYALES20. The few sessions that exist are used in this analysis and are listed in table 1. The sessions with only one of the stations observing have also been analyzed, but those sessions are naturally not used in the analysis of baseline length and baseline length repeatability.

Numerous problems and issues occurred at both stations, which has affected the overall data quality and availablity. First of all, NYALE13S has been scheduled

---

Ann-Silje Kirkvik · Michael Dähnn · Ingrid Fausk
Kartverket, Postboks 600 Sentrum, 3507 Hønefoss, Norway

as a tag-along station for all these sessions. The station also observed with a warm receiver until R1945. However, the SEFD values used in the schedule were not updated to reflect the cold receiver until R1947. At the same time the receiver at NYALES20 started to heat up and the station observed with a warm receiver for the remaining sessions.

NYALE13S originally used a DBBC3 and FlexBuff system to record data. After a while the DBBC3 malfunctioned and had to be sent for repairs. The DBBC3 was later replaced with a new DBBC2, but by then the elevation encoder at NYALES20 had malfunctioned and also had to be sent for repairs. The elevation encoder was eventually fixed and NYALES20 started observing again for R1995 but as tag-along and with a warm receiver.

Shortly afterwards, the phase calibration unit at NYALE13S malfunctioned during the R1996 experiment. The phase calibration unit is now replaced but no more sessions have been recorded and correlated at the time of writing. From R1997 and onwards NYALES20 is no longer in tag-along and the receiver will be cooled shortly. In addition, some individual sessions failed to record any usable data for NYALE13S. These sessions are not included in table 1.

Session	Date	Warm	Tag-along
R1934	2020 02 17	Ns	Ns
R1935	2020 02 24	Ns	Ns
R1936	2020 03 02	Ns	Ns
R1937	2020 03 09	Ns	Ns
R1939	2020 03 23	Ns	Ns
R1940	2020 03 30	Ns	Ns
R1944	2020 04 27	Ns	Ns
R1945	2020 05 04	Ny	Ns
R1946	2020 05 11	Ny	Ns
R1947	2020 05 18	Ny	Ns
R1948	2020 05 26	Ny	Ns
R1949	2020 06 02	Ny	Ns
R1951	2020 06 15	Ny	Ns
R1952	2020 06 22	Ny	Ns
R1995	2021 04 19	Ny	Ns, Ny
R4995	2021 04 22	Ny	Ns, Ny
R1996	2021 04 26	Ny	Ns, Ny

Table 1: Sessions used in analysis of baseline length between NYALE13S and NYALES20. The last two columns summarize the receiver temperature and tag-along status for both stations.

3 Analysis

Multiple solutions were tested to see how the parameterization might affect the final results. The number of observations available from NYALE13S is very limited and the quality is for the most part poor due to the warm receiver and other problems with the sessions. This lowers the degrees of freedom and increases the uncertainty in the estimates. Different setups for troposphere parameterizations and fixing the celestial reference frame have been tested.

The analysis has been done using **Where** (see Hjelle et al. (2018)). The default solution is the same that is used for regular R1 and R4 processing. This means all station and source coordinates, EOPs, clocks and troposphere are estimated. For more information see Kirkvik et al. (2017) and Kirkvik (2019). A priori coordinates for NYALE13S used in the analysis are computed based on the local tie vector since the coordinates in the original database is off by almost a meter. The baseline length and repeatability is calculated according to Hofmeister (2016).

For comparision the same analysis is done for the baseline between WETTZELL (Wz) and WETTZ13N (Wn) with sessions from 2015 and 2016 when the WETTZ13N station was new. The local tie vector between WETTZELL and WETTZ13N is taken from Schüler et al. (2018). This baseline is almost 10 times shorter than the NYALES20/NYALE13S baseline, but both baselines are considered short in geodetic VLBI. This is a useful comparison since both locations routinely participate in the R1 and R4 sessions and should be affected by the same network effects.

Figure 1 shows the number of observations used in each session for the NYALES20/NYALE13S baseline. The baseline length results are summarized in table 2 and selected plots are shown in figure 2, 3 and 4.

4 Discussion

The length of the NYALES20/NYALE13S baseline vector is approximately 1.5km and there is a height difference between the stations of approximately 33 meters. In addition, the NYALE13S is very close to the coast. Are these stations close enough to experience the same troposphere? The baseline length seem to agree better with the local tie vector if the troposphere is

#	Baseline	Setup	WBL	WBLR	dL
0	Ns-Ny	Default	1539.1931 [m]	0.0033 [m]	0.0000 [m]
1	Ns-Ny	Troposphere gradients fixed (Ns)	1539.1944 [m]	0.0025 [m]	0.0013 [m]
2	Ns-Ny	Troposphere gradients fixed (Ns and Ny) Zenith wet delay fixed (Ns and Ny)	1539.1927 [m]	0.0032 [m]	-0.0004 [m]
3	Ns-Ny	Troposphere gradients fixed (Ns) Two hour zenith wet delay (Ns)	1539.1943 [m]	0.0023 [m]	0.0012 [m]
4	Ns-Ny	Troposphere gradients fixed (Ns and Ny) Two hour zenith wet delay (Ns and Ny)	1539.1924 [m]	0.0029 [m]	-0.0007 [m]
5	Ns-Ny	Radio sources fixed	1539.1938 [m]	0.0023 [m]	0.0007 [m]
6	Ns-Ny	Radio sources fixed Troposphere gradients fixed (Ns)	1539.1946 [m]	0.0025 [m]	0.0015 [m]
7	Ns-Ny	Radio sources fixed Troposphere gradients fixed (Ns and Ny) Zenith wet delay fixed (Ns and Ny)	1539.1927 [m]	0.0034 [m]	-0.0004 [m]
8	Ns-Ny	Radio sources fixed Troposphere gradients fixed (Ns) Two hour zenith wet delay (Ns)	1539.1945 [m]	0.0023 [m]	0.0014 [m]
9	Ns-Ny	Radio sources fixed Troposphere gradients fixed (Ns and Ny) Two hour zenith wet delay (Ns and Ny)	1539.1925 [m]	0.0028 [m]	-0.0006 [m]
10	Wn-Wz	Default	123.3064 [m]	0.0017 [m]	-0.0006 [m]

Table 2: Weighted baseline length (WBL), weighted baseline length repeatability (WBLR) and difference between weighted baseline length and local tie vector (dL) for the different solutions. The third column described how a solution differs from the default solution.

treated the same at both stations. But the repeatability is poor and the number of sessions available are low. As can been seen in 3, the uncertainty is mostly due to the perfomance of NYALE13S.

The worst solutions in terms of baseline length repeatabilities are the solutions where the troposphere (both gradients and zenith wet delay) are fixed to the a priori model. This seems to confirm the need to estimate the troposphere parameters.

The default solution is also one of the worst solutions. As can be seen in figure 4, the low number of available observations can cause the troposphere estimates to become unrealistic. This can be fixed by adding more constraints to the solution or changing the parameterization, as is done in solution 9. Comparing troposphere estimates from the two sites with estimates from GNSS receivers (figure 5) confirms that the differences between the sites are lower than the differences in zenith wet delay from solution 0 for some sessions. The GNSS results are total tropospheric delay estimated every 2 hours and are not directly comparable to the zenith wet delay corrections from VLBI.

It should be noted that the local tie vector is also just a preliminary result without known uncertainties at the moment.

5 Conclusions

The baseline length estimated from VLBI observations agree well with the local tie measurements, but the uncertainties are high. Nilsson et al. (2015) saw improvement in baseline length repeatabilites for baselines shorter than 1km when assuming the troposphere at both stations were the same. The limited number of observations available at NYALE13S causes high uncertainties in the position estimates and baseline lengths and the results might be improved by utilizing the troposphere information at NYALES20. Since the NYALES20/NYALE13S baseline is longer than 1km, more work is needed to investigate this possibility.

The local tie computations need to be finalized and ultimately, more and better observations are needed from the VLBI antennas. Only a few sessions have good quality and the weighted baseline length repeatability would be significantly better if more sessions were of this quality.

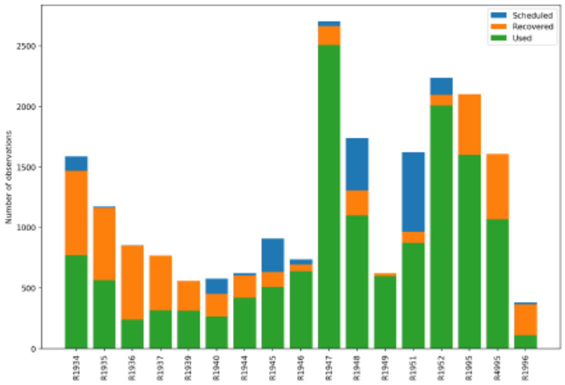

(a) Number of observations - NYALE13S.

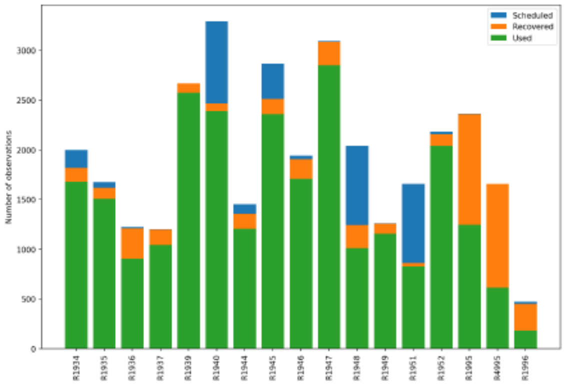

(b) Number of observations - NYALES20.

Fig. 1: Number of observations available from NYALES20 (1a) and NYALE13S (1b) for the sessions with both stations participating. The blue bar is the number of scheduled observations. The orange bar is the number of observations successfully recovered at the correlator and the green bar is the number of observations used in the analysis. The plots are from solution 0.

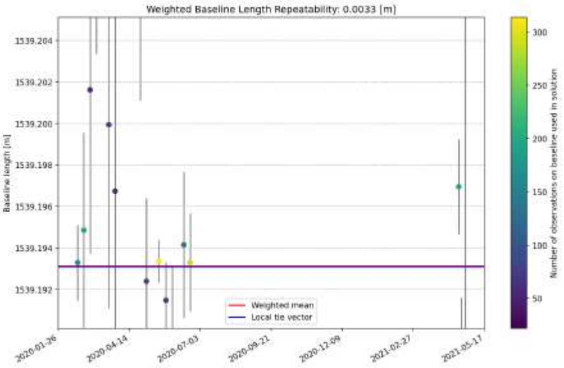

(a) Baseline length - NYALE13S/NYALES20.

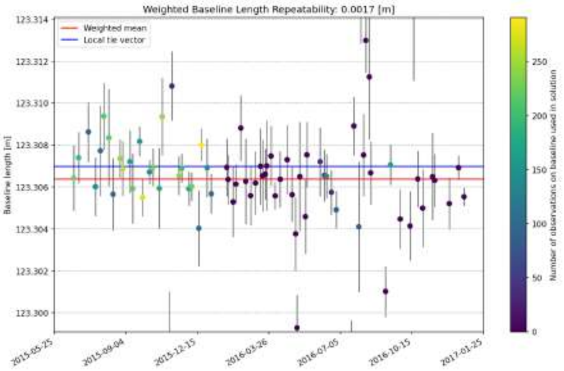

(b) Baseline length - WETTZELL/WETTZ13N.

Fig. 2: Estimated baseline lengths. The plot for the NYALES20/NYALE13S baseline (2a) is from solution 0 and the plot for the WETTZELL/WETTZ13N baseline (2b) is from solution 10. Although the baseline length for the station pairs are different, the size of the vertical axis is the same for the two plots.

References

Hjelle, G. A., Kirkvik, A.-S., Dähnn, M., Fausk, I. (2018) Making Where available to the community, in Behrend, D., Baver, K. D., Armstrong, K. L. (eds.), *Global Geodesy and the Role of VGOS - Fundamental to Sustainable Development*, IVS General Meeting Proceedings.

Hofmeister, A., (2016) Determination of path delays in the atmosphere for geodetic VLBI by means of ray-tracing. Ph.D. thesis, Technische Universität Wien. `http://resolver.obvsg.at/urn:nbn:at:at-ubtuw:1-3444`.

Kirkvik, A.-S., (2020) Norwegian mapping authority analysis center IVS biennial report 2017–2018, in Baver, K. D., Behrend, D., Armstrong, K. L. (eds.), *International VLBI Service for Geodesy and Astrometry 2017+2018 Biennial Report*.

Kirkvik, A.-S., Hjelle, A.-S., Dähnn, M., Fausk, I. (2017) Where - a new software for geodetic analysis, in Haas, R., Elgered, G. (eds.), *Proceedings of the 23rd European VLBI Group for Geodesy and Astrometry Working Meeting*.

Schüler, T., Klügel, T., Mähler, S., Plötz, C. (2018) Local Radio Telescope Ties from the Wettzell PrecisionEngineering Surveying Network, in Behrend, D., Baver, K. D., Armstrong, K. L. (eds.), *Global Geodesy and the Role of VGOS - Fundamental to Sustainable Development*, IVS General Meeting Proceedings.

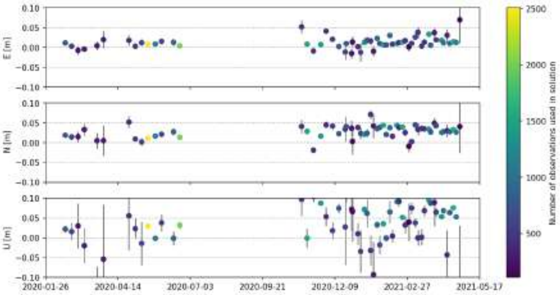

(a) Estimated position - NYALE13S.

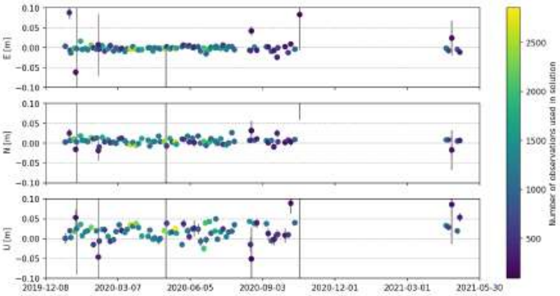

(b) Estimated position - NYALES20.

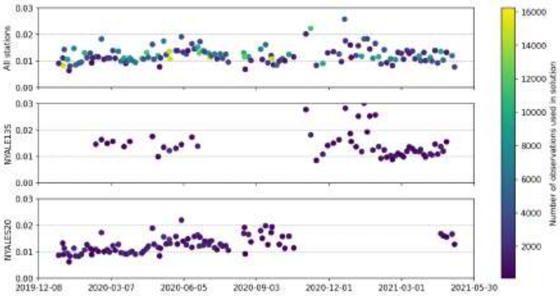

(c) Root mean square of postfit residuals [m].

Fig. 3: Estimated positions for NYALE13S (3a), NYALES20 (3b) and postfit residuals (3c) for all sessions including either NYALES20 or NYALE13S from 2020 until May 2021. The plots are from solution 0.

Nilsson, T., Karbon, M., Soja, B., Heinkelmann, R., Lu, C., Schuh, H. (2015) Atmospheric modeling for co-located VLBI antennas and twin telescopes. *Journal of Geodesy*, Volume 89, Issue 7, pp.655-665 doi: 10.1007/s00190-015-0804-6

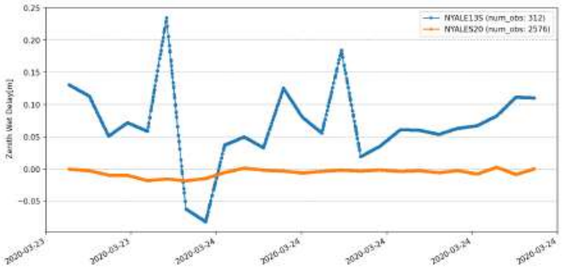

(a) Solution 0.

(b) Solution 9.

Fig. 4: Estimated correction to a priori zenith wet delay for R1939 for solution 0 (4a) and solution 9 (4b). Notice the change in scale between solutions.

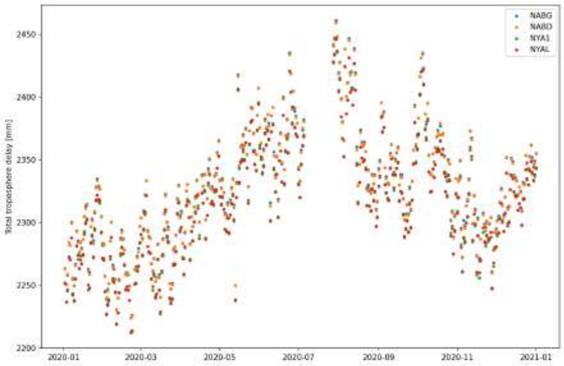

Fig. 5: Estimated total troposphere delay from four GNSS sites in Ny-Ålesund in 2020. The results are produced with the GNSS Bernese Software Version 5.2. NABG and NABD is located close to NYALE13S and NYAL and NYA1 is located close to NYALES20.

Combination of IVS Intensive sessions using SINCOM software

S. Mironova, S. Kurdubov, I. Gayazov

Abstract The SINEX files of hourly VLBI sessions were combined in order to calculate the series of corrections to the Earth orientation parameter UT1-UTC. SINEX files provided by a number of VLBI analysis centers (BKG, GSFC, IAA RAS, USNO) as a result of processing of 1131 VLBI Intensive sessions from the period for 2015 to 2020 were used in combination. The combination was performed by SINCOM software, developed in the IAA RAS for the combination of SINEX files. Combined series was calculated as a result of combining the individual series. The comparison of individual and combined series with the recommended series IERS EOP C04 and ”finals” was made. The combined series has better consistency with recommended series than individual series.

Keywords IVS Intensive sessions, combination

1 SINCOM software

SINCOM software has been developed by IAA RAS (Brattseva et al., 2015) for combining SINEX files as a result of processing VLBI, GNSS, SLR data. SINCOM uses the method of solving combining normal equation systems stored in SINEX files (Thaller , 2008). In this work we use SINCOM software to combine SINEX files of IVS Intensive sessions of 2015-2020 years processed by different VLBI analysis centers. Most of VLBI analysis centers consider ΔUT1 and its rate, terrestrial pole coordinates and their rates, station coordinates as estimated parameters. SINCOM makes combined series of ΔUT1 by two steps: making individual series of ΔUT1 (one series for the each analysis center) and making combined series of ΔUT1. Individual series are made by fixing station coordinates and deleting ΔUT1 rate, terrestrial pole coordinates and their rates. Combined series are made by eliminating station coordinates.

2 Combining ΔUT1 estimations using SINCOM software

We find the parameter ΔUT1 from the results of processing the hourly IVS Intensive sessions on a five-year interval, processed by four centers of analysis. The stations KASHIM34, KOKEE, MK-VLBA, NYALDBBC, NYALES20, SESHAN25, SVETLOE, TSUKUB32, WETTDBBC, WETTVDIF, WETTZ13N, WETTZELL participated in the observations. The largest number of delays corresponds to observations made with radio telescopes based on KOKEE and WETTZELL. Therefore, from the set of existing SINEX files we made a subset of SINEX files, in the observations of which the stations KOKEE and WETTZELL participated. Both sets had SINEX files from all analysis centers on the same date. The first and second sets of SINEX files were combined separately from each other according to the following scheme.

The combination process was divided into two stages. The first stage consisted in making the SINEX files of different analysis centers to the same a priori EOP and station coordinates. In this case, the coor-

---

Svetlana Mironova, Sergei Kurdubov · Iskander Gayazov
Institute of Applied Astronomy of the Russian Academy of Sciences, Kutuzov embankment, 10, Saint Petersburg, 191187 Russian Federation

dinates of the stations were fixed, and a priori EOP were taken from the reference IERS series ”finals”. The result of the first stage is new SINEX files and corresponding individual ΔUT1 series of analysis centers BKG, GSFC, IAA, USNO. At the second stage, the process of combining new SINEX files and extracting corrections to the ΔUT1 parameter was performed to create a combined series. SINEX files of various centers of analysis were combined with each other in one day, while all EOP except the ΔUT1 parameter were deleted. Finally, the ΔUT1 parameter and the coordinates of the stations were recorded in SINEX files as estimated parameters.

3 Method

The hourly VLBI sessions of the IVS Intensive program for 2015-2020 were processed by the QUASAR program (Kurdubov et al., 2012). The parameters were estimated: ΔUT1, zenith wet delay, and station clock offsets with a linear trend. Other parameters were pre-eliminated. The results of VLBI data processing are presented in the standard SINEX format. To record the result in the SINEX file, the parameters of the station coordinates, ΔUT1 with a linear trend, the coordinates of the earth pole with a linear trend were fixed and saved in the block of estimated parameters of the SINEX file.

The method for processing VLBI observations at the IAA RAS Analysis Center assumes the use of a set of software, a priori catalogs, models, and refined parameters, which are summarized in Table 1 for a clear demonstration of differences from other processing centers. The table shows the columns corresponding to the centers of Das Bundesamt für Kartographie und Geodäsie (BKG), Goddard Space Flight Center (GSFC), IAA RAS (IAA), US Naval Observatory (USNO) (https://www.iers.org). The third line of the table shows what parameters are given in the SINEX files of a particular center. The set of parameters (1) includes the coordinates of the stations, the coordinates of the celestial pole and their derivatives with respect to time, ΔUT1 and the length of the day. Parameter set (2) includes ΔUT1 only. Realizations of the celestial and terrestrial coordinate systems used in individual series when obtaining are presented in the CRF and TRF lines. The processing method of the IAA RAS also differs from other centers with the software used (QUASAR instead of Calc/Solve), as well as the model for accounting for ocean loadings, and the no reweighing of observations of radio sources below 50 degrees above the horizon at the time of observation.

Table 1 The processing of IVS Intensive sessions by the different analysis centers

Analysis center	BKG	GSFC	IAA	USNO
Solution	bkg2014a	gsf2020a	-	usn2020b
Software	Calc/Solve	Calc/Solve	QUASAR	Calc/Solve
Set of parameters	(1)	(2)	(1)	(1)
CRF	ICRF2	gsf2020a	ICRF2	usn2020b
TRF	VTRF2008a	gsf2020a	ITRF2014	usn2020b
Epoch	2000	2014	2010	2014
Loadings	TPXO.7.2	TPXO.7.2	GOT4.10	SPOTL software
Height	50°	50°	-	50°

4 Comparison of individual and combined ΔUT1 series with C04 and ”finals” series

We make two combined series of ΔUT1 parameters based on all SINEX files and SINEX files containing the KOKEE-WETTZELL baseline. Table 2 shows the results of comparing the individual series BKG, GSFC, IAA, USNO and the combined series ”comb”, built from SINEX files of all sessions, with the recommended series C04 and ”finals”. Table 3 contains the results of comparing the series constructed using SINEX files containing observations of the KOKEE and WETTZELL stations. The first column of the tables contains the name of the reference series (C04 or ”finals”), the second column contains the name of the individual or combined series compared with it. The fourth and fifth columns contain the results of comparing the first and second series: the average difference between the ΔUT1 parameter and its standard deviation. The average differences between the reference and individual ΔUT1 series do not exceed 12 microseconds. The maximum standard deviation of 27 microseconds is achieved when the individual BKG and IAA series are compared with the C04 series. The standard deviation between the combined series for all stations and the ”finals” turned out to be 19 μs, between the same combined series and C04 – 23 μs. The root mean square between the combined series containing observations from the KOKEE and WETTZELL stations and the ”finals” row decreased to 17 μs. So the combined series is closer to the ”finals” saries than to C04.

Figure 1 shows the differences between the individual series BKG, GSFC, IAA, USNO, the combined ”comb” series (all SINEX files) and the recommended series C04/”finals”. The combined series is located on the average between the individual results. The differences between the individual and reference rows do not exceed 100 μs, between the combined and reference series do not exceed 80 μs.

Table 2 Comparison of the C04/”finals” series with the ΔUT1 combined by the SINCOM software (all SINEX files)

Reference series	Combined series	Number of series	Mean difference ΔUT1, μs	Standard deviation ΔUT1, μs
C04	BKG	1131	-6	27
C04	GSFC	1131	12	23
C04	IAA	1131	2	27
C04	USNO	1131	-6	23
C04	comb	1131	1	23
finals	BKG	1106	-6	23
finals	GSFC	1106	12	19
finals	IAA	1106	2	23
finals	USNO	1106	-6	19
finals	comb	1106	1	19

Table 3 Comparison of the C04/”finals” series with the ΔUT1 combined by the SINCOM software (KOKEE and WETTZELL)

Reference series	Combined series	Number of series	Mean difference ΔUT1, μs	Standard deviation ΔUT1, μs
C04	BKG	842	-4	25
C04	GSFC	842	10	23
C04	IAA	842	0	24
C04	USNO	842	-5	23
C04	comb	842	0	23
finals	BKG	823	-3	21
finals	GSFC	823	11	18
finals	IAA	823	1	20
finals	USNO	823	-4	18
finals	comb	823	1	17

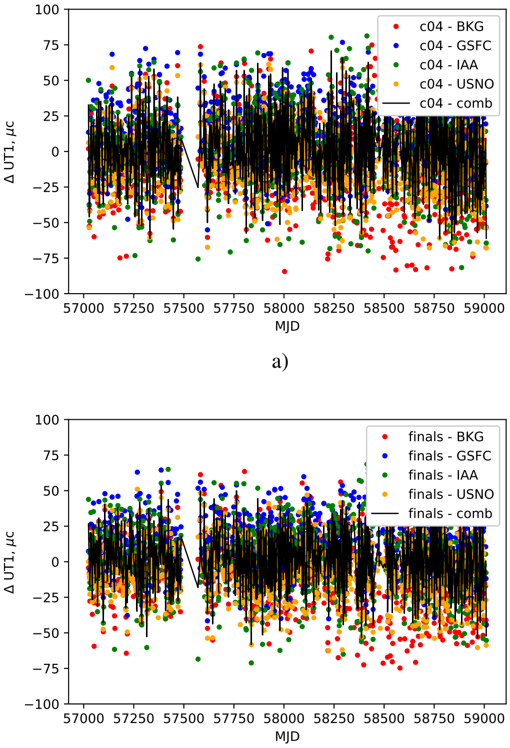

a)

b)

Fig. 1 The difference between ΔUT1 series combined by SINCOM software and ΔUT1 sevies from C04 (a) and ”finals” (b), all stations (in μs)

5 Conclusions

1. IVS Intensive series for 2015-2020 years was processed using QUASAR software.
2. Individual ΔUT1 series was combined from the solutions made by BKG, GSFC, IAA RAS, USNO analysis centers.
3. Combined ΔUT1 series was made from individual series. The standard deviation between combined series and C04 is 23 μs, between combined series and ”finals” is 19 μs.
4. The standard deviation between combined series obtained from by KOKEE-WETTZELL VLBI observations and C04 is 23 μs, between combined series and ”finals” is 17 μs.

The work was made using the equipment of the Center for Collective Use / UNU ”Radio interferometric complex ”Kvazar-KVO” and the Center for Collec-

tive Use ”Supercomputer Center ”High-performance computing in radio astrometry and space geodesy”.

References

Brattseva O., Gayazov I., Kurdubov S., Suvorkin V. (2015) SIN-Com - the new program package for combined processing of space geodetic observations. Proceedings of the Journees 2014 ”Systemes de Reference Spatio-Temporels”, Malkin and N. Capitaine (eds), Pulkovo observatory, 250–251.

Daniela Thaller (2008) Inter-technique combination based on homogeneous normal equation systems including station coordinates, Earth orientation and troposphere parameters.

S. L. Kurdubov, V. S. Gubanov (2012) Global analysis of VLBI data. *IAA RAS Transactions*, 23, 244–246.

Reference epochs in VLBI estimations of clock parameters

A. Nothnagel[1] and H. Krásná[1,2]

Abstract By default, the reference epoch of the relative clock offsets has always been the start of the sessions. If we consider a simple first order model for the relative clock parameters, i.e., just an offset and a rate, the formal errors of the parameters improve if the reference epoch is chosen to be at the middle of the session. In Altamimi et al. (2002), this is called the epoch of minimum variance. In a small study we have investigated whether this fact could be exploited in VLBI data analysis. For the CONT17-L2 series of sessions, we ran solutions with the reference epochs of the clocks being the middle of the session and compared the results to those of standard solutions. We found that even for more sophisticated parameterizations of the clocks, i.e., with polynomials and piece-wise linear polygons, the formal errors of all clock parameters did improve significantly. Although the correlation matrices change as well, there, unfortunately, is no improvement for the formal errors of any other, (non-clock) parameter. At the same time, the condition numbers of the solutions did not change significantly either. We conclude that the effects of changing the reference epoch in VLBI estimations of clock parameters are confined to the clock parameter space alone.

Keywords VLBI clock parameters, epoch of minimal variance

1 Introduction

In most analysis packages using least squares adjustments in Gauß-Markov models, the clock parameters are modelled with a second order polynomial and a superimposed series of piece-wise linear polygons (Fig. 1). The polygons can be formulated in two different ways. The first one is an initial offset at a reference epoch t_0 plus a new rate parameter for every segment of predefined duration (e.g., 20, 30 or 60 minutes). The functional values for each observation epoch t can be formulated according to Eq. 1 depending on the rates r_i and the segment limits t_i. This also serves as (part of) the VLBI observation equation which is the basis for the partial derivatives of the offset $f(t_0)$ and rate parameters r_i.

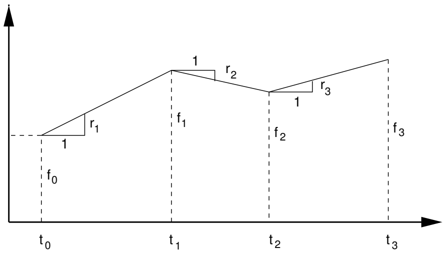

$$f(t) = f(t_0) + r_1(t_1 - t_0) + r_2(t_2 - t_1) \\ + \ldots + r_n(t - t_{n-1}) \qquad (1)$$

The rates also depend on the functional values f_i at the limits of the intervals.

Axel Nothnagel[1] · Hana Krásná[1,2]
[1]TU Wien, Department für Geodäsie und Geoinformation,
Wiedner Hauptstraße 8, A-1040 Wien, Austria

[2]Astronomical Institute, Czech Academy of Sciences,
Boční II 1401, CZ-14100 Prague, Czech Republic

$$r_i = \frac{f(t_i) - f(t_{i-1})}{t_i - t_{i-1}} \tag{2}$$

Consequently, we can introduce Eq. 2 in 1 and get a functional model purely based on the functional values (offsets) f_i (Eq. 3).

$$\begin{aligned} f(t) &= f(t_0) \\ &+ \frac{f(t_1) - f(t_0)}{t_1 - t_0}(t_1 - t_0) \\ &+ \frac{f(t_2) - f(t_1)}{t_2 - t_1}(t_2 - t_1) \\ &+ \frac{f(t_{i+1}) - f(t_i)}{t_{i+1} - t_i}(t - t_i) \\ &+ \ldots \end{aligned} \tag{3}$$

From this we can derive the partial derivatives for the offsets at the interval boundaries for the least squares adjustment. They have the form

$$\frac{\partial f}{\partial f_{i-1}} = \begin{cases} 1 - \frac{t - t_{i-1}}{t_i - t_{i-1}} & \text{for } t_{i-1} < t < t_i \\ 0 & \text{for all other epochs} \end{cases}$$

$$\frac{\partial f}{\partial f_i} = \begin{cases} \frac{t - t_{i-1}}{t_i - t_{i-1}} & \text{for } t_i < t < t_{i+1} \\ 0 & \text{for all other epochs} \end{cases}$$

This leads to a block diagonal scheme of the partials in the design matrix as depicted in Fig. 1.

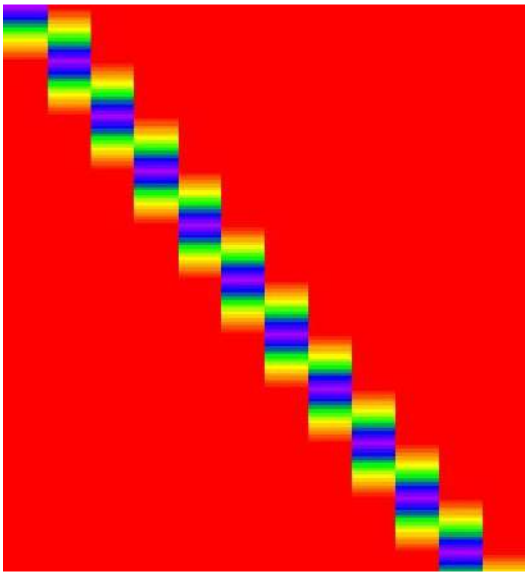

Fig. 1 Schematic distribution of magnitudes of partial derivatives for piece-wise linear offsets (red = 0, blue = 1)

The approach using the functional values or offsets (Eq. 3) is equivalent to that applying and estimating the rates (Eq. 1).

For convenience, the reference epoch of the first relative clock offset parameter $f(t_0)$ has always been set to the start of the respective session in almost all VLBI analysis packages. This has the consequence that, due to error propagation, the formal errors of the estimated clock offsets increase with time as can be seen in Fig. 2 (bottom/red) part. This obvious deficit of the piece-wise linear offset adjustment triggered the idea to investigate the effects of changes in the reference epoch.

We started with a simple fact of the estimation process. If we consider a first order model, i.e., just an offset and a rate, for observations ordered in time, such as the relative clock parameters, the formal errors of the regression parameters improve if the reference epoch is chosen to be at the middle of the session. In Altamimi et al. (2002), this is called the epoch of minimum variance. The question was whether the results of the VLBI parameter estimation change if we select the mean epoch instead of the beginning of the session for the clock offset parameters.

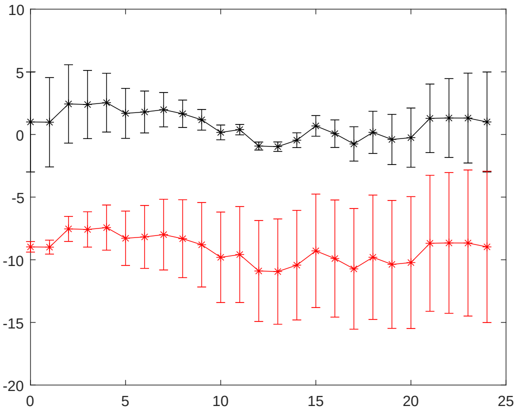

Fig. 2 Estimates [cm] of clock piece-wise linear polygons for OV-VLBA in session 17NOV28XA. 1 cm $\hat{=}$ 33 ps. Units of x axis are hours since the session start. Bottom = Reference epoch at beginning of session, Top = reference epoch at middle of session.

2 Analysis

In a small study we have investigated whether the selection of a different clock reference epoch could be exploited in VLBI data analysis. For the CONT17-L2 series of sessions (Behrend et al., 2020), we ran solutions with the reference epochs of the clocks being the middle of the session and compared the results to those of standard solutions. The clock parameterization for all stations except of a reference station consists of a second order clock polynomial plus piece-wise linear segments of 1 hour duration represented as a clock offset polygon. Zenith wet delays and gradients, all EOP, station coordinate offsets constraint by NNR/NNT conditions and source position offsets constraint by NNR conditions are the other parameters.

3 Results

We found that for simple clock polynomials as well as for any standard parameterizations of the clocks, e.g., with polynomials and piece-wise linear polygons, the absolute values of the offsets changed but not the values of the other parameters. For the piece-wise linear polygons, the differences changed in the form of a constant bias for every epoch.

The most noticeable effect is that the formal errors of all clock offset parameters do improve significantly (see example Fig. 2). We see that the monotonous deterioration of the formal errors is restricted by the reference epoch lying in the middle of the session. Significant improvements also apply to the formal errors of all clock rates but not to those of the quadratic terms which remain unchanged.

For the changes in the correlation matrices, we show this for session 17NOV28XA as an example as well (Fig. 3). The first 297 parameters in the list are the clock parameters. We see station-wise block-diagonal patterns for the 273 clock offsets and distinct changes between the clock offsets and the 24 rate and quadratic terms of the clock functions. On the other hand there is a number of very small changes in the correlations of the clock offset parameters with other non-clock parameters (see also zoomed graph Fig. 4). Most noticeable are the changes for the zenith wet delays at the middle of the session. Within the block of non-clock parameters vs. non-clock parameters, no changes are discernible at all.

Although we had hoped for it, the changes in the correlations do not affect the formal errors of these other parameters beyond some small numerical differences. So, unfortunately, there is no improvement for the formal errors of any other, non-clock parameter.

We also looked at the condition numbers of the normal matrices but did not find any significant effects either.

4 Conclusions

Except of the fact that the formal errors of the clock offsets improve considerably, we did not find any evidence that the selection of the reference epoch for the clock offset estimates can improve VLBI solutions in general. We conclude that the effects of changing the reference epoch are confined to the clock offset and rate parameters alone.

References

Altamimi Z, Sillard P, Boucher C (2002) ITRF2000: A new release of the International Terrestrial Reference Frame for earth science applications. *JGR*, 107:B10, 2214, doi: 10.1029/2001JB000561.

Behrend D, Thomas C, Gipson J, Himwich E, Le Bail K (2020) On the organization of CONT17. *J Geod*, 94:100, doi: 10.1007/s00190-020-01436-x.

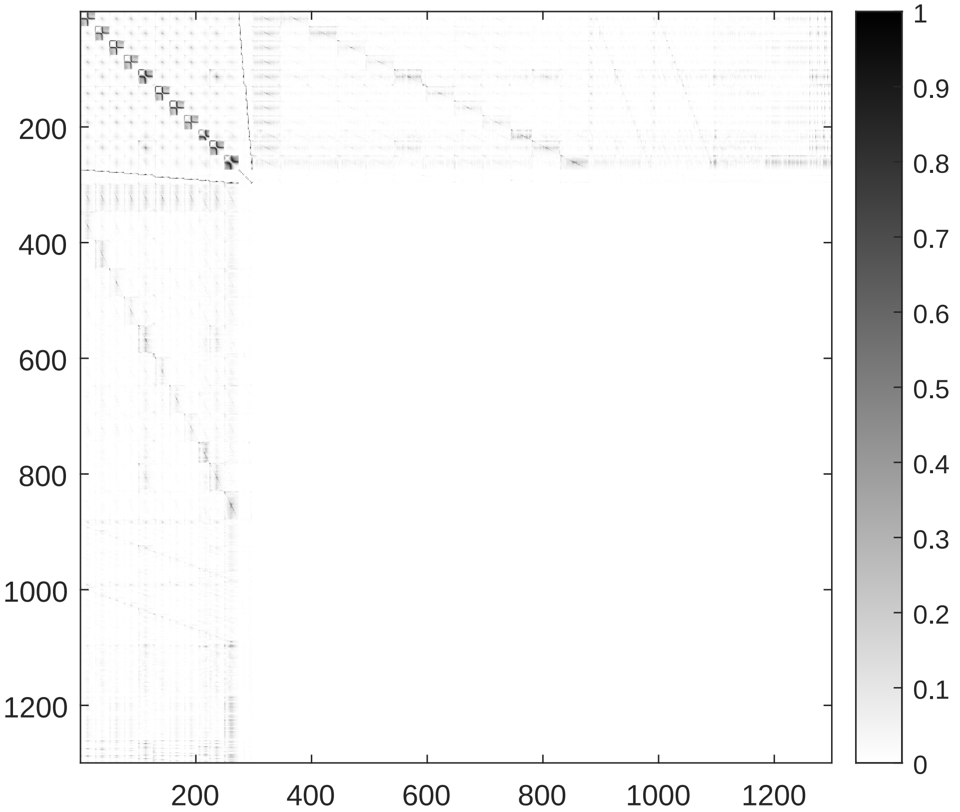

Fig. 3 Absolute differences in correlation coefficients in session 17NOV28XA. Order of parameters: 273 clock offsets, 24 rate and quad. terms of clock functions, 581 zenith wet delays, 216 gradients, 10 EOP and their rates, 156 source position components, and 39 station coordinate offsets.

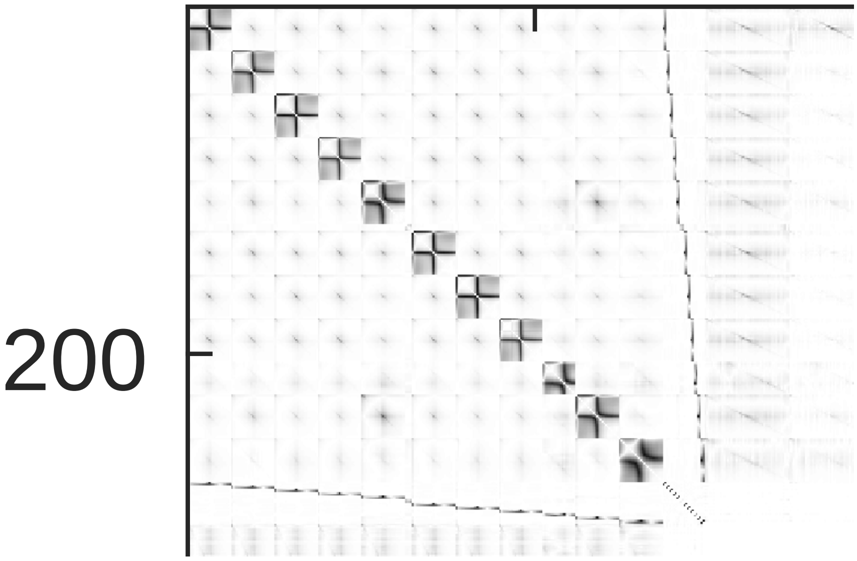

Fig. 4 Enlarged excerpt of Fig. 3 (Absolute differences in correlation coefficients).

Assessment of sub-daily Earth Rotation Parameters from VLBI with GNSS during the CONT17 campaign

S. Raut, R. Heinkelmann, S. Modiri, C. Kitpracha, H. Schuh

Abstract Monitoring the Earth rotation variation is a fundamental topic for several fields and applications such as astronomical and geodetic reference systems, precise satellite orbit determination, and space navigation. Very Long Baseline Interferometry (VLBI) and Global Navigation Satellite Systems (GNSS) provide high accurate observation of sub-daily changes in Earth rotation, mainly caused by ocean tides and small effects from the atmosphere interact the solid Earth.

In this work, we analyzed the sub-daily Earth Rotation Parameters (ERP) estimates from VLBI using VieVs@GFZ software during the CONT17 campaign. We chose the CONT17 campaign as it provides 15 days of continuous VLBI data from the two legacy networks i.e., legacy-1 (IVS) and legacy-2 (VLBA), having different network geometry, and five days of new-generation VGOS sessions. We derived ERP by combining the two legacy networks at the normal equation level for better precision. We assessed the VLBI results with polar motion (PM) and length of day (LOD) estimated from the GNSS using EPOS software at GFZ at the hourly resolution. As GNSS only provides LOD estimates, we computed LOD from VLBI-derived UT1-UTC (dUT1) parameters. This is possible as LOD is the negative time-derivative of dUT1. Besides, we evaluated the VGOS performance with the legacy networks at the sub-daily resolution.

We do not estimate Celestial Pole Offsets (CPO) due to their correlation with sub-daily PM for the analysis. Our preliminary results show that sub-daily ERP from a combined legacy network shows better agreement with the GNSS and smaller formal errors than ERP from the individual legacy networks. The dUT1 estimates from the VGOS network show good agreement with the legacy networks.

Keywords Earth Rotation Parameters, CONT17, VGOS

1 Introduction

Investigation of the sub-daily Earth Orientation Parameters is vital for scientific research. In this work, we present the sub-daily Polar Motion (PM), UT1-UTC, and Length of day (LOD) estimated from the CONT17 campaign. We chose the CONT17 campaign as in that three independent networks were observed instead of just one: two legacy networks observed at S/X band, one VGOS network performed broadband observing. The VGOS broadband network had a smaller size and was observed for about a third of the CONT17 period (five days). We also compared our results with GNSS, which serves as an external reference.

Shrishail Raut · Chaiyaporn Kitpracha · Harald Schuh
GFZ German Research Centre for Geosciences, Telegrafenberg, 14473 Potsdam
Chair of Satellite Geodesy, Technische Universität Berlin, Institute of Geodesy and Geoinformation Science, Faculty VI, Kaiserin-Augusta-Allee 104-106, Room KAI 2221, 10553 Berlin

Robert Heinkelmann
GFZ German Research Centre for Geosciences, Telegrafenberg, 14473 Potsdam

Sadegh Modiri
GFZ German Research Centre for Geosciences, Telegrafenberg, 14473 Potsdam
now at Bundesamt für Kartographie und Geodäsie BKG, Frankfurt, Germany

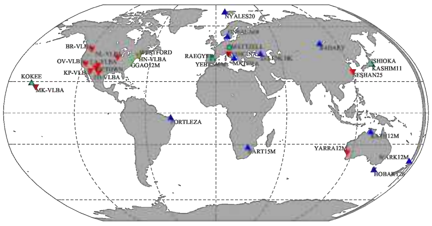

Fig. 1: Global map of stations (3 networks) that participated during CONT17 campaign from 28th Nov to 12th Dec, 2017.(Behrend, D., 2020). *The blue triangle, red inverted triangle and green circle represents legacy-1 (IVS), legacy-2 (VLBA) and VGOS stations, respectively.*
$*$VGOS sessions only took place from 3rd Dec to 7th Dec, 2017. $^{\#}$RAEGYEB station was excluded from our analysis.

2 Method

We used VieVs@GFZ software (Nilsson, T. et al., 2015) to analyze VLBI CONT17 sessions. There are 30 sessions in total i.e., 15 sessions for each legacy network and 5 additional VGOS sessions. We performed multi-session analysis (i.e., global solution) for each network to estimate more precise ERP. Besides, we also estimated ERP by combining the two legacy networks. In this analysis, we did not apply any relative or absolute constraint on ERP to allow for sub-daily variations. As we estimate hourly polar motion (PM), we fixed CPO to their a priori values (i.e., finals.all). This is done as there is a high correlation between CPO and sub-daily PM. We estimated ERP from VGOS for two hours resolution and then linearly interpolated it to hourly resolution. This was done as the VGOS sessions have fewer observations and stations as compared to legacy networks. We derived LOD and the corresponding errors from VLBI-derived dUT1 using the equations 1 and 2, respectively. We used GFZ software package EPOS.P8 group to determine hourly ERP (PM and LOD) from GNSS data during the CONT17 period (Uhlemann, M. et al., 2015; Männel, B. et al., 2020, 2021).

$$LOD = -\frac{dUT1_{i+1} - dUT1_i}{t_{i+1} - t_i} \tag{1}$$

where, t = epoch of estimate.

$$LOD_{sigma} = \sqrt{dUT1^2_{sigma_{i+1}} + dUT1^2_{sigma_i}} \tag{2}$$

The parameterization used in VLBI and GNSS is given in table 1. Table 2 refers to the models and a priori values used in this work. The models and a priori values used in GNSS analysis were consistent with the VLBI analysis. We also de-trended (i.e., mean offset was removed from the time-series) the ERP time series from VLBI and GNSS before comparing them. We computed the weighted-root mean square, $WRMS$ (see equation 3) and mean error, $sigma_{mean}$ of the entire time-series for an overall quantification of the estimated ERP time-series (see equation 4).

$$WRMS = \sqrt{\frac{\sum_{i=1}^{n} \frac{erp_i^2}{sigma_i^2}}{\sum_{i=1}^{n} \frac{1}{sigma_i^2}}} \tag{3}$$

$$sigma_{mean} = \frac{\sum_{i=1}^{n} sigma_i}{n} \tag{4}$$

where, erp = xpole, ypole, dUT1, LOD and $sigma$ = corresponding formal errors of erp.

Table 1: Parameterization used for the VLBI and GNSS analysis.

PARAMETERS	**VLBI**		**GNSS**
	LEAST-SQUARE ESTIMATION (CONSTRAINT)	**MULTI-SESSION ANALYSIS**	
PM	60 min (unconstained)	Estimated	60 min
UT1-UTC	60 min (unconstained)	Estimated	n.a.
LOD	n.a.	n.a.	60 min
CPO	Fixed to a priori	Reduced	n.a.
Station Coord.	1 day	Reduced	1 day
Source Coord.	1 day	Reduced	n.a.
Zenith Wet Delay (ZWD)	60 min (1.5 cm)	Reduced	60 min
Gradients (NGR & EGR)	360 min (0.05 cm)	Reduced	1 day
Clock	60 min (1.5 min)	Reduced	Epoch-wise

Table 2: Some models and a priori series used in the VLBI analysis.

MODELS/REFERENCE FRAME		TYPE
EOP	A priori series	finals.all (IAU2000)
	Precession/ Nutation Model	IAU 2006/20A
Reference Frames (RF)	Terrestrial RF	ITRF2014 (Altamimi, Z, 2016)
	Celestial RF	ICRF3, VLBI
Ephemerides	Ephemerides	JPL 421
Troposphere	Pressure	GPT2
	Temperature	GPT2
	Mapping functions	Vienna Mapping Function (VMF)
	Gradients	APG (Bohm)
Ionosphere	Ionosphere delay	From NGS file, VLBI
Station Models	Tidal Ocean loading	FES2004, VLBI & FES2014b, GNSS
	Tidal Atmosphere loading	vandam
	Mean pole model	IERS 2015

3 Results

We performed the analysis separately for legacy and VGOS networks w.r.t. the GNSS.

3.1 Legacy network

Polar motion

We can observe from the figure 2, that the sub-daily variations in x-pole from all networks. The hourly x-pole values from the combined network has a smaller scatter compared to an individual legacy network. The x-pole values from the combined network has smaller WRMS and formal errors than the individual legacy networks (figure 3a). This is because of better global coverage and twice (approx.) the number of observations in the combined network w.r.t. individual networks. The WRMS and mean error of x-pole from GNSS w.r.t. apriori values are smaller in comparison to the x-pole from VLBI networks (see figure 3b), this is possible as GNSS has better global coverage, and a high number of observations (approximately 20 times more observations than combined VLBI network!).

Coming to the results from the individual legacy networks, the agreement between the x-pole from legacy-1 and GNSS is slightly better than x-pole from legacy-2 and GNSS. This is expected as x-pole is sensitive to longer baselines in the north-south direction. Legacy-1 network is better distributed globally than the legacy-2 network (it has only one station in the southern hemisphere) (Nilsson, T. et al., 2019). The x-pole from the combined network has significantly better agreement with GNSS, as it has more stations and number of observations compared to individual legacy networks.

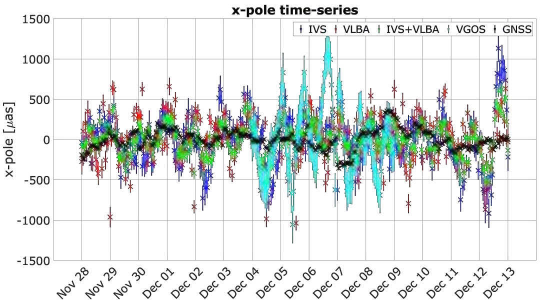

Fig. 2: Time series of hourly x-pole resp., (differences to finals.all a priori) estimated from legacy-1, legacy-2, combined legacy network, VGOS (5 days), and GNSS, during the CONT17 period.

A similar analysis was performed for hourly y-pole and we found that agreement between y-pole from legacy-1 and GNSS is significantly better than y-pole from legacy-2 and GNSS. This is possible since the y-pole is more sensitive to larger baseline extensions in the y-direction. Apart from the above observation, we got similar results as x-pole for the y-pole.

UT1-UTC and LOD

Hourly UT1-UTC from a combined legacy network has a smaller scatter compared to an individual legacy and VGOS network (see figure 4). From figure 5a, UT1-UTC from the legacy-1 and legacy-2 networks show comparable agreement with each other. This should be possible as both the networks have several long east-west baselines. The UT1-UTC is sensitive to baselines having longer east-west extension (Schuh,

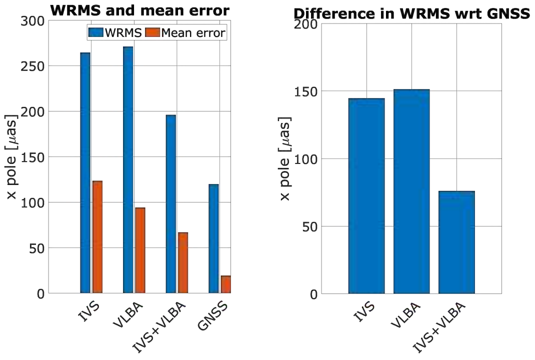

(a) WRMS and mean error of x-pole estimates

(b) Differences between the WRMS of x-pole estimates

Fig. 3: x-pole estimates w.r.t. finals.all a priori from legacy-1, legacy-2, combined and GNSS, for the entire duration of CONT17 campaign.

H., 2000). However, from combined network shows slightly better agreement compared to legacy-1 and legacy-2, possibly due to and more stations and a higher number of observations compared to individual legacy networks.

LOD from combined legacy network shows better agreement with GNSS (see figure 5b), possibly due to more number of observations and stations.

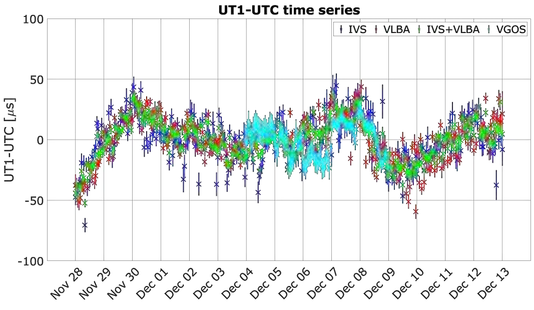

Fig. 4: Time series of hourly UT1-UTC resp., (differences to finals.all a priori) estimated from legacy-1, legacy-1, combined legacy network, VGOS (5 days), and GNSS, during the CONT17 period.

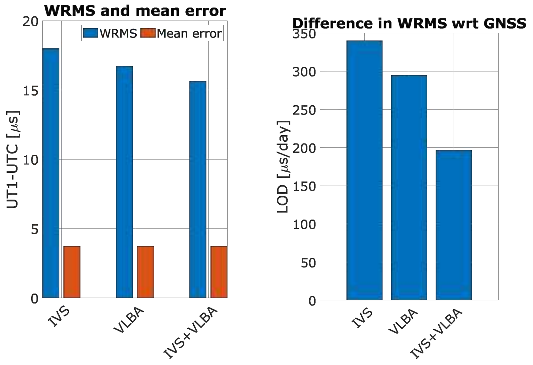

(a) WRMS and mean error of UT-UTC estimates

(b) Differences between the WRMS of LOD estimates

Fig. 5: The estimates are w.r.t. finals.all a priori from legacy-1, legacy-2, combined and GNSS, for the entire duration of CONT17 campaign.

3.2 VGOS network

The following analysis between legacy, VGOS, and GNSS networks is done for 5 days to align with the VGOS period during CONT17 (i.e., 3rd to 7th December 2017). This is done to have a fair assessment of the results from legacy and VGOS networks.

Polar motion

The hourly x-pole from VGOS has a larger scatter compared to legacy networks and GNSS (figure 2). From figure 6a, hourly x-pole from VGOS have a larger WRMS and mean error as compared to individual and combined legacy networks. We can observe that the hourly x-pole from VGOS doesn't show better agreement with GNSS as compared to individual and combined legacy networks (figure 6b). The possible reason for the above observations could be poor global coverage (no station in the southern hemisphere).

UT1-UTC and LOD

From figure 7a, hourly UT1-UTC from VGOS shows a good agreement with legacy networks. It is possible as VGOS has long east-west baseline which sensitive to the UT1-UTC parameters. However, the precision of UT1-UTC from VGOS is comparable to UT1-

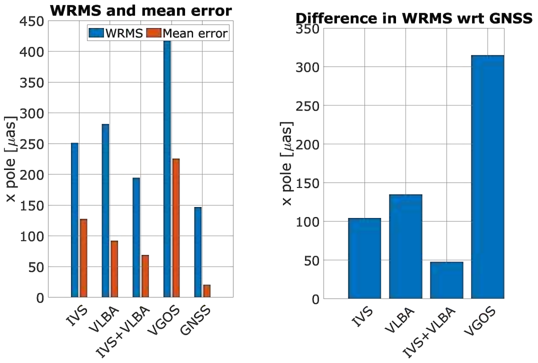

(a) WRMS and mean error of x-pole estimates

(b) Differences between the WRMS of x-pole estimates

Fig. 6: x-pole estimates w.r.t. finals.all a priori from legacy-1, legacy-2, combined and GNSS, for the 5 days of CONT17 campaign.

UTC from IVS (figure 7b). This is despite the fact that VGOS has 3 times less observations and stations than IVS network.

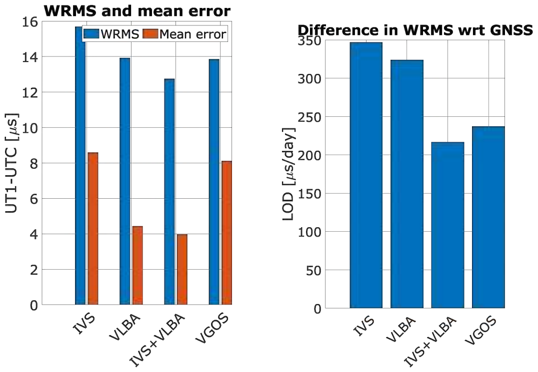

(a) WRMS and mean error of UT-UTC estimates

(b) Differences between the WRMS of LOD estimates

Fig. 7: The estimates are w.r.t. finals.all a priori from legacy-1, legacy-2, combined and GNSS, for the 5 days of CONT17 campaign.

4 Conclusions and outlook

Hourly PM from the legacy-1 network shows better agreement w.r.t. GNSS than legacy-2. This is due to the better network geometry of legacy-1 (i.e. more north-south baselines). ERP (PM and LOD derived from dUT1) estimated from combined networks show better agreement with ERP from GNSS as compared to individual legacy networks for hourly resolution. PM from VGOS does not perform well w.r.t. legacy networks and GNSS. This might be due to poor network geometry, i.e., no station in southern hemisphere (PM is sensitive to longer north-south baseline). The hourly UT1-UTC quality from VGOS are comparable with individual and combined legacy networks despite of less stations and observations than legacy network. Hourly LOD (derived from dUT1) from VGOS shows better agreement with GNSS than the individual legacy networks. This might be due to the long east-west baselines in present VGOS sessions (UT1-UTC and LOD are sensitive to longer east-west baseline). It is evident that EOP are sensitive to the network geometry.

References

Nilsson, T., Soja, B., Karbon, M., Heinkelmann, R., Schuh (2015) Application of Kalman filtering in VLBI data analysis. *Earth, Planets and Space*, 67(1), 1-9, doi: .

Behrend, D., Thomas, C., Gipson, J., Himwich, E., Le Bail, K. (2020) On the organization of CONT17. *Journal of Geodesy*, 94(10), 1-13, doi: .

Männel, B., Brandt, A., Bradke, M., Sakic, P., Brack, A., Nischan, T. (2020) Status of IGS reprocessing activities at GFZ. , 1, 1–99, doi: .

Männel, B.; Brandt, A.; Bradke, M.; Sakic, P.; Back, A.; Nischan, T. (2021) GFZ repro3 product series for the International GNSS Service (IGS). *GFZ Data Services.*, doi: https://doi.org/10.5880/GFZ.1.1.2021.001.

Uhlemann, M., Gendt, G., Ramatschi, M., Deng, Z. (2015) GFZ global multi-GNSS network and data processing results. *IAG 150 years, 673-679.*, doi: .

Altamimi, Z., Rebischung, P., Métivier, L., Collilieux, X. (2016). ITRF2014: A new release of the International Terrestrial Reference Frame modeling nonlinear station motions. *Journal of Geophysical Research: Solid Earth*, 121(8), 6109-6131, doi: .

Schuh, H., Schmitz-Hübsch, H. (2000) Short period variations in Earth rotation as seen by VLBI. *Surveys in Geophysics*, 21(5), 499-520, doi: .

Nilsson, T., Balidakis, K., Heinkelmann, R., Schuh, H. (2019). Earth orientation parameters from the CONT17 campaign. *Geophysica/Geofysiikan Seura*, 54(1), 19-25, doi: .

First VLBI-only TRF/CRF solution based on DGFI-TUM data for ITRF2020

M. Glomsda, M. Seitz, M. Bloßfeld, A. Kehm, M. Gerstl, D. Angermann

Abstract DGFI-TUM is an operational Analysis Center (AC) of the International VLBI Service for Geodesy and Astrometry (IVS). In this role, we reprocessed almost all VLBI sessions between 1979 and 2020 for the IVS contribution to the upcoming realization of the International Terrestrial Reference System (ITRS), the ITRF2020. The reprocessed solution contains all requested new geophysical models, including the latest realization of the International Celestial Reference System (ICRS), the ICRF3, as a priori reference frame for the estimated source coordinates. We used our homogeneously reprocessed data to create a preliminary VLBI-only TRF/CRF solution, in which we consistently estimated station positions and velocities, Earth Orientation Parameters (EOP), and radio source positions. It could serve as a new reference for a priori station and source coordinates and will be a good basis for further (inter-technique) combination studies. In this work, we describe the input data, the estimation process, as well as the results of the combination of our session-wise solutions, which has been performed at the normal equation level with our DGFI Orbit and Geodetic parameter estimation Software (DOGS). We also discuss the impact of recently observed and VGOS sessions on the CRF.

Keywords VLBI, VGOS, ITRF2020, CRF, consistent estimation

Deutsches Geodätisches Forschungsinstitut
der Technischen Universität München,
Arcisstraße 21, 80333 München, Germany

1 Introduction

The IVS AC DGFI-TUM has contributed to the ITRF2020 with its reprocessed solution *dgf2020a_woNTAL*. It is based on the latest IERS Conventions of 2010 (Petit and Luzum, 2010) and its updates, including the new models requested for ITRF2020. Furthermore, it contains partial derivatives w.r.t. the radio source coordinates, which was a requirement to be fulfilled by all participating ACs for the first time. The only methodological difference to our current operational IVS contribution, *dgf2020a*, is the missing correction for non-tidal atmospheric loading (at the observation level; Glomsda et al., 2020). Since *dgf2020a_woNTAL* represents a homogeneous set of almost all 24h VLBI sessions of the last 40 years, including VGOS and mixed-mode observations, we took the opportunity to estimate preliminary VLBI-only TRF/CRF solutions with this data. After all, the consistent estimation of TRF, CRF and EOP is an important goal for the future (Kwak et al., 2018).

2 Input data and estimation process

For the TRF/CRF solutions presented here, the session-wise datum-free normal equations of *dgf2020a_woNTAL* have been combined with the DOGS library CS (“Combination and Solution“; Gerstl et al., 2000). In each session, station coordinates, EOP and radio source coordinates are estimated, after clock and tropospheric parameters have been reduced from the normal equation system. Since all parameters are estimated simultaneously, we obtain a consistent combination of TRF, CRF and EOP.

For the long-term solutions, we estimated a linear TRF, i.e. station coordinates at a reference epoch t_0 as well as constant velocities. For the time being, the EOP are reduced, which means their session-wise information is only implicitly contained in the combined normal equation system. The CRF, on the other hand, is again explicitly estimated. In alignment with the ICRF3 (Charlot et al., 2020), we considered Galactic Aberration (GA), which is an apparent linear motion of the radio sources generated from the acceleration of the solar system barycenter towards the Galactic Center. First, we introduced parameters for source coordinates and velocities at the same reference epoch 2015.0 as used for the ICRF3. Then, the a priori values for the velocities were derived from the formula for GA given in Charlot et al. (2020). Finally, the velocities were fixed to these a priori values and only the corresponding source coordinates were estimated.

To realize the geodetic datum, no-net-translation and no-net-rotation conditions w.r.t. the DTRF2014 as well as no-net-rotation conditions w.r.t. the ICRF3 have been applied to the stations and sources, respectively. As the reference epoch, we chose $t_0 = 2000.0$, which is close to the midpoint of the more than 40 years of VLBI observations.

Basically all sessions relevant for the ITRF2020 (i.e. those with at least three stations) have been considered. Only a small fraction of sessions could not be analysed properly and was neglected. Table 1 provides a summary of the input data.

We analysed several TRF/CRF solutions, which will be explained in the upcoming sections. The most critical issue is the inclusion of the VGOS sessions, where newly constructed or converted telescopes are performing broadband observations of the radio sources (e.g., Petrachenko et al., 2009). These VGOS observations and networks are not readily connected with the legacy S/X observations and networks. Hence, one must either introduce local ties between co-located VGOS and legacy antennas, or make use of the mixed-mode sessions, where VGOS and legacy antennas are jointly performing S/X observations. For the future, we plan to also apply local ties at co-locations such as Wettzell or Kokee Park. In the current solutions, however, the networks are tied together by the three mixed-mode sessions only.

Table 1 Summary of the data included in the distinct CRF/TRF solutions. VCS is the abbreviation for "VLBA Calibrator Survey" (Gordon et al., 2016), and "VCS-like" sessions are those with 1) a VLBA station network plus one additional station and 2) at least 100 observed sources.

time span	1979 - 2020
sessions	6,238
VCS sessions	24 VCS-I + 8 VCS-II
VCS-like sessions	52
VGOS sessions	33
mixed-mode sessions	3
S/X stations [solutions]	114 [158]
VGOS stations [solutions]	8 [8]
datum stations	41 (DTRF2014)
sources	5,044
single-session sources	322
VCS sources	2,458
datum sources	303 (ICRF3 defining sources)
observations	18,266,534
active variables	11,066

3 TRF/CRF solutions

3.1 Basic scenario

The basic TRF/CRF solution S1 is the one where all legacy but no VGOS sessions are used. Hence, all estimated coordinates and velocities refer to observations in the S/X-bands.

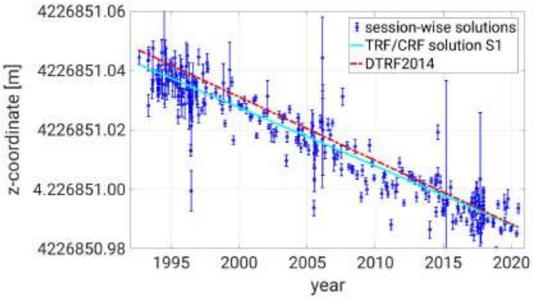

Fig. 1 The estimated linear motion of the z-coordinate of station NL-VLBA in our basic TRF/CRF solution S1 (solid cyan line), based on the session-wise solutions (blue), and compared to the a priori TRF (dash-dotted red line).

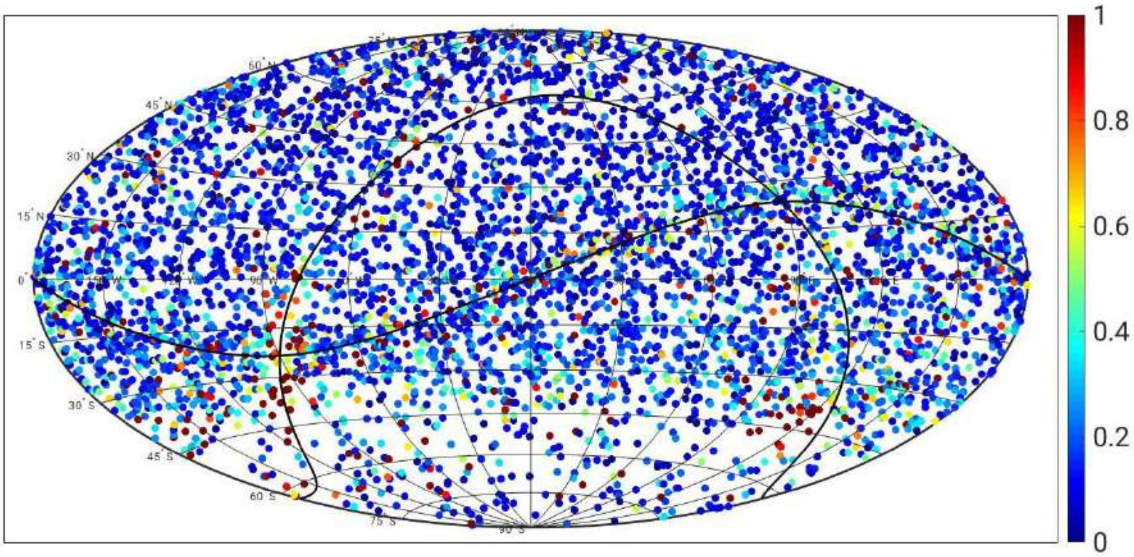

Fig. 2 Formal errors (in [mas]) of the estimated radio source coordinates in the basic TRF/CRF solution S1.

3.1.1 TRF

When comparing the estimated linear station coordinates with the time series of single-session coordinates, we usually found a good fit. On the other hand, a 14-parameter Helmert transformation w.r.t. the DTRF2014, DGFI-TUM´s latest realization of the ITRS (Seitz et al., 2016), revealed a quite significant change in network geometry for transformation epoch 2000.0, which must be analysed in more detail. At the very least, our TRF/CRF solution has been created from six years of additional data, which will likely lead to different station motions, cf. Fig. 1. The new models used for ITRF2020, such as the gravitational deformation of six antennas and the updated mean pole formula, might also have some influence.

3.1.2 CRF

Figure 2 shows the estimated radio source positions $p = (\alpha, \delta)$ at epoch 2015.0 on the celestial sphere together with their formal errors (standard deviations)

$$\sigma_p = \sqrt{\sigma_\delta^2 + [\sigma_\alpha \cdot \cos(\delta)]^2}, \qquad (1)$$

where α and δ represent the right ascension and the declination of a radio source, respectively. The errors are generally larger at the Galactic (impeded observations through the Milky Way) and the Ecliptic plane (many single-session sources). The plot looks very similar to the S/X-band component of the ICRF3 (Charlot et al., 2020).

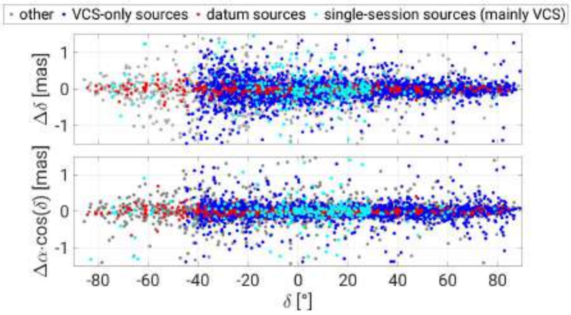

Fig. 3 Changes in declination δ and right ascension α for the sources estimated in our basic TRF/CRF solution S1 w.r.t. their a priori values from the ICRF3, separated by source type.

In Fig. 3, the changes in the declinations and right ascensions of the sources w.r.t. the ICRF3 are plotted (separated by particular source types). There are no systematic deviations, but we can observe that the datum sources have the smallest differences (showing a good agreement with ICRF3), and that the single-session sources are concentrated at declinations $|\delta| < 23.44°$ (Ecliptic).

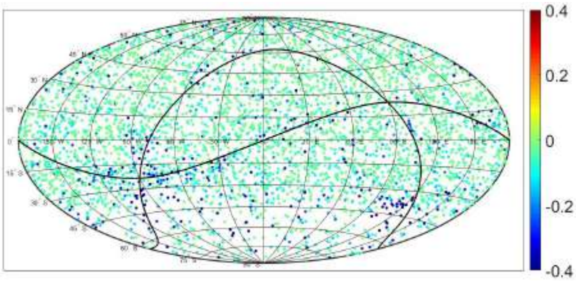

Fig. 4 Changes in standard deviations (in [mas]) when adding the data of the years 2018–2020 to the TRF/CRF solution.

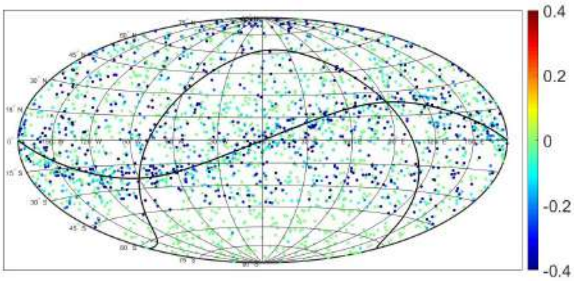

Fig. 5 Changes in standard deviations (in [mas]) when adding the VCS and VCS-like sessions to the TRF/CRF solution. The set of sources is much smaller without the VCS (-like) sessions.

3.2 Impact of post-ICRF3 period

The ICRF3 was generated from VLBI data up to the beginning of 2018 (Charlot et al., 2020). Hence, solution S1 contains three more years of data. To investigate the corresponding impact, we computed another TRF/CRF solution, S2, without the sessions of the years 2018–2020. Figure 4 shows the changes in the source positions' standard deviations of Eq. (1) when including these sessions, i.e. when moving from solution S2 to solution S1. As expected, the additional data improves the formal errors of all estimated radio source positions. The mean and median decrease in standard deviations are about -0.05 and -0.03 mas, respectively.

In particular, additional VCS or VCS-like sessions were scheduled during the last three years. These are specifically designed to improve the formal errors of rarely observed radio sources. To confirm their benefit, we computed the TRF/CRF solution S3, where all (i.e. also before 2018) VCS and VCS-like sessions are neglected. In Fig. 5, we see that the standard deviations of all remaining radio sources actually decrease when the VCS (-like) sessions are included, especially near the Ecliptic plane. The mean and median drop in formal errors are about -0.2 and -0.05 mas, respectively.

3.3 Impact of VGOS observations

It is of particular interest how the new VGOS sessions affect the TRF/CRF solution. As mentioned before, we did not apply local ties between co-located VGOS and legacy antennas, but only used the mixed-mode sessions for the connection of the two distinct networks. And there is another issue when including the VGOS sessions: the observed frequency bands differ w.r.t. the legacy S/X sessions. Since the structure of radio sources changes with frequency (e.g., Petrachenko et al., 2009), the source positions will probably deviate between VGOS and legacy observations.

To investigate this, we created two further TRF/CRF solutions: in S4, there is a single parameter for each source coordinate, irrespective of whether the source is observed in a VGOS or a legacy session. In S5, on the other hand, there contingently are two right ascension and two declination parameters for each source: one referring to the VGOS observations, and one referring to the legacy observations.

3.3.1 CRF

Compared to solution S1, the impact of the VGOS sessions on the radio source positions is rather small in both cases. However, when comparing the formal position errors between the solutions S4 and S5, we find that the standard deviations of the coordinates estimated from the VGOS sessions only significantly deteriorate (see Fig. 6), while those estimated from the legacy sessions are hardly affected by the separation (see Fig. 7). This is no surprise, as the number of VGOS sessions is very small. Nevertheless, the separation might be justified by the frequency-dependent source structure, and hence the increased formal errors must be accepted until more VGOS data is available.

3.3.2 TRF

The estimated station motions are not separated for VGOS and legacy sessions. Even though some stations

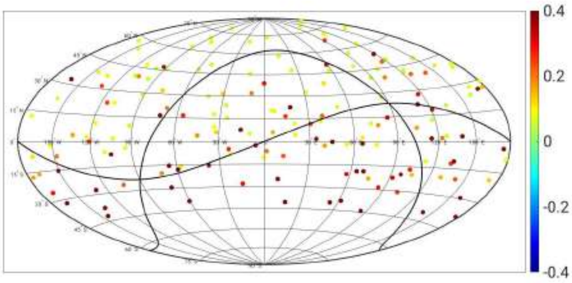

Fig. 6 Changes in standard deviations (in [mas]) when separating the estimated source positions for VGOS and legacy sessions: VGOS session parameters.

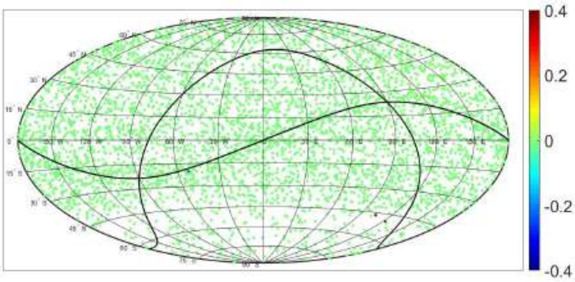

Fig. 7 Changes in standard deviations (in [mas]) when separating the estimated source positions for VGOS and legacy sessions: legacy session parameters.

have switched from S/X legacy to VGOS broadband receivers in the past (e.g., WESTFORD and ISHIOKA), their reference points are supposed to remain the same. Nevertheless, to investigate whether the new observations have an impact on the station network, we analysed 14-parameter Helmert transformations between our basic solution S1 and the two VGOS solutions S4 and S5, as well as the transformation between S4 and S5 themselves.

In Table 2, we list the transformation residuals for ISHIOKA. It was striking, because there is a large residual in the up components when the source coordinates are separated by frequency (S5), which disappears if VGOS and legacy positions are equalized (S4). The residuals of the VGOS stations generally are quite large in both cases, which might implicate that the small number of VGOS sessions is only weakly tied to the legacy network by the mixed-mode sessions. Station heights seem to be affected most, but there is no unique pattern and hence no obvious VGOS-related scale issue, either. All in all, however, there are subtle effects created by the inclusion of the VGOS data.

Table 2 Residuals of the two solutions A01 and A02 for VGOS station ISHIOKA in the 14-parameter Helmert-transformations. N, E and U represent the coordinate residuals in North, East and up direction, respectively. The unit is [mm]. VN, VE and VU represent the velocity residuals in North, East and up direction, respectively. The unit is [mm/yr].

transformation	solnr	N	E	U	VN	VE	VU
S1 to S4	A01	-0.44	-1.17	0.40	0.03	0.08	-0.02
	A02	-4.53	0.36	-3.48	0.24	-0.01	0.18
S1 to S5	A01	0.50	-0.19	-7.07	-0.03	0.01	0.43
	A02	-3.38	0.39	-2.28	0.18	-0.02	0.12
S5 to S4	A01	-0.94	-0.97	7.48	0.06	0.06	-0.45
	A02	-1.14	-0.03	-1.20	0.06	0.01	0.07

3.4 Conclusion

We have estimated several consistent VLBI-only TRF/CRF solutions from our ITRF2020-contribution *dgf2020a_woNTAL*, which look promising in the first place. Nevertheless, some aspects need further investigation, e.g. the proper inclusion and corresponding effects of the VGOS observations.

References

Charlot P., Jacobs C.S., et al. (2020): The third realization of the International Celestial Reference Frame by very long baseline interferometry. *Astronomy & Astrophysics*, 644.

Gerstl M., Kelm R., Müller H., and Ehrnsperger W. (2000): DOGS-CS – Kombination und Lösung großer Gleichungssysteme. *Internal Report*, DGFI-TUM.

Glomsda M., Bloßfeld M., Seitz M., and Seitz F. (2020): Benefits of non-tidal loading applied at distinct levels in VLBI analysis. *Journal of Geodesy*, Vol. 94 (90).

Gordon D., Jacobs C., Beasley A., et al. (2016): Second Epoch VLBA Calibrator Survey Observations: VCS-II. *The Astronomical Journal*, Vol. 151, No. 6.

Kwak Y., Bloßfeld M., Schmid R., Angermann D., Gerstl M., and Seitz M. (2018): Consistent realization of Celestial and Terrestrial Reference Frames. *Journal of Geodesy*, Vol. 92, pp. 1047–1061.

Petit G. and Luzum B. (2010): IERS Technical Note 36, Version 1.3.0. *Verlag des Bundesamts für Kartographie und Geodäsie*, Frankfurt am Main.

Petrachenko B., Niell A., et al. (2009): Design aspects of the VLBI2010 system. Progress report of the VLBI2010 committee. *NASA/TM-2009-214180*.

Seitz M., Bloßfeld M., Angermann D., Schmid R., Gerstl M., and Seitz F. (2016): The new DGFI-TUM realization of the ITRS: DTRF2014 (data). *http://doi.pangaea.de/10.1594/PANGAEA.864046*

Source position differences between Gaia and VLBI

M.H. Xu, T. Savolainen, S. Lunz, J.M. Anderson, N. Zubko, H. Schuh

Abstract We report here the comparison of positions of the sources 1038+52A and 1038+52B from VLBI phase referencing, geodetic VLBI, and Gaia observations.

Keywords 1038+52A, 1038+52B, Gaia EDR3, phase referencing, geodetic VLBI, IVS

1 Introduction

In standard Active Galactic Nuclei (AGNs) models, the radio emission arises from a collimated beam of plasma which is ejected from a region close to a central massive object such as a black hole. The AGNs typically have "core-jet" morphologies at the mas scales; the core is thought to be a highly compact feature located at a relatively stable location, which is the base of an extended, line of lower, although not always especially at lower frequencies, brightness components (the jets). Recently a number of studies have demonstrated that the VLBI-to-Gaia position vectors are likely parallel to the jets, with the majority along the jet directions (see, e.g., Kovalev et al., 2017; Petrov et al., 2019; Xu et al., 2021; Lambert et al., 2021). The presence of parsec-scale optical jet structure in the directions of radio jets is proposed to explain the phenomenon in these studies. However, it is still a highly open question where the optical emission is located with respect to the radio features at scales of tens of microarcseconds (μas) for a given source. In order to draw the Gaia position and/or the position from the global astrometric/geodetic VLBI on a source image, one has to assume that, for example, the VLBI position is formally located at a specific radio component in the image. This assumption is well known to be not true, but it is needed because the radio images do not have absolute positions accurate better than several milliarcseconds (mas) and source structure affects the positions from global VLBI to somewhere away from any distinguished features, such as the core and the jet components.

The radio sources 1038+528 and 1038+529, also known as 1038+52A and 1038+52B, respectively, are only $\sim 33''$ apart on the sky and were observed in the phase referencing mode to have the relative position between the features of their structure with the accuracy at the level of tens of microarcseconds. We will make the detailed comparison of the positions from Gaia, geodetic VLBI, and phase referencing observations for this quasar pair and locate the Gaia positions on their radio images as a pilot study. This will help to understand where the optical emission comes from relative to the radio core and jets.

Ming H. Xu · Tuomas Savolainen
Aalto University Metsähovi Radio Observatory, Metsähovintie 114, 02540 Kylmälä, Finland; Aalto University Department of Electronics and Nanoengineering, PL15500, FI-00076 Aalto, Finland
`minghui.xu@aalto.fi`

Susanne Lunz · Harald Schuh
DeutschesGeoForschungsZentrum (GFZ), Potsdam, Telegrafenberg, 14473 Potsdam, Germany

James M. Anderson
Technische Universität Berlin, Institut für Geodäsie und Geoinformationstechnik, Kaiserin-Augusta-Allee 104-106, 10553 Berlin, Germany

Nataliya Zubko
Finnish Geospatial Research Institute, Geodeetinrinne 2, FIN-02430 Masala, Finland

2 Position measurements

The source pair of 1038+528 and 1038+529, with redshifts 0.678 and 2.296 and an angular separation of $\sim 33''$, provides a great opportunity of determining the relative positions between the radio features in their structure with a high accuracy, by using the full precision of the phase referencing observations; almost all of the phase errors are common for them. With one as the reference, it will allow us to locate the absolute positions from Gaia and geodetic VLBI on the radio image for another one to that high accuracy.

2.1 Phase reference

Their structure shown in Fig. 1 was obtained based on VLBA observations at the wavelength 3.6 cm in 1995.9 by Rioja & Porcas (2000). There are phase referencing observations at 3.6 cm for them at four epochs, in 1981.3 by Marcaide & Shapiro (1983), in 1983.4 by Marcaide et al. (1994), in 1990.5 by Rioja et al. (1997), and in 1995.9 by Rioja & Porcas (2000). The core of 1038+528 and the northeast jet component of 1038+529, marked by the blue pluses in Fig 1, were used as the reference points for the astrometric position measurements. The relative positions between them from the four-epoch measurements are presented in Table 1. The angular distances between the jet component (the reference point for the relative position measurements for the quasar pair) and the core of 1038+529 are presented in Table 2.

Table 1 Relative positions of the jet of 1038+529 with respect to the core of 1038+529 at λ 3.6 cm based on four-epoch phase reference measurements.

Epoch	$\Delta\alpha$	$\sigma(\Delta\alpha)$ (μas)	$\Delta\delta$	$\sigma(\Delta\delta)$ (μas)	Ref.
1981.2	$2^s.1160427$	25	$27''.376574$	36	(1)
1983.4	$2^s.1160439$	24	$27''.376510$	34	(2)
1990.5	$2^s.1160568$	28	$27''.376464$	36	(3)
1995.9	$2^s.1160588$	27	$27''.376325$	25	(4)

Note. References: (1) Marcaide & Shapiro (1983); (2) Marcaide et al. (1994); (3) Rioja et al. (1997);(4) Rioja & Porcas (2000).

Table 2 Position separations between the jet and the core of 1038+529 at λ 3.6 cm. The angular distance between the core and the jet is denoted by $R_{\text{core-jet}}$ and the jet position angle by $\theta_{\text{core-jet}}$, and $\alpha_{\text{core-jet}}$ and $\delta_{\text{core-jet}}$ are the projected position separations on right ascension and declination. The results from the first three epochs were reported in Rioja et al. (1997), and that in 1995.9 was reported in Rioja & Porcas (2000) without the error estimates available, which are expected to be the same level.

Epoch	$R_{\text{core-jet}}$ (μas)	$\theta_{\text{core-jet}}$ (degree)	$\alpha_{\text{core-jet}}$ (μas)	$\delta_{\text{core-jet}}$ (μas)
1981.2	1703±20	−53.3±0.4	−1365±18	1018±15
1983.4	1739±19	−53.4±0.5	−1396±18	1037±17
1990.5	1838±35	−52.8±0.8	−1464±32	1111±29
1995.9	1869	−52.9	−1491	1127

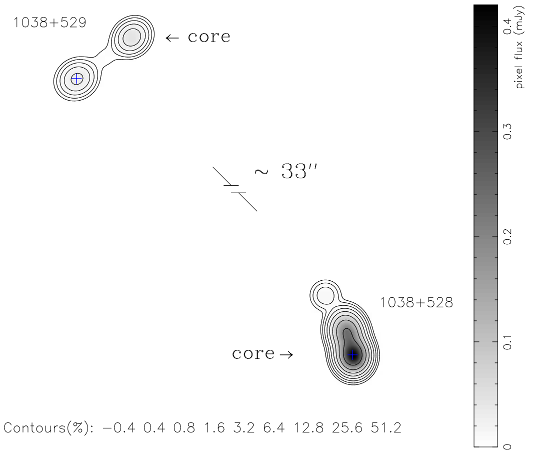

Fig. 1 Projection of the source pair of 1038+528 and 1038+529 on the sky. The maps were reproduced based on the model components in Table 1 of Rioja & Porcas (2000). The blue pluses are the features used for the reference points for the relative positions.

2.2 Absolute positions at radio and optical wavelengths

As officially adopted by the IAU in January 2019, the third realization of the ICRF (ICRF3; Charlot et al., 2020) is established based on 40 years of VLBI observations at S/X band. The European Space Agency mission *Gaia*[1] has published the Early Data Release 3 (EDR3; Gaia Collaboration et al., 2021) with optical positions of the sources in the ICRF3. The absolute positions of the quasar pair in the Gaia EDR3 and ICRF3 are listed in Table 3. Note that the effects of source

---

[1] `https://sci.esa.int/web/gaia`

structure (see, e.g., Xu et al., 2019) are not taken into account when the ICRF3 was built, and that the ICRF3 positions are determined based on group delay observables.

3 Where are the Gaia and ICRF3 positions on radio images?

3.1 Comparison of the relative positions

The relative positions of the quasar pair from Gaia and ICRF3 can be compared with the results from phase referencing observations. The difference in the relative positions, ($\Delta(\Delta\alpha)$, $\Delta(\Delta\delta)$), is defined as follows:

$$\begin{aligned}\Delta(\Delta\alpha) &=(\Delta\alpha-\Delta\alpha^{\mathrm{PR}})\cos(\delta),\\ \Delta(\Delta\delta) &=(\Delta\delta-\Delta\delta^{\mathrm{PR}}),\end{aligned} \tag{1}$$

where ($\Delta\alpha^{\mathrm{PR}},\Delta\delta^{\mathrm{PR}}$) is the relative position of the quasar pair based on phase referencing measurements, and ($\Delta\alpha,\Delta\delta$) is their relative position based on the absolute positions, for instance, from Gaia or ICRF3.

The results are presented in Table 4. Based on the results in Tables 2 and 4, the relative position from Gaia matches better with the angular distance between the cores of the two sources. The difference between the Gaia relative position and the core-core position at 1995.9 has an magnitude of $470\pm136\,\mu$as towards the position angle of $-24^\circ.5\pm10^\circ.9$. However, the ICRF3 relative position agrees with the core-jet position from the phase referencing measurements.

3.2 Absolute Gaia and ICRF3 positions on the images

By assuming the Gaia positions in the jet directions as demonstrated by several studies, it is possible to locate the Gaia positions on the images for both sources. Based on the projection of the Gaia relative positions onto the two jet directions of the quasar pair, the Gaia position of source 1038+528 with respect to the core is $242\pm57\,\mu$as towards the position angle of 195°, and the Gaia position of source 1038+529 with respect to its core is $323\pm74\,\mu$as towards the position angle of -53°. Therefore, the ICRF3 positions can also be located on the images. The Gaia and ICRF3 positions relative to the radio features based on the relative positions from phase referencing are shown in Fig 2.

4 Summary and discussion

The study for the first time attempts to locate the absolute source positions from Gaia and ICRF3 on the radio images to the accuracy level of the Gaia position uncertainties. It is done for the quasar pair of 1038+528 and 1038+529 based on the phase referencing observations.

For these two sources, the Gaia positions are located close to the cores towards the opposite directions of the jets, while the ICRF3 positions are somewhere between the jets and the cores due to source structure effects as expected and seem to be closer to the jets.

If the optical positions are assumed to be at the jet bases, the core shifts are likely to be $242\pm57\,\mu$as and $323\pm74\,\mu$as for this quasar pair.

The absolute positions of the radio features (the core and/or the jet) with a high accuracy can be very helpful in relative astrometry. For instance, if the core of a calibrator is determined with an absolute position at the accuracy of $100\,\mu$as, it can be used to determine the absolute position of a target, such as radio star, to that accuracy based on phase referencing observations. This will greatly improve the alignment between the radio and optical frames. It is possible that the future astrometric catalog of high accuracy will have both the absolute positions of the specified features and the radio images of the sources with those features explicitly labeled.

Acknowledgements

This research was supported by the Academy of Finland project No. 315721, the National Natural Science Foundation of China No. 11973023, and the DFG grant No. HE59372-2.

Table 3 Absolute positions of the sources 1038+528 and 1038+529 from the Gaia and astrometric/geodetic VLBI observations.

	Source	α	$\sigma_\alpha \cos\delta$ (μas)	δ	σ_δ (μas)
Gaia	1038+528	$10^h\,41^m\,46^s.7816366$	37	$52^\circ\,33'\,28''.231026$	50
	1038+529	$10^h\,41^m\,48^s.8975105$	71	$52^\circ\,33'\,55''.608906$	89
ICRF3	1038+528	$10^h\,41^m\,46^s.7816540$	34	$52^\circ\,33'\,28''.231796$	36
	1038+529	$10^h\,41^m\,48^s.8976707$	396	$52^\circ\,33'\,55''.608201$	355

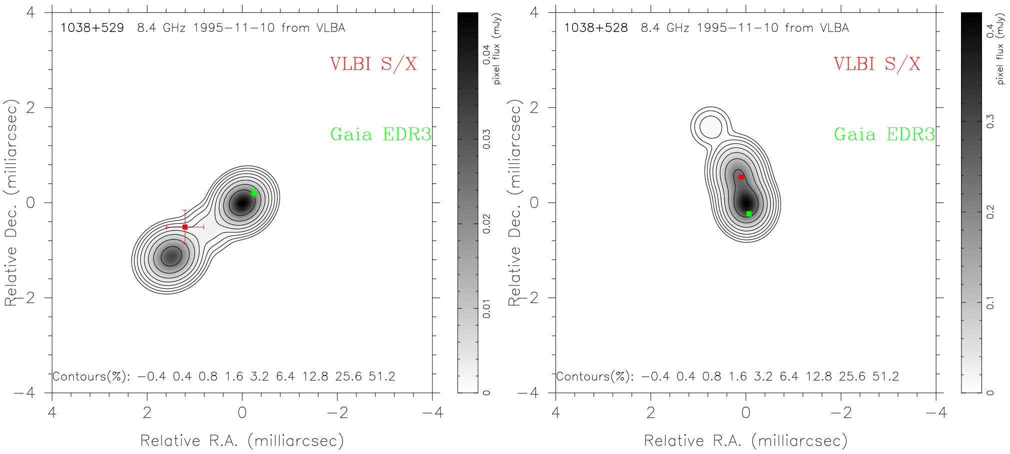

Fig. 2 Absolute positions of 1038+528 (right) and 1038+529 (left) on the radio images. The maps were reproduced based on the model components in Table 1 of Rioja & Porcas (2000).

Table 4 Comparing the relative positions of the quasar pair from the Gaia EDR3 and ICRF3 with the result from the phase referencing measurements in 1995.9. The uncertainties are the combined errors from that of both sources in the Gaia or ICRF3 catalog and of the phase referencing measurements.

	$\Delta(\Delta\alpha)$ (μas)	$\Delta(\Delta\alpha)$ (μas)
Gaia	−1686± 86	1555±105
ICRF3	−384±398	80±358

References

Charlot, P., Jacobs, C. S., Gordon, D., et al. 2020, A&A, 644, A159. doi:10.1051/0004-6361/202038368

Gaia Collaboration, Brown, A. G. A., Vallenari, A., et al. 2021, A&A, 649, A1. doi:10.1051/0004-6361/202039657

Kovalev, Y. Y., Petrov, L., & Plavin, A. V. 2017, A&A, 598, L1

Lambert S., Liu N., Arias E. F., et al. 2021, A&A, forthcoming. doi:10.1051/0004-6361/202140652

Marcaide, J. M. & Shapiro, I. I. 1983, AJ, 88, 1133. doi:10.1086/113402

Marcaide, J. M., Elosegui, P., & Shapiro, I. I. 1994, AJ, 108, 368. doi:10.1086/117075

Petrov, L., Kovalev, Y. Y., & Plavin, A. V. 2019, MNRAS, 482, 3023

Rioja, M. J., Marcaide, J. M., Elosegui, P., et al. 1997, A&A, 325, 383

Rioja, M. J. & Porcas, R. W. 2000, A&A, 355, 552

Xu, M. H., Anderson, J. M., Heinkelmann, R., et al. 2019, ApJS, 242, 5. doi:10.3847/1538-4365/ab16ea

Xu, M. H., Lunz, S., Anderson, J. M., et al. 2021, A&A, 647, A189. doi:10.1051/0004-6361/202040168

Data Unlimited - The IVS Seamless Auxiliary Data Archive at the Wettzell observatory

A. Neidhardt, S. Weston

Abstract During the Analysis Workshop of the IVS 2014 General Meeting in Shanghai, there was an idea put forward to collect and offer auxiliary data continuously. Auxiliary and meta data are usually recorded in log files which are created by the NASA Field System (FS) during and especially for the time of an observation session. Therefore, these data points - like meteorological values, clock offsets, cable calibrations, other calibration information, and so on - are just sporadically available from time to time between start and stop of an observation. But continuous data and especially auxiliary data become more and more important on the way to the accuracy of VGOS, because they help to improve data, correlation, and analysis quality. Therefore, the first seamless auxiliary data center started at the Wettzell observatory (https://vlbisysmon.evlbi.wettzell.de/zabbix). This presentation explains the technical background, the requirements at the stations, but also wants to encourage others to participate. The video can be watched under: https://youtu.be/HsVAisxZnio

Keywords Monitoring, seamless auxiliary data, ZABBIX

A. Neidhardt
FESG Wettzell, Technical University of Munich, Geodetic Observatory Wettzell, Sackenrieder Str. 25, D-93444 Bad Kötzting, Germany

Stuart Weston
Auckland University of Technology, Institute of Radio Astronomy and Space Research (IRASR), 55 Wellesley St E, Auckland, 1010, New Zealand

1 Introduction

The IVS Seamless Auxiliary Data Archive is a central database on a public server at the Wettzell observatory. It is a central data collector of supporting data for correlation and analysis. ”Auxiliary” herein means, that supplementary data sets (like meteorological values) are stored. They can be already available in log files or additionally gathered. The difference comes with the term ”Seamless”. All data are regularly sampled and continuously available. Users should be able to request individual data intervals with straight-forward techniques.

Therefore, the data archive offers a nice, interactive user interface in form of web pages at the URL https://vlbisysmon.evlbi.wettzell.de/zabbix/. The web page can be accessed with a specific user account, which can be used for the login.

A world map is presented after the login, which shows all participating sites (see a sample in Fig. 1). This map is used as menu and directly shows alert states with different colors. Depending on the site, alert levels show missing data up to even critical errors. Clicking on the antenna symbol opens a menu to switch to further web pages with plots of the data in the IVS Seamless Auxiliary Data Archive, plots of the data from the NASA Field System (if available), and a file archive for historic data sets older than 90 days.

Data of the archive usually arrive every 1 minute or every 5 minutes. Data from the NASA Field System can be sent up to a rate of one value per second. The data stay 90 days in the database and are then available as daily text files in a separate data file archive. Usual participants send the elementary data set of meteorological values (temperature, humidity, pressure, if avalibale: wind speed and wind direction) and the clock

Fig. 1 World map of the participating sites (Yebes and AGGO are under preparation).

offsets (dotmon and dotmon2 for VGOS antennas with two DBBCs) representing GPS PPS minus PPS of the formatter output. An extended version allows to send system temperatures, while it is currently not tested for continuous data (especially under VGOS scenarios).

The following sites currently participate: HOBART, MEDICINA, OHIGGINS, WARKWORTH, WETTZELL, WETTZ13N, WETTZ13S. Under preparation are YEBES, RAEGYEB, and AGGO.

Data sets can also be requested seamlessly from the database using a Python script, so that analysts can fetch data according to their needs, e.g. before, during, and after a specific session.

2 Participation of observatories

There are three different use cases for antenna sites to participate to the data archive (see Fig. 2).

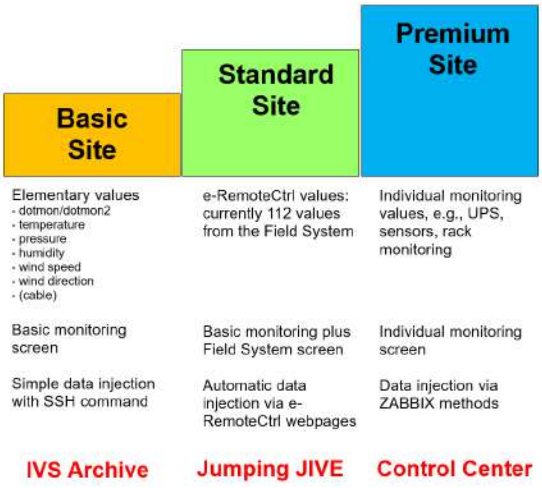

Basic Site	Standard Site	Premium Site
Elementary values - dotmon/dotmon2 - temperature - pressure - humidity - wind speed - wind direction - (cable)	e-RemoteCtrl values: currently 112 values from the Field System	Individual monitoring values, e.g., UPS, sensors, rack monitoring
Basic monitoring screen	Basic monitoring plus Field System screen	Individual monitoring screen
Simple data injection with SSH command	Automatic data injection via e-RemoteCtrl webpages	Data injection via ZABBIX methods
IVS Archive	Jumping JIVE	Control Center

Fig. 2 Use models of the data archive.

Basic users do not need special software on their computers. They need an SSH key and user account information for the central server and a working Secure Shell SSH (e.g. open port 22 in the firewalls to the monitoring servers). Antennas call the program ”zabbix_sender” via SSH on the central data server and pipe the individual data to the program. Therefore, timing is implemented by the antenna site in the calling programs. 179 different monitoring values can be sent which are grouped to logic sets, like values of Antenna Control Unit, System Status Monitor, System

Temperatures of Legacy Antennas, and so on. Basic sites usually start with a subset of the System Status Monitor which are additionally tagged as application of the seamless auxiliary data. A basic monitoring screen, where all elementary plots are combined, is available.

Standard users use the web server intergrated in the e-RemoteCtrl software. This software must be installed and configured on the NASA Field System PC. Observatories also need a working SSH like for the basic model. The difference is, that a script "autossh_run.sh" is used to initialize a permanent SSH connection which creates a reverse, continuously open tunnel from the monitoring server to the port of the web server on the Field System PC. Remote control ports are not forwarded and antennas can control transfers by starting and stopping the SSH connection.

The central server regularly loads the NASA Field System web pages every second and automatically updates all values. They are tagged with special HTML comment blocks in the web pages, so that scripts can find and inject them to the data archive. Additionally, these web pages can be made public on the central web server so that they can be opened from everywhere on the Internet.

Premium users are operation or control centers like Wettzell, where more than one antenna is monitored and controlled from a central control room. This requires special features and additional monitoring values of specific and special equipment, like cooling, heating, power, servers, PCs, SNMP devices. This hardware is independent from the pure functionality of the NASA Field System.

The monitoring is implemented with ZABBIX techniques, so that ZABBIX agents and proxies are used to request or send data over separate communication connections. These exchanges are also tunneled through SSH. Using individual accounts, it is possible to create own graphs, maps, and screens on the ZABBIX server, which give individual views on specific scenarios with a focus on operational requirements, like error detection, real-time alerting and trouble shooting.

The IVS Seamless Auxiliary Data Archive focuses on the basic use model to simplify things for antennas and limit administrative and security restrictions. To get more information about what to do if you want to participate, please watch the video at https://youtu.be/HsVAisxZnio.

3 Use of data for correlation and analysis

The benefits of the IVS Seamless Auxiliary Data Archive is currently under test especially by the Vienna VLBI group which already has access to the data sets. Interesting will be which advantages for correlation and analysis come from the seamless character of data and which additional types of data should be implemented. Therefore, it is also important that more and more antenna sites support at least the basic data sets, so that complete networks can be compared if seamless data are used or not.

If analysts want to use data, a straight-forward access method is implemented in form of a Python3 script "ZabbixAPI.py". It uses the HTTP interface of ZABBIX and can be used from everywhere on the Internet without knowledge about databases or the internal organization. Controlled with program arguments, individual data sets can be produced for specific time intervals. A sample call to return all clock offsets of the WETTZELL antenna for day "2021-04-23" for example is: *python3 ZabbixAPI.py -L -H WETTZELL_000_NASAFieldSystem -K ERC.DOTMON -TS "2021-04-23"*. The output is a simple table with date and time, Unix epoch, and the corresponding value for that time stamp. Outputs can directly be written to individual text files, so that they can be used with other programs.

A fast check can also be made with already mentioned graphs in the ZABBIX web interface. Users can zoom in graphs selecting intervals with menus or directly with the mouse on the graph. Minimum, maximum, mean, and trend values are shown for that interval. This is a possibility to get fast overview of the data for a special time interval.

Historic data older than three month can be directly downloaded as text file per UTC day. They have the same structure like the individually requested data sets described before. They are located on the web server and users can search them by following the folder structure defined by antenna name, year, month, item name (key), and finally the day-file. Names of daily files contain the date and item name. They can simply be downloaded like web pages to be used in own programs. There, they must be concatenated to get a seamless series again.

All of these access methods are already implemented now and can be used from different groups in-

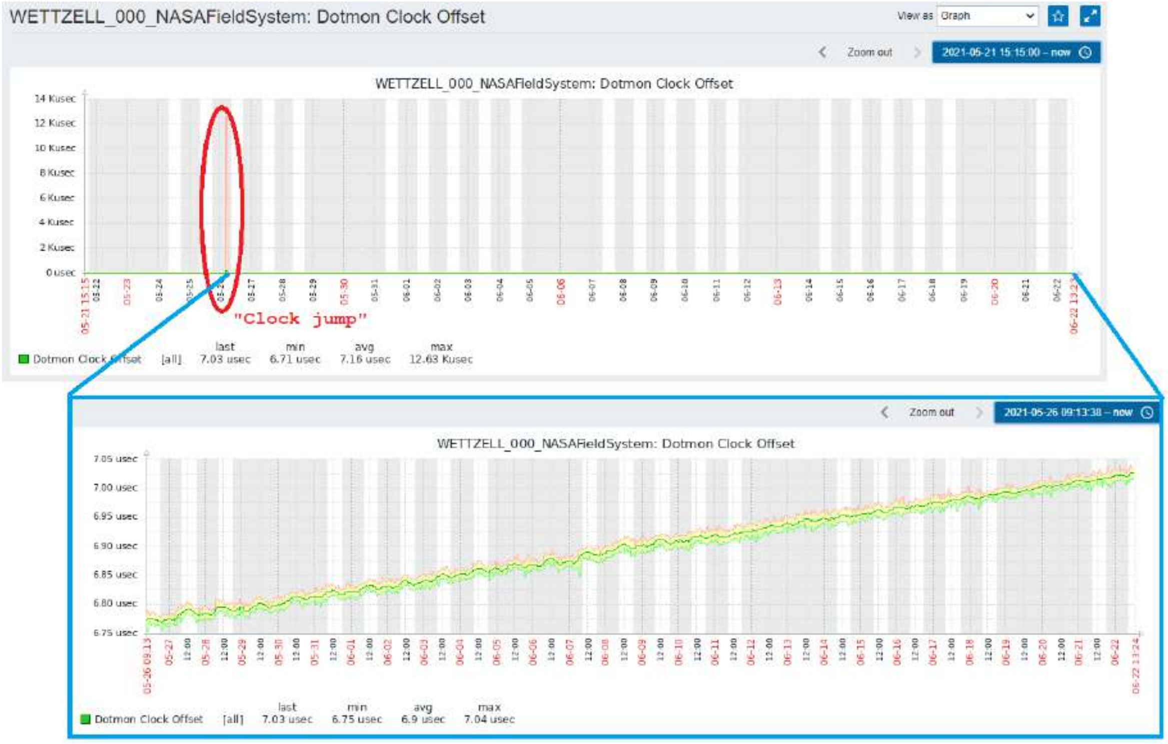

Fig. 3 Sample data set ”dotmon” showing errors and trends.

terested in these data sets. The data sets already help to identify possible error situations at the antenna sites (e.g. clock jumps) or demonstrate trends like maser behavior and quality (see Fig. 3).

4 Conclusions and outlook

The data archive will be improved and extended in the coming years. Additional, data sets should be usable, like system temperatures. Software will be updated permanently. There are currently implementations to directly support the seamless generation of a VGOSDB file ”Met.nc” for the meteorological data or to improve the web pages of the NASA Field System with style sheets.

Parts of the data archive were also financed by a Horizon 2020 program of the European Union. The resulting data archive ”EVN Monitor” was installed at JIVE, Dwingeloo, The Netherlands and started operating.

An essential part to gain success of the archive is to motivate antenna sites to send in data. Therefore, this paper shall also be a call to participate in the archive. Please contact the authors for more information.

Acknowledgment: This project has received funding from the European Union's Horizon 2020 research and innovation programme under grant agreement No 730884 - JUMPING JIVE. We also want to thank all participating student workers, who developed and tested parts of the software for the EU project: Rozerin Aktas, Edoardo Barbieri, Luca Carlin, Suwal Dipesh, Subhan Muhammad Hameed, Mansour Islam, Chenyang Liu, Sebastian Silva, Jingyao Su.

References

JIVE JUMPING JIVE https://jive.eu/jumping-jive, Download 2021-06-29.

Zabbix LLC The Ultimate Enterprise - class Monitoring Platform https://www.zabbix.com/, Download 2021-06-29.

Autonomous Observations at the Wettzell observatory

A. Neidhardt, Ch. Plötz, J. Eckl

Abstract The paper explains the current status of completely autonomous observations with the 20m legacy telescope and the TWIN telescopes of the Wettzell observatory. It shows requirements, current workflows, and demonstrates benefits of unattended observations. The video can be watched under: https://youtu.be/YbY565VABug

Keywords Autonomous, Unattended, Observations, Control&Monitoring

1 Introduction

Meanwhile, all standard observations of VLBI at the Wettzell observatory are operated without permanently available VLBI staff on location. The sessions of three following days are prepared in one step and scheduled to start autonomously in the NASA Field System. When a session starts and is processed, control and monitoring parameter are collected and evaluated to show active safety processes or to evaluate parts of the quality issues. After the session ends, post-processing activities are started. Some tasks in this final step still require manual actions by a person. All together, this runs under the statement of ”smart observations”.

This means that regular observation shifts for VLBI are not necessary anymore which releases manpower for other tasks like maintenance, becoming more and more important. Nevertheless, observatory wide operators are available who regularly check system states for all the different techniques and equipments on site. Safety critical issues are managed by the guard. This is now also possible because also the Laser Ranging Systems can be operated autonomously with an own ”Field System”-like software. Instead of the permanent staff for VLBI in shifts, an on-call service was established which can be activated in cases of critical issues. The service staff has remote access to the systems and can mostly interact and repair things without coming to the observatory in person.

The following reaction times are defined for such services:

Type	**Machine activity**	**On-call service**
Human safety	Machine uses internal safety equipment and automatically stops; alarms are triggered	Service is informed and can check from remote; if necessary, service has to come to the observatory
System safety	like human safety	like human safety
Data losses	Machine continues processing; monitoring shows alarm levels	Service checks situation during regular working hours; service is informed in specific situations and interacts from remote
Data quality	like data losses	Service checks situation during regular working hours;

The table above shows that data losses or data quality issues are possible. Therefore, maintenance and preparation are essential so that automation does not come at the expense of data quality.

A. Neidhardt
FESG Wettzell, Technical University of Munich, Geodetic Observatory Wettzell, Sackenrieder Str. 25, D-93444 Bad Kötzting, Germany

Ch. Plötz · J. Eckl
Federal Agency for Cartography and Geodesy, Geodetic Observatory Wettzell, Sackenrieder Str. 25, D-93444 Bad Kötzting, Germany

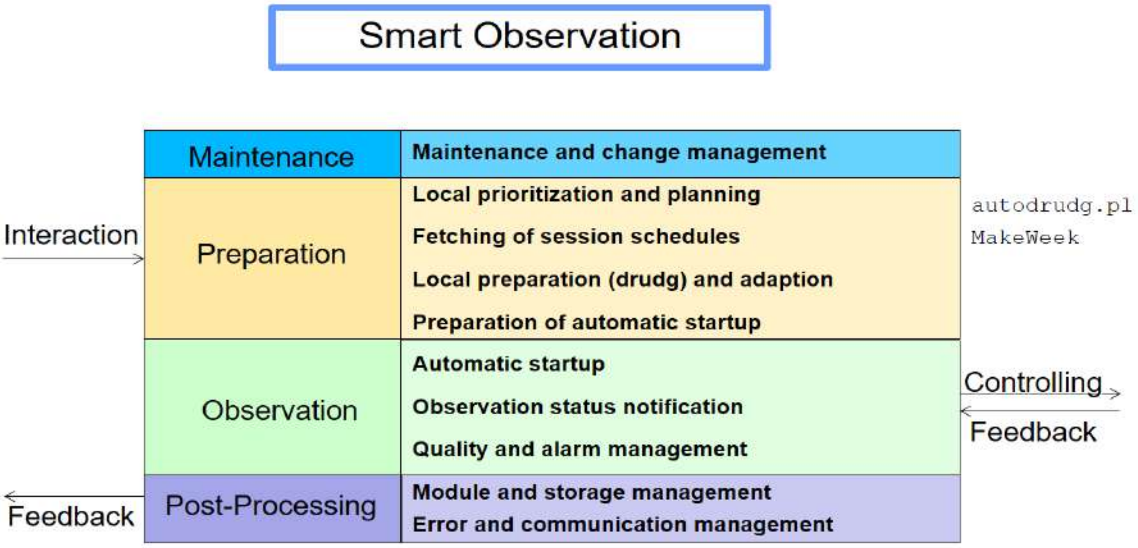

Fig. 1 The processes of a smart observation.

2 Maintenance and change management

Maintenance is one of the most essential work to keep systems on duty and in a good shape. It accompanies the entire process. Maintenance can be split into servicing keeping the system up and upgrading to improve safety, security, or to implement state-of-the-art techniques and reach better quality.

All of these tasks must be logged together with possible error situations, so that decisions can be driven. We use ELOG for that. It is a web based logging utility with predefined classifications and free-text parts to describe changes or error situations and the applied solutions to fix the bugs. Classifications help to search for individual error situations of specific devices at a single telescope. On-call services and operators can log errors using this tool. Engineers and maintenance service can describe changes. All entries are time-tagged and assigned to a person.

The tasks which must be done in servicing is described in a separate checkbook. It describes how often which task must be made how by which person. The checkbook contains sections for safety systems, hoists and cranes, outdoor areas, electrical equipment and air conditioning, cryogenic devices, electronics, mechanics, information technology, time and frequency, geodetic surveying, and other parts like workshops. Tasks are signed after they are finished and individual notes are made which are regularly checked to release larger repairs together with external companies.

3 Preparation of sessions

The preparation phase requires interaction to the external Internet services of the different services, like IVS, EVN, or local schedulers. A local software for the coordination of the observing program ”LEVIKA” (written by T. Schüler) is used to gather information and present on a web server with thinned out information just relevant for the telescopes in duty. It gives an overview in form of the ”big plan” for the coming days.

Schedule files are then fetched and prepared manually following this ”big plan”. In principle, these steps could also be made automatically. But we decided to keep the responsibility for system checks in the hands of a human being. Nevertheless, the steps are done with the script ”autodrudg.pl”, which does the download, the ”drudg”, an adapation of local oscillator frequencies and IF attenuation (if necessary).

Sessions are always prepared for the following 3 to 4 days usually on Monday, Wednesday, and Friday. Each time when sessions are prepared, the responsible person does some system checks, like evaluation of the pointing with ”fivept” and recording tests with a spectrum calculation to get feedback about the system health. General parameters are also gathered in the used web page offered by software ”e-RemotCtrl”.

If everything is alright, the automatic start is scheduled using the program ”MakeWeekend” which was originally be used to prepare the unattended weekend sessions. It checks the start times and boundary conditions (like session interrupts, e.g., with shorter one hour sessions) and injects the start commands with the start time tag to the NASA Field System, which holds the pre-programmed start times and processes the corresponding command right on time.

4 Autonomous observation

The NASA Field System plays the role of a ”chorus leader” sending commands to connected equipment. It does not implement safety and security regulations and just collects data and states from connected devices. These devices and lower-level equipment implement a certified safety and security. This gives a structure, which helps to individually evaluate safety requirements with certified equipment and allows to use external software without any safety regulations just for general purposes.

In the current setup, all alarms and system status information is shown in a central control room and in the room of the guards. We still have a general operator on duty with less knowledge about the VLBI system itself but with overview on different systems. A ZABBIX monitoring system is used to collect system parameters and to trigger alerts. Control tasks are not done by the operator or guard. These tasks with special know how is done by the specialists. They use the central control room to prepare sessions, to run extra observations with special requirements, and to test or solve critical situations. The control room offers access to almost all devices and also to the antenna sites, e.g. also to O’Higgins in the Antarctica.

To implement network security, different zones are established which have no direct forwarding of packages between each other. The basic layer is the antenna control network in the antenna tower which is behind the Antenna Control Unit (ACU). The ACU is the connection point to the system control network which contains all devices required for the complete VLBI system of one antenna, like counters, monitoring equipments, bus connectors, and the NASA Field System PC. This PC is the connection point to the VLBI and other networks of the observatory, which are logically separated into different IP zones. These zones are behind a firewall which protects them from the Internet. Each higher network layer is less responsible for pure control tasks. Safety devices (door switches, emergency stops, etc.) in the low-level bus systems and networks are implemented with hardware, programmable logic controllers, or low level software which are certified.

The pure monitoring is located on the highest level of network, because it just collects data and error states to present them and to assign alarm level and sound. If the presentation fails, the system still keeps the internal safety and security and stops the servos or other devices to avoid critical situations for humans and system components.

Because the monitoring uses web pages and is accessible from all over the Internet, on-call services can check system health states world-wide using a browser. Current system values can be plotted in graphs. Historic alarm states and conditions leading to these situations can be checked and evaluated. Finally, on-call service staff can use SSH tunnels with multi-factor authentication to connect to individual servers of the system or to start the operator input of the NASA Field System. Then, all commands usually entered in front of the system can also be entered from remote.

5 Post-processing

The post-processing is a mixture of automated and manual steps. While emails, log file uploads, or other quality notifications can easily be implemented with software, electronic data transfers and shipments of complete hard drive modules using postal services must be done by staff. Therefore, module and storage management is still operated by humans.

Also the check and evaluation of error and communication situations after the sessions must be done by staff. A manual assessment of monitoring events and logs help to understand the circumstances and to identify causes to avoid future situations under similar conditions.

6 Conclusions and outlook

The daily work at Wettzell observatory clearly demonstrate that autonomous observations are possible and that they have benefits for the personnel deployment. It is still necessary to continuously improve the different parts, tasks, and processing steps (e.g., automatic email sending with individual information at the start and end of a session). Another field is the activation of on-call services with automated phone calls independently from humans. We made some tests using the open source framework ”Asterisk” to do phone calls. Another aspect discusses the reduction of all shifts to automate all systems of the observatory.

References

The ELOG Home Page Home of the Electronic Logbook package by Stefan Ritt https://elog.psi.ch/elog/, Download 2021-06-29.

Neidhardt, A. Applied Computer Science for GGOS Observatories. Communication, Coordination and Automation of Future Geodetic Infrastructures. *Springer International Publishing Switzerland*, 2017. ISBN 978-3-319-40137-9.

Zabbix LLC The Ultimate Enterprise - class Monitoring Platform https://www.zabbix.com/, Download 2021-06-29.

10 years of AuScope VLBI

A. Jaradat, L. McCallum, G. Molera. Calvés, J. McCallum, T. McCarthy

Abstract The AuScope VLBI array, comprising 12-m telescopes in Hobart, Katherine and Yarragadee, has been participating in IVS observations since 2011, marking its ten year anniversary. Originally filling a gap in the global network, triggering a change in scheduling and recording speeds and being amongst the busiest telescopes in the IVS over the past years, the AuScope array has impacted global VLBI observations. This contribution covers 10 years of AuScope VLBI data. Concentrating on Australian stations and baselines, we highlight the achievements of our first decade: after only a short time series was used for ITRF 2014, we can now measure station velocities reliably, well in agreement with GNSS. Furthermore, intra-plate tectonics could be measured to sub-mm accuracy. Besides the overall results of the long time series, we discuss some systematics in the data, which could be linked to operational deficiencies at the telescopes themselves. This publication is corresponding with a video presented in EVGA21 working meeting[1].

Keywords Auscope, VLBI data analysis, IVS observations

1 Introduction

The Very Long Baseline Interferometry (VLBI) technique plays a primary role in geodesy. VLBI is unique in the sense that it is the only technique able to determine the International Celestial Reference Frame (ICRF), e.g., the latest version ICRF3, and the full set of Earth Orientation Parameters (EOP) [Charlot et al., 2020]. Moreover, VLBI is contributing in establishing the International Terrestrial Reference Frame (ITRF), e.g., latest version ITRF 2014 [Altamimi et al., 2016], alongside with other space geodetic techniques, namely Satellite Laser Ranging (SLR), Global Navigation Satellites System (GNSS), and Doppler Orbitography and Radiopositioning Integrated by Satellite (DORIS). The International VLBI Service for Geodesy and Astrometry (IVS) manages the global observations of VLBI [Nothnagel et al., 2017].

The AuScope geodetic VLBI array consists of three radio telescopes located in Hobart (Hb), Katherine (Ke), and Yarragadee (Yg), all of which are managed by the University of Tasmania, see Fig. 1. The AuScope VLBI array joined the global network in 2011 [Lovell et al., 2013]. These are fast slewing with a small dish-size (12-m), which allows a large amount of observation and ideally 24/7 observing time to serve the next generation of the VLBI, known as the VLBI global observing system (VGOS).

Ahmad Jaradat[1], Lucia McCallum[1], Guifré Molera Calvés[1], Jamie McCallum[1], Tiege McCarthy[1].
School of Natural Sciences, University of Tasmania, Private Bag 37, 7001 Hobart, Australia.
Corresponding author: Ahmad.Jaradat@utas.edu.au

[1] https://auscope.phys.utas.edu.au/

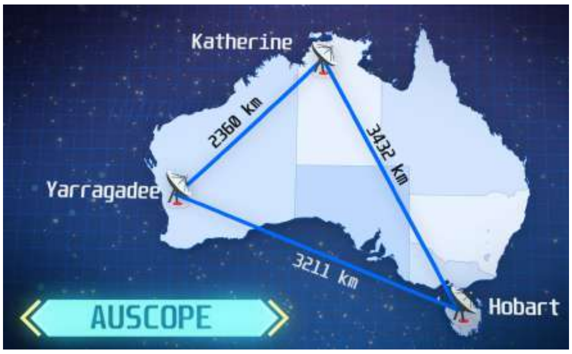

Fig. 1: AuScope VLBI array.

2 VLBI analysis

For 10 years, the Auscope VLBI array has participated in the IVS global observing network. It increases the density of the observation in the southern hemisphere. Plank et al. [2017] showed that this increasing of the observation makes the global observations more homogeneous, which improves the global VLBI results. However, Hb stopped participating in the IVS sessions in 2017 for upgrading to the next generation of the VLBI observing mode; VLBI Global Observing System (VGOS) [Petrachenko et al., 2009] . These 10 years provides a dense time series which make it possible to identify any signal or errors in the observations.

The IVS rapid-turnaround sessions (R1&R4) are carried out twice a week with a stable network, usually 7-11 antennas, therefore, a large amount of observation. This R sessions are considered a vital contributor to the IVS products; ICRF, EOP, and ITRF. In this research, the R1& R4 were collected in the period 2011-2020 and analysed using VieVS [Böhm et al., 2018]. AuScope VLBI telescopes are among the IVS most participating telescopes.

The precision of the observation is found in terms of the Baseline Length Repeatability (BLR) [e.g. MacMillan and Ma, 1994], and the running BLR. The running BLR is a time series of BLR for multiple certain period of time or number of sessions, e.g., BLR every 10 sessions , in order to investigate possible temporal changes of BLR. Moreover, the estimated stations' position residuals to the ITRF 2014 are found, and the stations' velocities are calculated and compared with the ITRF 2014 results.

3 Results

In this research, The estimated antenna positions residuals are the offset to the catalog, in this case to ITRF 2014. For every session, the antenna positions residuals to ITRF 2014 were estimated, as shown Fig. 2, which are divided into the local directions components; Up, East, and North. The Fig. 2a indicates that a seasonal signal may be detected in the Hb Up component, albeit this cannot be confirmed because the observation has been halted in 2017. Moreover, Yg became noisier in 2018 and subsequent years as presented in Fig. 3. The figure shows the standard deviation of the 3D station position every year. This might have been resulted from missing Hb since 2017 and Ke since 2020. To examine this assumption, a simulation was carried out by optimizing the scheduling of one R1 session with these variates; all AuScope stations are included, Yg and Hb are only included, Yg and Ke are only included, and only Yg is included, see Fig. 4. The scheduling optimization was done using VieSched ++ [Schartner and Böhm, 2019] and the simulation using VieVS. When all stations are included in the simulation the Root Mean Square error (RMS) of Yg is about 3.2 mm, while if Ke or Hb is missing the RMS becomes 3.7 mm, and if both are missing the RMS increases to 4.2 mm. These results agree with our assumption as the standard deviation increased in 2018 after Hb missed R1&R4 sessions and significantly increased in 2020 when both Hb and Ke were missed.

Additionally, Ke experienced a discontinuity in 2015, and the results thereafter became more compact. This discontinuity might be due to installing an air conditioner at the station.

Fig. 2 and Table. 1 present the visual and the statistical offset of the antenna positions to the ITRF 2014 model. The offset is up to 1.8 cm, with a relative large mean offset up to a centimeter. This poor priori modelling is apparently because of the short time period of AuScope stations participating in ITRF 2014.

Another aspect of the analysis is comparing the station velocity to the ITRF 2014 result derived solely

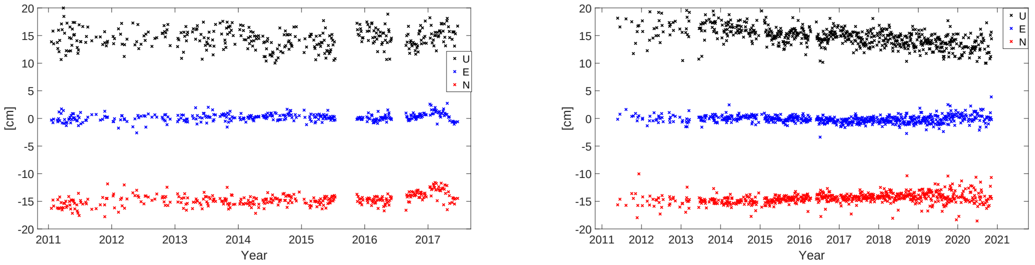

(a) Hb (b) Yg

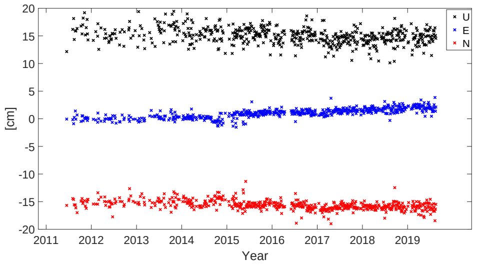

(c) Ke

Fig. 2: The estimated stations' position residuals to the ITRF 2014. Direction components; Up (black), East(blue), and North (red), are offset by 15 cm for better visualization.

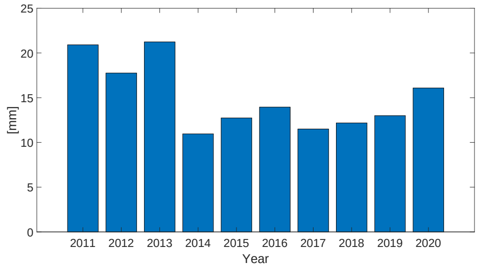

Fig. 3: The standard deviation of the Yg 3D station position every year.

	Up (cm)	East (cm)	North (cm)
Hb	-0.51 ± 1.77	0.20 ±0.69	0.29 ± 1.05
Yg	-0.29 ± 1.70	-0.14 ± 0.69	0.54 ± 0.98
Ke	0.00 ± 1.47	1.02 ± 0.86	-0.62 ± 0.85

Table 1: The estimated residuals statistics for all direction components. The mean offset (first number) and the standard deviation (second number).

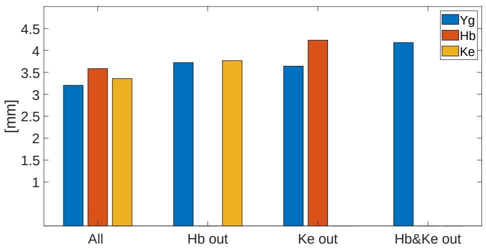

Fig. 4: The simulation results presented as RMS of the Yg 3D station position. The simulation was performed with all AuScope stations included, Yg (blue) and Ke (yellow), Yg and Hb (orange), and only Yg.

from VLBI observations, this illustrated in Fig. 5 and table 2. Fig 5 illustrates the difference in 3D norm vector of the stations velocity between ITRF 2014 GNSS and R1&R4 as estimated in this study, and ITRF 2014 GNSS and ITRF 2014 VLBI. Where the ITRF 2014 GNSS velocity is used as a point of comparison. The R1&R4 velocities of all AuScope stations are about 2 mm/y, and are significantly closer to the ITRF 2014 GNSS results at Yg and Ke. However, in Hb, the ITRF 2014 VLBI is much closer to the GNSS because Hb is linked with Hobart26 (Ho), which has been observing since 1989 [Plank et al., 2017]. This result indicates that the discrepancies between GNSS and VLBI will be much more petite in the upcoming ITRF 2020.

Theoretically, the relative velocities between the stations should be zero, i.e. implying no relative motion, because the stations are on the same tectonic plate, but ITRF 2014 based on only 3 years of data estimated intra-plate motion between telescopes. The presented analysis produced a more realistic result with estimated velocity in mm and sub-mm domain. As one can see in Table 2, the VLBI solution in ITRF2014 predicts an increase of 2.4 mm/yr of the Hb-Ke baseline. The new estimates show hardly any change (0.1 mm/y), which is considerably more consistent with the geophysical expectation as well as with the results measured by GNSS.

Baseline	R1&R4	ITRF2014 VLBI
Hb-Yg	0.08	2.41
Hb-Ke	-2.11	15.56
Yg-Ke	-0.49	8.21

Table 2: Relative stations velocity [mm/y]

Additionally, the BLR is relativity small, as presented in Table 3. The two baselines with Hb are a bit worse because Hb stopped contributing in R1&R4 sessions in 2017. However, the BLR improves on the result obtained by Plank et al. [2017] after analysing R1&R4 from 1/2011 to 11/2015. For instance, in Plank et al. [2017] analysis, the BLR at the Yg-Ke baseline was 8.6 mm, whereas in this study, the precision is doubled at 4.2 mm.

Baseline	R1&R4	Plank et al. [2017]
Hb-Yg	8.2	9
Hb-Ke	14.8	13
Yg-Ke	4.2	8.6

Table 3: BLR of R1&R4 sessions from our analysis and Plank et al. [2017] at the AuScope baselines [mm].

We use the running BLR to detect any possible changes over time. Indeed, we discovered significantly higher values at the beginning of the years, which occurred during local summer months. Some deeper investigations revealed issues with the stability of a calibration signal (phasecal tone) when the temperature reaches certain threshold values during these periods. These effects manifest themselves as so called clock-breaks in the VLBI analysis [Balidakis et al., 2021, this edition]. While this issue certainly requires further investigation, we recommend not to use phasecal corrections at Yg any more and disconnected the phasecal tones at Yg , see Fig. 6.

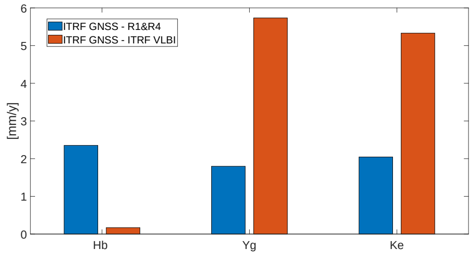

Fig. 5: The difference in the norm vector of the stations velocity. The blue is the norm velocity vector of ITRF GNSS velocity minus the norm velocity vector of 10 years of R1&R4 data. The orange color presents the norm velocity vector of ITRF GNSS velocity minus the norm velocity vector of ITRF VLBI.

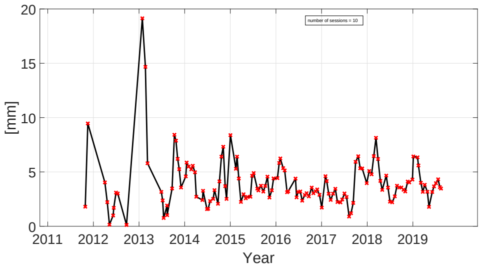

Fig. 6: The running BLR of R1&R4 sessions at the baseline Ke-Yg every 10 sessions.

If you would like to emphasize a few of the main results, you could add a sentence like: "Analysing 10 years of data shows that we can measure the VLBI station positions in a global frame with a precision of about 15 mm in the height component and 7-10 mm in the horizontal components. " (but up to you)

4 Conclusions and outlook

Since 2011, the AuScope VLBI array has been collecting data. Analysing these 10 years of data reveals that we can measure the VLBI station positions in a global frame with a precision of about 15 mm in the height component and 7-10 mm in the horizontal components. When compared to ITRF 2014, the estimated station velocities have improved significantly. Moreover, some signals were identified, such as a discontinuity in the Ke station coordinate in 2011 and a signal in Hb station coordinate. The Yg station coordinate has been noisy since 2018, which could be due to missing Hb in 2017 and Ke in 2020 and beyond as they begin their VGOS upgrades, as investigated in a simulation study. Another explanation might be technical issues with temperature-sensitive calibration signals. The stations velocities in our analysis are in better agreement with ITRF 2014 GNSS results than ITRF 2014 VLBI at Yg and Ke.

In addition, in the southern hemisphere, the BLR is negatively correlated with the summer time of year. The correlation may be due to the phascal tone with the high temperature. As a consequence, the manual phascal will be used instead from now on.

5 Acknowledgement

This study made use of data collected through the AuScope array. The array is being operated by the University of Tasmania, contracted through Geoscience Australia. The authors are grateful to the International VLBI Service for Geodesy and Astrometry (IVS) for access to VLBI data products used in this paper. L. M. thanks the Australian research council for supporting her project (ARC DE180100245).

References

Altamimi, Z., Rebischung, P., Métivier, L., and Collilieux, X. (2016). ITRF2014: A new release of the international terrestrial reference frame modeling nonlinear station motions. *Journal of Geophysical Research: Solid Earth*, 121(8):6109–6131.

Balidakis, K., Anderson, J. M., McCallum, L., McCallum, J., Wang, J., Heinkelmann, R., and Schuh, H. (2021). On the Origin of Clock Breaks Detected in Geodetic VLBI Data Analysis . In *Proceedings of the 25th Meeting of the European VLBI Group for Geodesy and Astronomy, this edition*.

Böhm, J., Böhm, S., Boisits, J., Girdiuk, A., Gruber, J., Hellerschmied, A., Krásná, H., Landskron, D., Madzak, M., Mayer, D., et al. (2018). Vienna VLBI and satellite software (VieVS) for geodesy and astrometry. *Publications of the Astronomical Society of the Pacific*, 130(986):044503.

Charlot, P., Jacobs, C., Gordon, D., Lambert, S., de Witt, A., Böhm, J., Fey, A., Heinkelmann, R., Skurikhina, E., Titov, O., et al. (2020). The third realization of the international celestial reference frame by very long baseline interferometry. *Astronomy & Astrophysics*, 644:A159.

Lovell, J., McCallum, J., Reid, P., McCulloch, P., Baynes, B., Dickey, J., Shabala, S., Watson, C., Titov, O., Ruddick, R., et al. (2013). The AuScope geodetic VLBI array. *Journal of Geodesy*, 87(6):527–538.

MacMillan, D. and Ma, C. (1994). Evaluation of very long baseline interferometry atmospheric modeling improvements. *Journal of Geophysical Research: Solid Earth*, 99(B1):637–651.

Nothnagel, A., Artz, T., Behrend, D., and Malkin, Z. (2017). International VLBI service for geodesy and astrometry. *Journal of Geodesy*, 91(7):711–721.

Petrachenko, B., Niell, A., Behrend, D., Corey, B., Boehm, J., Charlot, P., Collioud, A., Gipson, J., Haas, R., Hobiger, T., Koyama, Y., Macmillan, D., Malkin, Z., Nilsson, T., Pany, A., Tuccari, G., Whitney, A., and Wresnik, J. (2009). Design aspects of the VLBI2010 system. In *Progress report of the IVS VLBI2010 committee*, page pp 56.

Plank, L., Lovell, J., McCallum, J., Mayer, D., Reynolds, C., Quick, J., Weston, S., Titov, O., Shabala, S., Böhm, J., et al. (2017). The AUSTRAL VLBI observing program. *Journal of geodesy*, 91(7):803–817.

Schartner, M. and Böhm, J. (2019). VieSched++: a new VLBI scheduling software for geodesy and astrometry. *Publications of the Astronomical Society of the Pacific*, 131(1002):084501.

A jump in the VLBI position of the radio galaxy J1147+3501

O. Titov, S. Frey

Abstract The fundamental celestial reference frame is realized by regular VLBI observations of extragalactic radio sources. Compact radio-emitting active galactic nuclei also serve as reference points for relative positioning of other radio sources. For both purposes, the long-term positional stability of the reference objects is essential. VLBI absolute astrometric data indicate that the nucleus of the radio galaxy J1147+3501 (at redshift $z = 0.063$) apparently changed its position significantly, by more than 20 milliarcsec some time between 1999 and 2017. Based on high-resolution VLBI images of the source obtained at multiple epochs, we suggest that this is a consequence of a drastic change in its brightness distribution.

Keywords active galactic nuclei, celestial reference points, VLBI, astrometry, imaging

1 Introduction

Astrometric very long baseline interferometry (VLBI) observations have traditionally been performed at *S* and *X* bands, around the frequencies of 2.3 and 8.4 GHz, respectively. The structure of a typical radio-loud active galactic nucleus (AGN) is dominated by compact synchrorton self-absorbed emission on milliarcsecond (mas) or sub-mas angular scales. This makes the radio 'cores' suitable astrometric reference objects. However, the apparent location of these celestial reference points is affected by the actual brightness distribution of the source. In an ideal case of a compact featureless source that is (nearly) unresolved on the longest intereferometric baselines, the position is practically defined by the brightness peak at *X* band.

Over a long period of time (several decades), most of the reference AGN sources show only moderate astrometric instability, usually within 1 mas (e.g. Titov, 2007; Titov et al., 2011; Moór et al., 2011). This is the basis of the accurate VLBI-defined International Celestial Reference Frame (ICRF), an essential product for astrometric and astrophysical studies. However, long-term coordinate time series of certain radio AGNs can occasionally demonstrate dramatic positional changes in the order of $\sim 10 - 100$ mas, sometimes over a relatively short period of time, $5 - 20$ yr. We have recently identified a couple of them (Titov & Frey, 2020; Frey & Titov, 2021), and as the astrometric VLBI data accumulate, the list is growing. Such unforeseen dramatic changes in the source positions can cause problems for astrometric/geodetic VLBI data analysis because the software packages cannot properly handle them. Also, relying on these objects as phase-reference calibrator sources for relative VLBI astometric measurements could lead to a systematic offset in the target source position.

On the other hand, from astrophysical point of view, the sources that change their apparent position rapidly and by a large amount are potentially interesting cases that deserve detailed follow-up investigations. There can be various factors responsible for astrometric instablilities in radio-loud AGNs. In some cases, there are changes in the mas-scale core–jet stuctures which manifest themselves in apparent

---

Oleg Titov
Geoscience Australia, PO Box 378, Canberra 2601, Australia

Sándor Frey
Konkoly Observatory, ELKH Research Centre for Astronomy and Earth Sciences, Konkoly Thege Miklós út 15-17, 1121 Budapest, Hungary

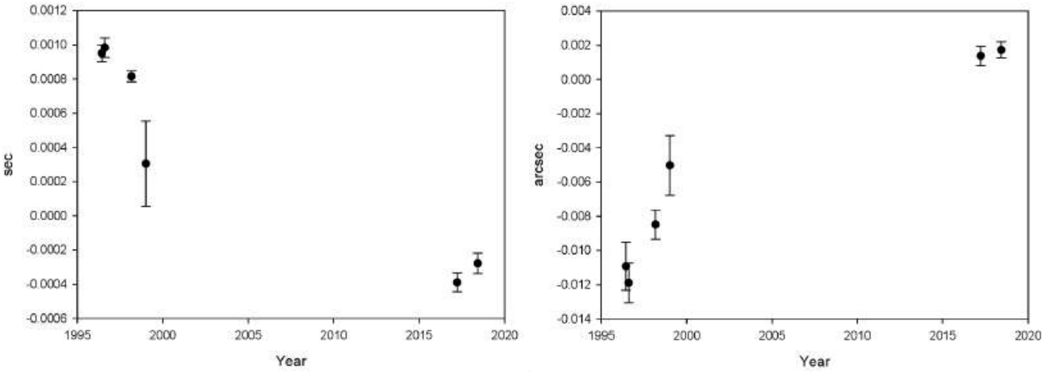

Fig. 1 Relative right ascension (measured in seconds; left) and declination (measured in arcseconds; right) of J1147+3501 as a function of time, based on the astrometric VLBI solutions. Between 1996 and 2017, the reference position apparently shifted by nearly -20 mas in right ascension and $+13$ mas in declination, consistently with the substantial changes of the source brightness distribution seen in the X-band images (Fig. 2).

superluminal component motions. This, especially if coupled with a significant brightening of a jet component, could result in a sudden displacement of the brightness peak and thus the reference point within the extended source structure. Rapid and high-amplitude flux density variability in a VLBI core (i.e. the optically thick base of a relativisic jet whose emission is Doppler-boosted because it is directed close to the line of sight) that is embedded in a complex radio structure can also result in apparent displacement of the astrometric reference point. In other cases, the radio sources may belong to the class of compact symmetric objects (CSOs), a type of young AGNs with small (less than 1 kpc) overall projected size (e.g. An & Baan, 2012). Their prominent radio emission originates from powerful hotspots embedded in a symmetrically expanding radio lobe structure on both sides of a weak or often even undetected radio core. Astrometric instability can be caused by flux density variations in the hotspots. These cases can possibly be revealed by high-resolution multi-frequency VLBI imaging observations performed at multiple epochs.

Here we present the case of J1147+3501 (B2 1144+35B), the nucleus of a nearby giant radio galaxy at redshift $z = 0.063$, whose apparent position changed by more than 20 mas during the first two decades of this millennium.

2 Astrometric analysis of J1147+3501

The most recent 3rd realization of ICRF (Charlot et al., 2020) lists the coordinates of more than 4500 objects determined by S/X-band VLBI observations. The source J1147+3501 is included in the list. We processed six observing sessions (96JUN07XV, 96AUG07XO, 98MAR03XE, 99JAN05XE, 17MAR03XC, 18JUN03XC) of the permanent geodetic and astrometric VLBI program between 1996 and 2018. These sessions are coordinated by the International VLBI Service for Geodesy and Astrometry (IVS, Nothnagel et al., 2017). Radio source coordinates were estimated once per session, together with Earth orientation parameters and station coordinates by the OCCAM 6.3 software (Titov et al., 2004). More details of the standard analysis procedure can be found in Titov & Frey (2020).

Albeit sparsely sampled in time, the positions of J1147+3501 for all six available epochs expose a large apparent displacement of the radio source between 1999 and 2017, as indicated in Fig. 1. Assuming a linear change, our estimates of the proper motion are -0.84 ± 0.05 mas yr^{-1} in right ascension and 0.56 ± 0.05 mas yr^{-1} in declination, resulting in a total apparent proper motion of 1.01 ± 0.07 mas yr^{-1}. Such a large proper motion inferred from the change in the VLBI position of J1147+3501 is abnormally high among radio AGN over a long period of time.

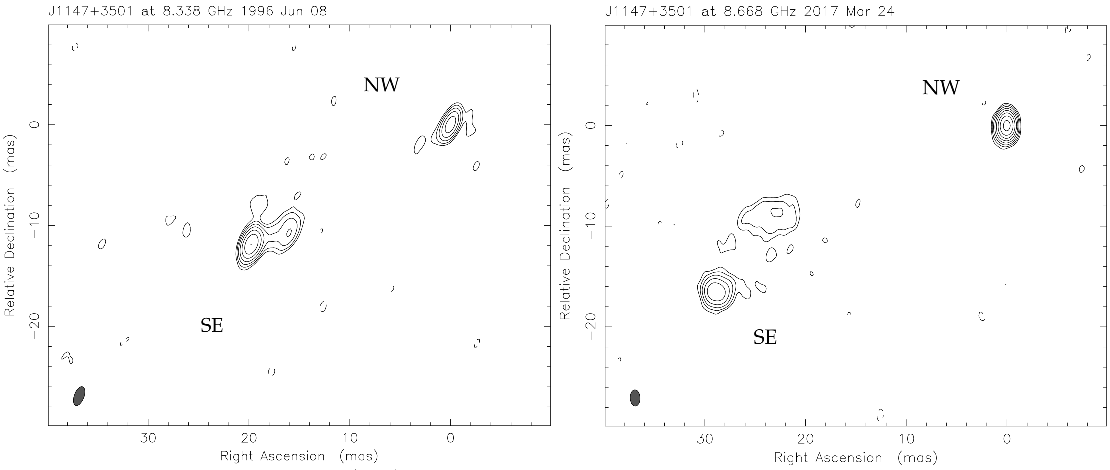

Fig. 2 X-band VLBA images of J1147+3501 made on 1996 Jun 8 (left) and 2017 Mar 24 (right). The (0,0) position of the 1996 image is shifted from the brightness peak so that the north-western (NW) components coincide at both epochs. The south-eastern (SE) feature was the brightest in 1996 but faded and moved away by 2017. The lowest contour levels are drawn at $\pm3\sigma$ image noise levels, 2.55 mJy beam^{-1} and 0.52 mJy beam^{-1} in 1996 and 2017, respectively. The positive contour levels increase by a factor of 2. The peak brightness is 164 mJy beam^{-1} in 1996, and 88.1 mJy beam^{-1} in 2017. The half-power width of the elliptical Gaussian restoring beam is shown as an ellipse in the lower-left corner of the images.

3 VLBI imaging of J1147+3501

The mas-scale radio structure of J1147+3501 has been intensively studied with VLBI imaging at cm wavelengths (e.g. Giovannini et al., 1990, 1999, 2007; Henstock et al., 1995). The inner jet structure is complex, characterized by flux density variability and apparent superluminal ($\sim 2c$) expansion.

To seek a plausible explanation for the large positional change, we turned to archival VLBI imaging data made available in the Astrogeo database[1]. We downloaded the calibrated X-band visibility data sets obtained with the U.S. Very Long Baseline Array (VLBA) on 1996 June 8 (project code BB023, observed in the framework of the VLBA Calibrator Survey, Beasley et al., 2002), and on 2017 Mar 24 (project code UF001E, imaging of ICRF3 sources). We performed standard hybrid mapping using the Difmap package (Shepherd, 1997). The resulting images are shown in Fig. 2. While both experiments were short snapshot observations, the two dominant features of the inner jet are clearly seen. According to the two images, the brightness distribution of the source changed significantly.

In the pc-scale radio jet, Giovannini et al. (1999) identified the radio core with the north-western (NW) component seen in Fig. 2 based on its inverted radio spectrum. This is supported by the accurate *Gaia* (Gaia Collaboration, 2018) optical position of J1147+3501 which is consistent with the NW component being located in the nucleus of the galaxy. On the other hand, the south-eastern (SE) feature is a complex jet component moving away from the core (Giovannini et al., 1999). As well as in 1993 (see the 5-GHz image of Henstock et al., 1995), the SE component was brighter than the core in 1996 (Fig. 2, left) and therefore served as the reference point in the astrometric VLBI observations. By 2017, the flux density of the SE jet component (as well as the total flux density of the entire radio source) significantly decreased, making the true core (NW) the brightest (Fig. 2, right). Based on their sensitive VLBI imaging performed in 2002 and 2005, Giovannini et al. (2007) still found the jet component (SW) brighter and determined the coordinates of the core (NW) with phase-referencing to nearby calibrators. That position agrees with our most recent coordinate solution from 2018, right ascension $11^{\mathrm{h}}47^{\mathrm{m}}22.12903^{\mathrm{s}} \pm 0.00006^{\mathrm{s}}$ and declination $+35^{\circ}01'07.5353'' \pm 0.0005''$.

---

[1] http://astrogeo.org/

4 Conclusions

The case of J1147+3501 demonstrates that the apparent position of certain VLBI reference sources may abruptly change because of structural and/or flux density variability. This underlines the need for regular astrometric monitoring and parallel VLBI imaging of these sources. Relative astrometric (phase-referencing) studies should make sure the catalogued positions of reference sources coincide with the actual brightness peak.

Acknowledgements

The National Radio Astronomy Observatory is a facility of the National Science Foundation operated under cooperative agreement by Associated Universities, Inc. We acknowledge the use of archival calibrated VLBI data from the Astrogeo Center database maintained by Leonid Petrov. S.F. was supported by the Hungarian National Research, Development and Innovation Office (OTKA K134213).

References

An T, Baan W A (2012) The Dynamic Evolution of Young Extragalactic Radio Sources. *Astrophys. J.*, 760, 77, doi: 10.1088/0004-637X/760/1/77.

Beasley A J, Gordon D, Peck A B, et al. (2002) The VLBA Calibrator Survey-VCS1. *Astrophys. J. Suppl. Ser.*, 141, 13–21, doi: 10.1086/339806.

Charlot P, Jacobs C S, Gordon D., et al. (2020) The third realization of the International Celestial Reference Frame by very long baseline interferometry. *Astron. Astrophys.*, 644, A159, doi: 10.1051/0004-6361/202038368.

Frey S, Titov O (2021) Change in the Radio Structure and Position of the Quasar CTA 21. *Res. Notes AAS*, 5, 60, doi: 10.3847/2515-5172/abf123.

Gaia Collaboration, Brown A G A, Vallenari A, Prusti T, et al. (2018) Gaia Data Release 2. *Astron. Astrophys.*, 616, A1, doi: 10.1051/0004-6361/201833051.

Giovannini G, Feretti L, Comoretto G. (1990) VLBI Observations of a Complete Sample of Radio Galaxies. I. Snapshot Data. *Astrophys. J.*, 358, 159–163, doi: 10.1086/168970.

Giovannini G, Taylor G B, Arbizzani E, et al. (1999) B2 1144+35: A Giant Low-Power Radio Galaxy with Superluminal Motion. *Astrophys. J.*, 522, 101–112, doi: 10.1086/307640.

Giovannini G, Giroletti M, Taylor G B (2007) B2 1144+35B, a giant low power radio galaxy with superluminal motion. Orientation and evidence for recurrent activity. *Astron. Astrophys.*, 474, 409–414, doi: 10.1051/0004-6361:20078058.

Henstock D R, Browne I W A, Wilkinson P N, et al. (1995) The Second Caltech–Jodrell Bank VLBI Survey. II. Observations of 102 of 193 Sources. *Astrophys. J. Suppl. Ser.*, 100, 1–36, doi: 10.1086/192206.

Moór A, Frey S, Lambert S B, Titov O A, Bakos J (2011) On the Connection of the Apparent Proper Motion and the VLBI Structure of Compact Radio Sources. *Astron. J.*, 141, 178, doi: 10.1088/0004-6256/141/6/178.

Nothnagel A, Artz T, Behrend D, Malkin Z (2017) International VLBI Service for Geodesy and Astrometry. Delivering high-quality products and embarking on observations of the next generation. *J. Geod.*, 91, 711–721, doi: 10.1007/s00190-016-0950-5.

Shepherd M C (1997) Difmap: an Interactive Program for Synthesis Imaging. *Astronomical Data Analysis Software and Systems VI*, ASP Conf. Ser. 125, eds. Hunt G, Payne H E, 77–84.

Titov O A (2007) Apparent proper motions of radio sources from geodetic VLBI data. *Astron. Lett.*, 33, 481–487, doi: 10.1134/S1063773707070055.

Titov O, Tesmer V, Böhm J (2004) OCCAM v.6.0 Software for VLBI Data Analysis. *Proc. International VLBI Service for Geodesy and Astrometry 2004 General Meeting*, NASA/CP-2004-212255, eds. Vandenberg N R, Baver K D, 267–271.

Titov O, Lambert S B, Gontier A-M (2011) VLBI measurement of the secular aberration drift. *Astron. Astrophys.*, 529, A91, doi: 10.1051/0004-6361/201015718.

Titov O, Frey S (2020) An Apparent Jump in the Radio Position of J1147+3501. *Res. Notes AAS*, 4, 108, doi: 10.3847/2515-5172/aba42c.

EVGA2021

Making VLBI Great Again!

European VLBI Group For
Geodesy and Astrometry

CHALMERS

ISBN: 978-91-88041-41-8